

DISSERTATION

MODELING DEFORMATION TWINNING IN BCC TRANSITION METALS

Submitted by

Anik H M Faisal

Department of Mechanical Engineering

In partial fulfillment of the requirements

For the Degree of Doctor of Philosophy

Colorado State University

Fort Collins, Colorado

Fall 2023

Doctoral Committee:

Advisor: Christopher Weinberger

Donald Radford

Kaka Ma

Paul Hyeliger

Copyright by Anik Faisal 2023

All Rights Reserved

ABSTRACT

MODELING DEFORMATION TWINNING IN BCC TRANSITION METALS

Deformation twinning is one of the important deformation mechanisms in body centered cubic (BCC) transition metals, especially under low temperature and high strain rate conditions. Plastic deformation via deformation twinning has been studied for decades both experimentally and computationally however, atomic level insights such as critical nuclei size, their local atomic structures and energetics which are important parameters in modeling twin nucleation has been lacking. In this work, deformation twins in BCC transition metals and their atomic level structures and energetics have been rigorously studied to reveal the full atomic level details of twin nucleation and propagation. As such, critical thickness of deformation twins in BCC transition metals have been a topic of debate with many computational and experimental studies accepting a three-layer twin thickness based on nucleation from a screw dislocation without proof whereas recent in-situ experiments suggest six-layer thick twin nuclei observed via High resolution transmission electron microscopy (HRTEM). In this study, we have determined the critical twin nuclei thickness in these metals using atomistic simulations to examine atomic structure and energetics of deformation twins under both zero and nonzero finite pure shear stresses. Our study reveals that twins in group VB BCC transition metals nucleate as two-layer thick nuclei under stress as opposed to the three-layer thick twin nuclei under zero stress. For group VIB BCC transition metals, for both zero and nonzero stresses, the critical twin nuclei thickness is two layer near reflection. As the twins grow and stress is relieved, twins under finite stresses adopt configurations that are much closer to the zero stress stability predictions. In addition to nucleation, growth of mechanisms of twins are explored and computational insights into the growth of twins in Tungsten bicrystals explaining multi-layer growth as opposed to layer-by-layer growth associated with small barriers.

Free-end string simulations were used to investigate energy barrier associated with homogeneous twin nucleation using embedded atom method (EAM) potentials. Since homogeneous twin nucleation occurs near the ideal strengths of the material described by the potentials, energy barrier calculations were not possible for all BCC transition metals as some available potentials break down under large stresses. Moreover, density functional theory (DFT) simulations are known to be more accurate in describing atomic bonding but direct nucleation simulations in bulk crystals is prohibitively expensive. Hence, existing dislocation nucleation models are thoroughly analyzed to examine the behavior of these models near ideal strength of the material because spontaneous nucleation of dislocations occurs at high stresses. From there, a robust homogeneous twin nucleation model that includes elastic interaction among the twinning dislocation loops is developed which is able to replicate energy barrier data from free-end string simulations for multiple interatomic potentials. This model takes atomistic simulation inputs such as the concurrent twinning generalized stacking fault (GSF) energy curves and corresponding burgers vector of the twinning dislocations to compute the energy barriers as a function of applied stress. This model can be useful in modeling homogeneous twin nucleation all BCC transition metals and has the potential advantage of using DFT simulation inputs for accurate description of atomic bonding within the twin nuclei.

Finally, nucleation stresses for twinning in bulk crystals have been studied to investigate whether the formation of twinning in experimental studies were initiated by homogeneous nucleation. Upper and lower bounds of stress values required for homogeneous twin nucleation has been computed and a semi-empirical model has been developed to predict homogeneous twin nucleation stresses as a function of temperature and strain rate. This analysis shows that reported critical resolved shear stress (CRSS) values in experimental studies are not associated with homogeneous twin nucleation despite some modeling studies claiming otherwise.

ACKNOWLEDGEMENTS

I would like to express my gratitude towards my advisor, Professor Dr. Chris Weinberger, for his continued support, mentorship and relentless guidance during this work. I would also like to thank past and present members of the Advanced Computational Materials Engineering (ACME) lab: Ian Bakst, Matt Guziewski, Xiaochuan Tang, Rofiques Salehin, Brennan Watkins, Carter Stotts, Hunter Brumblay and Sajjad Hossain for insightful conversations and general camaraderie they provided.

Additionally, I would like to recognize the members of my committee, Dr. Paul Heyliger, Dr. Donald Radford, and Dr. Kaka Ma, for their useful input and guidance during this process.

This research was supported through grants from Office of Naval Research under Grant Nos. N00014-17-1-2810 and N00014-20-1-2788. This work utilized the RMACC Summit and Alpine supercomputers, which are supported by the National Science Foundation (awards ACI-1532235 and ACI-1532236), the University of Colorado Boulder and Colorado State University. The RMACC Summit and Alpine supercomputers are a joint effort of the University of Colorado Boulder and Colorado State University. This work also utilized computing resources provided by CSU engineering technology services especially the ASHA computing cluster.

DEDICATION

To my parents for their unwavering support and love.

TABLE OF CONTENTS

ABSTRACT	ii
ACKNOWLEDGEMENTS	iv
DEDICATION	v
LIST OF TABLES	viii
LIST OF FIGURES	ix
Chapter 1 Introduction	1
Chapter 2 Literature review	3
2.1 Twinning in crystalline materials	3
2.2 Deformation twinning in BCC transition metals	6
2.3 Twin Boundary Structures in BCC transition metals	12
2.4 Nucleation and propagation of twins in BCC transition metals	15
2.5 Twinning stress in BCC transition metals	21
Chapter 3 Methodology	24
3.1 Atomistic Modeling	24
3.1.1 EAM Potentials	24
3.1.2 The Potential Energy Surface	25
3.1.3 Energy Minimization	27
3.1.4 Methods for Finding Saddle Points	28
3.2 Electronic Structure	29
3.2.1 Schrodinger’s Equation	29
3.2.2 Density Functional Theory	30
3.2.3 DFT Simulation Parameters	38
3.2.4 Structural Relaxation	39
3.3 Metastable Twin Boundary Structures	41
3.4 Twin boundary GSF curve	43
3.5 Twinning GSF curve	44
3.5.1 Sequential TGSF curves	44
3.5.2 Concurrent TGSF curves	45
3.6 Direct simulation of twin nucleation	46
3.7 Bond length comparison analysis to determine twin thickness	47
3.7.1 Derivation of reference BLC parameters	54
3.8 Constrained twin stability analysis	60
3.9 Twin Boundary Migration GSF Curve	62
Chapter 4 Modeling twin boundary structures in BCC transition metals	63
4.1 Atomic structures of twin boundaries in BCC transition metals	63
4.2 Modeling twin boundary structures	65
4.2.1 Interatomic Potentials	65

4.2.2	Density Function Theory	76
4.2.3	Analytical model of the TBGSF curve	81
4.3	Conclusions	84
Chapter 5	Modeling twin nucleation and growth	87
5.1	Critical twin nuclei thicknesses in BCC transition metals	90
5.1.1	Empirical potential predictions of twin nucleation	90
5.1.2	DFT predictions of critical twin thickness in BCC transition metals . . .	105
5.1.3	Conclusion	128
5.2	Growth of twins in BCC transition metals	130
5.2.1	Twin growth in BCC Tungsten	131
Chapter 6	Modeling energetics of twin nucleation	137
6.1	Modeling partial dislocation nucleation	137
6.1.1	Analysis of MD simulation results and the exponent α	141
6.1.2	Continuum Models	143
6.2	Continuum model of twin nucleation in BCC transition metals	167
Chapter 7	Modeling twinning stress in BCC transition metals	174
7.1	Upper and lower limits of twin nucleation stress	175
7.1.1	Upper bound	175
7.1.2	Lower bound	177
7.2	Twin stress prediction as a function of temperature and strain rate	179
Chapter 8	Concluding Remarks	184
Chapter 9	Future Work	187
Bibliography	190

LIST OF TABLES

2.1	Experimental twinning stresses in BCC metals	23
4.1	TBGSF curve predictions from EAM potentials	73
4.2	Equilibrium structures from EAM potentials	75
4.3	Equilibrium structures from DFT	81
5.1	BLC analysis results for constrained equilibrium structures found in the twin stability curves under 5.49 GPa pure shear stress for BCC Ta, described by Ravelo2 EAM potential [77] shown in Figure 5.3(a). Faulted layers are counted if the bond length difference, δ deviates from the bond length differences in strained BCC crystals by more than 10% of the magnitude of the repeat lattice vector.	93
5.2	BLC analysis results for constrained equilibrium structures found in the twin stability curves under 12.51 GPa pure shear stress for BCC Mo, described by ATFS EAM potential [78] shown in Figure 5.9(a). Faulted layers are counted if the bond length difference, δ deviates from the bond length differences in strained BCC crystals by more than 10% of the magnitude of the repeat lattice vector.	99
5.3	BLC analysis results for constrained equilibrium structures found in the twin stability curves with DFT simulations under 6.42 GPa pure shear stress for BCC Ta shown in Figure 5.15(b) in the main text. Faulted layers are counted if the bond length difference, δ deviates from the bond length differences in strained BCC crystals by more than 10%.	106
5.4	BLC analysis results for constrained equilibrium structures found in the twin stability curves with DFT simulations under 14.07 GPa pure shear stress for BCC Mo shown in Figure 5.20(b). Faulted layers are counted if the bond length difference, δ deviates from the bond length differences in strained BCC crystals by more than 10%.	111
6.1	The best fit parameters for Equation (6.2) for the atomistic data surveyed in the literature.	143
7.1	Maximum stresses computed from sequential TGSF curves and $\sigma - \epsilon$ curves.	177
7.2	Minimum stress for twin nucleation in BCC transition metals	178
7.3	Minimum stress for twin nucleation compared against Ojha et al. prediction	179
7.4	Experimental CRSS values for BCC Ta, Mo, W, and Fe in literature compared with our prediction of homogeneous nucleation strength using nucleation energy barriers computed using Ravelo 2 [77] for Ta, ATFS [78] potentials for Mo and Fe as well as Zhou potential [80] for W.	182

LIST OF FIGURES

2.1	A pure reflection twin in BCC crystal [2].	4
2.2	Five out of the six twinning elements shown schematically. Reproduced from [3] . . .	5
2.3	The change in shape of a hemispheric crystal because of deformation twinning. Re- produced from [4] with permission.	5
2.4	Diagram showing how the hemispherical crystal becomes deformed to an ellipsoid by deformation twinning. Reproduced from [4] with permission.	5
2.5	(a) K_1 and S planes shown in the conventional BCC unit cell, (b) Atomic movement required for twinning in BCC crystal with projection vector $[1\bar{1}0]$. Reproduced from [1] with permission.	6
2.6	One of the earliest direct observation of deformation twinning in BCC transition metal, Ta was made by Shields et al. [11]. Slip and twin trace analyses in Single crystal Ta deformed at 4.2K adopted from Shields et al. (a) Typical fine slip traces observed in Ta tested in tension (T.A = tensile axis) (b) Evenly distributed twins observed on Ta tested in compression (C.A = compression axis). The micrographs are reproduced from [11] with permission.	8
2.7	(a) Deformation twins in tantalum (zoomed in 100x). Specimen mechanically polished and etched in 2 parts lactic acid, 1 part HF, and 1 part HNO_3 for 40 minutes and then in equal parts in HF and HNO_3 for 5 minutes. (b) same specimen zoomed in 500x. Reproduced from [25] with permission.	10
2.8	(a) Transmission electron micrograph of the intersecting twins in nanocrystalline Ta. The twinning directions are marked with two white arrows. (b) High-resolution TEM image of a nanograin, featuring a deformation twin. Reproduced from [28] with per- mission.	11
2.9	The two different twin structures are shown in (a) pure reflection and (b) isosceles. The dashed lines show the approximate location of the boundary between the two twinned structures while the blue boxes illustrate a detail view shown in (c) and (d) for each twin boundary structure, respectively.	13
2.10	An illustration of twin nucleation model via pole mechanism in bcc lattice [3, 48]. An expanding slip loop stemming from sessile dislocation (pole) cross-slips into a perpendicular plane. Subsequently, the dislocation continues to revolve around the pole assisted by further cross-slips and hence generates layers of stacking faults, i.e., the twin embryo. Reproduced from [52] with permission from author.	16
2.11	The dissociation of a screw dislocation with three-fold core in bcc materials into three frac- tion dislocations under applied stress [36, 37, 51, 53]. Two of the fractional dis- locations (the most stressed ones) cross-glide and become parallel to the third one, thereby forming a three-layer twin nucleus. Reproduced from [52] with permission from author.	17

3.1	A schematic representation of a 3N-dimensional energy landscape. Minima are the darkest regions, maxima the lightest regions and saddle points are indicated by “s”. The solids lines correspond to contours of constant energy. The dashed lines are the “dividing surfaces” separating the different minima. The region enclosed by dashed lines around each minimum is its “basin of attraction”. (Adapted from [88] with permission.)	26
3.2	The construction of the TBGSF curve starts with a pure reflection twin boundary. The structure is then rigidly shifted by $x = \lambda b_p$ to form a faulted twin boundary. The energy per unit area is measured relative to the pure reflection when $x = 0$	43
3.3	The creation of the TGSF curve through incremental discontinuous shearing of the BCC crystal structure. (a) The initial BCC crystal (b) is sheared by λb_p incrementally up to (c) b_p which forms the first part of the curve. (d) Next, all the atomic layers above the plane that was initially sheared are sheared again up to b_p , creating a total shear of $2b_p$. This is repeated again in (e) to create a three layer twin and is repeated up to n layers.	45
3.4	The creation of the concurrent TGSF curve through incremental shearing of the BCC crystal structure. (a) The initial BCC crystal (b) is sheared by λu incrementally up to predetermined displacements for creating a three layer isosceles-reflection-isosceles twin structure (c).	46
3.5	(a) Pure reflection TB (b) Pure isosceles TB.	48
3.6	A pure reflection TB (a) can be considered a three layer thick twin if half of composition plane is included or (b) a four layer thick twin if full composition plane is included.	49
3.7	A pure isosceles TB (a) can be considered a two layer thick twin if the atom layers bounded by the TB plane are considered or (b) a four layer thick twin if full isosceles triangles are considered.	49
3.8	(a) Three layer pure reflection twin created by the passage of three $\frac{b}{3}$ partial dislocations on three successive $\{112\}$ planes. (b) Three layer pure isosceles twin created by the passage of $\frac{b}{6}$, $\frac{b}{3}$ and $\frac{b}{6}$ partial dislocations on three successive $\{112\}$ planes. Dislocation pairs are colored red for $\frac{b}{6}$ dislocations and $\frac{b}{3}$ is denoted with blue to distinguish between the type of partial dislocations.	50
3.9	(a) Three layer pure reflection twin created by the passage of three $\frac{b}{3}$ partial dislocations on three successive $\{112\}$ planes. (b) Three layer pure isosceles twin created by the passage of $\frac{b}{6}$, $\frac{b}{3}$ and $\frac{b}{6}$ partial dislocations on three successive $\{112\}$ planes. Dislocation pairs are colored red for $\frac{b}{6}$ dislocations and $\frac{b}{3}$ is denoted with blue to distinguish between the type of partial dislocations.	51
3.10	(a) A Few examples of BLC parameter δ calculation in (a) a three layer thick pure reflection twin, and (b) a three layer thick pure isosceles twin.	52

3.11	(a) A crystal structure with three-layer thick pure isosceles twin (b) and the BLC parameter δ plotted in the horizontal axis against the BLC layer numbers, labeled on the left, on the vertical axis. The δ value changes from +0.155 to 0 for layer #4 and #6 indicating pure isosceles TBs and the δ value for layer #5 is -0.155 representing a pure twinned layer. (c) A crystal structure with two-layer thick pure reflection twin and (d) the BLC parameter δ plotted on the horizontal axis against the BLC layer number on the vertical axis. The δ value changes from +0.155 to -0.155 for layer #4 and #5 indicating a two layer double reflection boundary.	53
3.12	Bond length calculations in pure BCC crystal.	54
3.13	Bond length calculations for pure reflection layer.	56
3.14	Bond length calculations for a pure isosceles layer.	58
3.15	A schematic of the steps required to generate the constrained twin stability curves. (a) A pure BCC structure under zero stress with 6 atoms, (b) the BCC structure is strained to reach specific values of pure shear stress, (c) an extended sheared crystal with 24 atoms (not drawn to scale), (d) a vacuum gap of $\Delta = 15\text{\AA}$ added to the extended crystal to prevent interactions between periodic images in the [112] direction and, (e) the upper half atoms (blue block) are displaced by incremental displacement u . At each displacement u , the 12 bottom atoms (maroon block) are held completely fixed, the uppermost atoms in the yellow block are only allowed to relax in the [112] direction and the atoms in the middle block (lime) are allowed to fully relax.	60
3.16	(a) a twinned crystal with the twin boundary shown by the dashed line and (b) the twin boundary has migrated by 3 layers and moved upwards.	62
4.1	TGSF curves obtained for the BCC transition metals obtained by shearing n consecutive $\{112\}$ layers by a displacement of $\frac{a}{6}\langle 111 \rangle$. Adopted from [42].	64
4.2	The (a) The TBGSF curve and (b) the TGSF curve for Ta modeled using the Ravelo 2 EAM potential.	66
4.3	(a) The isosceles twin structure is distorted by a small shift of the two atom layers that are closest to the twin boundary plane. (b) The distorted structure can be described by a shift of η in the direction shown.	67
4.4	The (a) TBGSF curve and (b) TGSF curve for Mo modeled using the ATFS potential. (c) The local twin structure associated with the predicted minima in the TBGSF curve along with the initial pure reflection structure.	68
4.5	(a) The initial and final structure associated with a pure reflection and distorted (or δ shifted) pure reflection twin boundary structure. (b) The local twin boundary structure associated with the initial pure reflection (shaded atoms) structure and the relaxed distorted pure reflection structure where the δ shift can be seen.	69
4.6	The TBGSF curve up to $3b_p$ for Ta modeled with Guellil potential.	71
4.7	The (a) TBGSF curve and (b) TGSF curve for Nb modeled using the Fellingner potential.	72
4.8	The TBGSF curves for (a) Ta, (b) Nb, (c) V and (d) Fe using DFT.	77
4.9	The TGSF curve for Ta computed using DFT.	78
4.10	The TBGSF curves for (a) Mo, (b) W, and (c) Cr using DFT.	78
4.11	(a) The TGSF curve for Mo and (b) a zoomed in image of (a) showing the very small cusps that emerge due to the instability associated with the pure reflection twin boundary.	80

4.12	The TBGSF curves predicted from the analytical model of bonding across the cut plane. The energy has arbitrary units since the prefactor α is not specified and we simply have scaled the two curves to visually match.	83
5.1	(a) The energy barrier for twin nucleation plotted as a function of the applied stress from the free-end string simulations [100] for the model Ta system described by Ravelo2 potential [77]. (b) An example of a minimum energy path of twin nucleation for the smallest stress in (a), which is 5.49 GPa, (c) the twin nucleus at the activated state for an applied stress of 5.49 GPa. The atoms are colored by using common neighbor analysis (CNA) [151] which allows for convenient for locating a twin nucleus in a bulk crystal with nearly 13000 atoms but can be misleading in determining twin thickness, and (d) BLC analysis of the atomic positions of the twin nucleus (blue dots) indicating the presence of a three layer isosceles twin if the BLC parameter δ values are compared to those of an ideal three layer pure isosceles (black dots).	90
5.2	BLC analysis of the saddle point atomic configurations of Ta modeled using the Ravelo2 potential for 4 different stress levels, taken from the curve in Figure 5.1(a). As the stress increases, the magnitude of the BLC values decrease, nearly vanishing at the highest stress. However, the structure of the twin seems to remain despite the decrease in magnitude.	91
5.3	(a) The constrained twin stability curves for BCC Ta, described by the Ravelo2 EAM potential [77], under 5.49 GPa pure shear stress. (b) The BLC parameter, δ , plotted for both the saddle structure (black dots) and one of the constrained equilibrium structures exhibiting a similar 3 layer distorted isosceles twin (red dots).	92
5.4	Twin thickness vs. normalized displacement for the constrained twin stability curves in Figure 5.3(a).	94
5.5	(a) Energy barrier for twin nucleation vs. applied pure shear stress using Ta-ATFS potential (b) Determination of twin thickness in the saddle structures found in the free-end string simulations using the BLC analysis for 3 stresses.	95
5.6	(a) Energy barrier for twin nucleation vs. applied pure shear stress in Ta-Zhou EAM potential (b) Determination of twin thickness in the saddle structures found in the free-end string simulations using the BLC analysis for 3 stresses.	96
5.7	(a) The energy barrier for twin nucleation plotted as a function of the applied stress from the free-end string simulations [100] for the model Mo system described by ATFS potential [78]. (b) An example of a minimum energy path of twin nucleation for the smallest stress in (a), which is 12.51 GPa, (c) the twin nucleus at the activated state for an applied stress of 12.51 GPa. The atoms are colored by using common neighbor analysis (CNA) [151] which allows for convenient for locating a twin nucleus in a bulk crystal with nearly 13000 atoms but can be misleading in determining twin thickness, and (d) BLC analysis of the atomic positions of the twin nucleus (blue dots) indicating the presence of a single layer reflection twin if the BLC parameter δ values are compared to those of an ideal one layer pure reflection (black dots).	97

5.8	BLC analysis of the saddle point atomic configurations of Mo modeled using the ATFS potential for 6 different stress levels, taken from the curve in Figure 5.7(a). As the stress increases, the magnitude of the BLC values decrease, nearly vanishing at the highest stress. However, the structure of the twin seems to remain despite the decrease in magnitude.	98
5.9	(a) The constrained twin stability curves for BCC Mo, described by the ATFS EAM potential [78], under 12.51 GPa pure shear stress. (b) The BLC parameter, δ , plotted for both the saddle structure (black dots) and one of the constrained equilibrium structure exhibiting a 1 layer distorted reflection twin (blue dots).	99
5.10	Twin thickness vs. normalized displacement for the constrained twin stability curves in Figure 5.9(a).	100
5.11	(a) Energy barrier for twin nucleation vs. applied pure shear stress for Mo-Zhou EAM potential(b) Determination of twin thickness in the saddle structures found in the free-end string simulations using the BLC analysis for 3 stresses.	101
5.12	(a) Energy barrier for twin nucleation vs. applied pure shear stress in W-Zhou EAM potential(b) Determination of twin thickness in the saddle structures found in the free-end string simulations using the BLC analysis for 3 stresses.	102
5.13	(a) Energy barrier for twin nucleation vs. applied pure shear stress for string simulations with ATFS Fe potential. (b) Determination of twin thickness in the saddle structures found in the free-end string simulations using the BLC analysis for 3 stresses.	103
5.14	(a) Energy barrier for twin nucleation vs. applied pure shear stress for string simulations with Fe-Chamati potential. (b) Determination of twin thickness in the saddle structures found in the free-end string simulations using the BLC analysis for 3 stresses.	104
5.15	(a) The pure shear stress-strain curves in BCC Ta as computed by our DFT simulations. (b) The constrained twin stability curves for BCC Ta with DFT simulations under 6.42 GPa pure shear stress. (c) The smallest and most prevalent observed twin structure identified by our constrained GSF curves as identified by BLC analysis.	105
5.16	Twin thickness vs normalized displacement for the constrained twin stability curves in Figure 5.15(b)	107
5.17	The TBGSF curves for BCC Ta. Minimums near $\lambda = \frac{1}{6}$ indicates a preference for an isosceles twin boundary	108
5.18	The sequential twinning GSF curves for BCC Ta using DFT simulations demonstrating that in Ta the double-isosceles structure is always unstable while the isosceles-reflection structure is unstable at zero stress but becomes stable under an applied stress of 6.42GPa.	108
5.19	The sequential twinning GSF curves for BCC Ta using DFT simulations under three large pure shear stresses.	109
5.20	(a) The pure shear stress-strain curves in BCC Ta as computed by our DFT simulations. (b) The constrained twin stability curves for BCC Ta with DFT simulations under 6.42 GPa pure shear stress. (c) The smallest and most prevalent observed twin structure identified by our constrained GSF curves as identified by BLC analysis.	110
5.21	Twin thickness vs normalized displacement for the constrained twin stability curves in Figure 5.20(b)	111
5.22	The sequential twinning GSF curves for BCC Mo using DFT simulations under 14.07GPa.	112

5.23	(a) Stress-strain curve in BCC Nb with DFT. 1.69 GPa stress is selected (highlighted by red circle) to probe twin nucleation. (b) Constrained twin stability curves (CTSC) with $n = 6$ atom layers allowed to relax at each incremental displacement $u = \lambda b$. (c) Sequential twinning GSF curve under 1.69 GPa; the metastable point is highlighted. (d) BLC analysis to show that the metastable point in the TGSF curve is a two layer isosceles-reflection twin whereas the structure at the red circle of (b) also closely approximate the metastable structure.	114
5.24	(a) Stress-strain curve in BCC Nb with DFT. 3.37 GPa stress is selected (highlighted by red circle) to probe twin nucleation. (b) Constrained twin stability curves (CTSC) with $n = 6$ atom layers allowed to relax at each incremental displacement $u = \lambda b$. (c) Sequential twinning GSF curve under 3.37 GPa; the metastable point is highlighted. (d) BLC analysis to show that the metastable point in the TGSF curve is a two layer isosceles-reflection twin whereas the structure at the red circle of (b) also closely approximate the metastable structure.	115
5.25	(a) Stress-strain curve in BCC Nb with DFT. 6.02 GPa stress is selected (highlighted by red circle) to probe twin nucleation. (b) Constrained twin stability curves (CTSC) with $n = 6$ atom layers allowed to relax at each incremental displacement $u = \lambda b$. (c) Sequential twinning GSF curve under 6.02 GPa; the metastable point is highlighted. (d) BLC analysis to show that the metastable point in the TGSF curve is a two layer isosceles-reflection twin whereas the structure at the red circle of (b) also closely approximate the metastable structure.	116
5.26	(a) Stress-strain curve in BCC V with DFT. 1.64 GPa stress is selected (highlighted by red circle) to probe twin nucleation. (b) Constrained twin stability curves (CTSC) with $n = 6$ atom layers allowed to relax at each incremental displacement $u = \lambda b$. (c) Sequential twinning GSF curve under 1.64 GPa; the metastable point is highlighted. (d) BLC analysis to show that the metastable point in the TGSF curve is a two layer isosceles-reflection twin whereas the structure at the red circle of (b) also closely approximate the metastable structure.	117
5.27	(a) Stress-strain curve in BCC V with DFT. 4.95 GPa stress is selected (highlighted by red circle) to probe twin nucleation. (b) Constrained twin stability curves (CTSC) with $n = 6$ atom layers allowed to relax at each incremental displacement $u = \lambda b$. (c) Sequential twinning GSF curve under 4.95 GPa; the metastable point is highlighted. (d) BLC analysis to show that the metastable point in the TGSF curve is a two layer isosceles-reflection twin whereas the structure at the red circle of (b) also closely approximate the metastable structure.	118
5.28	(a) Stress-strain curve in BCC V with DFT. 5.96 GPa stress is selected (highlighted by red circle) to probe twin nucleation. (b) Constrained twin stability curves (CTSC) with $n = 6$ atom layers allowed to relax at each incremental displacement $u = \lambda b$. (c) Sequential twinning GSF curve under 6.02 GPa; the metastable point is highlighted. (d) BLC analysis to show that the metastable point in the TGSF curve is a two layer isosceles-reflection twin whereas the structure at the red circle of (b) also closely approximate the metastable structure.	119

5.29	(a) Stress-strain curve in BCC W with DFT. 9.76 GPa stress is selected (highlighted by red circle) to probe twin nucleation. (b) Constrained twin stability curves (CTSC) with $n = 6$ atom layers allowed to relax at each incremental displacement $u = \lambda b$. (c) Sequential twinning GSF curve under 9.76 GPa; the metastable point is highlighted. (d) BLC analysis to show that the metastable point in the TGSF curve is a two layer reflection twin whereas the structure at the red circle of (b) also closely approximate the metastable structure.	120
5.30	(a) Stress-strain curve in BCC W with DFT. 12.43 GPa stress is selected (highlighted by red circle) to probe twin nucleation. (b) Constrained twin stability curves (CTSC) with $n = 6$ atom layers allowed to relax at each incremental displacement $u = \lambda b$. (c) Sequential twinning GSF curve under 12.43 GPa; the metastable point is highlighted. (d) BLC analysis to show that the metastable point in the TGSF curve is a two layer reflection twin whereas the structure at the red circle of (b) also closely approximate the metastable structure.	121
5.31	(a) Stress-strain curve in BCC W with DFT. 17.38 GPa stress is selected (highlighted by red circle) to probe twin nucleation. (b) Constrained twin stability curves (CTSC) with $n = 6$ atom layers allowed to relax at each incremental displacement $u = \lambda b$. (c) Sequential twinning GSF curve under 17.38 GPa; the metastable point is highlighted. (d) BLC analysis to show that the metastable point in the TGSF curve is a two layer reflection twin whereas the structure at the red circle of (b) also closely approximate the metastable structure.	122
5.32	(a) Stress-strain curve in BCC Cr with DFT. 9.15 GPa stress is selected (highlighted by red circle) to probe twin nucleation. (b) Constrained twin stability curves (CTSC) with $n = 6$ atom layers allowed to relax at each incremental displacement $u = \lambda b$. (c) Sequential twinning GSF curve under 9.15 GPa; the metastable point is highlighted. (d) BLC analysis to show that the metastable point in the TGSF curve is a two layer reflection twin whereas the structure at the red circle of (b) also closely approximate the metastable structure.	123
5.33	(a) Stress-strain curve in BCC Cr with DFT. 12.94 GPa stress is selected (highlighted by red circle) to probe twin nucleation. (b) Constrained twin stability curves (CTSC) with $n = 6$ atom layers allowed to relax at each incremental displacement $u = \lambda b$. (c) Sequential twinning GSF curve under 12.94 GPa; the metastable point is highlighted. (d) BLC analysis to show that the metastable point in the TGSF curve is a two layer reflection twin whereas the structure at the red circle of (b) also closely approximate the metastable structure.	124
5.34	(a) Stress-strain curve in BCC Cr with DFT. 16.37 GPa stress is selected (highlighted by red circle) to probe twin nucleation. (b) Constrained twin stability curves (CTSC) with $n = 6$ atom layers allowed to relax at each incremental displacement $u = \lambda b$. (c) Sequential twinning GSF curve under 16.37 GPa; the metastable point is highlighted. (d) BLC analysis to show that the metastable point in the TGSF curve is a two layer reflection twin whereas the structure at the red circle of (b) also closely approximate the metastable structure.	125

5.35	(a) Stress-strain curve in BCC Fe with DFT. 6.77 GPa stress is selected (highlighted by red circle) to probe twin nucleation. (b) Constrained twin stability curves (CTSC) with $n = 6$ atom layers allowed to relax at each incremental displacement $u = \lambda b$. (c) Sequential twinning GSF curve under 6.77 GPa; the metastable point is highlighted. (d) BLC analysis to show that the metastable point in the TGSF curve is a two layer reflection twin whereas the structure at the red circle of (b) also closely approximate the metastable structure.	126
5.36	Graphical description of twin formation in (a) group VB and (b) group VIB BCC transition metals. First, two layer thick twin embryos nucleate under the appropriate applied stresses as twinning dislocations. Isosceles type twinning dislocations for group VB are shown as red dislocation pairs and are denoted as $\pm \frac{1}{6}b$ while reflection type twinning dislocations for both groups are shown as blue dislocation pairs and are denoted as $\pm \frac{1}{3}b$. Then these nascent twins grow laterally on $\{112\}$ planes while causing stress levels to drop. Finally, at smaller stresses twin embryos grow vertically to become three layers twins. The magnitude of the Burgers vector can deviate by small amounts depending on the stress applied.	128
5.37	(a) a twinned crystal with the twin boundary shown by the dashed line and (b) the twin boundary has migrated by 3 layers and moved upwards.	132
5.38	TBMGSF curves for simultaneous nucleation in BCC Tungsten of more than one twinning partials.	133
5.39	TEM images of deformation twins in BCC Tungsten	134
5.40	The TGSF curve generated for BCC W with DFT simulations, peak-trough data from 2bp to 16bp are shown in the inset.	135
5.41	Fourier analysis of the peak-trough data from TGSF curve of BCC W.	136
6.1	(a) The energy barrier vs. stress for Cu under pure shear (Aubry et al.) and compression (Zhu et al.) (b) The energy barrier vs. stress for Au, Ag, Al and Ni (Jennings et al.).	142
6.2	The real valued Lambert W-function with branches W_0 and W_{-1} [193].	145
6.3	A dislocation loop under pure shear loading	147
6.4	(a) The activation free energy barrier vs. stress behavior for homogeneous dislocation nucleation for the model with variable Burgers vector, i.e. model 2. Activation energies are calculated from Equation (6.43). (b) The activation volume vs. stress behavior for dislocation nucleation for the augmented model proposed in Equation (6.43).	160
6.5	(a) A contour plot of the free energy surface, $\Delta G(R, b_f)$ modeled as Equation (6.44) for $\frac{\tau}{\tau_0} = 0.683$ over the range $R \in [0, 50]$ and $b \in [0, 1]$. (b) the free energy surface over the range $R \in [0, 1]$ and $b \in [0, 1]$	162
6.6	(a) The activation volume vs. stress behavior for dislocation nucleation modeled by Equation (6.44). (b) A log-log plot of $\frac{d \log \Delta G^*}{d \log(1 - \frac{\tau}{\tau_0})}$ as a function of $(1 - \frac{\tau}{\tau_0})$ for the augmented model of Equation (6.44). The exponent α approaches a value of 0.4 as $\tau \rightarrow \tau_0$	163
6.7	(a) A contour plot of the free energy surface, $\Delta G(R, b_f)$ modeled as Equation (6.43) for $\frac{\tau}{\tau_0} = 0.683$ over the range $R \in [0, 50]$ and $b \in [0, 1]$. (b) the free energy surface over the range $R \in [0, 1]$ and $b \in [0, 1]$	163

6.8	Three twinning dislocation loops (denoted by numbers 1, 2 and 3) nucleated in bulk BCC crystal. The loops have equal Radii, R and they are separated by distance z_{ij} . The displacement (Burgers vector) associated with each loop is determined from twin structures found or produced in string or DFT simulations.	168
6.9	(a) a single layer fault produced from rigidly translating a pure BCC crystal by an amount $\frac{a}{6}\langle 111 \rangle$, (b) TGSF curve for Ta and (c) TGSF curve for W with relative displacement, $\lambda = \frac{u}{b_p}$ where u is any arbitrary amount of displacement and $b_p = \frac{a}{6}\langle 111 \rangle$ is the twinning partial, in the horizontal axis and the stacking fault energy γ in the vertical axis.	169
6.10	Energy barrier vs stress in BCC Ta for varying number of twinning dislocation loops calculated by finding saddle points for Equation 6.46.	170
6.11	Energy barrier vs stress in BCC Ta modeled by Ravelo2 potential. The energy barrier predictions from the continuum model is very close to the string simulations.	172
6.12	Energy barrier vs stress in BCC Ta modeled by Ravelo2 potential. The energy barrier predictions from the continuum model is very close to the string simulations.	173
9.1	Schematic diagram of heterogeneous dislocation nucleation. Reproduced from [126] with permission.	189

Chapter 1

Introduction

When a solid is subjected to external or internal forces, it undergoes shape change. Depending on the magnitude of forces and material characteristics, the response of a material to external and internal forces can be substantially distinct. For example, if the forces are large in magnitude, the solid may fracture. Smaller values of forces may cause permanent deformation in the solid without fracture and if the forces are small enough, the deformation may only be elastic. Elastic deformation is a macroscopic manifestation of atomic bonding in the solid. In case of plastic deformation, when the load is released, the solid does not return to the shape it had prior to the application of the load. For elastic deformation the body assumes the dimensions it had before the load was applied. The extent of elastic deformation is generally quite limited i.e., most solids are capable of being elastically deformed only to strains on the order of several tenths of a percent. Beyond the elastic limit, the material starts to deform permanently i.e., the strain no longer disappears after the removal of stress. The remaining permanent strain is known as the plastic strain and additional incremental plastic strains can be accumulated on subsequent loading and unloading which lead ultimately to material failure. In crystalline materials, plastic deformation is caused by the motion of one-dimensional crystallographic defects called dislocations. Plastic deformation in crystalline materials can occur via several mechanisms such as slip of atomic planes and deformation twinning. Slip which implies the movement or propagation of dislocations can occur via glide of mixed dislocations, cross-slip of screw dislocations, and climb of edge dislocations whereas deformation twinning is initiated by the nucleation and growth phenomenon of twinning partial dislocations. At room temperature and below, plastic deformation can occur by slip and deformation twinning whereas at high temperatures, plastic deformation is controlled by diffusional creep. In body centered cubic transition metals, mechanical response is known to be more temperature and strain rate dependent due to the intrinsic lattice resistance associated screw dislocations. At sufficiently low temperatures and/or at sufficiently high loading rates, deforma-

tion twinning is observed as a competing mechanical deformation mechanism along with slip in many experimental and computational studies. Even though the existing literature acknowledge the competition in deformation mechanisms at low temperature and high strain rate conditions, there are unresolved scientific questions regarding atomic level structure of deformation twins as well as their nucleation and propagation. In this light, This work seeks to answer the following questions by utilizing atomistic and continuum modeling techniques:

1. What is the atomic level structure of twin boundaries in BCC metals? Specifically, are the reported stable structures the only stable structures or are their multiple meta stable structures and, if there are, what are the relative energetics?
2. Is there a critical size of a twin nucleus in BCC metals and, if so, what is it?
3. Is it energetically more favorable to grow deformation twins layer by layer in a BCC metal or does growth occur by zonal twinning dislocations?
4. Are the bulk stress values obtained from experiments the local stresses required for twin nucleation?

Chapter 2

Literature review

2.1 Twinning in crystalline materials

If a crystal is composed of parts/components that are oriented with respect to one another according to some kind of symmetry rule, the crystal is said to be twinned [1]. The most common symmetry rule for twinning in crystals is reflection symmetry of twinned components. In this case, one of the components is the mirror image of the crystal structure of the other component about a crystallographic plane known as the twinning plane. The plane of contact between the twinned components is called the composition plane and in case of cubic crystals the composition plane and the twin plane coincide. In Figure 2.1, a pure reflection twinned BCC crystal is shown with the twin components as well as the twin plane.

Twinned crystals can be produced during crystal growth from the vapor or liquid phases as well as via recrystallization of the solid phase and this type of twins are called growth twins. A single crystal can become twinned via mechanical deformation and this type of twin is called deformation twin. Another type of twinning can be found as a result of martensitic transformations where highly organized structures with alternate twin lamella of fixed thickness ratios form regular array. These types of twins are known as transformation twins. We will study deformation twins in this work although the discussion on twin boundary structures applies to other types of twins too.

In the crystallographic theory of twinning, the parent lattice is reoriented by atomic displacements which are equivalent to a simple shear of the lattice points or some integral fraction of these lattice points [3]. The invariant plane of this shear is called K_1 otherwise known as the twin plane whereas the direction of the simple shear is denoted by η_1 which is the twinning direction. The second undistorted plane is called the K_2 or conjugate twin plane. The plane containing η_1 direction and the normal vectors to both K_1 and K_2 is called the plane of shear and it is denoted by S in Figure 2.2. The vector that intersects both K_2 and S planes is the conjugate shear direction η_2 .

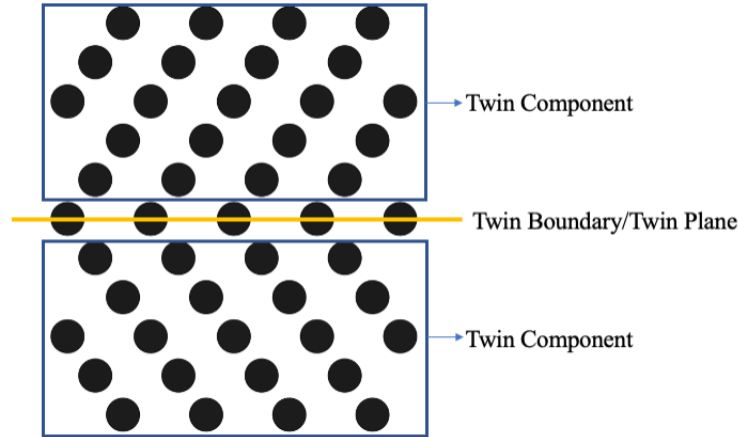


Figure 2.1: A pure reflection twin in BCC crystal [2].

The final twinning element for a complete crystallographic description of deformation twins is the magnitude of simple shear γ which reorients the crystal.

To better understand the geometry of deformation twins, let us consider a hemispherical crystal undergoing a simple shear as shown in Figure 2.3. As the hemispherical crystal undergoes such a deformation it changes into an ellipsoidal shape. In Figure 2.3, the hemisphere has experienced a uniform shear γ , where Ox_1 is the direction η_1 and Ox_2 is perpendicular to the twin plane K_1 . So upon deformation, each K_1 plane has been displaced in the η_1 direction by an amount proportional to its distance from the base of the original hemisphere.

It is important to note that the size and shape of each K_1 plane remain unaffected by the deformation process and this is why K_1 planes are called first undistorted planes. Now from Figure 2.4, it can be seen that the line OP of the hemisphere is reoriented to OP' but its length is unchanged despite the application of simple shear γ . The second undistorted plane K_2 is defined by this line OP and the axis Ox_3 which is normal to the screen. After twinning, this plane gets reoriented to K'_2 which is defined by the intersection between the original hemisphere and the deformed ellipsoid.

As the hemisphere in Figure 2.4 is sheared, the amount of shear can be calculated from this figure:

$$\gamma = \frac{PP'}{OP \sin \theta} = 2 \cot \theta \quad (2.1)$$

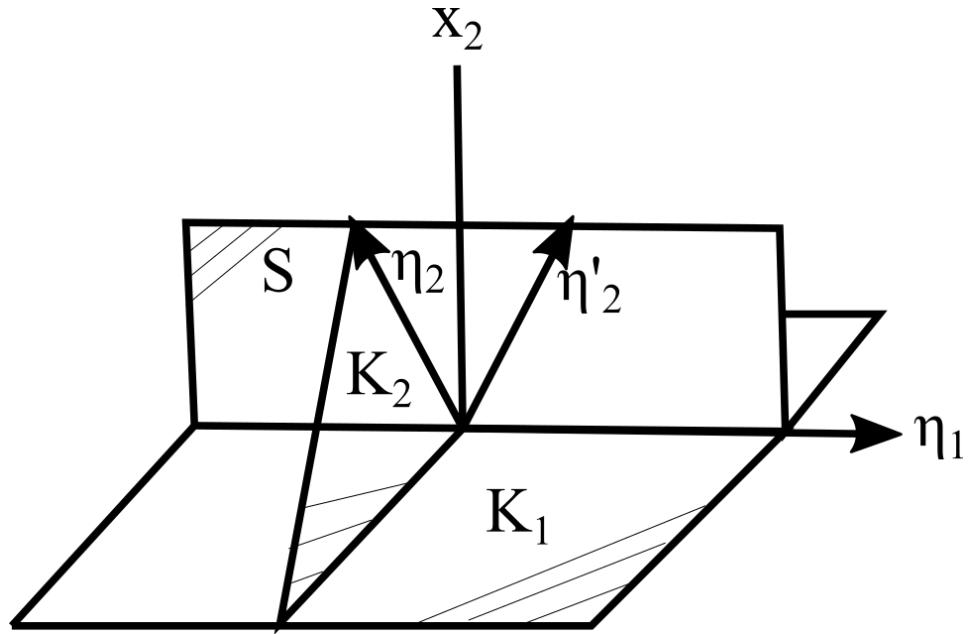


Figure 2.2: Five out of the six twinning elements shown schematically. Reproduced from [3] with permission.

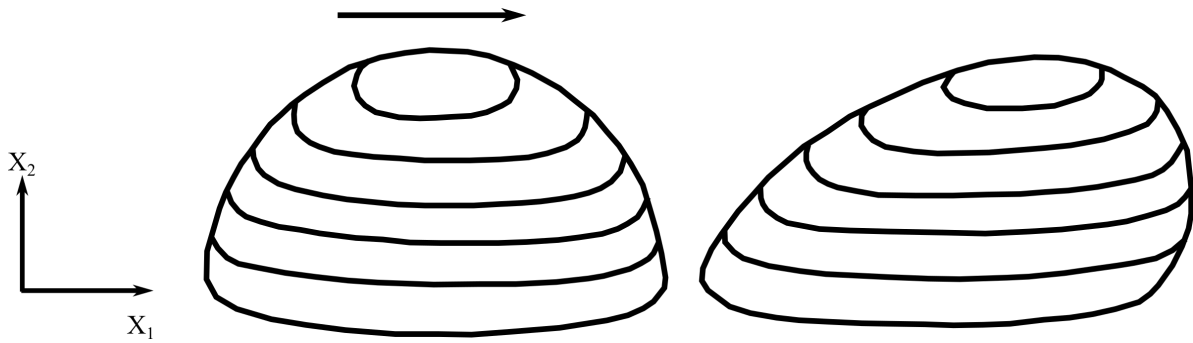


Figure 2.3: The change in shape of a hemispherical crystal because of deformation twinning. Reproduced from [4] with permission.

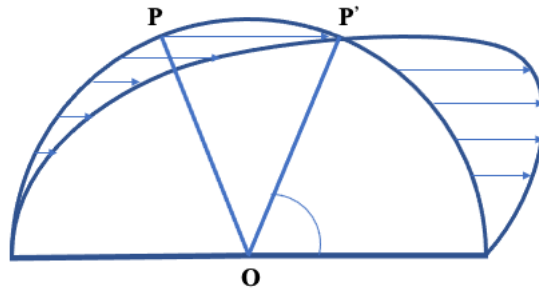


Figure 2.4: Diagram showing how the hemispherical crystal becomes deformed to an ellipsoid by deformation twinning. Reproduced from [4] with permission.

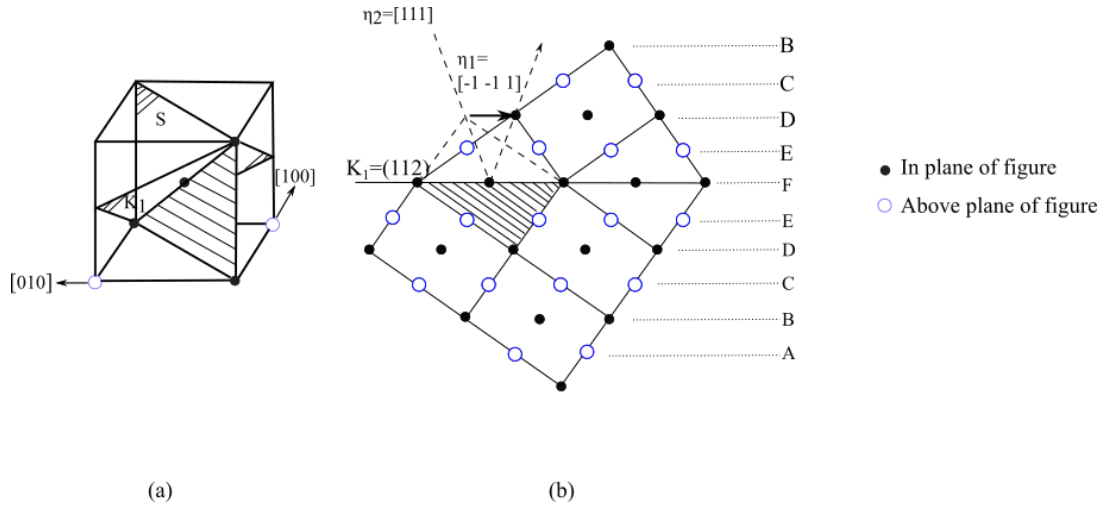


Figure 2.5: (a) K_1 and S planes shown in the conventional BCC unit cell, (b) Atomic movement required for twinning in BCC crystal with projection vector $[1\bar{1}0]$. Reproduced from [1] with permission.

where θ is the angle between the normal vectors of the planes K_1 and K_2 .

The twinning elements in body centered cubic (BCC) crystal structures are $K_1 = (112)$, $\eta_1 = [1\bar{1}\bar{1}]$, $K_2 = (11\bar{2})$, $\eta_2 = [111]$ and $\gamma = \frac{1}{\sqrt{2}}$. The invariant planes as well as twinning and conjugate twinning directions are shown in Figure 2.5. The atomic movements described by these twinning elements corresponds to a shift of $\frac{a}{6}\langle 111 \rangle$ on successive $\{112\}$ planes where a is the lattice constant of the BCC metal under consideration. The BCC crystal structure can be formed from horizontal $\{112\}$ layers with a stacking sequence ...ABCDEFABCDEF... meaning six $\{112\}$ atomic layers can be stacked on top of each other before seventh layer falls vertically on top of the first [4]. The passage of a single partial dislocation with $\frac{a}{6}\langle 111 \rangle$ Burgers vector produces a stacking fault of the form ...ABCDEFEFAB.... The passage of $\frac{a}{6}\langle 111 \rangle$ partials on successive planes would produce the twin sequence ...ABCDEFEDCB...

2.2 Deformation twinning in BCC transition metals

As mentioned briefly in the introduction, the mechanical response of body centered cubic (BCC) metals is well known to be more temperature and strain rate dependent as compared to face centered cubic (FCC) metals [5]. This is attributed to the intrinsic lattice resistance associated with screw dislocations, which regulate their low temperature plastic response [5, 6]. At suffi-

ciently high temperatures, BCC metals transition from parabolic hardening to three-stage hardening akin to the stages of hardening in FCC metals which is attributed to sufficient thermal energy to overcome their intrinsic lattice resistance [7–10]. However, at sufficiently low temperatures or sufficiently high loading rates, mechanical twinning has been observed as a competing mechanical deformation mechanism in several experimental studies on BCC transition metals.

Mitchell et al. [8] deformed Tantalum single crystals in tension with a view to understanding three-stage hardening behavior. Orientation, temperature and strain rate dependence of plastic deformation was investigated by deforming Tantalum single crystals with nine different orientations, with a range of temperature from 4.2K to 573K and with seven distinct strain rates respectively. Deformation twinning of the type $\langle 111 \rangle \{112\}$ was observed at 4.2K in this study for a $[213]$ oriented crystal with an effective strain rate $9.3 \times 10^{-4} \text{s}^{-1}$. The orientation and strain rate dependence experiments were also performed at 373K and no twinning phenomenon was observed at this temperature even in the $[213]$ oriented crystal. Shields et al. [11] also deformed Tantalum single crystals at 4.2 K with a strain rate $5 \times 10^{-4} \text{s}^{-1}$ under both tensile and compressive loading conditions (see Figure 2.6 for the slip trace analysis in this study). Slip trace analyses of deformed specimens indicated that tensile specimens deformed almost entirely by slip with the exception of orientations near $[001]$. Alternatively, compression specimens almost always twinned except on specimens oriented near $[001]$ which exhibited some evidence of slip and even then twinning was the dominant deformation mechanism.

Sherwood et al. [12] also observed twinning in Tantalum single crystals at 77K with a strain rate of $4.9 \times 10^{-4} \text{s}^{-1}$ under tensile loading in the $\langle 100 \rangle$ oriented crystals whereas in compression for the $\langle 110 \rangle$ orientation repeated discontinuous slip occurred after a strain of 0.03. A more recent Kolsky bar compression experimental study by Chen et al. [13] confirmed the existence of deformation twins in Tantalum at 77K with strain rates $\sim 10^3 \text{s}^{-1}$ however, the same study showed no twinning at 300 K even with strain rates up to $\sim 10^4 \text{s}^{-1}$. Florando et al. [14] used polycrystalline Tantalum for uniaxial compression at 77K and observed twinning at strain rate 1s^{-1} . However, they did not observe any twinning for a much smaller strain rate 10^{-4}s^{-1} at 77 K.

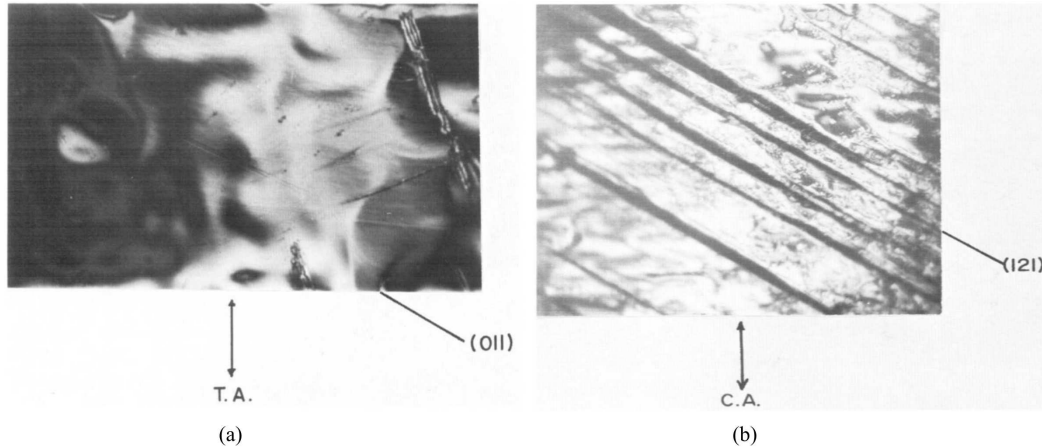


Figure 2.6: One of the earliest direct observation of deformation twinning in BCC transition metal, Ta was made by Shields et al. [11]. Slip and twin trace analyses in Single crystal Ta deformed at 4.2K adopted from Shields et al. (a) Typical fine slip traces observed in Ta tested in tension (T.A = tensile axis) (b) Evenly distributed twins observed on Ta tested in compression (C.A = compression axis). The micrographs are reproduced from [11] with permission.

Sherwood et al. [12] observed deformation twinning in BCC Niobium single crystals with $\langle 110 \rangle$ orientation under compressive loading at 77K with a strain rate of $4.5 \times 10^{-4} \text{s}^{-1}$. Niobium single crystals with orientation axis near $[011]$ also exhibited twinning under compression at 77K with a strain rate of $6.7 \times 10^{-4} \text{s}^{-1}$ in another experimental study by Reid et al. [15]. Groger et al. [16] tested Niobium single crystals with the center-triangle orientation as well as orientations near the $[011] - [1\bar{1}1]$ edge of the stereographic triangle at 77K under compression with a strain rate of $3 \times 10^{-5} \text{s}^{-1}$ and also observed deformation twins. Furthermore, B. J. Shaw [17] observed twinning in polycrystalline Niobium under both tensile and compressive loading with strain rate $4.2 \times 10^{-4} \text{s}^{-1}$ and at a slightly higher temperature of 104K.

Edington et al. [18] compressed Vanadium single crystals with compression axes near $[111]$ at a strain rate $8 \times 10^{-4} \text{s}^{-1}$ with pre-straining at 293K and 373K. Deformation twins were observed at 77K regardless of the pre-straining temperature and duration. Tensile tests were conducted on commercially pure polycrystalline Vanadium by Lindley et al. [19] with temperatures ranging from 20K to 293K. They found that at and above 77 K, the Vanadium polycrystals deformed solely or predominantly by slip whereas at 20K deformation was associated with twinning. B. J. Shaw [17] also observed twinning in polycrystalline Molybdenum under both tensile and compressive loading

with strain rate $4.2 \times 10^{-4} \text{s}^{-1}$ and at temperatures 4.2, 77, 173 and 223K. Moreover, Sherwood et al. [12] observed deformation twinning in Molybdenum single crystals oriented in the $\langle 100 \rangle$ and $\langle 110 \rangle$ directions under tensile loading at 77K with a strain rate of $7 \times 10^{-5} \text{s}^{-1}$. Chiem et al. [20] investigated the plastic deformation behavior of $[111]$ oriented Tungsten single crystals with a split Hopkinson bar under dynamic loading applied in simple shear at room temperature. Deformation by twinning were observed in this study at a strain rate of $1.8 \times 10^3 \text{s}^{-1}$. Marcinkowski et al. [21] tested Chromium polycrystals under compression with a strain rate of 10^{-3}s^{-1} at temperatures ranging from 77K to 373K and found that twinning only occurs at 123K. J. Harding [22] deformed BCC Iron single crystals in tension at two different strain rates: 10^{-3}s^{-1} and 10^3s^{-1} as well as at four different temperatures: 77K, 113K and 195K and observed deformation twinning in all of the cases regardless of orientation.

Apart from low temperature, twinning is observed at high strain rates or during dynamic loading events. As mentioned earlier, Kolsky bar compression study by Chen et al. [13] has shown the existence of deformation twins in Tantalum at 77K with strain rates $\sim 10^3 \text{s}^{-1}$. Livescu et al. [23] investigated deformation twins in polycrystalline Tantalum under high explosive driven shock loading which implies very high strain rate and they observed that $\langle 111 \rangle \{112\}$ twinning play a significant role in the deformation and damage evolution of shock-loaded Tantalum. Shock-wave deformation of polycrystalline Tantalum to a pressure of 45 GPa and duration of 1.8 microsecond generated profuse twinning in an experimental study conducted by Murr et al. [24] where a strain rate of $3 \times 10^3 \text{s}^{-1}$ was achieved by using a split Hopkinson pressure bar. Anderson et al. [25] impact tested polycrystalline Tantalum at room temperature with a hammer (which also implies high strain rates) and observed deformation twins shown in Figure 2.7. Besides Tantalum, explosive working of zone-refined Tungsten single crystals produced deformation twins at room temperature [26]. These general observations have led to the conclusion that deformation twinning becomes active at high strain rates and low temperatures.

With the development of nanomechanical testing, the influence of size on initiation of mechanical twinning has also been investigated. Wang et al. [27] deformed Tungsten bi-crystal nanowires

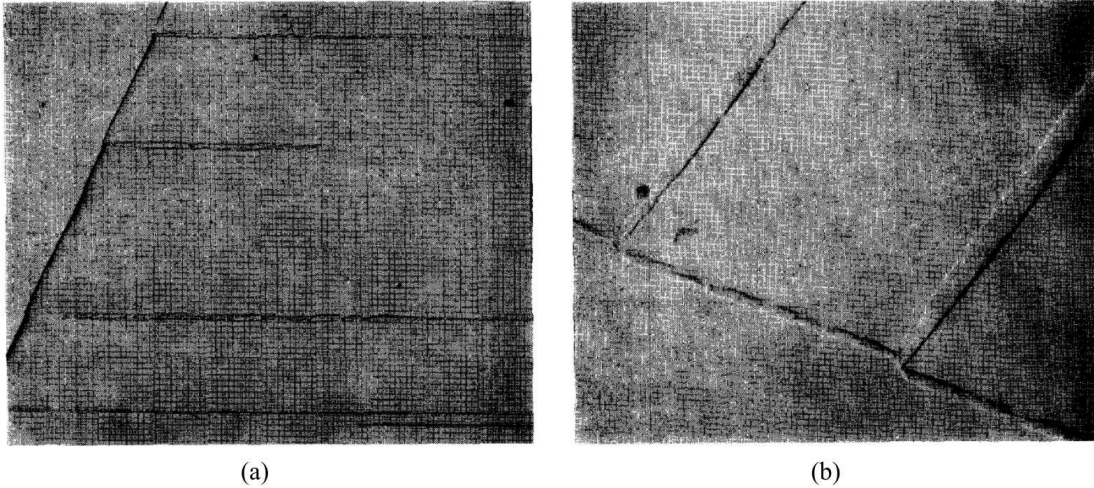


Figure 2.7: (a) Deformation twins in tantalum (zoomed in 100x). Specimen mechanically polished and etched in 2 parts lactic acid, 1 part HF, and 1 part HNO₃ for 40 minutes and then in equal parts in HF and HNO₃ for 5 minutes. (b) same specimen zoomed in 500x. Reproduced from [25] with permission.

using in-situ nanomechanical testing at room temperature under a strain rate of 10^{-3}s^{-1} and observed that on compressive loading, after a relatively large lattice strain (4.9%) is achieved, a small twin embryo was nucleated from the intersection between the grain boundary and free surface. This twin embryo grew and traversed the entire Tungsten bi-crystal sample under continued loading. They also found, in the absence of pre-existing dislocations, that twinning and slip compete at room temperature and that competition is orientation dependent. Nanoscale sized grains can also promote the transition from slip to twinning and is evidenced (see Figure 2.8) by nanoindentation conducted on nanocrystalline Tantalum [28]. In this study, nanocrystalline Ta films with thickness of ~ 0.1 micrometer were probed using a depth-sensing nanoindentation mechanism which allows well-controlled local deformation. The authors investigated the deformed nanocrystals with both scanning electron microscopy and high-resolution TEM and observed that plastic deformation during nanoindentation is controlled by deformation twinning. These observations can be explained by the idea that twin nucleation requires high stresses, which can be achieved in nanocrystalline metals through the removal of more classical sources, a.k.a. dislocation starvation [29, 30]. Thus, the occurrence of deformation twinning can be enhanced through the reduction of material length scales.

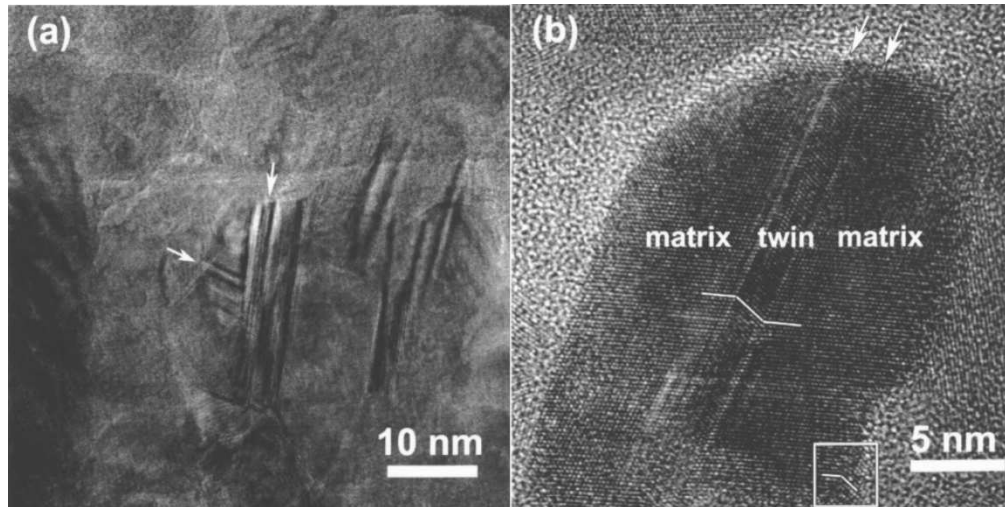


Figure 2.8: (a) Transmission electron micrograph of the intersecting twins in nanocrystalline Ta. The twinning directions are marked with two white arrows. (b) High-resolution TEM image of a nanograin, featuring a deformation twin. Reproduced from [28] with permission.

These reports of twinning dominated deformation are supported by several studies involving simulations. For example, Zhang et al. [31] studied deformation twins in nanocrystalline BCC Mo through molecular dynamics (MD) simulations. They found that in $\langle 110 \rangle$ columnar grains, the deformation is dominated by twinning and twins were nucleated primarily from the grain boundaries by successive emission of twinning partials and thickened by jog nucleation in the grain interiors. Frederiksen et al. [32] also used MD simulations to investigate the plastic deformation of nanocrystalline Mo. Their simulations showed that plastic deformation involved both grain boundary processes and dislocation migration which in some cases lead to twin boundary formation. Pan et al. [33] studied tensile behavior of nanocrystalline Ta using MD simulations and found that deformation twinning is one of the deformation mechanisms among others such as dislocation motion, grain rotation, grain boundary sliding etc. Sainath [34] et al. studied the effect of orientation on the deformation behavior of BCC Iron with MD simulations on nanowires initially oriented $\langle 100 \rangle$, $\langle 110 \rangle$, $\langle 111 \rangle$, $\langle 112 \rangle$ and $\langle 102 \rangle$. Their MD simulation results showed that the deformation mechanisms vary with crystal orientation. Under tensile loading, the nanowires with initial orientations of $\langle 100 \rangle$, $\langle 112 \rangle$ and $\langle 102 \rangle$ deformed predominantly by deformation twinning on the $\langle 111 \rangle \{112\}$ twinning system, whereas $\langle 110 \rangle$ and $\langle 111 \rangle$ oriented nanowires deformed by dislocation slip. Fur-

thermore, the nanowires with $\langle 100 \rangle$ and $\langle 110 \rangle$ orientations displayed opposite tension-compression asymmetry in deformation mechanisms. Under compressive loading, the nanowire with $\langle 100 \rangle$ orientation deformed by dislocation slip, while twinning was observed in $\langle 110 \rangle$ orientation. Another MD simulation study on BCC Mo nanowires by Wang et al. [35] showed that both axial orientation and wire thickness play important roles in determining the dominant deformation mechanism. The nanowires with orientation $\langle 110 \rangle \{111\}$ exhibited dislocation glide controlled plastic deformation occurring on $\{110\}$ planes whereas for both $\langle 100 \rangle \{110\}$ and $\langle 100 \rangle \{100\}$ orientation twinning was the dominant mechanism with $\{112\}$ being the coherent twin boundaries.

2.3 Twin Boundary Structures in BCC transition metals

Even though numerous experimental evidence confirm the role of deformation twinning in plastic deformation of BCC transition metals, almost no information is available in these studies about the atomic level structures of twins. Based on the twinning elements, deformation twins in BCC metals are well known to form on the $\{112\}$ planes with $\langle 111 \rangle$ shear direction. Formation of deformation twins in BCC metals can proceed by several different mechanisms including nucleation from surfaces and boundaries, as should occur in nanoscale materials [27, 28, 31] or the dissociation of a screw dislocations, which has been argued to be the source in bulk materials [13, 36, 37]. However, these studies involving the nucleation and propagation of deformation twins assumes that the twin nucleus maintains a pure reflection symmetry despite lack of experimental evidence.

The twinning elements outlined earlier can describe the macroscopic degrees of freedom of the twin. However, they do not fully describe the local atomic structure. A common interpretation of the local atomic twin structures in BCC metals is a reflection symmetry about a single $\{112\}$ plane. This type of twin structure, shown in Figure 2.9(a), is readily reproduced by the passage of the $\frac{a}{6}\langle 111 \rangle$ twinning dislocations described above. However, this is not the only postulated twin boundary structure. Vitek proposed the isosceles twin boundary structure [38], shown in Figure 2.9(b), which can be created from the reflection twin boundary by a translation of one half of the crystal relative to the other half by an amount of $\frac{a}{12}\langle 111 \rangle$. This twin boundary structure still sat-

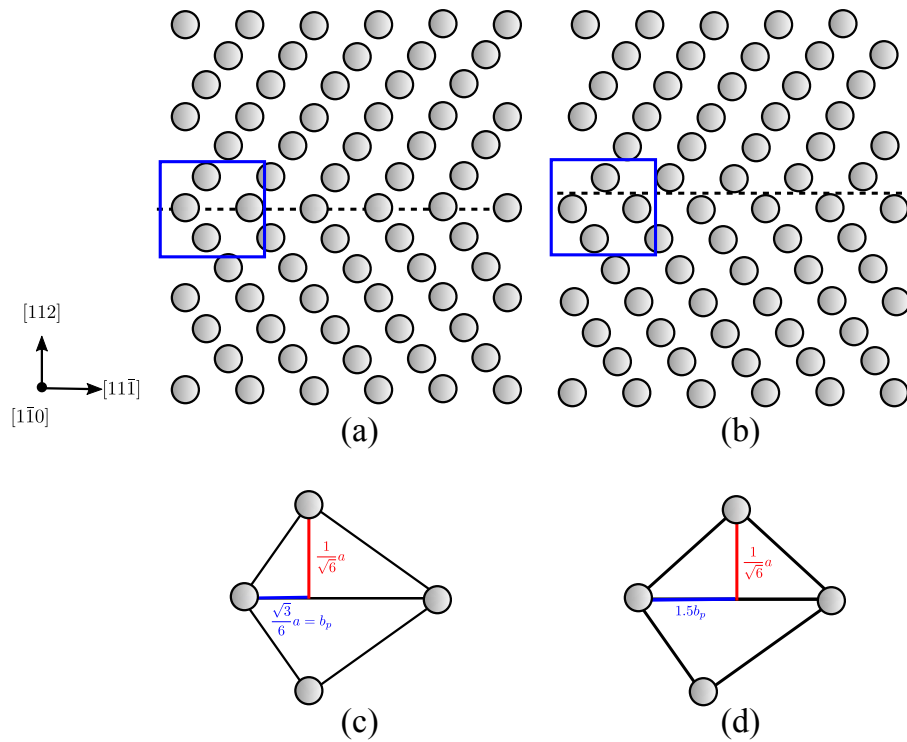


Figure 2.9: The two different twin structures are shown in (a) pure reflection and (b) isosceles. The dashed lines show the approximate location of the boundary between the two twinned structures while the blue boxes illustrate a detail view shown in (c) and (d) for each twin boundary structure, respectively.

ifies the macroscopic orientation relationship between the two crystals and has the advantage of minimizing bond lengths across the twin boundary plane. While experimental work can help provide clear identification of the local atomic structure, we are only aware of one in-situ experiment in Tungsten in which the observed deformation band was confirmed to be a twin band with Fast Fourier Transform pattern analysis with the atomic level structure of the twin boundary assumed to be a pure reflection twin boundary structure [27].

Despite the potential for the existence of more than one twin boundary structures in BCC metals, the isosceles structure is often overlooked in computational studies [39,40]. However, recent atomistic work by Shi et al. demonstrated that some empirical potentials produce the isosceles twin boundary structure and that this should alter both the energetics of nucleation as well as the shape of the twinning generalized stacking fault (TGSF) energy curve [41]. Additionally, recent computational work by Ojha et al. computed the TGSF curves for many of the BCC metals using electronic structure density functional theory (DFT) and concluded that the reflection twin boundary structure was favorable in Mo, W while the isosceles structure is favorable in Ta, Nb, V and α -Fe [42]. Since DFT reasonably reproduces the bonding in BCC transition metals, it can be assumed to be an accurate description of the structure. However, this study did not actually examine the actual produced structure from the simulations nor did it conclusively provide insight into the metastability of the other twin boundary structures, let alone actually quantitatively or qualitatively demonstrate the preference of the specified structure. This raises the question of the actual local atomic structure of twin boundaries in BCC metals. Hence, we have attempted to answer this question using both empirical potentials as well as electronic density functional theory. In this work, we fully relax the twin boundary structures to determine which structures, reflection or isosceles, are stable and if multiple twin boundary structures are metastable and hence their relative stability. We further use the GSF energy curves to explore if other twin boundary structures are metastable as well. The GSF curves further provide insight into how the twins may nucleate. These results provide the first concrete identification of not only the energetics of the twin boundaries, but also their local atomic structure. While we expect the DFT results to accurately represent twin boundary

structure, we compare these results with empirical potentials which are frequently used to model twin nucleation and growth in BCC metals.

2.4 Nucleation and propagation of twins in BCC transition metals

The formation of a deformation twin can be envisaged as occurring in two stages: nucleation of an embryonic twin and its subsequent growth into a macroscopically observable twin. Due to the presence of the intrinsic stacking faults in FCC metals, twins can nucleate and grow layer-by-layer by successive emission of Shockley partials [3, 43–45]. In BCC metals, however, there is no stable stacking fault associated with a twinning partial dislocation (with the Burgers vector of $\frac{a}{6}\langle 111 \rangle$ [38, 46], which suggests that a twin nucleus is unlikely to consist of a single twinning dislocation and thus likely consist of two or more twinning dislocations on adjacent $\{112\}$ planes. Therefore, the instability of a single layer fault has led to the speculation that twin nuclei in BCC crystals likely consist of two or more twinning dislocations on adjacent $\{112\}$ planes and if the twin is nucleated from a perfect dislocations with a Burgers vector of $\frac{a}{2}\langle 111 \rangle$, especially screw, it may dissociate into three partial dislocations (the so-called “zonal dislocation”), forming a three-layer twin nucleus [36, 37, 46].

Twin nucleation and growth have been a topic of debate in the past few decades. Orowan [47] visualized that a twin embryo could nucleate homogeneously in a region of high stress concentration even though he did not specify the origin of the stress concentrations. Cottrell and Bilby [48], Sleeswyk [49], Ogawa [50] and Priestner and Leslie [51] proposed that a twin could nucleate from a heterogeneity such as a specific dislocation arrangement. The well-known pole mechanism proposed by Cottrell and Bilby [48] envisions that under applied stress an $\frac{a}{2}\langle 111 \rangle$ dislocation could dissociate according to the reaction:

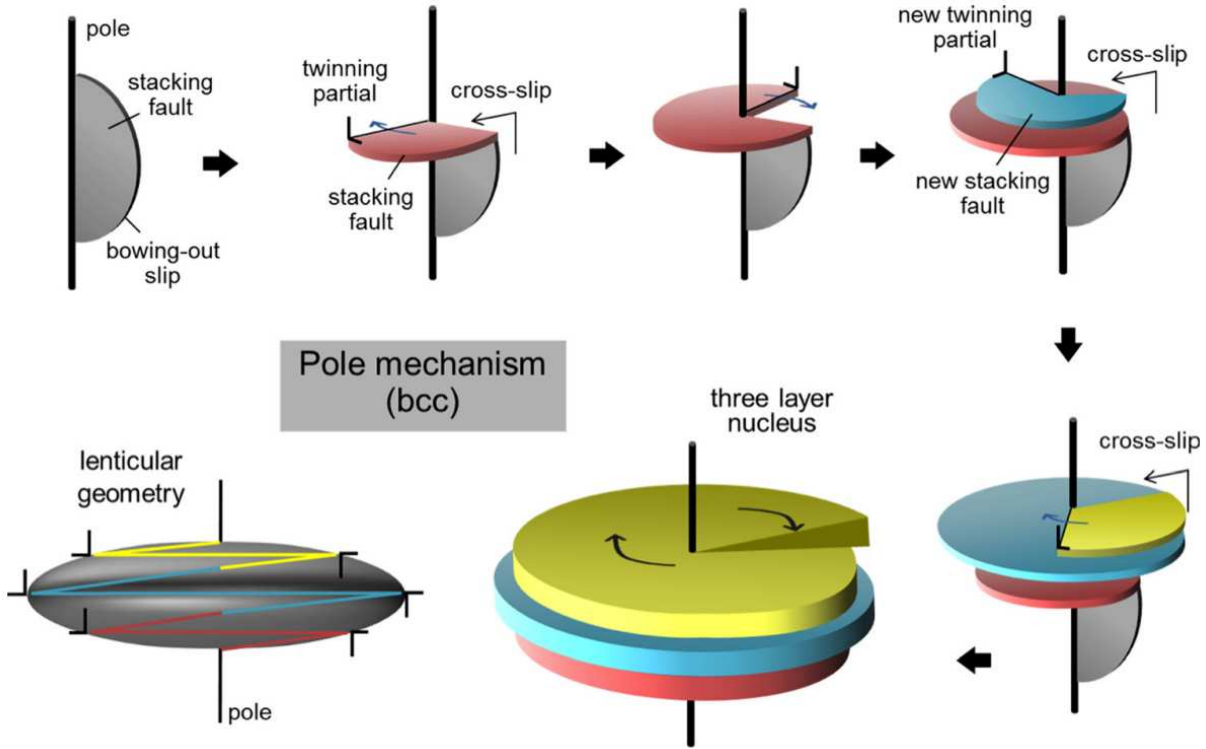
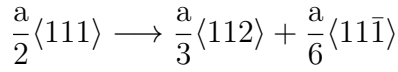
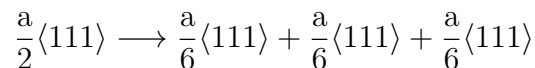


Figure 2.10: An illustration of twin nucleation model via pole mechanism in bcc lattice [3,48]. An expanding slip loop stemming from sessile dislocation (pole) cross-slips into a perpendicular plane. Subsequently, the dislocation continues to revolve around the pole assisted by further cross-slips and hence generates layers of stacking faults, i.e., the twin embryo. Reproduced from [52] with permission from author.

After dissociation, Cottrell and Bilby proposed that $\frac{a}{6}\langle 11\bar{1} \rangle$ twinning dislocation spirals around the $\frac{a}{3}\langle 112 \rangle$ pole dislocation and thus could result in a twin. A schematic diagram of the pole mechanism is shown in Figure 2.10. Sleswyk [49] proposed a different dissociation reaction of $\frac{a}{2}\langle 111 \rangle$ screw dislocations:



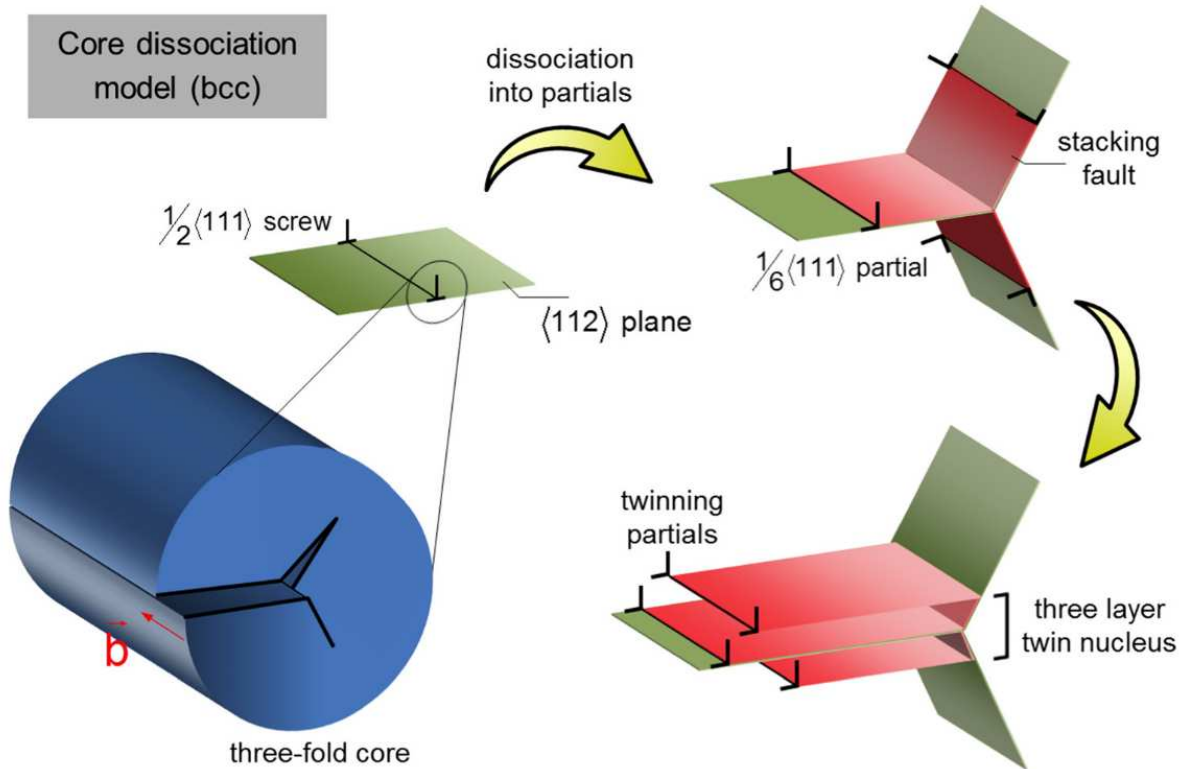


Figure 2.11: The dissociation of a screw dislocation with three-fold core in bcc materials into three fraction dislocations under applied stress [36, 37, 51, 53]. Two of the fractional dislocations (the most stressed ones) cross-glide and become parallel to the third one, thereby forming a three-layer twin nucleus. Reproduced from [52] with permission from author.

He hypothesized that an $\frac{a}{2}\langle 111 \rangle$ screw dislocation could be considered as equivalent to three $\frac{a}{6}\langle 111 \rangle$ twinning partials, each residing in one of the three $\{11\bar{2}\}$ planes. These planes intersect each other symmetrically about the direction of the Burgers vector and under applied stress this symmetrical configuration is unstable and could result into a three-layer twin [54]. See Figure 2.11 for a schematic of the dislocation dissociation mechanism. Ogawa's hypothesis [50] is basically analogous to that of Sleswyk, however, he envisaged that the twins originate from the dissociation of $\frac{a}{2}\langle 111 \rangle$ edge dislocation. Priestner and Leslie [51] proposed a very detailed model for nucleation of three-layer twins from the intersecting slip bands on $\{110\}$ and $\{11\bar{2}\}$ planes in order to account for the restricted slip bands observed in association with twins in shock-loaded Fe-Ni alloy. However, based on their observations of post-deformation debris, the question of whether the twins originated from slip bands or vice-versa cannot be resolved conclusively. A more recent

model proposed by Lagerlof [36] refines Sleswyk's hypothesis of dissociation of an $\frac{a}{2}\langle 111 \rangle$ screw dislocations. This model proposes that a short screw segment of zonal dislocation bows out under an applied stress similar to a Frank-Read source where each of the three twinning partials glides on its individual $\{11\bar{2}\}$ plane and the motion of these three partials on three successive $\{11\bar{2}\}$ planes forms a three-layer micro twin. This model also describes the growth process by imagining that after one Frank-Read zonal dislocation loop is nucleated, the screw segment cross-slips in a similar manner as the model proposed by Pirouz for twinning in Silicon [55] because the formation of a second Frank-Read zonal dislocation loop would produce high stacking fault energy. After cross-slip the screw segment may again bow out on a new set of $\{11\bar{2}\}$ planes to form another three-layer twin.

Ogawa et al. [53] deformed Mo-35 at%Re alloy specimens at room temperature and Mo-18% Re alloy at liquid Nitrogen temperature (77K) and the authors hypothesized from their study that dissociation of edge dislocations in $\{112\}$ planes into three twinning dislocations could be the dislocation nucleation mechanism. Mahajan [54,56] also deformed Mo-35 at% Re alloy specimens at 77K under tension and claimed that twins very probably nucleated from the dissociation of $\frac{a}{2}\langle 111 \rangle$ screw dislocations. These experiments rather than observing three-layer thick twin nuclei, assumed either Ogawa's or Sleswyk's hypothesis is accurate and the authors attempted to explain their experimental findings based on dissociation of perfect dislocations into twinning partials. So these experimental studies have confirmed the existence of deformation twins but fell short of confirming that the critical thicknesses of twins are multiple of 3 [54, 57]. However, most deformation twins in BCC metals typically possess stepwise twin boundaries with the step heights much larger than the size of a single twinning dislocation [58,59]. Validation of models describing the critical thickness of twin nuclei in BCC metals via in-situ observations is also very difficult and this is why the nucleation and growth of twins remain a topic of active research. Hence, atomistic simulations were employed as an option to explore the nucleation and growth of twins. Marian et al. [60], from their MD simulations using an Ackland-Finnis-Sinclair [61] type potential for BCC Iron, observed that depending on the magnitude of stress and temperature, screw dislocations in

BCC Iron move in three different regimes. First, under low stress, the dislocations moved smoothly through the formation and migration of atomic-sized kinks. As the stress increased, the dislocation line became rugged and its motion became jerky by producing a large amount of vacancies and interstitial clusters. Under further high stress, the dislocation line ruggedness continued to increase until, at some point, the dislocation ceased its turbulent motion and initiate a three-layer twin. Chu et al. [62] performed a series of MD simulations to show that when two coplanar, oppositely signed dislocations gliding on $\{112\}$ planes were driven toward one another at supersonic speeds, they did not annihilate but simultaneously nucleated two more twin faults on adjacent planes. This study also revealed that the subsequent nucleation events, along with the original fault, produced a three-layer twin. Ogata et al. [63, 64] determined the $(2\bar{1}\bar{1})\langle 111\rangle$ twinning energy landscape of BCC Molybdenum by generating a TGSF curve using density functional theory for twin embryos containing 2 to 7 layers. They found that the 2-layer embryo is metastable but more surprisingly the 3 and 4-layer thick twins were unstable. The critical thickness estimated by the authors is six-layer thick even though metastable points can be identified from their TGSF curve at shear displacements corresponding to 2 and 5-layer thick twin. However, our work suggests that the thickness are two for a reflection twin and three for an isosceles twin [65]. However, these results focus on twin stability at zero stress, while the energetic pathway for twin nucleation occurs under very high stresses, even for heterogenous twin nucleation [27, 31, 32, 66, 67]. Since the energetics and the structure of a nucleating twin in a BCC metal has never been carefully studied, it is unclear how large the nuclei are and what controls this size. In this light, we have addressed this outstanding question directly using atomic level modeling and settle the size debate once and for all. However, in answering the question of fundamental twin thickness, it is critical to be consistent in how one measures twin thickness in BCC metals and, in fact, all materials. It is natural to try to assign atoms to twinned and untwinned regions and count the thickness of the twin as the number of atoms inside these regions. However, the potential for twin boundaries to exist on top of atomic layers (e.g., reflection) or between atomic layers (isosceles) creates ambiguity of how atomic layers should be partitioned to twinned and untwinned regions. Examples of this are discussed in detail

in Chapter 5. The alternative method is to count twin thickness by counting the number of shearing events that occur between atomic layers, which is the same as counting the number of twinning dislocations. This approach removes the ambiguity, see Chapter 5, and is the method we will employ.

Mahajan's classic experimental studies on Mo-35 at% Re alloy specimens [54, 56, 57] mentioned earlier also explored the growth of deformation twins. He suggested that if the twins were nucleated by dissociation of perfect dislocations, they can thicken by chance encounters with one another as the twinning faults extend in the $\{112\}$ planes. He further visualized the coalescence of multiple twin embryos and thus creating $3n$ -thick twins. Although this seems to require a high density of dislocations to produce a macroscopic twin, Mahajan suggested that this slip band conversion might obviate the need for pole type mechanism of twin thickening, especially if the screw dislocations are able to multiply by cross slip over short distances under combined effects of applied and internal stress fields [3]. Lagerlof's work [36] based on Sleeswyk's hypothesis proposed that lateral propagation and thickening can occur by double cross slip of the screw dislocations. Based on the double cross slip mechanism, Chen et al. [58] argued that after a three-layer twin embryo is nucleated a subsequent screw dislocation cannot dissociate and glide on the same $\{112\}$ plane in the same way as the prior one did, since a second $\frac{a}{6}\langle 111 \rangle$ dislocation on the same $\{112\}$ layer would result in $\frac{a}{6}\langle 111 \rangle$ displacement which is the same as the situation caused by a partial dislocation in the anti-twinning direction and would require prohibitively high stress and energy. Thus the authors of this experimental study speculate that a subsequent dislocation will tend to grow the existing twin nucleus by three layers. The aforementioned study by Ogata et al. [63] on BCC Mo by density functional theory simulations suggests that once a deformation twin reaches critical thickness, subsequent growth is easy and proceeds in a layer-by-layer fashion. As mentioned earlier most deformation twins in BCC metals typically possess stepwise twin boundaries (TBs) with the step heights much larger than the size of a single twinning dislocation [58, 59]. Recent in-situ observations in Tantalum and Niobium films [59] show that twin lamella grow from coherent twin boundaries by repeatedly extruding and subsequently expanding of bulges on the

twin boundaries and the twin growth was described by a self-thickening mechanism through dislocation reactions at steps on coherent twin boundaries without a continuous supply of dislocations. These observations suggest that the twinning front in BCC metals may proceed in a completely different mode of growth, e.g. via stable zonal dislocations, rather than the well-accepted mode of single-layer twinning dislocation [3, 40, 45]. The above discussion raises the question whether it is energetically more favorable to grow deformation twins layer by layer in a BCC metal or does growth occur by zonal twinning dislocations. We have addressed this question using twin boundary migration GSF curves described in Chapter 3.

2.5 Twinning stress in BCC transition metals

A related concept to the minimum size of a twin nucleus and its structure is the stress required to nucleate deformation twins in BCC metals since this stress must be achieved to initiate deformation twinning. A major topic for debate has been the existence and importance of a critical resolved shear stress for deformation twinning. A comprehensive review by Christian and Mahajan [3] argues that the significance of a CRSS may be negligible because of considerable variation in twinning stress depending on the nucleation mechanism. Homogeneous nucleation of twins requires the resolved shear stress on K_1 plane resolved along η_1 direction to approach the theoretical strength of the material whereas for heterogeneous nucleation the stress required to nucleate twins are not as high and will depend on the nature of the defect. Several other factors such as the three dimensional non-planar geometry of dislocations in BCC metals [68], composition, pressure or temperature can play a role in twin nucleation and thus affecting the twinning stress. Despite the debate about the significance of CRSS for twinning in BCC metals, modeling of twinning stresses has been an ongoing topic of research. As discussed earlier, several mechanisms have been proposed for nucleation of twins in BCC metals such as the pole mechanism by Cottrell and Bilby [48], the slip dislocation interaction mechanism proposed by Priestner and Leslie [51], the screw dislocation core dissociation mechanism suggested by Sleswyk [37] and Lagerlof [36] and the edge dislocation dissociation mechanism by Ogawa [50]. The twinning stress prediction from the pole

mechanism is given by $\tau = \frac{\gamma_{us}}{b_p}$ where γ_{us} is the unstable stacking fault energy and b_p is the Burgers vector of the twinning dislocation. Based on this formulation, the twinning stress is estimated to be around 1050 MPa for alpha-Fe which is at least five times higher than the experimental value of 206 MPa [22]. Sleeswyk's hypothesis yields a twinning stress equation of the form $\tau = \frac{\gamma_{sf}}{3b_p}$ where γ_{sf} is the energy associated with a stable twin nucleus. Using this expression, the twinning stress obtained for α -Fe is close to 250 MPa [39]. Ogawa's edge dislocation dissociation model gives $\tau = k_t \frac{\mu}{2\pi(1-\nu)}$ where μ is the shear modulus, ν is the Poisson's ratio and k_t is an empirical constant. The calculation based on this model predicts a twinning stress of 430 MPa for alpha-Fe. A few papers [39, 42] on modeling twin nucleation stresses incorrectly points to the expression $\tau = \frac{\pi\gamma_{TBM}}{b_p}$ derived by Ogata et al. [63, 64] as the theoretical twinning stress model, however, it is clear from the expression itself that this stress prediction pertains to twin boundary migration aka twin growth rather than twin nucleation. Meyers et al. proposed a model that takes grain size and Hall-Petch effects into consideration [69] and the twinning stress predictions they made were only fit to experimental data from a single paper [22] on Iron single crystals. Ojha et al. proposed a modified Peierls-Nabarro formalism to predict twinning stresses in BCC transition metals [42] by incorporating energy barriers from TGSF curves. The twinning stresses obtained from this study are compared with some experimental data in an attempt to validate this approach of predicting twinning stress although this comparison is not comprehensive as not all experimental twinning stress observations are included as evident from Table 2.1. Moreover, in deriving their twinning stress expression Ojha et al. assumes equilibrium conditions for the twinning dislocations which cannot be the case during nucleation. One other issue with this work is the stacking fault energy term used in the analytical model. This term was taken as a difference of the stacking fault energy due to unstable one layer fault and the metastable 3-layer fault. This approach clearly demonstrates that the model proposed by Ojha et al. is not applicable to twin nucleation because to nucleate a twin the energy barrier related to the unstable stacking fault must first be overcome to reach the metastable thickness of the twin embryo. However, their model may provide some insights into the twin growth in BCC metals.

There are numerous experimental studies on deformation twinning in BCC metals where twinning stresses are reported, and these resolved shear stresses are compiled in Table 2.1. The stress values reported in this table are the lowest stress values found in the referenced experimental papers which is not the case in [42] where experimental stress values are only reported if the experimental values have similar orders of magnitude to the stresses predicted by their model. Hence in this work, we have addressed whether the bulk stress values obtained from experiments are indeed the local stresses required for twin nucleation.

Table 2.1: Experimental twinning stresses in BCC metals

BCC Metal	Reference	Temperature (K)	Strain rate (s ⁻¹)	Stress (MPa)
Tantalum	Mitchell <i>et al.</i> [8]	4.2	9.3×10^{-4}	198
	Shields <i>et al.</i> [11]	4.2	5.0×10^{-4}	345
	Sherwood <i>et al.</i> [12]	4.2	9.0×10^{-4}	181
	Chen <i>et al.</i> [58]	77	1.0×10^4	520
	Florando <i>et al.</i> [14]	77	1	224
Niobium	Sherwood <i>et al.</i> [12]	4.2	9.0×10^{-4}	137
	Reid <i>et al.</i> [15]	77	6.7×10^{-4}	228
	Shaw <i>et al.</i> [17]	104	4.2×10^{-4}	198
	Groger <i>et al.</i> [16]	77	3.0×10^{-5}	212
Vanadium	Edington <i>et al.</i> [18]	77	8.0×10^{-4}	221
	Lindley <i>et al.</i> [19]	20	1.5×10^{-4}	456
Molybdenum	Shaw <i>et al.</i> [17]	104	4.2×10^{-4}	333
	Sherwood <i>et al.</i> [12]	77	7.0×10^{-5}	440
Tungsten	Chiem <i>et al.</i> [20]	298	1.8×10^3	750
Chromium	Marcinkowski <i>et al.</i> [21]	123	1.0×10^{-3}	648
Iron	Harding [22]	195	1.0×10^{-3}	206

Chapter 3

Methodology

3.1 Atomistic Modeling

Due to computational cost, interatomic potentials, those that directly relate position to energy without direct computation of the electronic structure, are the most commonly used methods to simulate extended defects in BCC metals including deformation twinning [33, 60, 70–72]. Atomistic simulations however, are only as effective as the interatomic potentials they use and ceramics are notoriously difficult to model. It therefore becomes necessary to consider multiple interatomic potentials, and while there many different formulations, the Embedded Atom Method (EAM) type interatomic potentials are considered which are widely used and readily available on the NIST interatomic potential repository [73].

3.1.1 EAM Potentials

This formulation approximates the energy of each atom as the sum of a pair wise interaction and an embedding term representing the energy cost of placing the atom in the electron cloud [74]. It is given by the expression:

$$E_i = F_\alpha \left(\sum_{i \neq j} \rho_\beta (r_{ij}) \right) + \frac{1}{2} \sum_{i \neq j} \phi_{\alpha\beta} (r_{ij}) \quad (3.1)$$

where r_{ij} is the distance between atoms i and j , $\phi_{\alpha\beta}$ is the pair potential between atom i of type α and atom j of type β , ρ_β is the charge contributed at distance r_{ij} by an atom of type β , and F_α the embedding function for an atom of type α in the electron cloud. The pair potential, charge density function, and embedding function are fit to the material properties of the system. In this work, as mentioned earlier, we primarily analyze potentials based on the embedded atom method [74]. Specifically, we examine the potentials for V [75], Nb [76], Ta [77–81], Cr [82, 83],

Mo [80, 84, 85], W [75, 80, 84], and α -Fe [84]. These potentials are widely used and readily available on the NIST interatomic potential repository [73].

3.1.2 The Potential Energy Surface

In the EAM potentials, the potential energy function is dependent on the interatomic distances r_{ij} . It is not possible to plot the potential energy function for a system of more than one atom. However, it is still useful to think of it as a $3N$ -dimensional potential energy landscape, with topography analogous to the mountains, craters, valleys and mountain passes familiar to us from our terrestrial landscape. In particular, much can be learned about the predictions of a potential energy function from the extremal points (maxima, minima and saddle points) of this landscape [86]. Given any point r_0 in configuration space, one can associate with it a unique minimum on the potential energy surface by performing a steepest descent (SD) minimization. Mathematically, this corresponds to solving

$$\dot{\mathbf{r}} = -\nabla_{\mathbf{r}}E \quad (3.2)$$

starting from the initial guess $r_{ij} = r_0$. Physically, this corresponds to an infinitely rapid quench at zero temperature [87]. Configuration space is divided in this way into disjoint regions, each of which corresponds to the set of all points that quench to the same minimum. These regions are referred to as basins of attraction (or “basins” for short). They are separated by dividing surfaces and connected by saddle points. This is depicted schematically in Figure 3.1.

The deepest minima on the energy landscape are associated with defect-free crystalline structures. Minima with somewhat higher energies are associated with crystals containing internal defects, such as vacancies, interstitials, dislocations, grain boundaries and so on. A rough estimate for a system containing only one atomic species gives the number of minima as $N! \exp(\nu N)$ where ν is some positive number [89]. The first term counts the number of ways a given minimum energy structure can be made with N indistinguishable particles. It accounts for the permutation symmetry of the atoms. The second term counts the number of distinct structural minima. It is based on the assumption that nearby minima are related through local rearrangements and therefore the total

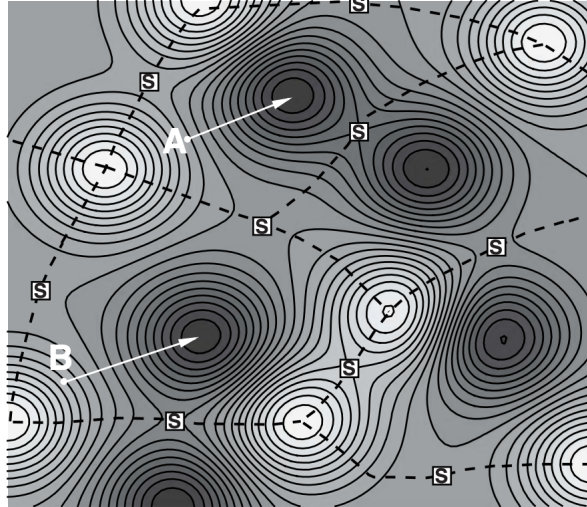


Figure 3.1: A schematic representation of a $3N$ -dimensional energy landscape. Minima are the darkest regions, maxima the lightest regions and saddle points are indicated by “s”. The solids lines correspond to contours of constant energy. The dashed lines are the “dividing surfaces” separating the different minima. The region enclosed by dashed lines around each minimum is its “basin of attraction”. (Adapted from [88] with permission.)

number of such minima is exponential in N [87]. Using this relation, Stillinger and Weber [88] estimated that 1 gram of argon would have of the order of $10^{10^{22}}$ distinct structural minima! The minima and the basins around them are perhaps the most physically relevant of the features in $E(\mathbf{r}_{ij})$. These show us the energetically stable configurations that the system is likely to adopt and how these atomic arrangements will respond to small perturbations. The curvature of the energy function around a minimum determines such things as the elastic moduli of a solid.

Given the primacy of energy minima in understanding materials, it is no surprise that the search for these minima receives a lot of attention. One key type of Molecular Statics (MS) simulation refers to this search for minima in the atomic potential energy landscape. Another important implementation of MS uses methods to find saddle points and transition paths (the lowest energy trajectory connecting two minima). These tell us something about the likely ways that materials deform and the rates at which deformation take place.

3.1.3 Energy Minimization

The search for the minima of a nonconvex, multi-dimensional function is one of the great challenges of computational mathematics. It is interesting that the human eye and brain can look at a hilly landscape and almost immediately find the point of lowest elevation, in addition to establishing where most of the other local minima lie. To do the same with a high-dimensional mathematical function on a computer is much more difficult. Although finding any minimum is not too difficult, finding it quickly is a bit more of a challenge, and finding the global minimum confidently and quickly is still an open field of research. The entire branch of numerical mathematics known as “optimization” is essentially dedicated to these goals. It is not our intention to discuss nonlinear optimization exhaustively. Rather, we list commonly used methods: the steepest descent (SD), conjugate gradient (CG) and Newton Raphson (NR). The ideas behind these methods serve as the basis for more advanced optimization approaches. Entire textbooks on optimization exist (see for example [90, 91]), and the interested reader may find more rigorous detail and advanced topics there.

The CG and NR methods are also classified as “local” minimization methods in the sense that they will only find some “nearby” energy minimum; there is no guarantee that this is the global minimum or even the closest energy minimum to the starting configuration. For atomistic systems, there are also global optimization techniques such as simulated annealing. Simulated annealing uses so-called Monte Carlo sampling to randomly change the configuration of atoms in order to probe new regions of phase space that might be closer to the global minimum. Acceptance of such a stochastic change is probabilistic, with higher-energy configurations being more likely to be rejected.

In Molecular Statics, it is usual to refer to the “unrelaxed” and the “relaxed” structure. The unrelaxed structure is the starting configuration or the initial guess for the equilibrium structure. Running the algorithm to search for a minimum is the “relaxation” process that takes us to the local minimum, where we find the relaxed structure.

3.1.4 Methods for Finding Saddle Points

Defect nucleation, dislocation motion, chemical reactions, diffusion, and fracture are just a few important materials processes that can be viewed as pathways through the potential energy surface. Specifically, each of these processes take us between two configurations of atoms that are local minima. The transition path between them can be important for our understanding of how these processes take place. It also tells us the activation energy of the process and what intermediate equilibrium configurations may exist along the transition. Mathematically speaking, local minima are much simpler entities than saddle points. Both have zero first derivatives, but whereas minima have positive curvature in all directions, saddle points have at least one direction along which the curvature of the energy landscape is negative. Most methods for finding saddle points depend on analyzing the Hessian matrix, which can be expensive for many systems. Saddle point searches are usually based on methods of eigenvector-following, whereby search directions along eigenvectors of the Hessian with the lowest eigenvalues are chosen to systematically locate saddle points. In systems where the Hessian is too expensive to compute, there are methods whereby only the lowest eigenvalues need to be found, or where numerical approximations are used to estimate the search directions. Techniques such as that of Wales and coworkers [92–95], the activation-relaxation technique (ART nouveau) of Barkema and Mousseau [96, 97], and the dimer method of Henkelman and Jonsson [98] are all methods based on eigenvector following. The transition path, or more precisely minimum energy path (MEP), for systems where the Hessian matrix is not readily available can be obtained by the drag method and several variations of the Nudged elastic band (NEB) [99] methods which only require the first derivatives of the potential energy surface.

Once a saddle point is determined, it is relatively simple to find transition paths through the saddle point by systematically perturbing the configuration and following steepest descent pathways to the neighboring minima. It is really the search for the saddle points themselves that can be costly and difficult for complex energy landscapes involving many atoms. For some physical phenomena, we may already know (or be willing to guess) the two local minima at the start and end of a transition path. In this case, the search for the path and any intervening saddle point is

simplified and can be carried out without any recourse to the Hessian matrix or its eigenvectors. In this work, we have used string method simulations devised by E et al. [100] to directly observe twin nucleation using EAM potentials. Also Free End Nudged Elastic Band (FENEb) method [101] has been used for finding saddle points in our continuum models of twin nucleation.

3.2 Electronic Structure

Density functional theory (DFT) is a simulation technique part of a broader class of simulation methods known as ab initio (latin for “from the beginning”) methods. In this work, DFT is used to calculate the electronic structure of a simulation box containing a specified number of ionic cores and electrons. This overview of the fundamentals of DFT is by no means exhaustive. Further reading on electronic structure calculation can be found in any of several textbooks [102–104]. All of the calculations in this work utilize a commercial DFT code suite: the Vienna Ab initio Simulation Package, or VASP [105, 106]. Brief outlines of the concepts used in this work are presented below.

3.2.1 Schrodinger’s Equation

The time-dependent Schrodinger’s Equation for a single, non-relativistic particle:

$$i\hbar \frac{\partial}{\partial t} \psi(\mathbf{r}, t) = \hat{\mathcal{H}}\{\psi(\mathbf{r}, t)\} \quad (3.3)$$

The momentum operator of a particle can be written as $\mathbf{p} = i\hbar\nabla$. The Hamiltonian operator ($\hat{\mathcal{H}}$) is the sum of total kinetic and potential energy of the particle such that:

$$\hat{\mathcal{H}} = \hat{\mathcal{T}} + \hat{\mathcal{V}} = \frac{\mathbf{p}^2}{2m} + \hat{\mathcal{V}}(\mathbf{r}, t) = -\frac{\hbar^2}{2m} \nabla^2 + \hat{\mathcal{V}}(\mathbf{r}, t) \quad (3.4)$$

The Schrodinger’s Equation can now be rewritten as:

$$i\hbar \frac{\partial}{\partial t} \psi = -\frac{\hbar^2}{2m} \nabla^2 \psi + \hat{\mathcal{V}}\psi \quad (3.5)$$

If the wave function comes from a stationary state, e.g., atomic orbitals, then the Hamiltonian is not dependent on time. In this case, $\psi(\mathbf{r}, t) = A(t)\psi(\mathbf{r})$ and $E\psi = \hat{\mathcal{H}}\psi$. The wave function is still a function of time, but only in its amplitude. Hence for a single, non-relativistic particle:

$$E\psi = (\hat{\mathcal{T}} + \hat{\mathcal{V}})\psi = \left[-\frac{\hbar^2}{2m}\nabla^2 + \hat{\mathcal{V}} \right] \psi(\mathbf{r}) \quad (3.6)$$

3.2.2 Density Functional Theory

For many-body electronic structure calculations, the nuclei of the molecules or clusters are treated as fixed. This is known as the Born-Oppenheimer Approximation. This generates a static external (from the perspective of the electrons) potential V through which the electrons are moving. The stationary electronic state is then defined as a wavefunction ψ that satisfies the many-electron, time-dependent Schrodinger equation.

$$\hat{\mathcal{H}}\psi = [\hat{\mathcal{T}} + \hat{\mathcal{V}} + \hat{\mathcal{U}}]\psi = \sum_i^N \left[-\frac{\hbar^2}{2m}\nabla^2 + \sum_i^N V(\mathbf{r}_i) + \sum_{i<j}^N U(\mathbf{r}_i, \mathbf{r}_j) \right] \psi \quad (3.7)$$

Here $\hat{\mathcal{T}}$ is the kinetic energy, $\hat{\mathcal{V}}$ is the potential energy from the external field of positively charged nuclei, and $\hat{\mathcal{U}}$ is the electron-electron interaction energy. The $\hat{\mathcal{U}}$ term is not separable into single-particle equations since the interaction term is complicated. There are many possible ways to solve this equation using Slater determinants [107]. The simplest version is the Hartree-Fock method, which is also known as the self-consistent field (SCF) method. The Fock operator for the i th electron is given by:

$$\hat{F}(i) = \frac{1}{2}\nabla_i^2 - \sum_{\alpha} \frac{Z_{\alpha}}{r_{i\alpha}} + \sum_{j=1}^{N/2} (2\hat{J}_j(i) - \hat{K}_j(i)) \quad (3.8)$$

where the first two terms are the non-interaction terms of the Hamiltonian for the given electron, kinetic energy and static potential energy, respectively. Here Z_{α} is the charge of the α th nucleus and $r_{i\alpha}$ is the distance between the electron and that nucleus. The term $\hat{J}_j(i)$ is the Coulomb operator,

which defines the repulsion of electron i by electron j as:

$$\hat{J}_j(\psi_i) = \psi_i \int |\psi_j|^2 \frac{1}{|r_{ij}|} dr_j \quad (3.9)$$

The electron exchange energy $\hat{K}_j(i)$ is represented by:

$$\hat{K}_j(\psi_i) = \psi_j \int \frac{\psi_j^* \psi_i}{|r_{ij}|} dr_j \quad (3.10)$$

This represents the asymmetry of the wavefunctions and also addresses the antisymmetry of the Slater determinant by satisfying the Pauli exclusion principle. The Fock operator is then used on relevant wavefunctions producing and eigenvalue-like expressions:

$$\hat{F}\psi_i = \varepsilon_i \psi_i \quad (3.11)$$

Eigenfunctions which satisfy this equation are the basis functions for the electron orbitals. The Hartree-Fock method iteratively solves this formulation through the following steps [108] which are computationally expensive, and has numerical stability issues.:

1. Input coordinates and charges of atomic nuclei, as well as number of electrons in the system
2. Make an initial guess for the electronic orbital basis functions
3. Construct the Fock Matrix
4. Diagonalize the Fock Matrix to solve for the new basis functions
5. Check for convergence of the basis functions. If not converged, repeat from Step 3

Finding a solution to the many-body Schrodinger's Equation with the electron-electron interaction is a complicated problem. It would be more convenient if this many-body problem is converted into a series of single-body problems which sufficiently approximates the many-body problem without sacrificing the underlying physics. In addition to the computational difficulties, it

is also impossible to experimentally probe the individual wavefunctions of a system of electrons. In order to make this approximation, the concept of electron density is introduced. The electron density of a normalized N-electron wavefunction is:

$$\rho(\bar{x}) = N \sum_s \int \dots \int |\psi(\bar{x}_1, \bar{x}_2, \dots, \bar{x}_N, s)|^2 d\bar{x}_2 \dots d\bar{x}_N \quad (3.12)$$

This represents the electron density at position \bar{x} based on the wavefunctions of all electrons and both spin up and spin down possibilities, s . The primary advantage of using the electron density is it is experimentally observable which is extremely useful for comparison with experimental data. Also the electron density decays i.e., $\rho \rightarrow 0$ as we move away from the point of interest ($r \rightarrow \infty$). Integration of electron density over all of space gives the total number of electron, $\int \rho(\bar{r}) d^3r = N$.

Based on the uniform electron gas approximation, the kinetic energy of the system can be computed by using the Thomas-Fermi model:

$$T(\bar{r}) = \frac{3h}{10m_e} \left(\frac{3}{8\pi} \right)^{2/3} \int \rho(\bar{r})^{5/3} d^3r \quad (3.13)$$

Here \bar{r} is the spatial position vector and ρ is the electron density. Also the potential energy term consists of two components. An attraction to positively charged nuclei:

$$V(\bar{r}) = \int -\rho(\bar{r}) \frac{Ze^2}{\bar{r}} d^3r \quad (3.14)$$

and the repulsion between electrons:

$$U(\bar{r}) = \frac{1}{2} e^2 \int \frac{\rho(\bar{r})\rho(\bar{r}')}{|\bar{r} - \bar{r}'|} d^3r d^3r' \quad (3.15)$$

With this model, the system can be represented in terms of electron density only. Minimizing the energy given by these expressions theoretically should lead to a solution of the appropriate electron density. But this model is not a good approximation of a real system, especially for kinetic energy of the system. Moreover, there is no term which considers the electron exchange (Pauli exclu-

sion principle). But this model is extremely useful for approximating the kinetic energy from wavefunctions, ψ_i . If an analytical relation can be established between the wavefunctions and electron density, a more accurate approximation can be achieved and this is where the Hohenberg-Kohn Theorem comes in. This theorem proves that the electron density uniquely describes the many-electron system, and that also, the energy of the system is a functional of the electron density: $E = E[\rho]$. The main takeaways from this theorem are as follows:

- In the ground state, the electron density uniquely determines the external potential of the nuclei, $V_\rho = f(\rho)$.
- In any quantum state, the external potential uniquely determines the many-electron wavefunction $\psi = f(V_n)$.
- In any quantum state, the total energy E is a functional of the many-body wavefunction $E = f(\psi)$.

The energy operator of a system can be written as:

$$\hat{E} = \int \rho(\bar{r}) V_n(\bar{r}) d\bar{r} + \langle \psi(\rho) | \hat{T} + \hat{U} | \psi(\rho) \rangle \quad (3.16)$$

This can be rewritten as the Kohn-Sham equations:

$$E(\bar{r}) = \int \rho(\bar{r}) V_n(\bar{r}) d\bar{r} - \sum_i \left[\int \frac{\nabla^2 \chi_i(\mathbf{r})}{2} d^3\mathbf{r} + \frac{1}{2} \int \int \frac{\rho(\bar{r}) - \rho(\mathbf{r}')}{|\bar{r} - \mathbf{r}'|} d^3\mathbf{r} d^3\mathbf{r}' + E_{XC} \right] \quad (3.17)$$

where E_{XC} represents the electron exchange or correlation. This term states that if an electron is at point \bar{r} , there is a diminished likelihood that another electron will be in the vicinity. For a long time, there was much debate over how the exchange-correlation term should be calculated. Now one of the most common approaches, the Local Density Approximation (LDA) calculates the exchange-correlation term as a function of the electron density. This approach was originally proposed by Kohn and Sham along with their equations, but was largely overlooked for decades [108]. The

exchange-correlation energy of a system is approximated to be a sum of the exchange energy E_X and the correlation energy E_C as $E_{XC} \approx E_X + E_C$.

This formulation of the Hamiltonian converges on a solution to the eigenvalue problem:

$$\hat{\mathcal{H}}\chi_i = \varepsilon_i\chi_i \quad (3.18)$$

DFT attempts to find solutions which satisfy the time-independent Schrodinger equation:

$$\hat{H}\psi = E\psi \quad (3.19)$$

This states that if the system is stationary, the Hamiltonian operation (\hat{H}) on the many-body electron wave function (ψ) is proportional to the wave function itself. Furthermore, the proportionality is, in fact, the energy of the state (E) [109]. Here the Hamiltonian operator can be thought of as the kinetic energy of each electron wave function (\hat{T}), and the potential energy of each electron, which itself is comprised of the potential energy in reference to attraction between electrons and nuclei (\hat{V}), and the potential energy between electrons (\hat{U}). Thus the time-dependent Schrodinger equation can be expressed as:

$$\hat{H}\psi = \hat{T} + \hat{V} + \hat{U} = \left[\sum_i^N -\frac{\hbar}{2m} \nabla_i^2 + \sum_i^N V(r_i) + \sum_i^N \sum_{i<j} U(r_i, r_j) \right] \psi = E\psi \quad (3.20)$$

Since it is impossible to distinguish which electron is which, a more useful description is the point-wise electron density n , which can be expressed as:

$$\rho(r) = 2 \sum_i \psi_i^*(r) \psi_i(r) \quad (3.21)$$

Hohenberg and Kohn stated that in the ground state, the energy E can be expressed as a functional of the electron density: $E = E[\rho(r)]$. The energy functional can be written as a functional of the

individual wave functions, and divided into parts that we know, and parts that we don't know:

$$E[\{\psi_i\}] = E_{\text{known}}[\{\psi_i\}] + E_{\text{XC}}[\{\psi_i\}] \quad (3.22)$$

The contributions to the electron energy that we know include: the kinetic energy, the interactions between the electrons and the nuclei, the interactions between electrons, and the interactions between nuclei. This can be written as:

$$E_{\text{known}}[\{\psi_i\}] = -\frac{\hbar^2}{m} \sum_i \int \psi_i^* \nabla^2 \psi_i d^3r + \int V(\mathbf{r}) \rho(\mathbf{r}) d^3r + \frac{e^2}{2} \int \int \frac{\rho(\mathbf{r}) \rho(\mathbf{r}')}{|\mathbf{r} - \mathbf{r}'|} d^3r d^3r' + E_{\text{ion}} \quad (3.23)$$

The unknown term, $E_{\text{XC}}[\{\psi_i\}]$, is called the exchange-correlation (XC) functional, which incorporates quantum mechanical effects such as correcting the non-physical self-interaction and Pauli exclusion effects. Kohn and Sham further made the problem more manageable by showing that the electron density can be solved through a set of simultaneous equations, one for each electron. These are known as the Kohn-Sham equations and they resemble the time-independent Schrodinger's equation:

$$\left[-\frac{\hbar^2}{2m} \nabla^2 + V(\mathbf{r}) + V_{\text{H}}(\mathbf{r}) + V_{\text{XC}}(\mathbf{r}) \right] \psi_i(\mathbf{r}) = \varepsilon_i \psi_i(\mathbf{r}) \quad (3.24)$$

where the exchange-correlation term is some functional derivative of the exchange-correlation energy with respect to electron density, as such:

$$V_{\text{XC}}(\mathbf{r}) = \frac{\delta E_{\text{XC}}(\mathbf{r})}{\delta \rho(\mathbf{r})} \quad (3.25)$$

The interactions between electrons are by far the most computationally expensive part of DFT calculations [108]. There have been many proposed ways of calculating this term, however in this work, we have exclusively used the generalized gradient approximation (GGA) XC functional. But before discussing the GGA, we will briefly look at the local density approximation (LDA) which

is one of the simplest methods of calculating the exchange-correlation term. It is also one of the first methods to be effective in calculating XC functional. The XC term is calculated at each point as a functional of the electron density at that point [110]. Since the exchange correlation energy for a homogeneous electron gas is known, the XC term can be approximated by the XC energy of a homogeneous electron gas evaluated at the local density.

$$E_{XC}^{LDA}[\rho(\mathbf{r})] = \int \rho(\mathbf{r}) \epsilon_{XC}^{HEG}(\rho(\mathbf{r})) d\mathbf{r} \quad (3.26)$$

Despite its simplicity, DFT simulations which utilize the LDA XC functionals are prone to overbinding the unit cell, predicting lattice constants somewhat smaller than experimentally observed values [111].

Efforts to improve upon the LDA method led to a class of higher-order XC functionals known as generalized gradient approximations (GGA). The GGA class of methods adds one higher order term to the XC functional. In these methods, the pointwise interaction energy is a function of the local electron density, as well as the gradient of the electron density at that point.

$$V_{XC}^{LDA}[\rho(\mathbf{r})] = V_{XC}[\rho(\mathbf{r}), \nabla\rho(\mathbf{r})] \quad (3.27)$$

One of the most widely-used GGA methods was developed by Perdew, Burke, and Erzerhof (PBE) [112] which can often offer better predictions than LDA. The PBE XC is expected to underbind unit cells, providing lattice constants which are somewhat larger than those experimentally measured [113].

The simulation of individual electrons is rather costly with computational cost scaling approximately $O(N^3)$ where N is the number of electrons [114, 115]. So reducing the number of electrons needed in the simulation goes a long way toward increasing the speed of a DFT calculation. Furthermore, simulating waves which are confined to relatively small length scales, such as the core electrons, require increased computational efforts. For these reasons, it may be beneficial to only simulate the valence electrons involved with bonding. However, it would be incorrect to assume

that the core electrons (those in the inner shells) do not have a measurable effect on the valence electrons. These core electrons shield the positive charges of the atomic nuclei to which they are attached. These effects are accounted for by defining a fixed electron density near the ionic center. These "frozen-core" fields are known as pseudopotentials. The potentials are "pseudo" since they do not represent how an electron interacts with an lone atomic nucleus, but instead how it interacts with a nucleus surrounded by a specified set of core electrons. There are a few types of pseudopotentials, but the most commonly used are ultra-soft pseudopotentials (USPP) and projector augmented-wave pseudopotentials (PAW) [116]. This study exclusively employs the PAW pseudopotentials for BCC transition metals.

Since the solutions to Schrodinger's equations are the electron plane-waves in periodic super-cells, it is useful to solve for these waves in reciprocal space. The reciprocal space vectors, k , must satisfy Bloch's theorem:

$$\phi_K(r) = \exp(ik \cdot r) u_k(r) \quad (3.28)$$

Here the function $\exp(ik \cdot r)$ is a plane wave, which is periodic over the simulation cell. It is easier to evaluate this integral in reciprocal space, or k -space, than in 3-dimensional real space. Just like real space, the reciprocal lattice has associated basis vectors in reciprocal space, known as reciprocal lattice vectors. They are defined such that:

$$b_1 = 2\pi \frac{a_2 \times a_3}{a_1 \cdot (a_2 \times a_3)}, b_2 = 2\pi \frac{a_3 \times a_1}{a_2 \cdot (a_3 \times a_1)}, b_3 = 2\pi \frac{a_1 \times a_2}{a_3 \cdot (a_1 \times a_2)} \quad (3.29)$$

This means that the magnitudes of the reciprocal lattice vectors, $|b_i|$, are inversely related to the magnitudes of the real-space lattice vectors by: $\frac{2\pi}{|a_i|}$. The primitive unit cell in reciprocal space is known as the Brillouin zone, and contains a great deal of information regarding band theory. The volume of the Brillouin zone is given by:

$$V_{BZ} = \frac{(2\pi)^3}{V_{cell}} \quad (3.30)$$

Since DFT is solving for the solutions of integrals of plane-wave functions, it is easier to compute them in k-space. For speed, the k-space integration is performed with quadrature, and the domain is meshed to provide integration points. While there are many ways to choose these points, one of the most common, and the one used exclusively in this work, is the Monkhorst-Pack k-space meshing algorithm [117].

Solving for the electronic ground state is important however our goal is to be able to calculate forces on the ions, and stresses in the crystal. The forces on a particle at a point \mathbf{R} in a quantum-mechanical system is given by the derivative of the energy at that point:

$$\mathbf{F} = -\nabla_{\mathbf{R}}\langle E \rangle \quad (3.31)$$

In our system, $\langle E \rangle = \langle \psi | \hat{\mathcal{H}} | \psi \rangle$, and our wavefunctions are normalized. Thus we can use the Hellman-Feynman Theorem [118] to calculate the derivative of the total energy with respect to a given parameter (λ) as:

$$\frac{\partial E}{\partial \lambda} = \langle \psi | \frac{\partial \hat{\mathcal{H}}}{\partial \lambda} | \psi \rangle \quad (3.32)$$

Since in our DFT simulations, we are dealing with the Kohn-Sham Hamiltonian of the electronic density:

$$\hat{\mathcal{H}}_{\mathbf{R}} = -\frac{1}{2}\nabla_{\mathbf{r}}^2 + V_{e-e}(\mathbf{r}) + V_{\text{ion}-e}(\mathbf{r}, \mathbf{R}) + V_{\text{XC}}(\mathbf{r}) + V_{\text{ion-ion}}(\mathbf{R}) \quad (3.33)$$

we can see that for the force on a given ionic nucleus, there are only contributions from the inter-ionic Coulombic forces and the interaction between ions and electrons from the pseudo-potential. To calculate the stress tensor in the simulation cell, the derivative of energy is taken with respect to cell geometry parameters.

3.2.3 DFT Simulation Parameters

As mentioned earlier, the DFT simulations reported in this work were carried out using VASP, which is a plane-wave DFT code [106]. To approximate the exchange-correlation energies, we utilized the generalized gradient approximation parameterized by Perdew, Burke and Ernzerhoff

[112]. For all the BCC metals, we approximated the core-valence electron interactions with the PAW pseudopotentials [116] and the valence electrons used were $3d^34s^2$, $4p^64d^45s^1$, $5d^36s^2$, $3d^54s^1$, $4d^55s^1$, $5d^46s^2$, $3d^64s^2$ for V, Nb, Ta, Cr, Mo, W, and α -Fe respectively. The plane wave energy cutoff used is 450 eV and integration in reciprocal space was carried out using the Monkhorst Pack method [117] of $24 \times 24 \times 1$ for all the GSF curves and twin boundary structures.

To simulate α -Fe, we used spin polarized DFT in order to accurately model its ferromagnetism. This results in a magnetic moment on the α -Fe atoms of $2.2\mu_B$, where μ_B is the Bohr magneton. All other materials were simulated without spin polarization.

In order to construct the GSF curves using DFT, we had to determine the equilibrium lattice constants predicted by DFT. These were computed examining the lattice constant as a function of both K-point density and the plane-wave energy cutoff. When these were sufficiently converged, we fixed the lattice constant, plane wave energy cutoff and K-point density.

For applying pure shear stresses on simulation cell of size $a [1\bar{1}0] \times \frac{a}{2} [11\bar{1}] \times \frac{Na}{6} [112]$ with $N = 6$, we used constant k-point density that is equivalent to $7 \times 13 \times 5$ mesh.

To perform constrained twin stability analysis and to generate TGFSF curves for determining the thickness of metastable twin, we used k-point density equivalent to $7 \times 13 \times 1$ mesh for simulation cells of size $a [1\bar{1}0] \times \frac{a}{2} [11\bar{1}] \times \left(\frac{Na}{6} + \Delta\right) [112]$ with $N = 24$ and $\Delta = 15\text{\AA}$.

3.2.4 Structural Relaxation

The relaxation of the crystal, ionic coordinates and cell size and shape, is a fundamental tool to this work. The computation of the structural minimum is accomplished in VASP with the Conjugate Gradient (CG) method [119]. This method iteratively seeks to find the minimum of a system of equations described by: $f(x) = \frac{1}{2}x^T Ax - x^T b$. The minimum of this linear system of equations is the solution to: $Ax = b$. The initial direction towards solving is taken to be the residual of system of equations at the chosen starting point:

$$d_{(0)} = r_{(0)} = b - Ax_{(0)} \quad (3.34)$$

$$x_{(i+1)} = x_{(i)} + \alpha_{(i)} d_{(i)} \quad (3.35)$$

The magnitude of search along that vector is based on the residual:

$$\alpha_{(i)} = \frac{\mathbf{r}_{(i)}^T \mathbf{r}_{(i)}}{\mathbf{d}_{(i)}^T \mathbf{A} \mathbf{d}_{(i)}} \quad (3.36)$$

After each step, a new residual is computed, the next direction is chosen, and the process is repeated:

$$\mathbf{r}_{i+1} = \mathbf{r}_{(i)} - \alpha_i \mathbf{A} \mathbf{d}_{(i)} \quad (3.37)$$

$$\beta_{(i+1)} = \frac{\mathbf{r}_{(i+1)}^T \mathbf{r}_{(i+1)}}{\mathbf{r}_{(i)}^T \mathbf{r}_{(i)}} \quad (3.38)$$

$$\mathbf{d}_{(i+1)} = \mathbf{r}_{(i+1)} + \beta_{(i+1)} \mathbf{d}_{(i)} \quad (3.39)$$

This is repeated until some convergence criterion is met. The strength of CG minimization, over, for example, Steepest Descent, is that each successive search direction is orthogonal to all previous search directions. So the solution to a linear system of equations with an n th order basis set should only take n steps. Of course, this would not be useful to us if it only solved linear systems of equations. This method can be generalized for a nonlinear system of equations, where the solution is found to be where the gradient of the function is zero:

$$\nabla_x f(x) = 2\mathbf{A}^T (\mathbf{A}x - \mathbf{b}) = 0 \quad (3.40)$$

The initial step (Δx_0) is chosen by computing the steepest descent of the initial position (x_0):

$$\Delta x_0 = -\nabla_x f(x_0) \quad (3.41)$$

The step size (α) is chosen along that direction which minimizes the function by:

$$\alpha_0 = \min_{\alpha} f(x_0 + \alpha \Delta x_0) \quad (3.42)$$

The position is then updated by that step length in that direction:

$$x_1 = x_0 + \alpha_0 \Delta x_0 \quad (3.43)$$

This process is then repeated. However, in subsequent iterations, the search direction (s_n) is updated to be a conjugate to previous directions as:

$$s_n = \Delta x_n + \beta s_{n-1} \quad (3.44)$$

For the second iteration, $s_0 = \Delta x_0$. There are many methods of computing β , one of the most common being the Fletcher-Reeves method [120]:

$$\beta_n^{\text{FR}} = \frac{\Delta x_n^T \Delta x_n}{\Delta x_{n-1}^T \Delta x_{n-1}} \quad (3.45)$$

The line search now finds the step size which minimizes the function in the s_n direction:

$$\alpha_n = \min_{\alpha} f(x_n + \alpha s_n) \quad (3.46)$$

3.3 Metastable Twin Boundary Structures

In order to determine what metastable twin structures exist in the BCC transition metals, we utilized both electronic density functional theory, as implemented in Vienna Ab initio Simulation Package (VASP) [106], as well as classical atomistic simulations, using LAMMPS [121]. For each of our methods, we used the conjugate gradient method to find the local energy minimum nearest to a set of initial atomic positions because of its speed and robustness. Our initial atomic positions included the perfect reflection structure, Figure 2.9(a), and perfect isosceles structure, Figure 2.9(b), as well as two other structures in which the top half of the structure is translated by $\frac{1}{4}b_p$ and $\frac{3}{4}b_p$ (where $b_p = \frac{a}{6}\langle 111 \rangle$) to the right of the bottom half of the crystal structure as shown in Figure 2.9(a). The choice of the latter two points were made because, as noted above, the pure

reflection and pure isosceles structures have high symmetry which can trap the system in a local metastable equilibrium point while the use of the other structures breaks this symmetry and has the potential to find other metastable structures.

For density functional theory simulations, the initial twin boundary structure was created using a periodic simulation cell that has a geometry specified by:

$$a[1\bar{1}0] \times \frac{a}{2}[11\bar{1}] \times \left(\frac{Na}{6} + \Delta \right) [112]$$

where N is the number of atomic layers used in the simulation and Δ is a vacuum gap introduced into the simulation cell to prevent the periodic images along the [112] direction from interacting. For simulations of the relaxation of the twin boundary structure, N=21 and $\Delta = 15$. The energy tolerance for the convergence of the electronic structure was set to 10^{-7} eV and the tolerance for structural convergence was set to 10^{-6} eV to ensure that the twin structures are fully relaxed and the computed energies have sufficient precision.

For our classical atomistic simulations using empirical potentials, a similar simulation setup was used. However, in this case the simulation cell size is $a[1\bar{1}0] \times \frac{a}{2}[11\bar{1}] \times \frac{Na}{6}[112]$ with free boundary conditions applied along the [112] direction and periodic boundary conditions were applied in the other two directions. Since computational cost is not a concern for classical atomistic simulations, the number of atomic layers was set to N=35 and the energy tolerance was set to a relative error of 10^{-10} .

The twin boundary energy was then computed using the converged energy of our simulation cell, E, and the energy computed with the same number of atoms in a perfect BCC crystal (but with the same free surfaces), E_0 . The twin boundary energy is computed as:

$$\gamma = \frac{E - E_0}{A} \quad (3.47)$$

where A is the area of the twin boundary plane: $a[1\bar{1}0] \times \frac{a}{2}[11\bar{1}]$.

3.4 Twin boundary GSF curve

To provide insight into the potential metastable twin boundary structures and bonding across the twin plane, we have also computed a twin boundary GSF curve (TBGSF). This idea is borrowed from Mrovec *et al.* [122] who used this methodology to determine the low energy symmetry tilt grain boundaries in Nb and Mo. The TBGSF curve is then similar to any GSF curve but represents the energy per unit area variation as a function of the relative displacement of the twins in the $[11\bar{1}]$ direction and must be fully periodic for a displacement of $\frac{a}{2}[11\bar{1}]$. For our TBGSF computations,

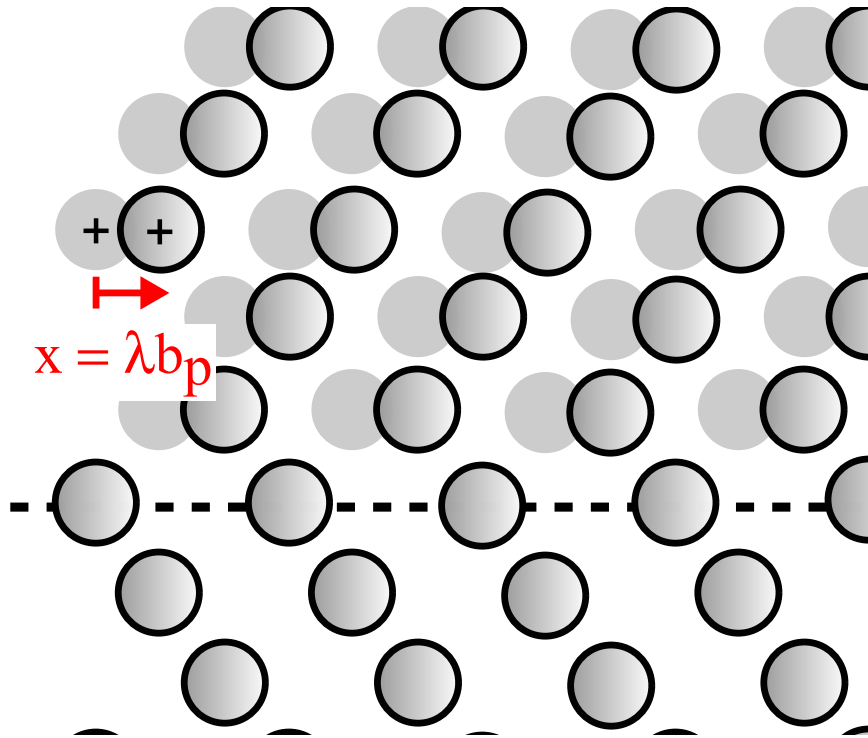


Figure 3.2: The construction of the TBGSF curve starts with a pure reflection twin boundary. The structure is then rigidly shifted by $x = \lambda b_p$ to form a faulted twin boundary. The energy per unit area is measured relative to the pure reflection when $x = 0$.

we start with the pure reflection twin boundary structure for both DFT and atomistics as described above. Then, we displace the atoms above the twin boundary (TB), denoted by the dashed line in Figure 3.2, in the positive $[11\bar{1}]$ direction relative to atoms below the TB plane. The structure is relaxed, using conjugate gradient, in a constrained fashion such that the atoms are only able to

move in the $[112]$ direction. The TBGSF energy is then computed using Equation (3.47) where γ is a function of the normalized displacement $\lambda = \frac{x}{b_p}$, in the $[11\bar{1}]$ direction, E is the energy of the translated and relaxed structure and E_0 is the energy of the relaxed and constrained pure reflection TB. As noted above, the TBGSF curve has a period of $\frac{a}{2}[11\bar{1}]$, although most of the TBGSF curves plotted in this work are only up to $\frac{a}{6}[11\bar{1}]$, which represents part of the twinning GSF (denoted TGSF here) curve commonly reported in the literature [41,42,64]. The TGSF curve is commonly used to represent both the nucleation and growth of twins in BCC metals but is expensive to compute and is affected by twin-twin interactions while the TBGSF described here is not. The method for computing TGSF curves is described below.

3.5 Twinning GSF curve

In addition to the TBGSF, we also computed the twinning GSF (GSF) curves. Here we generate two types of TGSF curves:

1. Sequential TGSF curves
2. Concurrent TGSF curves

3.5.1 Sequential TGSF curves

For this TGSF curves, the starting point is a pure BCC crystal as schematically illustrated in Figure 3.3(a). The crystal is then sheared incrementally, by λb_p , along a single plane in the $[11\bar{1}]$ direction up to an amount b_p (Figure 3.3(c)). The GSF curve is continued by changing the shear plane to one above the plane most recently sheared, as shown in Figure 3.3(d)-(e). The GSF energy is computed using Equation (3.47) with the reference E_0 being the energy of the pure BCC crystal, shown schematically in Figure 3.3(a). In each step, the structure is geometrically optimized under the constraint that motion can only occur in the $[112]$ direction.

Note that for the sequential TGSF curves computed for analyzing TB structures and twin growth, the incremental shearing was carried out for up to $8b_p$. To mitigate the effects of free

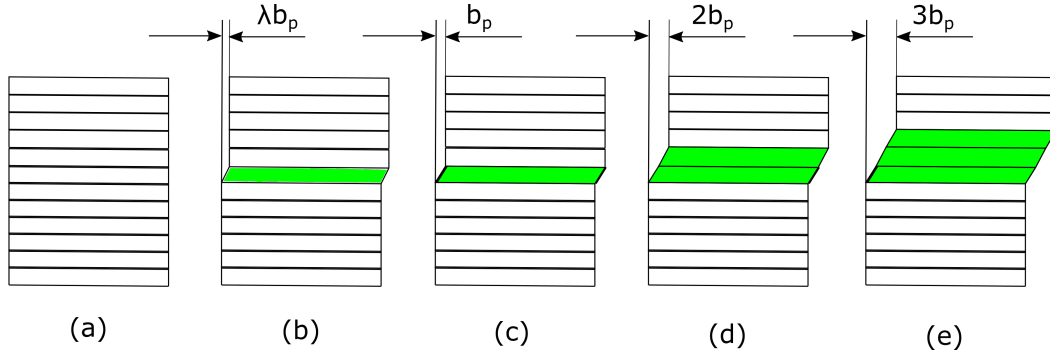


Figure 3.3: The creation of the TGSF curve through incremental discontinuous shearing of the BCC crystal structure. (a) The initial BCC crystal (b) is sheared by λb_p incrementally up to (c) b_p which forms the first part of the curve. (d) Next, all the atomic layers above the plane that was initially sheared are sheared again up to b_p , creating a total shear of $2b_p$. This is repeated again in (e) to create a three layer twin and is repeated up to n layers.

surfaces for these 8 layer twins, the number of atomic layers was increased to $N = 30$ in lieu of $N = 24$ we have used more frequently for the DFT simulations.

This process will produce a standard pure reflection twin boundary structure. However, the process of the creation of the TGSF must be altered to correctly capture the formation of the isosceles TB structure. The main change in the construct shown in Figure 3.3 is that the first incremental shear does not stop at b_p but rather at $\frac{1}{2}b_p$, with all other procedures being equal. This produces an alternative TGSF curve in which a double isosceles TB structure is formed at the terminus, rather than a double reflection twin boundary structure. It is further worth noting, in both cases, that the TGSF curve is naturally discontinuous in which the planes of shear continually change and there is no expectation that the curves are smooth despite many reports that they are, an important point we will revisit later in Chapter 4.

3.5.2 Concurrent TGSF curves

An important observation by inspecting the snapshots of the string simulations is that twinning is initiated by concurrent nucleation of twinning dislocation loops instead of sequential displacements on successive $\{112\}$ planes as conceived by Ogata et al. [64], Shi et al. [41] and Ojha et al. [42]. This implies that sequential TGSF curves, even though useful in determining twin stability in BCC transition metals, do not model the lattice resistance accurately. For this reason,

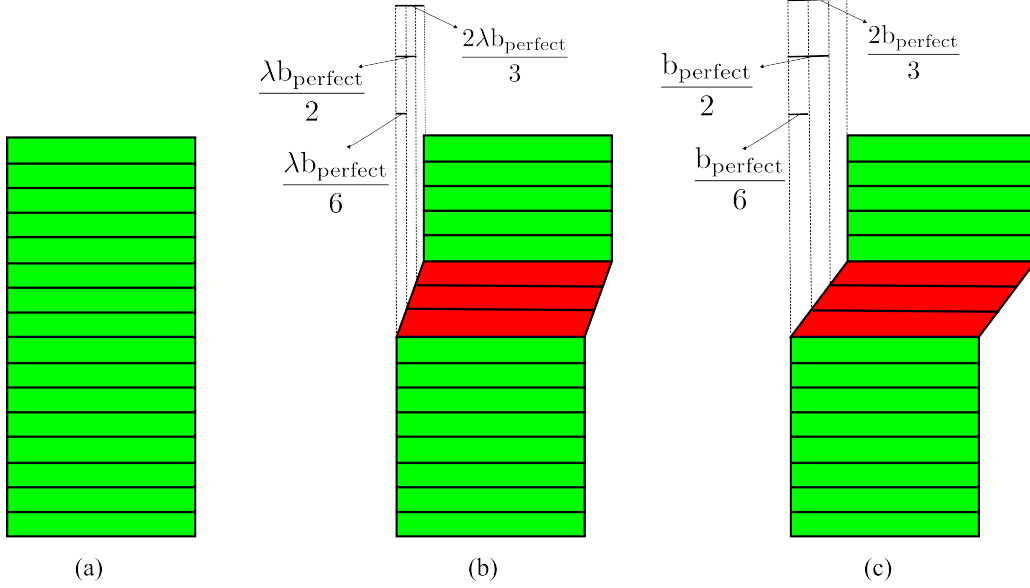


Figure 3.4: The creation of the concurrent TGSF curve through incremental shearing of the BCC crystal structure. (a) The initial BCC crystal (b) is sheared by λu incrementally up to predetermined displacements for creating a three layer isosceles-reflection-isosceles twin structure (c).

we have developed a new TGSF curve that, instead of rigidly displacing individual $\{112\}$ planes, allows displacement of multiple $\{112\}$ planes concurrently (hence the name). For these TGSF curves, the starting point is also a pure BCC crystal as schematically illustrated in Figure 3.4(a). In 3.4 a schematic example of concurrent TGSF curve that produces a three layer twin with two isosceles TBs and a reflection layer sandwiched between them, same as the critical twin nuclei suggested by Vitek [38]. In this case, the total displacement of the bottom most atomic layer of the upper half atoms in Figure 3.4 is $\frac{b}{6} = \frac{b_{\text{perfect}}}{6}$, the second layer displacement $\frac{b}{2} = \frac{b_{\text{perfect}}}{2}$ and the third layer $\frac{2b}{3} = \frac{2b_{\text{perfect}}}{3}$. These displacements take place in these three atom layers incrementally as shown in Figure 3.4(c).

3.6 Direct simulation of twin nucleation

In order to observe the nucleation of twins directly, the interatomic interactions were modeled using the embedded atom method (EAM) for Ta using the parameterization of Ravelo et al [77] (both Ravelo1 and Ravelo2), Ackland-Thetford-Finnis-Sinclair [78], and Zhou [80], for Mo Ackland-Thetford-Finnis-Sinclair [78] and Zhou [80], for W Zhou [80], and for Fe Ackland-

Thetford-Finnis-Sinclair [78] and Chamati [123]. The energy barrier between a perfect crystal and a crystal with a twin was computed using the free-end string [100] method which has been used to study dislocation nucleation [124] and whose implementation can be found in [125, 126] using 24-32 images along the path. The simulations are carried out with periodic boundary conditions under pure applied shear stresses on a $\{112\}$ plane in a box with 12960 atoms of size $15 [1\bar{1}0] \times 24 [11\bar{1}] \times 6 [112]$. A simulation cell with doubled dimensions in all directions was also simulated and the activation energy was the same as the aforementioned smaller cell.

3.7 Bond length comparison analysis to determine twin thickness

Sleeswyk's dislocation dissociation mechanism [37] is widely accepted twin nucleation mechanism which can be interpreted as the nucleation of a three layer pure reflection twin by the passage of twinning dislocations $b_p = b_t = \frac{a}{6} \langle 11\bar{1} \rangle$ on successive $\{112\}$ planes in BCC crystals. Upon reviewing the existing literature, however, it is noticeable that many studies that support this nucleation mechanism do not provide clear evidence of the presence of three layer twins by any form of rigorous analysis. For example, Marian et al. [60] claim that under 2 GPa shear stress at 300K, the twin nucleus observed is three atom layers thick even though the snapshots of MD simulation they provide, include 6-8 atom layers. A more recent computational study by Chu et al. [62] demonstrate that when two oppositely signed, coplanar dislocations glide towards one another at supersonic speeds, they can nucleate twins. They suggest that twins nucleate with two atom layers and then two such twin nuclei collapse to create a three atom layer thick micro twin. However, similar to Marian et al. this study also assumes the micro twin consists of three atom layers without quantitatively determining twin thickness. A closer look at their simulation snapshots reveals that shear exists in 4 atomic layers in the twin nuclei whereas this number goes up to 6 for the micro twin. So, the inconsistency in the number of sheared atom layers and the above-mentioned authors' propensity to accept the Sleeswyk mechanism without quantitative analysis give rise to debate on the critical twin nucleus size in BCC transition metals.

Another source of ambiguity in measuring twin thickness comes from the nature of the twin boundaries for reflection and isosceles twins. For a reflection twin, the reflection symmetry occurs about an atomic plane as shown in Figure 3.5(a) which is called the twin plane. On the other hand, in case of an isosceles twin boundary, the twin plane is not an actual atomic layer but is a hypothetical plane that lies between two atomic planes as shown in Figure 3.5(b). This difference in

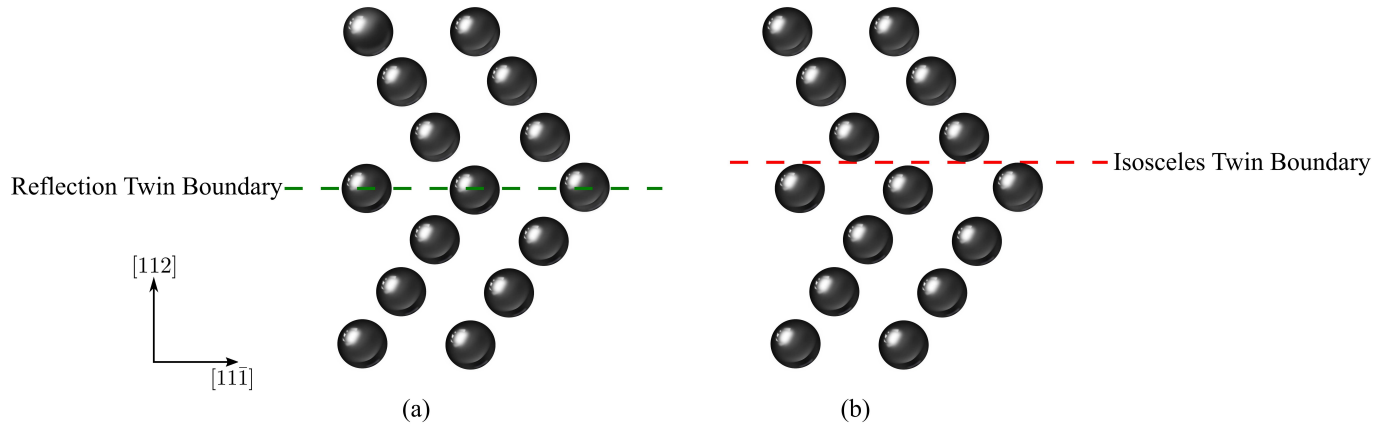


Figure 3.5: (a) Pure reflection TB (b) Pure isosceles TB.

TB type as well as the chosen method for including or excluding atomic layers in the twin structure can lead different reported twin thicknesses. For example, the twinned BCC crystal with a pure reflection twin structure shown in Figure 3.6 can be considered a three layer thick twin if the TB plane is taken to be half of the composition plane for both TBs as shown in Figure 3.6(a) or even a two layer thick twin if those planes are excluded. However, if the planes are completely included (as in Figure 3.6(b)), then the twin is four layers thick. From this discussion, it is obvious that determining twin thickness by counting the atom layers involved results in some ambiguity regarding the twin thickness. Similar inconsistencies can arise in counting twin thickness for twins with isosceles TBs. In this case, one can exclude the atom layers outside of the isosceles TBs and that can lead to counting just two atom layers for the isosceles twin shown in Figure 3.7(a). However, if the atom layers that constitute the isosceles triangles at the TBs are all included, then the same twin can be interpreted as a four layer twin (as in Figure 3.7(b)). Hence, similar to reflection twins, counting atom layers for determining twin thickness for isosceles twins leads to ambiguities.

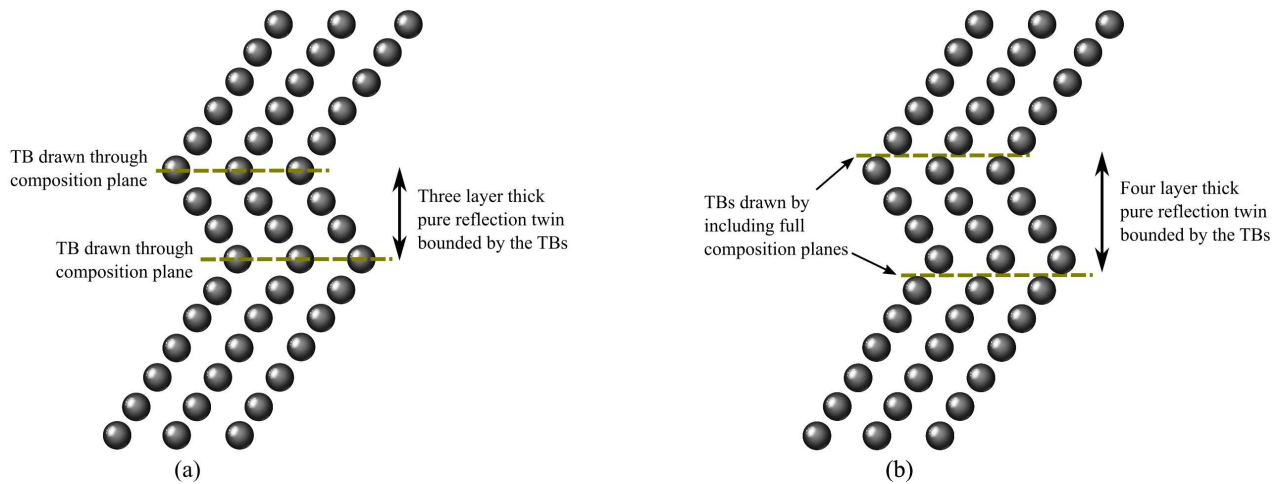


Figure 3.6: A pure reflection TB (a) can be considered a three layer thick twin if half of composition plane is included or (b) a four layer thick twin if full composition plane is included.

Another option would be to rely on symmetry to determine thickness, however, in bulk crystal it is very difficult to determine atom layers that maintain a particular symmetry with respect to atom layers nearby because it is rare that the distribution of atomic displacements is uniform across the entire defect. These sources of ambiguities related to counting atom layers lead us to seek a robust method that not only identify thickness unambiguously but also determine the TB type. We have

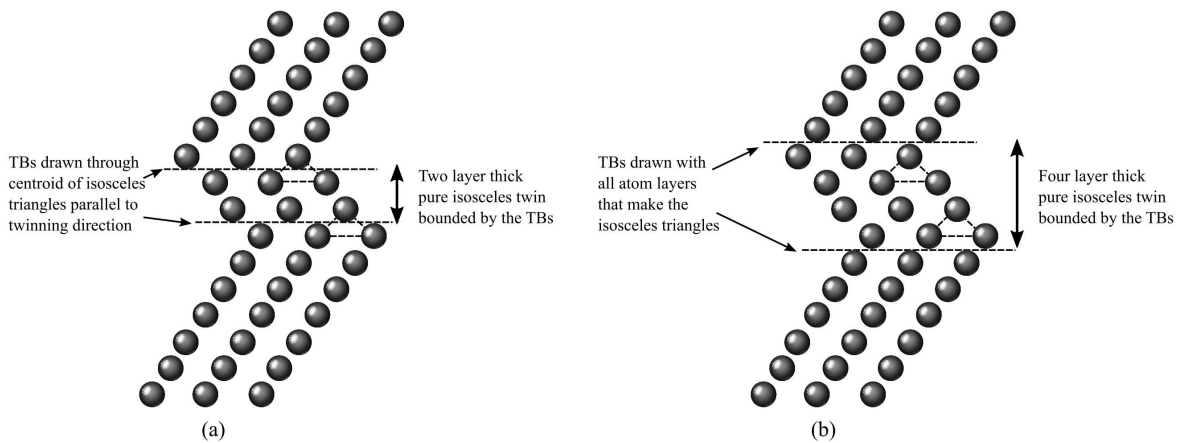


Figure 3.7: A pure isosceles TB (a) can be considered a two layer thick twin if the atom layers bounded by the TB plane are considered or (b) a four layer thick twin if full isosceles triangles are considered.

found that one such robust method of counting twin thicknesses is to count the number of layer that are sheared during the formation of a twin which is essentially the ideas adopted by Vitek [38] and

Sleeswyk [37]. This is a natural counting method because each sheared layer occurs by the passage of a partial dislocation that forms the twin and thus the twin thickness is defined by the number of partial dislocations required to form it. It is also the method implicitly used in atomic level calculations using GSF curves which follow a shearing process. However, the main advantage is that the thickness accounting is less ambiguous, but the drawback is that it requires an analytical method to count the layers. While other methods such as slip vector analysis (SVA) [127] and dislocation analysis (DXA) [128] can be used to quantify relative slip between planes, we found their application to high stresses to have insufficient sensitivity to distinguish between the number of sheared layers which necessitated the development of bond length comparison analysis. To de-

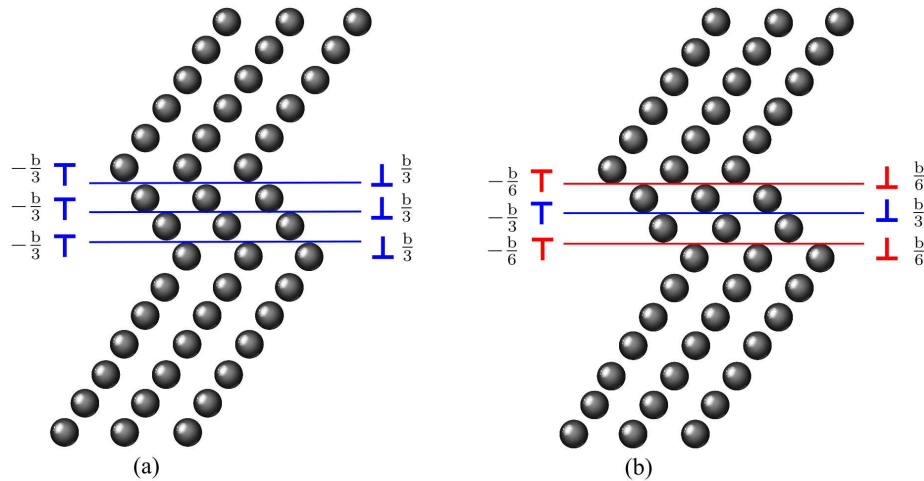


Figure 3.8: (a) Three layer pure reflection twin created by the passage of three $\frac{b}{3}$ partial dislocations on three successive $\{112\}$ planes. (b) Three layer pure isosceles twin created by the passage of $\frac{b}{6}$, $\frac{b}{3}$ and $\frac{b}{6}$ partial dislocations on three successive $\{112\}$ planes. Dislocation pairs are colored red for $\frac{b}{6}$ dislocations and $\frac{b}{3}$ is denoted with blue to distinguish between the type of partial dislocations.

termine the twin layer thickness and associated shear amount, we develop a measurement of the change in bond lengths across a $\{112\}$ slip plane in the $\langle 11\bar{1} \rangle$ direction, which we term the bond length comparison (BLC) analysis. This measurement is termed as the BLC parameter, δ , which is a dimensionless number and measures the difference of the bond lengths between adjacent $\{112\}$ atomic layers relative to the perfect Burgers vector ($b = \frac{\sqrt{3}a}{2}$). Under zero applied stress, the BLC parameter, δ has a value of 0.155 for the perfect BCC crystal structure, 0.0 for a pure isosceles twin

boundary, and -0.155 for a perfect reflection twin boundary. These calculations are shown in Figure 3.9. In the Bond Length Comparison (BLC) analysis, relative shear between adjacent atomic

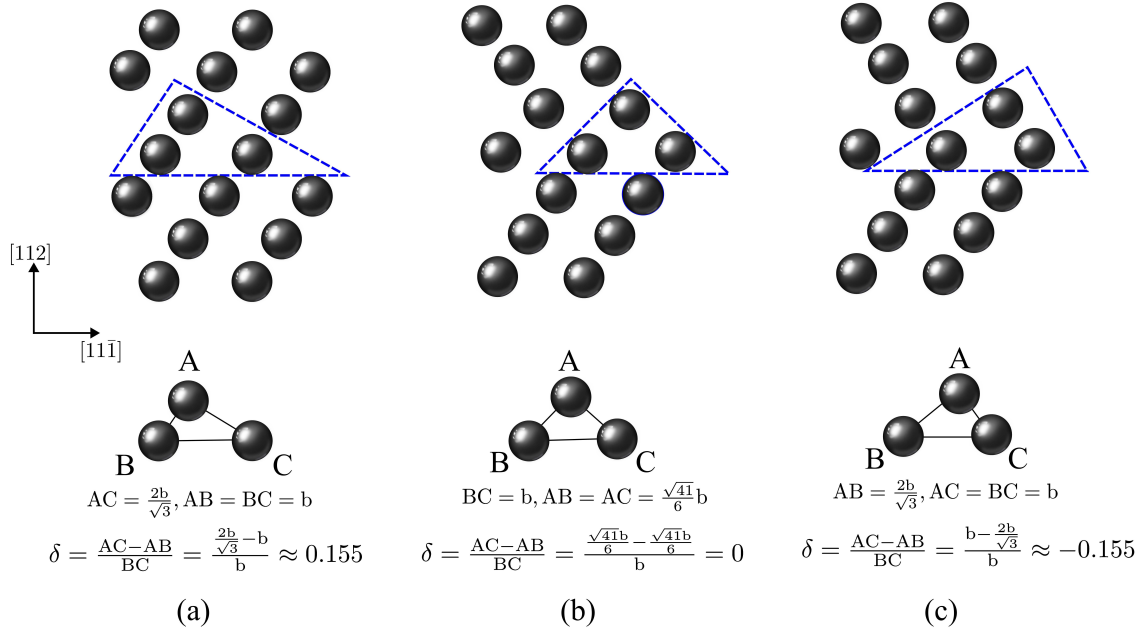


Figure 3.9: (a) Three layer pure reflection twin created by the passage of three $\frac{b}{3}$ partial dislocations on three successive {112} planes. (b) Three layer pure isosceles twin created by the passage of $\frac{b}{6}$, $\frac{b}{3}$ and $\frac{b}{6}$ partial dislocations on three successive {112} planes. Dislocation pairs are colored red for $\frac{b}{6}$ dislocations and $\frac{b}{3}$ is denoted with blue to distinguish between the type of partial dislocations.

layers is computed by introducing a parameter δ . To compute the BLC parameter, imaginary BLC layers are first drawn to keep track of relative shears between atomic layers as shown in Figure 3.10. Next, the length of the bonds that intersect these BLC layers (AB and AC) are computed for adjacent atomic layers. Then we compute δ such that $\delta = \frac{AC-AB}{BC}$ where BC is the repeat lattice vector of the crystal. Figure 3.10 shows examples of BLC parameter values in the twin structures shown in Figures 3.6 and 3.7.

As mentioned earlier, under zero applied stress, the BLC parameter, δ has a value of 0.155 for the perfect BCC crystal structure, 0.0 for a pure isosceles twin boundary, and -0.155 for a perfect reflection twin boundary. The derivation of these values are shown next. We can now compute the δ values for a twinned crystal and compare each of them with the reference values above to determine

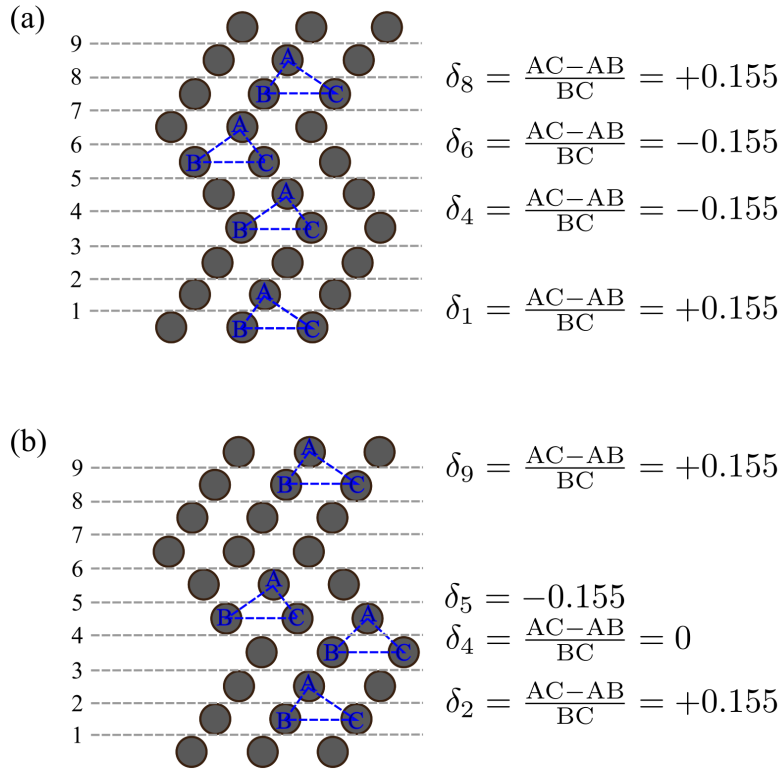


Figure 3.10: (a) A Few examples of BLC parameter δ calculation in (a) a three layer thick pure reflection twin, and (b) a three layer thick pure isosceles twin.

how many BLC layers have relative shear associated with them. This then allows us to count twin thickness by counting the number sheared layers with δ values that differ at least 10% from that of a pure BCC layer. Notably, this method of determining twin thickness avoids the ambiguities caused by counting atom layers, discussed earlier. Additionally, the δ values can also tell us whether the relative shear is associated with a reflection fault or an isosceles fault. In Figure 3.10(a), sample calculations of δ are shown for BLC layers 1, 4, 6, and 8. This is a three layer pure reflection twin because BLC layers 4, 5, and 6 all have $\delta = -0.155$; i.e., this crystal has 3 pure reflection faults. This is the critical twin nucleus structure proposed by Sleswyk [37] which is created by the passage of $\frac{a}{6} [11\bar{1}]$ twinning dislocations on consecutive (112) atomic layers. In Figure 3.10(b) sample calculations of δ are shown for BLC layers 2, 4, 5, and 9. This is three layer pure isosceles twin because BLC layers 4, and 6 all have $\delta = 0$ and layer 5 has have $\delta = -0.155$. This means that the crystal has two BLC layers with isosceles fault and one reflection layer. This twin boundaries are created by the passage of $\frac{a}{12} [11\bar{1}]$ dislocations. Sandwiched between the isosceles TBs, there

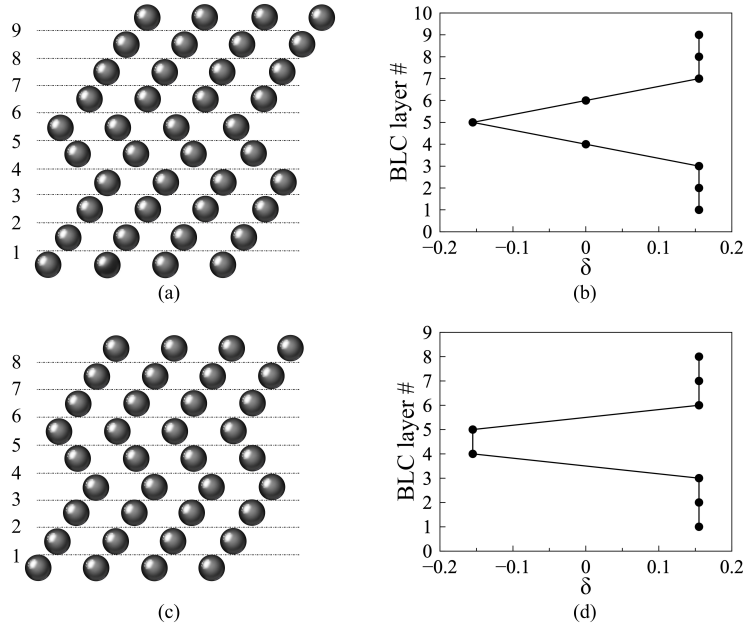


Figure 3.11: (a) A crystal structure with three-layer thick pure isosceles twin (b) and the BLC parameter δ plotted in the horizontal axis against the BLC layer numbers, labeled on the left, on the vertical axis. The δ value changes from $+0.155$ to 0 for layer #4 and #6 indicating pure isosceles TBs and the δ value for layer #5 is -0.155 representing a pure twinned layer. (c) A crystal structure with two-layer thick pure reflection twin and (d) the BLC parameter δ plotted on the horizontal axis against the BLC layer number on the vertical axis. The δ value changes from $+0.155$ to -0.155 for layer #4 and #5 indicating a two layer double reflection boundary.

is a pure reflection atomic layer created by the passage of an $\frac{a}{6} [11\bar{1}]$ twinning dislocation. Vitek concluded that this three layer twin with two isosceles TBs is the smallest metastable twin nucleus in BCC crystals under zero stress from his study on stacking faults on $\{211\}$ planes in BCC metals with central force potentials [38] and was confirmed in DFT by our work for group VB metals and iron [65]. The determination of twin thickness is facilitated by computing δ for several BLC layers, and then plotting δ vs. BLC layer number as shown in Figure 3.11. The BLC parameters can now be used to determine the type and number of shearing events required to form their structure. To demonstrate this, let us consider the twin structures in Figure 3.11(a) and (c). The twin structure in Figure 3.11(a) consists of two pure isosceles TBs, created by the passage of $\frac{a}{12} [11\bar{1}]$ dislocations. Sandwiched between the isosceles TBs, there is a pure reflection atom layer created by the passage of an $\frac{a}{6} [11\bar{1}]$ twinning dislocation. Vitek concluded that this three layer twin with two isosceles TBs is the smallest metastable twin nucleus in BCC crystals under zero stress in his study on stacking

faults on $\{211\}$ planes in BCC metals with central force potentials [38] and was confirmed in DFT by this study for group VB BCC transition metals and iron [65]. To perform the BLC analysis on this crystal structure, imaginary BLC layers are drawn to keep track of relative shears between atom layers. BLC analysis results shown in Figure 3.11(b) demonstrate that BLC layers #4 and #6 have $\delta = 0$ whereas the δ value for layer #5 is -0.155 . So, the twinned crystal in Figure 3.11(a) can be considered to possess a three-layer thick pure isosceles twin nucleus using BLC analysis.

The twinned crystal in Figure 3.11(c) is created by the passage of two $\frac{a}{6} [11\bar{1}]$ twinning dislocations on two consecutive (112) atomic layers in the BCC crystal under zero stress. These displacements cause the value of the BLC parameter, δ to change from $+0.155$ to -0.155 for layers #4 and #5. This can be seen in Figure 3.11(d) where all the layers have values of 0.155 except for layers #4 and #5. The δ values for these two layers correspond to a local pure reflection structure allowing us to measure the twin thickness, which is 2. Thus, the BLC analysis demonstrated in Figure 3.11(d) conclusively points to a two-layer thick pure reflection twin. It is worth noting that this twin structure is the smallest metastable structure in the twinning GSF curve by Ogata et al. in BCC Mo [63, 64] and our work [65].

3.7.1 Derivation of reference BLC parameters

3.7.1.1 BLC parameter in perfect BCC crystal

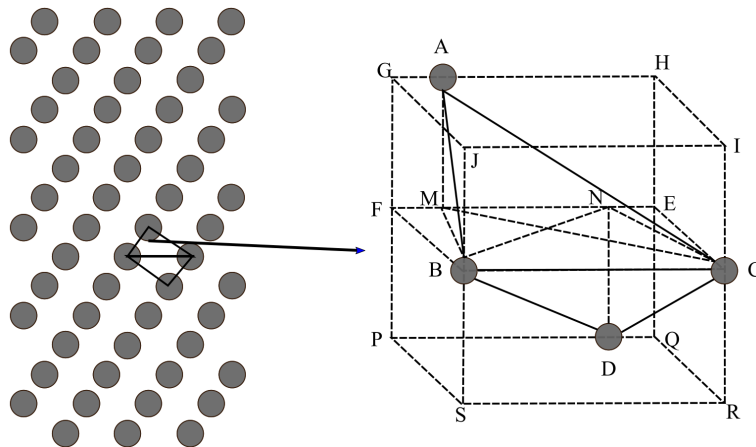


Figure 3.12: Bond length calculations in pure BCC crystal.

In Figure 3.12, we show a pure BCC crystal (left) and zoom in on the atoms A, B, C and D shown in the right figure. Again from the crystallographic description of BCC crystal we know the following:

$$BC = FE = SR = PQ = GH = IJ = b = \frac{\sqrt{3}a}{2}$$

$$BF = CE = GJ = HI = PS = QR = \frac{a}{\sqrt{2}}$$

$$AM = DN = PF = FG = QE = EH = CR = IC = BS = BJ = \frac{a}{\sqrt{6}}$$

$$AG = FM = NE = DQ = \frac{\sqrt{3}a}{6}$$

Now we can compute BM and CM, which are sides of right triangles AMB and AMC. Since we already know the length of AM, we can then use BM and CM to compute the length of our bond lengths AB and AC.

$$BM = \sqrt{BF^2 + FM^2} = \sqrt{\left[\frac{a}{\sqrt{2}}\right]^2 + \left[\frac{\sqrt{3}a}{6}\right]^2} = \frac{\sqrt{21}a}{6}$$

$$CM = \sqrt{CE^2 + EM^2} = \sqrt{\left[\frac{a}{\sqrt{2}}\right]^2 + \left[\frac{a}{\sqrt{3}}\right]^2} = \frac{\sqrt{30}a}{6}$$

$$AB = \sqrt{AM^2 + BM^2} = \sqrt{\left[\frac{a}{\sqrt{6}}\right]^2 + \left[\frac{\sqrt{21}a}{6}\right]^2} = \frac{\sqrt{3}a}{2} = b$$

$$AC = \sqrt{AM^2 + CM^2} = \sqrt{\left[\frac{a}{\sqrt{6}}\right]^2 + \left[\frac{\sqrt{30}a}{6}\right]^2} = a = \frac{2b}{\sqrt{3}}$$

Now that we know all three bond lengths AB, AC, and BC, we proceed to compute the BLC parameter:

$$\delta_{\text{BCC}} = \frac{AC - AB}{BC} = \frac{\left(\frac{2}{\sqrt{3}} - 1\right)b}{b} \approx 0.155$$

3.7.1.2 BLC parameter for pure reflection layer

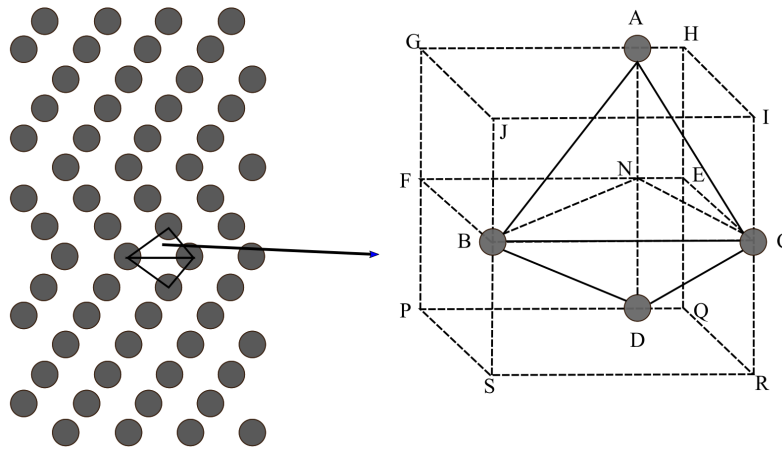


Figure 3.13: Bond length calculations for pure reflection layer.

In Figure 3.13, we show a BCC crystal (left) with pure reflection twin boundary layer and zoom in on the atoms A, B, C and D shown in the right figure. Again from the crystallographic description of BCC crystal we know the following:

$$BC = FE = SR = PQ = GH = IJ = b = \frac{\sqrt{3}a}{2}$$

$$BF = CE = GJ = HI = PS = QR = \frac{a}{\sqrt{2}}$$

Since the atom A is now directly on top of the atom D to maintain reflection symmetry,

$$AN = DN = PF = FG = QE = EH = CR = IC = BS = BJ = \frac{a}{\sqrt{6}}$$

Also the atom A is displaced by $\frac{\sqrt{3}a}{6}$ from its pure BCC position so

$$AG = FN = PD = \frac{\sqrt{3}a}{3}$$

Now we can compute BN and CN which are sides of right triangles ANB and ANC. Since we already know the length of AN, we can then use BN and CN to compute the length of our bond lengths AB and AC.

$$BN = \sqrt{BF^2 + FN^2} = \sqrt{\left[\frac{a}{\sqrt{2}}\right]^2 + \left[\frac{\sqrt{3}a}{3}\right]^2} = \frac{\sqrt{30}a}{6}$$

$$CN = \sqrt{CE^2 + EN^2} = \sqrt{\left[\frac{a}{\sqrt{2}}\right]^2 + \left[\frac{\sqrt{3}a}{6}\right]^2} = \frac{\sqrt{21}a}{6}$$

$$AB = \sqrt{AN^2 + BN^2} = \sqrt{\left[\frac{a}{\sqrt{6}}\right]^2 + \left[\frac{\sqrt{30}a}{6}\right]^2} = a = \frac{2b}{\sqrt{3}}$$

$$AC = \sqrt{AN^2 + CN^2} = \sqrt{\left[\frac{a}{\sqrt{6}}\right]^2 + \left[\frac{\sqrt{21}a}{6}\right]^2} = \frac{\sqrt{3}a}{2} = b$$

Now that we know all three bond lengths AB, AC and BC, we proceed to compute the BLC parameter:

$$\delta_{\text{reflection}} = \frac{AC - AB}{BC} = \frac{\left(1 - \frac{2}{\sqrt{3}}\right) b}{b} \approx -0.155$$

3.7.1.3 BLC parameter for pure isosceles layer

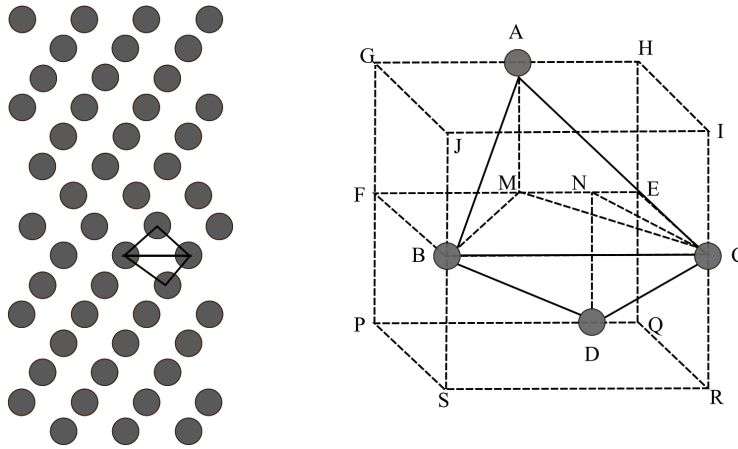


Figure 3.14: Bond length calculations for a pure isosceles layer.

In Figure 3.14, we show a BCC crystal (left) with pure isosceles twin boundary layer and zoom in on the atoms A, B, C and D shown in the right figure. Again from the crystallographic description of BCC crystal we know the following:

$$BC = FE = SR = PQ = GH = IJ = b = \frac{\sqrt{3}a}{2}$$

$$BF = CE = GJ = HI = PS = QR = \frac{a}{\sqrt{2}}$$

$$AM = DN = PF = FG = QE = EH = CR = IC = BS = BJ = \frac{a}{\sqrt{6}}$$

Also the atom A is displaced by $\frac{\sqrt{3}a}{12}$ from its pure BCC position so

$$AG = FM = \frac{\sqrt{3}a}{4}$$

Now we can compute BM and CM which are sides of right triangles AMB and AMC. Since we already know the length of AM, we can then use BM and CM to compute the length of our bond lengths AB and AC.

$$BM = \sqrt{BF^2 + FM^2} = \sqrt{\left[\frac{a}{\sqrt{2}}\right]^2 + \left[\frac{\sqrt{3}a}{4}\right]^2} = \frac{\sqrt{11}a}{4}$$

$$CM = \sqrt{CE^2 + EM^2} = \sqrt{\left[\frac{a}{\sqrt{2}}\right]^2 + \left[\frac{\sqrt{3}a}{4}\right]^2} = \frac{\sqrt{11}a}{4}$$

$$AB = \sqrt{AM^2 + BM^2} = \sqrt{\left[\frac{a}{\sqrt{6}}\right]^2 + \left[\frac{\sqrt{11}a}{4}\right]^2} = \frac{\sqrt{123}a}{12} = \frac{\sqrt{41}b}{6}$$

$$AC = \sqrt{AM^2 + CM^2} = \sqrt{\left[\frac{a}{\sqrt{6}}\right]^2 + \left[\frac{\sqrt{11}a}{4}\right]^2} = \frac{\sqrt{123}a}{12} = \frac{\sqrt{41}b}{6}$$

Now that we know all three bond lengths AB, AC and BC, we proceed to compute the BLC parameter

$$\delta_{\text{isosceles}} = \frac{AC - AB}{BC} = \frac{\left(\frac{\sqrt{41}}{6} - \frac{\sqrt{41}}{6}\right) b}{b} = 0$$

3.8 Constrained twin stability analysis

The purpose of the constrained twin stability analysis is to determine the metastable twin structures that should exist under an applied stress. The goal is to create a crystal under an applied shear stress and allow some flexibility to the atoms so that they can relax to a lower energy configuration without allowing complete relaxation, which would transform them back to an unstressed BCC crystal. Thus, we created the constrained twin stability curves which allow us to do just that. To

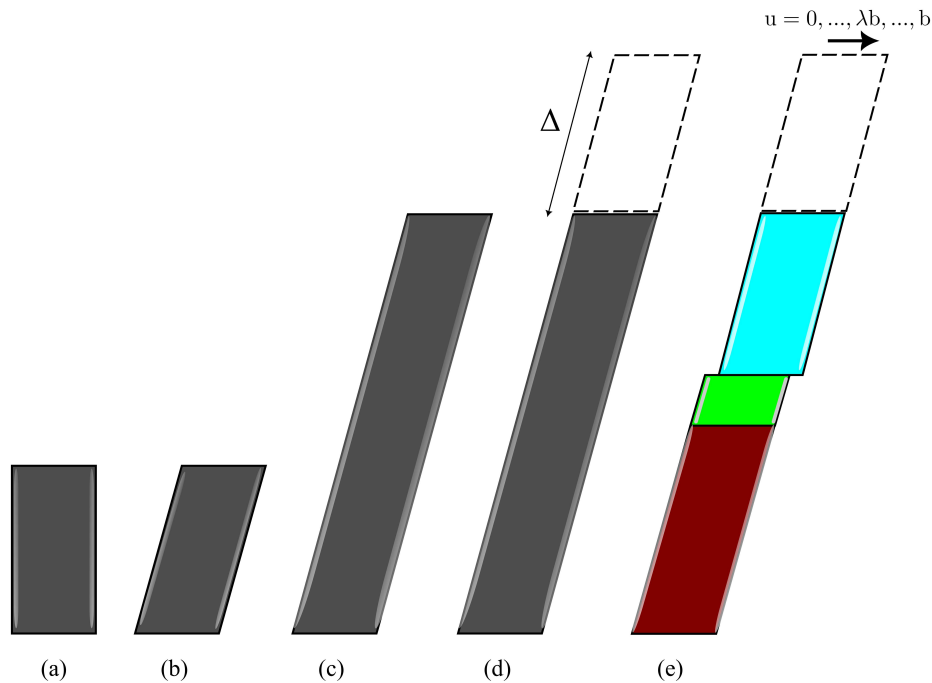


Figure 3.15: A schematic of the steps required to generate the constrained twin stability curves. (a) A pure BCC structure under zero stress with 6 atoms, (b) the BCC structure is strained to reach specific values of pure shear stress, (c) an extended sheared crystal with 24 atoms (not drawn to scale), (d) a vacuum gap of $\Delta = 15\text{\AA}$ added to the extended crystal to prevent interactions between periodic images in the $[112]$ direction and, (e) the upper half atoms (blue block) are displaced by incremental displacement u . At each displacement u , the 12 bottom atoms (maroon block) are held completely fixed, the uppermost atoms in the yellow block are only allowed to relax in the $[112]$ direction and the atoms in the middle block (lime) are allowed to fully relax.

generate constrained twin stability curves, the starting point is a pure BCC crystal with a simulation cell of geometry $a[1\bar{1}0] \times \frac{a}{2}[11\bar{1}] \times \frac{Na}{6}[112]$ with $N = 6$ with periodic boundary conditions in all three directions and a is the lattice constant zero shear stress. We then applied a specified state

of pure shear stress to the crystal, extracted the strain, and applied the same strain to a simulation cell with 24 atoms and vacuum gap of $\Delta = 15\text{\AA}$ perpendicular to the composition plane so as to ensure no interaction takes place between periodic images in the $[112]$ direction. These steps are schematically shown in Figures 3.15(a) - (d). We then rigidly displace the 11 uppermost atomic layers (denoted by the yellow block in Figure 3.15(e)) incrementally in the $[11\bar{1}]$ direction by a fraction the magnitude of the Burgers vector, λ , of a perfect dislocation in the $[11\bar{1}]$ direction. At each increment, we only allow atomic relaxations in the $[112]$ direction for these 11 atom layers (blue block in Figure 3.15(e)). The bottom 12 atomic layers (maroon block in Figure 3.15(e)) are completely fixed and only the remaining 1 atomic layer (lime block in Figure 3.15(e)) is allowed to fully relax.

This allows us to obtain different constrained equilibrium structures that represent twinning faults under nonzero pure shear stress at each incremental displacement. For this purpose, we have used the conjugate gradient method to find the constrained local energy minimum nearest to the set of atomic positions at each incremental displacement. The energy tolerance was set to a relative error of 10^{-10} for twin stability analysis with EAM potentials whereas the energy tolerance for the convergence of the electronic structure was set to 10^{-7}eV for twin stability analysis in DFT. The stacking fault energy is computed as:

$$\gamma = \frac{E(u) - E_0}{A} \quad (3.48)$$

where $E(u)$ is the converged energy of the simulation cell at each incremental displacement, E_0 is the converged energy of the strained BCC crystal without displacement and A is the area of the composition plane $a [1\bar{1}0] \times \frac{a}{2} [11\bar{1}]$. This process can then be repeated by increasing the number of planes that are allowed to completely relax and in this work that is a maximum of 6 atomic layers.

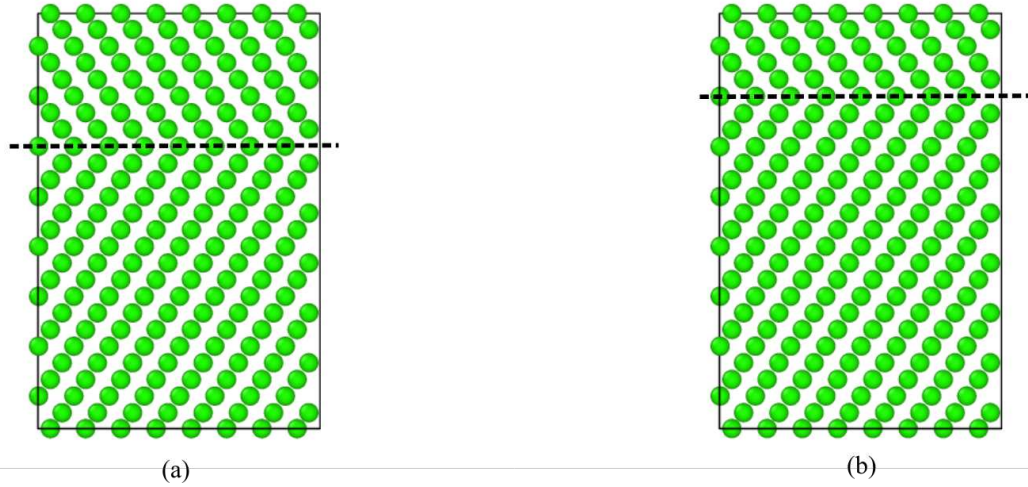


Figure 3.16: (a) a twinned crystal with the twin boundary shown by the dashed line and (b) the twin boundary has migrated by 3 layers and moved upwards.

3.9 Twin Boundary Migration GSF Curve

In order to generate twin boundary migration GSF curves, we start with a twinned BCC crystal as shown in Figure 2.9(a). Then we begin to incrementally translate the upper half crystal in the $[\bar{1}\bar{1}\bar{1}]$ direction as opposed to the translation in the $[111]$ direction for the twin boundary GSF curves mentioned earlier. However, the translation in the $[\bar{1}\bar{1}\bar{1}]$ direction has to be performed in such a manner that the migration of the twin boundary can be simulated accurately. For this reason, if we want to simulate twin boundary migration by 2 layers at a time rather than a layer-by-layer manner, we have to translate the atomic layer most adjacent to the twin boundary by $1b_p$ and all the atomic layers above this one by $2b_p$. Similarly, if we want to simulate twin boundary migration by 3 layers, we have to translate the atomic layer most adjacent to the twin boundary by $1b_p$, the atomic layers above this one by $2b_p$ and all the other layers above by $3b_p$. These TBMGSF curves were generated by DFT simulations in VASP with the same parameters used for TBGSF and TGSF curves. Figure 5.37(a) shows a twinned crystal and (b) shows that the twin boundary has migrated by 3 layers via the translation in the $[111]$ direction described above.

Chapter 4

Modeling twin boundary structures in BCC transition metals

4.1 Atomic structures of twin boundaries in BCC transition metals

The twinning elements outlined in the literature review (Chapter 2) can describe the macroscopic degrees of freedom of the twin. However, they do not fully describe the local atomic structure. A common interpretation of the local atomic twin structures in BCC metals is a reflection symmetry about a single $\{112\}$ plane. This type of twin structure, shown in Figure 2.9(a), is readily reproduced by the passage of the $\frac{a}{6}\langle 111 \rangle$ twinning dislocations described above. However, this is not the only postulated twin boundary structure. Vitek proposed the isosceles twin boundary structure [38], shown in Figure 2.9(b), which can be created from the reflection twin boundary by a translation of one half of the crystal relative to the other half by an amount of $\frac{a}{12}\langle 111 \rangle$. This twin boundary structure still satisfies the macroscopic orientation relationship between the two crystals and has the advantage of minimizing bond lengths across the twin boundary plane. While experimental work can help provide clear identification of the local atomic structure, we are only aware of one in-situ experiment in Tungsten in which the observed deformation band was confirmed to be a twin band with Fast Fourier Transform pattern analysis with the atomic level structure of the twin boundary assumed to be a pure reflection twin boundary structure [27].

Despite the potential for the existence of more than one twin boundary structures in BCC metals, the isosceles structure is often overlooked in computational studies [39, 40]. However, recent atomistic work by Shi et al. demonstrated that some empirical potentials produce the isosceles twin boundary structure and that this should alter both the energetics of nucleation as well as the shape of the twinning generalized stacking fault (TGFSF) energy curve [41]. Additionally, recent

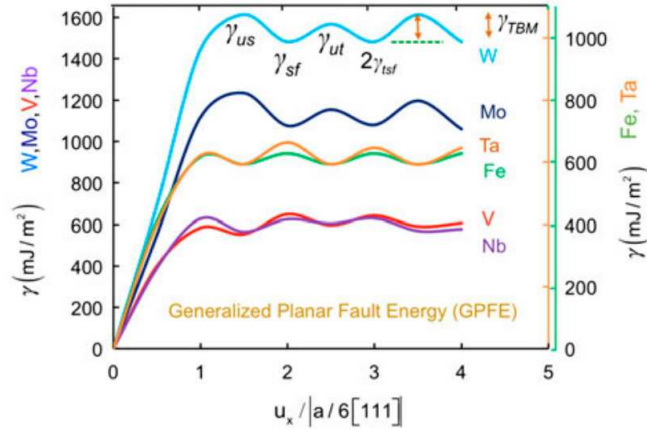


Figure 4.1: TGSF curves obtained for the BCC transition metals obtained by shearing n consecutive $\{112\}$ layers by a displacement of $\frac{a}{6}\langle 111 \rangle$. Adopted from [42].

computational work by Ojha et al. computed the TGSF curves (Figure 4.1) for many of the BCC metals using electronic structure density functional theory (DFT) and concluded that the reflection twin boundary structure was favorable in Mo, W while the isosceles structure is favorable in Ta, Nb, V and α -Fe [42].

Since DFT reasonably reproduces the bonding in BCC transition metals, it can be assumed to be an accurate description of the structure. However, this study did not actually examine the actual produced structure from the simulations nor did it conclusively provide insight into the metastability of the other twin boundary structures, let alone actually quantitatively or qualitatively demonstrate the preference of the specified structure.

This raises the question of the actual local atomic structure of twin boundaries in BCC metals. Here, we have investigated this problem using both EAM potentials as well as electronic density functional theory. In this light, we fully relax the twin boundary structures (see section 3.3 in Chapter 3) to determine which structures, reflection or isosceles, are stable and if multiple twin boundary structures are metastable and hence their relative stability. We further use the twinning GSF energy curves to explore if other twin boundary structures are metastable as well. The TGSF curves further provide insight into how the twins may nucleate. These results provide the first concrete identification of not only the energetics of the twin boundaries, but also their local atomic structure. While we expect the DFT results to accurately represent twin boundary structure, we

compare these results with empirical potentials which are frequently used to model twin nucleation and growth in BCC metals.

4.2 Modeling twin boundary structures

To investigate the stability and energetics of atomic level twin boundary structure, both empirical potentials as well as electronic density functional theory simulations have been utilized. Hence the findings of our modeling efforts are initially discussed separately for simulations using EAM potentials and DFT. Next, an analytical model is developed which is capable of explaining the physics behind the TBGSF curves shapes in BCC transition metals.

4.2.1 Interatomic Potentials

We will begin our investigation of the structure of twins in BCC metals with a survey of predictions using interatomic potentials. As noted, we believe the interatomic potentials to be less accurate in terms of modeling bonding in the BCC metals, but their wide use and wide range of parameterizations makes their investigation an important starting point to study the atomic structure of twins. However, it is worth noting that we don't know if certain EAM potentials correctly represent the twin structure of the metal they were fitted to, so we choose to present the results in a different fashion. We discuss potentials based on what they predict starting with a singular example followed with a list of potentials that predict the same overall behavior.

Our first example EAM potential is the Ravelo 2 potential that was fit to model Ta [77]. The TBGSF curve produced by this potential is shown in Figure 4.2(a). The first thing to notice is that the TBGSF curve shows a minimum only at $\lambda = \frac{1}{2}$, which implies, but does not prove, that the isosceles structure not only is the preferred twin structure energetically, but it suggests the pure reflection structure is not even metastable. This suggests that relaxation of the pure reflection twin should dissolve directly into the isosceles. In addition, we see that the TBGSF curve is fully periodic in a period of $3b_p$ since $3b_p = \frac{a}{2} \langle 111 \rangle$ is the perfect Burgers vector. For simplicity,

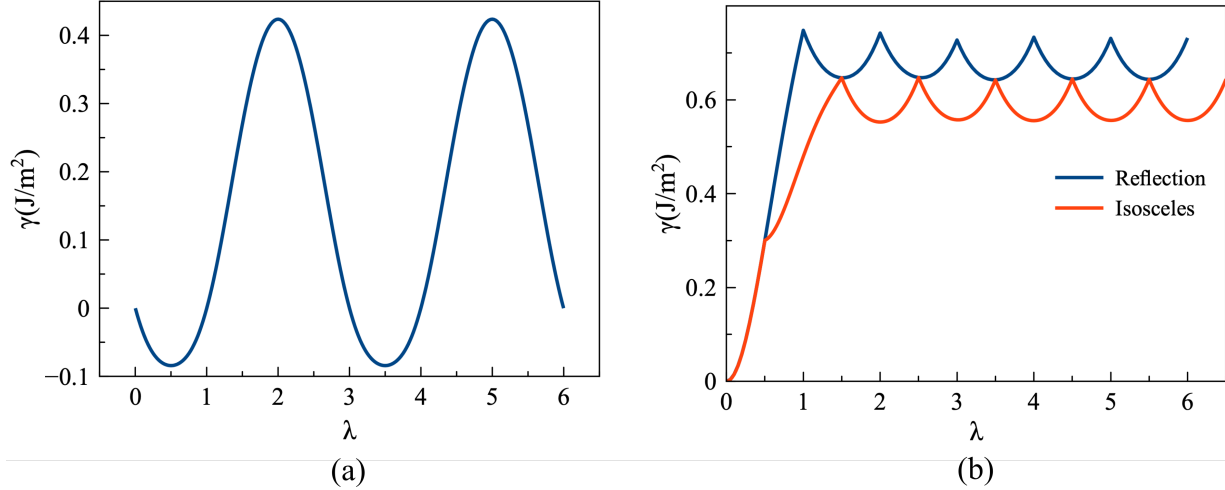


Figure 4.2: The (a) The TBGSF curve and (b) the TGSF curve for Ta modeled using the Ravelo 2 EAM potential.

future plots from interatomic potentials are simplified by excluding the range between 1 and $3b_p$ since this range is not relevant for predicting the twin boundary structures.

As expected, we were only able to identify one stable twin structure for this potential which is a distorted form of the isosceles structure as shown in Figure 4.3. This structure was found using full structural minimization of the atomic position using points from the TBGSF curve at $\lambda = 0, \frac{1}{4}, \frac{1}{2}$ and $\frac{3}{4}$. This relaxed isosceles twin structure is not the perfect structure as is generally reported. Instead, we note that the two atomic planes closest to the twin boundary plane, which lies in between these two atomic planes, roughly rigidly shift relative to the other atoms as shown in Figure 4.3 by an amount η . For the Ravelo 2 EAM potential, this shift amounts to $\eta = 0.177b_p$, which is small but not negligible.

The complete TGSF curves for both the pure reflection and isosceles for Ravelo 2 are shown in Figure 4.2(b). The TGSF curve for pure reflection matches well with the TBGSF curve as the cusped sections correspond to the TBGSF curve between $\lambda = 0$ and $\lambda = 1$. This demonstrates that the cusps that exist on the TGSF curve, both for the pure reflection and pure isosceles, are a direct result of the pure reflection not being an equilibrium structure, i.e. $\frac{d\gamma}{d\lambda} \neq 0$. If the TGSF curve is to be absent of cusps, then the pure reflection structure must be an equilibrium structure (i.e. $\frac{d\gamma}{d\lambda} = 0$); but it is not necessary for it to be a metastable equilibrium structure (i.e. $\frac{d^2\gamma}{d\lambda^2} > 0$). This

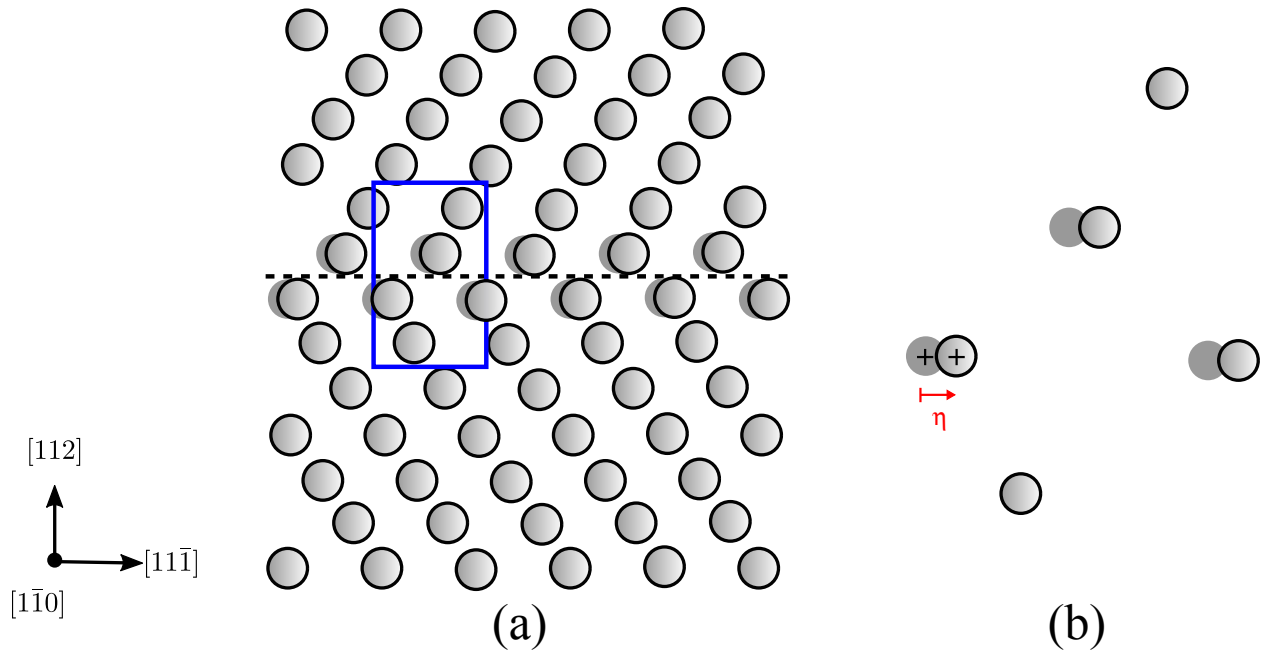


Figure 4.3: (a) The isosceles twin structure is distorted by a small shift of the two atom layers that are closest to the twin boundary plane. (b) The distorted structure can be described by a shift of η in the direction shown.

is an important note to make because many reports, including reports that use this potential, show a smooth TGSF curve [41]. While we cannot claim to understand how those results were obtained with certainty, we can speculate that it is due to under-sampling the GSF curve. Here we use 40 points for each b_p shift with the EAM potential, which highlights the cusps observed in the curve.

This behavior, the prediction of a single stable distorted isosceles structure, is shared by numerous EAM potentials including Ackland-Thetford Finnis-Sinclair (ATFS) [78], Zhong [79] and Zhou [80] for Ta, Howells [82] and Stukowski [83] for Chromium, Olsson [75] for Vanadium and Finnis-Sinclair (FS) [84] for α -Fe. For each of these potentials, only a single distorted isosceles structure is predicted with varying magnitudes of η , which are listed in Table 4.2. Similarly, the TBGSF curves and TGSF curves of these EAM potentials are similar to those described above for the Ravelo 2 EAM potential (see Table 4.1).

The next typical twin boundary behavior is exemplified by the Ackland-Thetford-Finnis-Sinclair potential for Molybdenum [78]. The TBGSF curve computed for this potential is shown in Figure 4.4(a). In this case, the TBGSF curve does not show a minimum at $\lambda = \frac{1}{2}$ as is observed for the

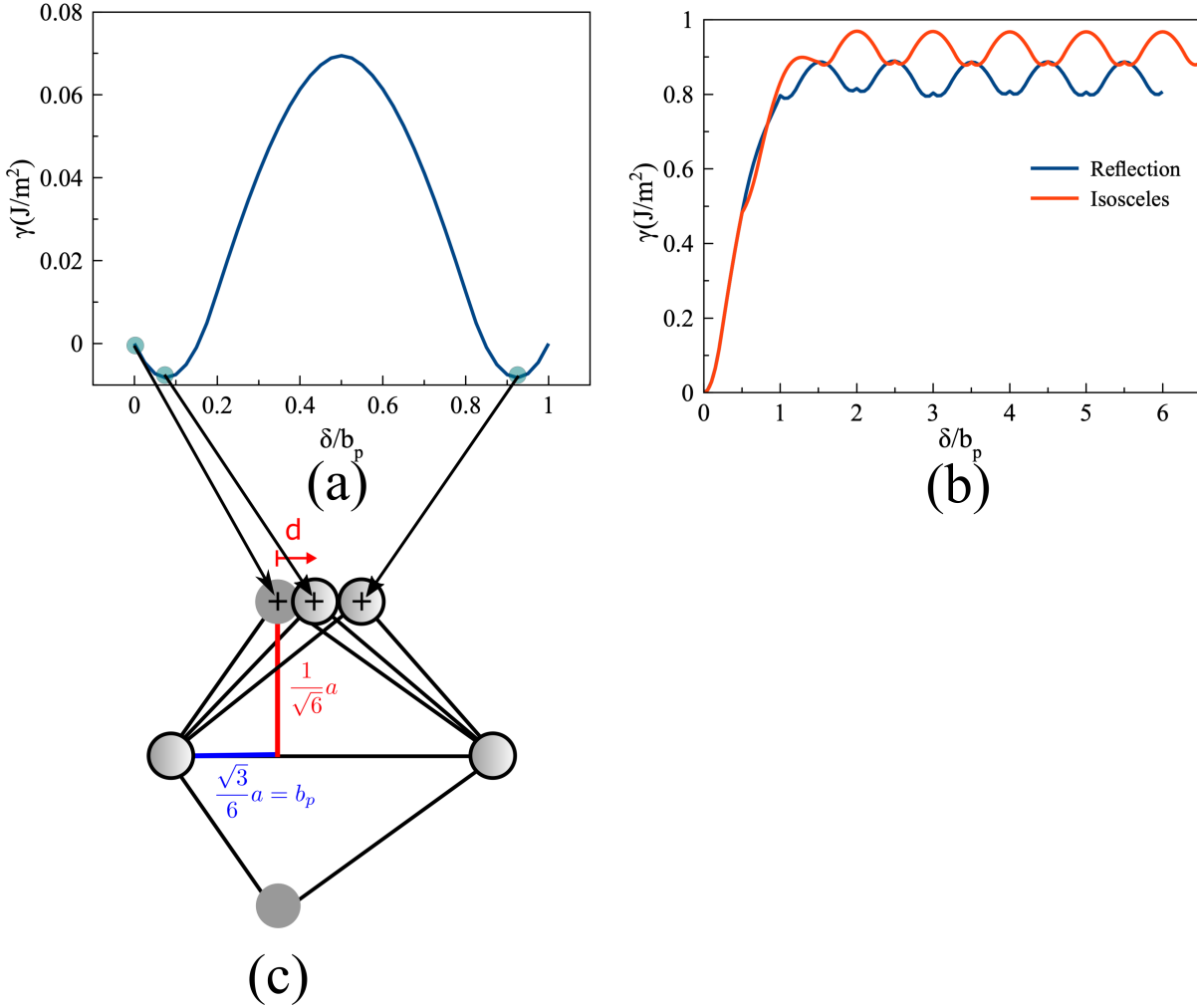


Figure 4.4: The (a) TBGSF curve and (b) TGSF curve for Mo modeled using the ATFS potential. (c) The local twin structure associated with the predicted minima in the TBGSF curve along with the initial pure reflection structure.

Ravelo 2 EAM potential which corresponds to an isosceles structure nor does it predict a minimum at $\lambda = 0$ corresponding to the pure reflection twin boundary. Instead, it produces two local minima at $\lambda = 0.075$ and $\lambda = 0.925$, which are symmetric about $\lambda = \frac{1}{2}$. In fact, the two structures are related by symmetry (assuming no atomic relaxations). If we compare this structure to the isosceles structure, they are similar except that the sides of the triangle that make up the twin boundary, Figure 4.4(c), are scalene, which we name this structure.

After full atomic structural relaxation, however, this structure is not maintained. Instead of maintaining the scalene triangle structures shown in Figure 4.4(c) predicted by the TBGSF curve,

the atomic layer below the TBGSF plane also shifts, resulting in a distorted form of the pure reflection, as shown in Figure 4.5. The TBGSF curve cannot predict this structure since its formation requires two shifts of a value $\pm\delta = 0.052b_p$ on two successive atomic planes. This same structure is reproduced from the full structural minimization of four points on the TBGSF curve, the same used above, and thus we can assume that neither the pure reflection nor the isosceles are stable structures while this distorted reflection is indeed both an equilibrium and stable structure. It is worth further pointing out that this structure includes a single atomic layer that no longer belongs to the structure of either of the twin elements. This is distinct from the pure reflection where the twin boundary plane belongs to both twin elements while in the isosceles structure, the twin boundary plane is not an atomic layer at all as it contains no atoms. Atomic planes that form a twin plane but do not belong to either twin element are common atomic features predicted by atomic level methods for HCP structures [129].

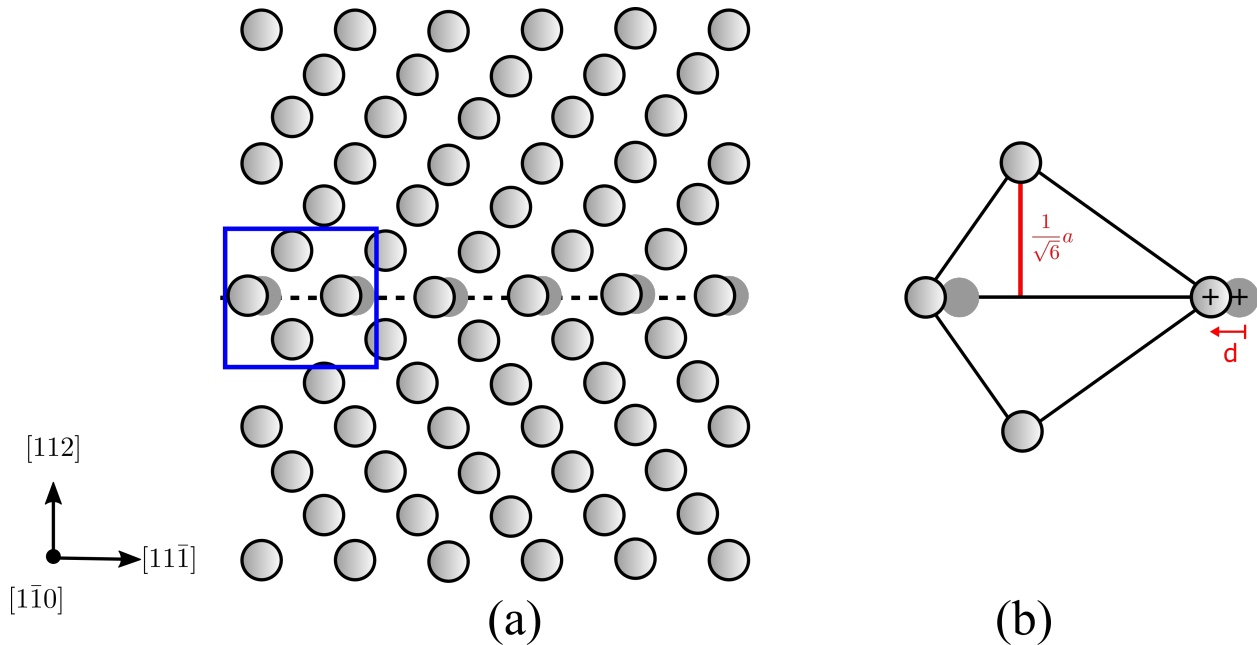


Figure 4.5: (a) The initial and final structure associated with a pure reflection and distorted (or δ shifted) pure reflection twin boundary structure. (b) The local twin boundary structure associated with the initial pure reflection (shaded atoms) structure and the relaxed distorted pure reflection structure where the δ shift can be seen.

The TGSF curves for Mo with the Finnis-Sinclair potential are shown in Figure 4.4(b) and are also affected by the lack of stability of the pure reflection and isosceles structure. Both of these curves have local maxima at λ values that represent isosceles twin boundary structure as predicted by the TBGSF curve shown in Figure 4.4(a). The position of these local maxima in these two curves differ from each other since atomic movement after $\lambda = 0.5$ is also different. Furthermore, both these curves also exhibit cusps where the twin boundary structure is pure reflection which is not an equilibrium structure (maximum or minimum). These cusps in the TGSF curves also do not appear at same λ values because the pure reflection twin boundary structure is produced at different values of λ of each curve. The actual local minimum on these curves correspond to the scalene structures described above. The actual curve that BCC Mo would follow is neither of these, but rather quite close to the pure reflection TGSF curve. The real twinning pathway requires the passing of very small zonal dislocations on the twin boundary to create the distorted reflection and an energetic local minimum.

This general behavior is also exhibited by other interatomic potentials. This includes the Smirnova [85] and Zhou [80] potential for Mo, ATFS [78], Zhou [80] and Olsson [75] potential for W and ADP potential for Cr [82]. However, the locations of the minimums that the potentials predict in the TBGSF curve and the structural shift they predict in the distorted reflection structure vary from potential to potential with the aforementioned ATFS potential for Mo predicting the smallest deviation from pure reflection symmetry. The TBGSF curve produced from the ATFS potential for W exhibits minima at $0.125b_p$ and $0.875b_p$ while the distorted reflection structure obtained from full structural relaxation demonstrate a structural shift of $\delta = 0.08b_p$. The largest structural shift for the distorted reflection structure is predicted by the Zhou potential for W with a value of $\delta = 0.158b_p$. The values of the structural changes as well as the twin energies are listed in Table 4.2.

There is one other interatomic potential that we found that predicts both the distorted isosceles and distorted reflection structures as being metastable: the EAM potential of Guellil for Ta [81]. The TBGSF for the Guellil potential is shown in Figure 4.6 which exhibits an interesting change

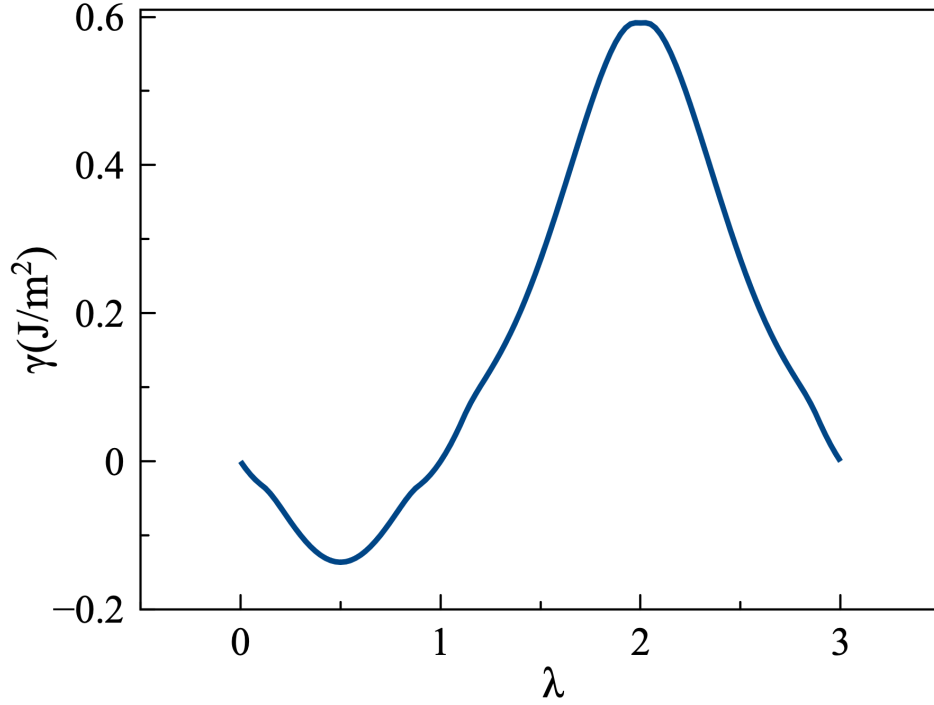


Figure 4.6: The TBGSF curve up to $3b_p$ for Ta modeled with Guellil potential.

from other TBGSF curves: it shows a definitive change in slope near $\lambda = 0$ and $\lambda = 1$. It is unclear if this change in slope is indicative of a stable distorted reflection as well as an isosceles structure or if it is coincidence. The resulting distortion of the reflection and the isosceles structures are stronger than those given above and have values of $\delta = 0.197b_p$ and $\eta = 0.418b_p$. Also, this potential predicts a lower energy for the isosceles structure, which is indicated by the TBGSF curve.

The final interatomic potential investigated is the Fellingner potential for Niobium [76] whose TBGSF curve is shown in Figure 4.7(a). The TBGSF curve appears similar to those described in the case of the distorted reflection structure as discussed for ATFS Mo. However, upon complete relaxation we see that multiple structures emerge. The relaxation of the pure reflection, $\lambda = 0$, creates a distorted reflection with $\delta = 0.160b_p$, as expected. However, relaxation from $\lambda = \frac{1}{4}$ relaxes to a new structure, a scalene triangle structure that we initially assumed the ATFS Mo would form. In this case, the structure can be described with an upper shift of $\lambda = 0.300$ as anticipated from the TBGSF curve. Relaxation from the $\lambda = \frac{3}{4}$ point forms the complimentary

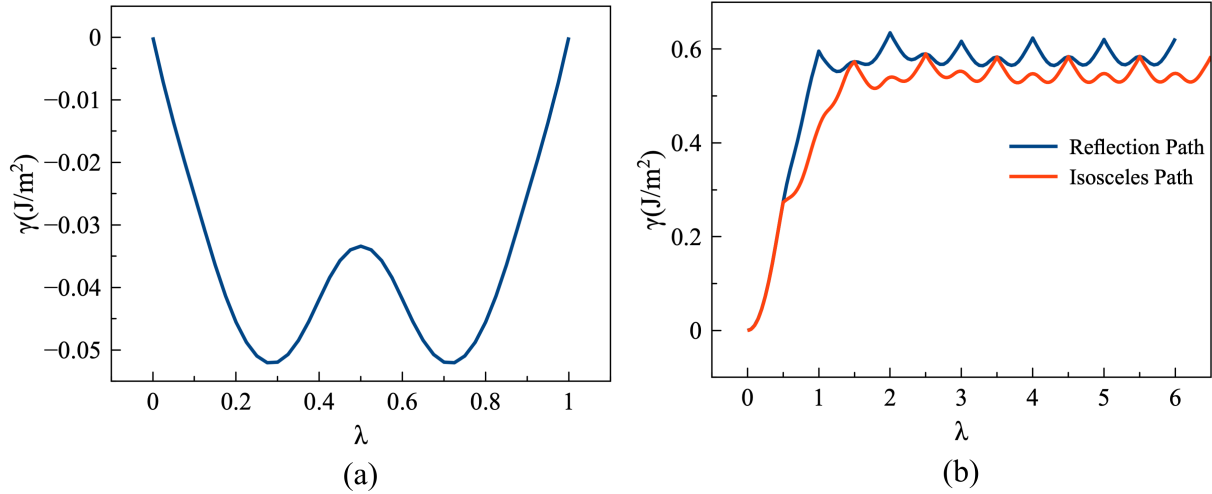


Figure 4.7: The (a) TBGSF curve and (b) TGSF curve for Nb modeled using the Fellingier potential.

scalene structure of $\lambda = 0.700$ as expected with the same twin boundary energy. Finally, what is perhaps the most intriguing result is that the $\lambda = \frac{1}{2}$ starting structure forms the distorted isosceles structure with an η shift of $0.365b_p$ even though the TBGSF curve implies isosceles is an unstable equilibrium point. As mentioned earlier, the TBGSF curve only deals with atomic movements above the twin boundary and in this case, even though an isosceles structure is maintained, the atomic layer below the twin boundary also shifts. This structure is illustrated in Figure 4.3. The two degenerate scalene structures end up being the most energetically favorable, followed by the distorted reflection and finally the distorted isosceles structure.

The impact the low energy scalene structures have on the TGSF curves are substantial, for both the isosceles and reflection curves. Neither of the TGSF curves (shown in Figures 4.4(b) and 4.7(b)) are the low energy pathways because both artificially constrain one of the boundaries to be either the isosceles or pure reflection boundary, neither of which is favorable to form compared to the scalene structure. We can create a TGSF that correctly produces the scalene structure which has the lowest energy pathway, but is complicated to describe and does not add to the conclusions of this work so we omit that digression.

Table 4.1: TBGSF curve predictions from EAM potentials

BCC Metal	EAM Potential	TBGSF curve	
		Predicted structure	location of minima (λ)
Ta	Ravelo2	Pure isosceles	0.500
	Ravelo1		
	Zhong		
	ATFS		
	Guellil		
	Zhou		
V	Olsson		
Fe	FS		
Nb	Fellinger	Scalene	0.300 and 0.700
Mo	FS		0.075 and 0.925
	Smirnova		0.150 and 0.850
	Zhou		0.225 and 0.775
W	FS		0.100 and 0.900
	Zhou		0.250 and 0.750
	Olsson		0.250 and 0.750
Cr	Howells		0.400 and 0.600

While interatomic potentials predict a range of metastable twin structures, we can make some important conclusions from these results. First, we note that none of the interatomic potentials predict a stable pure reflection twin boundary. The closest structure is the distorted reflection as modeled by the ATFS potential for Mo. Second, there are three types of potentially stable twin structures: the distorted reflection, distorted isosceles and the scalene structure. Third, the lack of an equilibrium pure reflection twin structure results in TGSF curves that have cusps, i.e., they lack continuity of their first derivatives. However, what is not clear is what the actual twin structure of

the BCC transition metals should be and if there are multiple metastable structures as predicted by some EAM potentials.

Table 4.2: Equilibrium structures from EAM potentials

		Distorted Reflection	Distorted Isosceles	Scalene1	Scalene2
Ta- Ravelo2	$\gamma(\text{Jm}^{-2})$	—	0.541	—	—
	δ / η shift	—	0.177b _p	—	—
Ta- Ravelo1	$\gamma(\text{Jm}^{-2})$	—	0.547	—	—
	δ / η shift	—	0.112b _p	—	—
Ta- Zhong	$\gamma(\text{Jm}^{-2})$	—	0.536	—	—
	δ / η shift	—	0.266b _p	—	—
Ta- ATFS	$\gamma(\text{Jm}^{-2})$	—	0.616	—	—
	δ / η shift	—	0.262b _p	—	—
Ta- Guellil	$\gamma(\text{Jm}^{-2})$	0.844	0.648	—	—
	δ / η shift	0.197b _p	0.418b _p	—	—
Ta- Zhou	$\gamma(\text{Jm}^{-2})$	—	0.534	—	—
	δ / η shift	—	0.367b _p	—	—
V- Olsson	$\gamma(\text{Jm}^{-2})$	—	0.398	—	—
	δ / η shift	—	0.138b _p	—	—
Fe- FS	$\gamma(\text{Jm}^{-2})$	—	0.397	—	—
	δ / η shift	—	0.204b _p	—	—
Nb- Fellinger	$\gamma(\text{Jm}^{-2})$	0.495	0.501	0.479	0.479
	δ / η shift	0.160b _p	0.365b _p	0.300b _p	0.700b _p
Mo- FS	$\gamma(\text{Jm}^{-2})$	0.774	—	—	—
	δ / η shift	0.052b _p	—	—	—
Mo- Smirnova	$\gamma(\text{Jm}^{-2})$	1.058	—	—	—
	δ / η shift	0.111b _p	—	—	—

Mo-	$\gamma(\text{Jm}^{-2})$	0.981	—	—	—
Zhou	δ / η shift	0.153b _p	—	—	—
W-	$\gamma(\text{Jm}^{-2})$	0.776	—	—	—
FS	δ / η shift	0.080b _p	—	—	—
W-	$\gamma(\text{Jm}^{-2})$	1.162	—	—	—
Zhou	δ / η shift	0.158b _p	—	—	—
W-	$\gamma(\text{Jm}^{-2})$	1.047	—	—	—
Olsson	δ / η shift	0.137b _p	—	—	—
Cr-	$\gamma(\text{Jm}^{-2})$	0.773	—	—	—
Howells	δ / η shift	0.142b _p	—	—	—

4.2.2 Density Function Theory

As noted previously, DFT is expected to better represent the bonding in BCC transition metals. Thus, we expect that the twin boundary structures predicted by DFT are more accurate and presentative of the actual structures. In addition, the results of the DFT simulations fall into two categories: those in the group VB and those in group VIB. α -Fe happens to behave like the group VB metals.

The TBGSF curves for Ta, Nb, V, and α -Fe are shown in Figure 4.8(a)-(d) which resembles the TBGSF curves for the interatomic potentials that predict an equilibrium isosceles structure. To examine the equilibrium structures, we relaxed four points on the TBGSF curves, the same as was done in the previous subsection. For $\lambda = 0$, the structure after relaxation is a distorted reflection structure (as illustrated in Figure 4.5), with $\delta = 0.154\text{b}_p$ for Ta, 0.125b_p for Nb, 0.172b_p for V and 0.115b_p for α -Fe. While for $\lambda = \frac{1}{4}, \frac{1}{2}$ and $\frac{3}{4}$, the structure obtained after full relaxation approximately resembles the distorted isosceles structure with $\eta = 0.090\text{b}_p$ for Ta, -0.110b_p for Nb, -0.010b_p for V and -0.057b_p for α -Fe. The structures obtained from structural relaxation is very similar to the distorted isosceles structures shown in Figure 4.3 with η shift of the atom layers nearest to the twin boundary plane. However, these fully relaxed structures fall short of

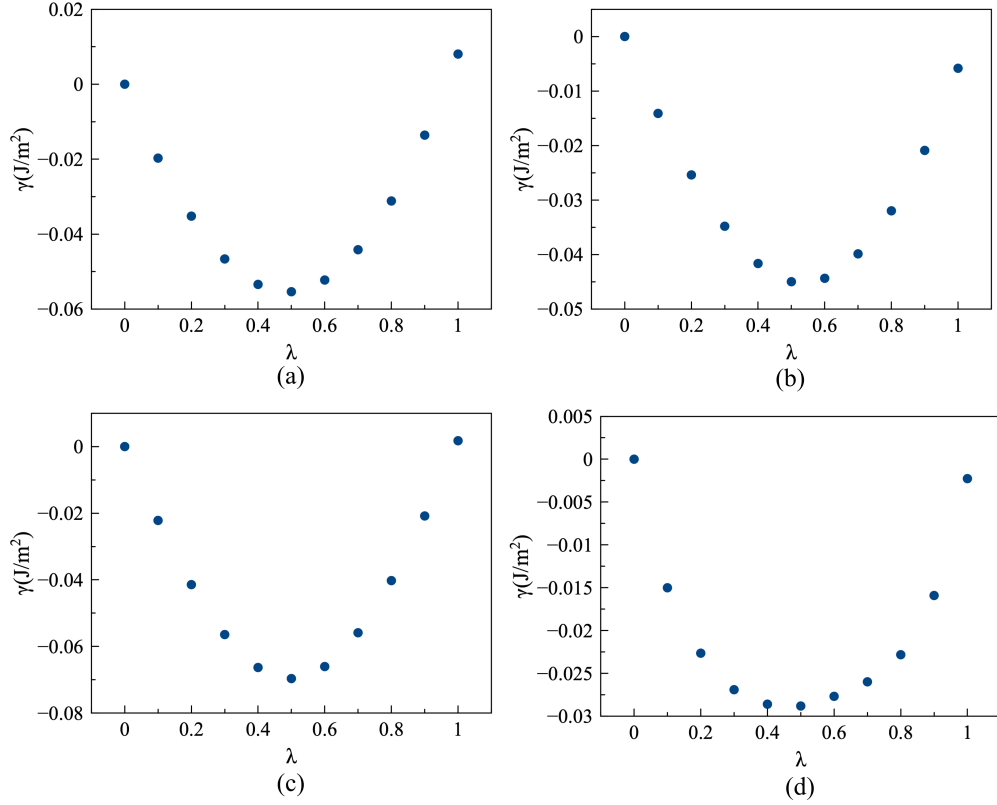


Figure 4.8: The TBGSF curves for (a) Ta, (b) Nb, (c) V and (d) Fe using DFT.

dissolving into the exact isosceles because the apex of the isosceles triangle deviates from the pure isosceles by a very small amount: $-0.015b_p$ for Ta, $+0.009b_p$ for Nb, $-0.009b_p$ for V and $-0.012b_p$ for α -Fe. These small deviations result from very small relaxations in each atomic layers in the simulation cell considered and are about five to ten times smaller than the η shift and can be regarded as inconsequential in describing the structure.

The twin boundary energies, as reported in Table 4.3, show that while the distorted reflection structure is metastable, the distorted isosceles obtained from fully relaxing has lower energy. These results are true for Ta, V, Nb and α -Fe. The notable difference between α -Fe and the group VB metals is α -Fe has a high twin boundary energy and a shallower (lower magnitude) TBGSF curve. In addition, the difference in energy between the two twin structures is much lower in α -Fe, over a 10 – 15% difference for the group VB metals compared to 6% difference in α -Fe.

The TGSF curves for Ta are shown in Figure 4.9 which has cusps at the same positions observed for the Ravelo 2 interatomic potential. In fact, Figure 4.9 compares quite well to Figure 4.2(b)

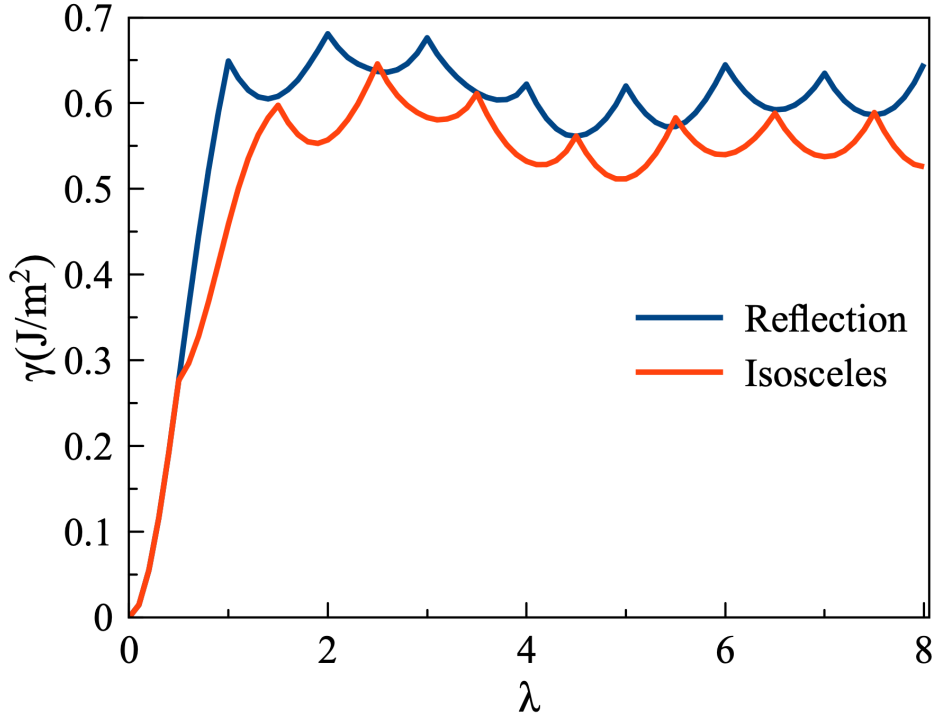


Figure 4.9: The TGSF curve for Ta computed using DFT.

except that we see a stronger variation in the peaks and valleys for lower values of λ in the twinning curve. This suggests that the twin-twin interactions are stronger in DFT than they are predicted by EAM potentials. These results are consistent with previous reports of the TGSF curves predicted by DFT [42]. The slight differences between the equilibrium isosceles structure and those created during the TGSF curve do not create additional cusps in the TGSF curve, but it does prevent the TGSF curve and the fully relaxed twin boundary energies from agreeing in numerical value.

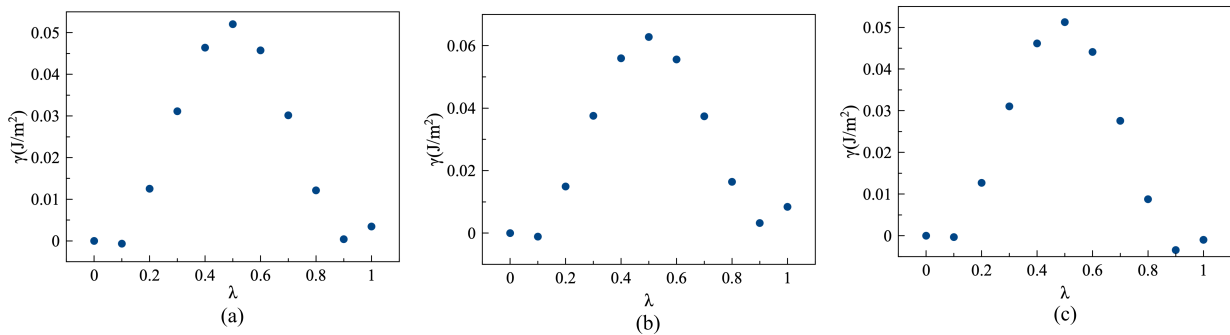


Figure 4.10: The TBGSF curves for (a) Mo, (b) W, and (c) Cr using DFT.

The TBGSF curves for the group VIB metals are shown in Figure 4.10(a)-(c) for Mo, W and Cr respectively. These curves show a slight shift of the minimum away from the pure reflection structure similar to the ATFS potential for Mo and the isosceles configuration is an unstable equilibrium structure. The minimum occurs at $\lambda = 0.1$ for all the metals, but has a large uncertainty due to the limited number of points. Thus, we can see that all the group VIB metals behave similarly, but we cannot assume their minima are at exactly the same λ shift value.

To determine the metastable twin boundary structures, we relaxed the atomic structures for the previously defined λ shifts to determine the equilibrium structures. For $\lambda = 0$, the equilibrium structure is a distorted reflection twin boundary with the δ values given in Table 4.3 consistent with the ATFS potential for Mo. For the other values of λ , the structure that forms is one of the two scalene structures similar to that observed for the Fellingner potential for Nb. For $\lambda = \frac{1}{4}$, the fully relaxed structure dissolves into a structure that closely approximates the scalene structure for $\lambda = 0.1$. For $\lambda = \frac{1}{2}$ and $\frac{3}{4}$, the fully relaxed structures dissolve into a structure that closely approximates the scalene structure for $\lambda = 0.9$. These fully relaxed structures fall short of dissolving into the exact scalene structures because the apex of the relaxed scalene triangle deviates from the apex of the exact scalene by a very small amount. Further deviation from the $\lambda = 0.1$ and 0.9 structures are observed in the atom layers further away from the twin boundary. In this case, similar to TBGSF curve produced using EAM potentials shown in Figure 4.4(a), the isosceles structure is not a metastable twin boundary structure. The structural parameters are listed in Table 4.3 as well as the energies for each of these structures.

The TGSF curve for Mo computed using DFT is shown in Figure 4.11(a). Here, we can see that the pure reflection curve is indeed lower than the isosceles as suggested by the TBGSF curves shown above. The DFT TGSF curves again show more fluctuations than those observed using interatomic potentials as noted for the VB metals as well. Our TGSF curve for Mo also does not match twinning energy pathway previously reported by Ogata *et al.* [63, 64] where $\lambda = 3$ is an unstable equilibrium point. This means a three layer twin is unstable but this is not the case for the TGSF curve for Mo shown in Figure 4.11(a). The choice of exchange correlation can be a reason

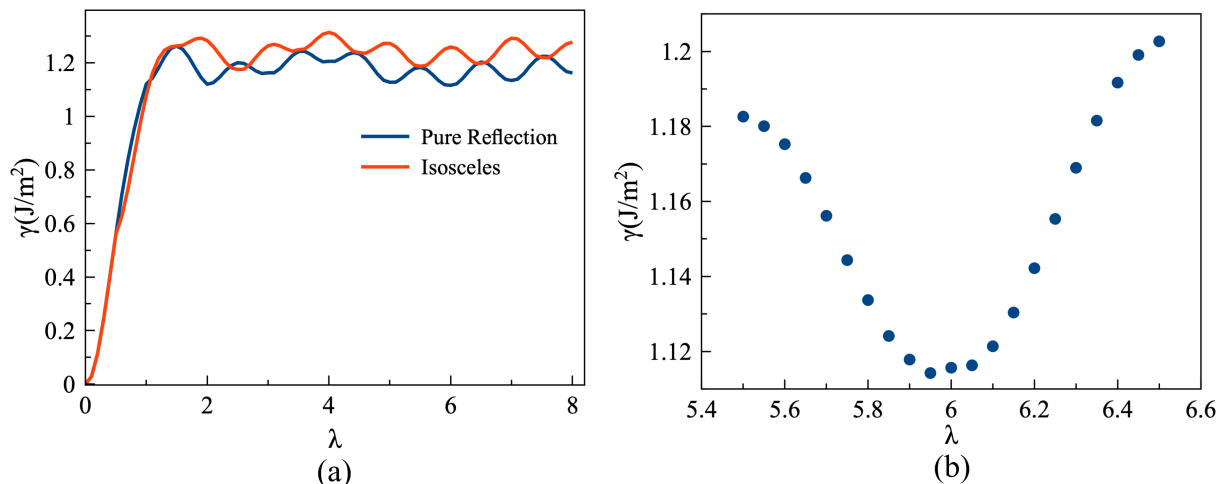


Figure 4.11: (a) The TGSF curve for Mo and (b) a zoomed in image of (a) showing the very small cusps that emerge due to the instability associated with the pure reflection twin boundary.

behind the discrepancy as Ogata *et al.* used PW91 [130] instead of the PBE exchange correlation function. However, the differences are more likely related to the choice of pseudopotential as the PAW was used here and Ogata *et al.* used the ultrasoft pseudopotential [131]. One feature of the TGSF curve that is more difficult to see, perhaps partially obscured by the twin-twin interactions, are the cusps in the TGSF curves. These cusps are smaller in the DFT simulations as compared to those observed for the EAM potentials, but they are indeed there. An enlarged image is shown in Figure 4.11(b) shows that there is a bump or rise in the energy at integer δ values. This is consistent with the TBGSF curve shown in Figure 4.10(a).

The results of the DFT simulations are a bit more consistent in their predictions when compared to the EAM potentials (see Table 4.3). Notably, each group of metals exhibit the same stable and metastable twin structures and even the magnitudes of the structural distortions are similar. All of the BCC metals exhibit a metastable distorted reflection twin boundary structure, but this structure is only favorable in the group VIB metals. In the group VIB metals, the distorted reflection structure is as energetically favorable as the scalene structure and the two scalene structures have slightly different energies due to very small variations in atomic positions. We also find that α -Fe behaves the same as the group VB metals, preferring a distorted isosceles structure with η shifts.

Table 4.3: Equilibrium structures from DFT

		Distorted Reflection	Distorted Isosceles	Scalene1	Scalene2
Ta	$\gamma(\text{Jm}^{-2})$	0.549	0.492	—	—
	δ / η shift	0.154b _p	-0.090b _p	—	—
Nb	$\gamma(\text{Jm}^{-2})$	0.524	0.453	—	—
	δ / η shift	0.125b _p	-0.110b _p	—	—
V	$\gamma(\text{Jm}^{-2})$	0.554	0.491	—	—
	δ / η shift	0.172b _p	-0.010b _p	—	—
Fe	$\gamma(\text{Jm}^{-2})$	0.909	0.861	—	—
	δ / η shift	0.115b _p	-0.057b _p	—	—
Mo	$\gamma(\text{Jm}^{-2})$	1.108	—	1.108	1.110
	δ / η shift	0.033b _p	—	-0.062b _p	0.016b _p
W	$\gamma(\text{Jm}^{-2})$	1.392	—	1.392	1.406
	δ / η shift	0.039b _p	—	-0.054b _p	-0.014b _p
Cr	$\gamma(\text{Jm}^{-2})$	1.263	—	1.254	1.254
	δ / η shift	0.032b _p	—	-0.042b _p	-0.064b _p

4.2.3 Analytical model of the TBGSF curve

In the previous sections, the interatomic potentials and DFT simulations have demonstrated different behaviors in the TBGSF curves. Specifically, we find that some predict a low energy at $\lambda = \frac{1}{2}$ while other predict a local maximum at this point and local minima at two other λ values. Of course, this is a direct result of the bonding in the materials (for DFT) and the parameterization and parameters used (for interatomic potentials). However, we have found it useful to develop an empirical model for this behavior to provide a bit more insight into this.

To model the TBGSF curve analytically, we consider two continuum blocks of material whose energy variation is determined solely by bonding of the atoms on either side of the cut plane

shown in Figure 4.12(a). Initially, we postulate that this excess energy can be written as a simple expression i.e., as a function of these bond lengths. The bond length between two atoms across the cut plane as a function of λ can be written as:

$$L = -\frac{a\sqrt{2}}{2}\hat{i} + \left(\frac{a\sqrt{3}}{6} + \lambda\right)\hat{j} + \frac{a}{\sqrt{6}}\hat{k} \quad (4.1)$$

where the unit vectors align with the coordinate system give in Figure 4.12; for y along the $[11\bar{1}]$ and z is along the $[112]$. If we then postulate that the energy of the bonds across the cut plane scale indirectly with the length of the form:

$$E_{\text{bond}} = \alpha|L|^{-n} \quad (4.2)$$

where α is a proportionality constant and n is an exponent. When $n = 2$, the energy scales inversely with the square of the distance. This results in an energy per unit area due to the bonds across the cut plane as:

$$\Gamma(\lambda) = A^{-1} \sum |L(\lambda)|^{-n} \quad (4.3)$$

where A is the area per unit atom on the cut plane and the (infinite) summation is for all atoms across the cut-plane. The twin boundary stacking fault energy then is defined as:

$$\gamma(\lambda) = \Gamma(\lambda) - \Gamma(0) \quad (4.4)$$

The results of this approximation are shown in Figure 4.12 for $n = 2$ (red curve). This curve shows two important features. The first is that the lowest energy structure is corresponds to the isosceles configuration. The second is that the pure reflection is not an equilibrium structure, stable or unstable, which suggests cusps in any twinning GSF curve. While the value of the exponent, n can alter the shape of the curve, reasonable values of n predict similar shapes of the stacking fault energy curve and thus we can take these results as a general prediction of this idea. Thus we can

conclude with some generality that the isosceles energy minimum is at least partially a result of the minimizing unfavorable bond lengths.

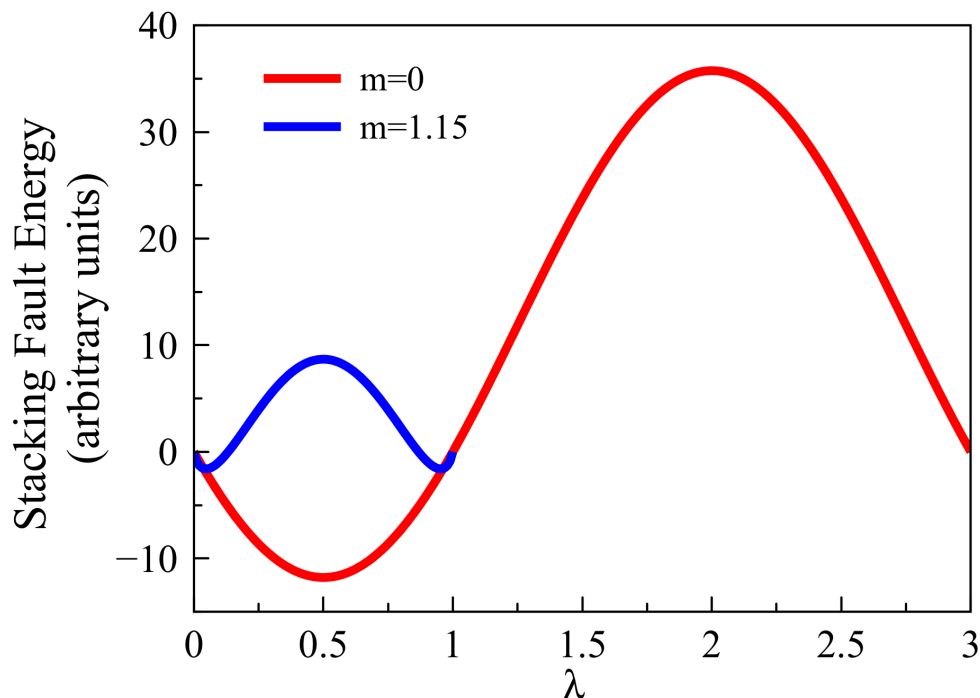


Figure 4.12: The TBGSF curves predicted from the analytical model of bonding across the cut plane. The energy has arbitrary units since the prefactor α is not specified and we simply have scaled the two curves to visually match.

However, this does not explain how we might create the GSF curves shown for the other cases in which the isosceles becomes an unstable equilibrium point and shift the minimum closer to the pure reflection point. To make the pure reflection more stable, we can penalize the bond energy term similar to empirical potentials like Stillinger-Weber [132] to favor the bond angles found in the pure reflection twin boundary. One such bond energy term is:

$$E_{\text{bond}} = \alpha \left| \frac{1}{9} - \cos^2 \theta \right|^m |L|^{-n} \quad (4.5)$$

where θ is the angle the bond atom makes with the y-axis across the cut-plane and cosine of the ideal angle for the pure reflection twin boundary is $\frac{1}{3}$. The results for $n = 2$, $m = 1.15$ are shown

in Figure 4.12 (blue curve). For $m = 1.15$ the minimum now lies between $\lambda = 0$ and $\lambda = \frac{1}{2}$, just as occurs in many of our simulations. With sufficiently strong energy penalty, it is possible to even force the minimum to be at $\lambda = 0$, despite this never being observed in any simulation conducted here. Furthermore, with larger values of m , the curve quickly transforms back to the case when the bond bending penalty term is excluded ($m = 2$ looks very similar to $m = 0$).

What this demonstrates is that a simple model that roughly approximates the energy of the bonds across the TB interface is able to reproduce the features of our TBGSF curves. They show that in the absence of (relatively) strong directional bonds, the isosceles structure is preferred while more directional bonding will cause the scalene structures to emerge as low energy points on the TBGSF curve with stronger directionality pushing the low energy structures closer and closer to the pure reflection structure.

4.3 Conclusions

In this chapter, we have analyzed the structure of twin boundaries in BCC transition metals using atomistic simulations which has led to some key observations and provide insights into twin nucleation phenomenon. Full structural relaxation with EAM potentials results in three equilibrium twin boundary structures: distorted isosceles structures described by small η shifts, distorted reflection structures described δ shifts and scalene structures. While structural relaxation with DFT also exhibits the same three equilibrium twin boundary structures, the observations are more consistent amongst the different groups. To verify the consistency of the DFT results we have also performed sensitivity analysis by performing similar simulations with $N = 25$ atoms as well as different boundary conditions by changing the degrees of freedom of the simulation cell. The twin energies from these set of simulations differ from the values listed in Table 4.2 by less than 5%. Also the deviations of the relaxed structures from the reference structures are also less than 5% of b_p . All of these simulations show that distorted isosceles is the stable equilibrium structure in group VB metals and α -Fe whereas scalene twin boundary structures are the stable equilibrium structures in Group VIB metals.

The TBGSF curves are a good starting point for analysis of the twin boundary structures because the minimum energy structures predicted by this set of curves correspond to the lower energy twinning pathways in TGSF curves and suggest the lowest energy structures. One essential take-away is the fact that the TGSF curves shown in this work exhibit cusps for shifts that correspond to the reflection twin boundary structures since this structure is not an equilibrium structure (stable or unstable). The TGSF curves for potentials that predict the lowest energy structure to be a distorted isosceles typically have very large cusps due to the large energy difference between the pure isosceles and pure reflection curves. On the other hand, the TGSF curves for those potentials that predict a stable distorted reflection or scalene typically have smaller cusps due to the small energy differences between the pure reflection and these equilibrium structures but cusps do not exist at the isosceles structure. The existence of these cusps can further be rationalized using analytical models of the TBGSF curve. The cusps in the TGSF curves are sometimes not seen in literature [41, 42] for both EAM and DFT simulations, presumably due to a low number of sampled points on the GSF curve. However, all of our calculations done here in detail demonstrate their universal existence for both EAM and DFT simulations alike.

It is worth noting that despite its usefulness, the TBGSF curves alone are not sufficient in predicting the stable twin boundary structures as we have shown that δ shifts associated with reflection structures involve simultaneous relaxations in atom layers above and below the twin boundary atoms as is the case for isosceles structures with η shifts. Thus, full relaxations of the twin boundary structures are needed, and should be done at different points along the TBGSF curve to test for the existence of multiple equilibrium structures.

These observations not only have direct implications on our understanding of twin boundary structure, but also impact our understanding of how the twins should nucleate and propagate. Notably, the general model of the nucleation of a deformation twin includes multiple lamella of twinning partials with Burgers vector b_p , i.e. nb_p , and our TGSF curves show this minimum is $n = 2$ two for the group VIB metals. However, as the isosceles structure is more favorable in the group VB and α -Fe, then the twin nucleus must contain approximately $2 \times \frac{1}{2}b_p + nb_p$ partial dis-

locations with the minimum stable number being $n=0$. Both of these descriptions are approximate as the real equilibrium structures are distorted from these and would involve the passage of very small zonal dislocations to achieve the actual equilibrium structures. The inclusion of these dislocations in a TG_{SF} curve would create true local minima, although at the expense of making such curves very complicated.

Chapter 5

Modeling twin nucleation and growth

Twins in crystalline materials are ubiquitous, occurring in structural, electronic, and geologic materials alike. Their existence can have a profound impact on properties, including dramatic changes in strength of metallic alloys [133–136] or a degradation of electronic properties [137–140]. They can form either during the crystal growth process, i.e., growth twins, during annealing, or they can nucleate inside the crystal, i.e., deformation twins, in response to an applied load [44]. Despite the importance of deformation twinning in the generation of new twins inside already formed crystals and its potential to supplant dislocations as a carrier of plastic deformation, exactly how the twins form is not well understood. This is because twin nuclei are usually thought to be extended defects, with their thickness extending over multiple crystal planes, and they nucleate so fast and at such small length scales that it is difficult to capture the nucleation event with the most advanced characterization tools [27, 67].

In face centered cubic metals (FCC), deformation twinning (DT) is well known to proceed by the sequential nucleation of Shockley partials on successive planes, forming a twin lamella [3, 43]. However, this process is the exception, since twins in body centered cubic (BCC) and hexagonal closed packed (HCP) are generally thought to nucleate on multiple atomic planes concurrently [54, 58, 141–144], as well as other crystalline materials [141, 145]. The twinning element in the BCC crystal is the $\langle 111 \rangle \{112\}$, and is generally thought to occur mechanically by the passage of $\frac{a}{6} \langle 111 \rangle$ twinning dislocations (where a is the lattice constant) which, with successive passage, results in a mirror symmetry across the $\{112\}$ plane [4]. These $\{112\}$ twins can have roughly two different atomic level structures, the reflection twin structure and the isosceles twin structures [38, 41, 65]. These two twin structures both obey the global mirror symmetry but differ from each other by a local atomic translation of $\frac{a}{12} \langle 111 \rangle$. It has been shown from density functional theory (DFT) simulations that the group VB transition metals stabilize the isosceles structure while the group VIB transition metals will form a distorted form of the reflection structure. The potential

for the two different twin structures is important because it plays a role in twin thickness and the nucleation of these defects [65].

The questions of how the twins nucleate and how many atomic layers is involved have been a debate for decades [3, 54, 58, 60, 64, 67] and the latter remains a significant open question. The most common nucleation methods are the pole mechanism of Bilby and Cottrell [48] (see Figure 2.10 for a schematic), and the heterogenous nucleation from other defects [47], e.g. dislocations [36, 37, 48, 50] (see Figure 2.11 for a schematic), grain boundaries [146–148], or free surfaces [149, 150].

The difficulty with twin sources and their identification is that twin nucleation is a sparse and fast event and directly observing it is difficult. Atomistic simulations have demonstrated that twins can indeed nucleate from free surfaces and grain boundaries in nanoscale BCC metals [39-41] [31–33] and from dislocations with sufficiently high strain rates [60, 62]. The direct observation of deformation twinning has also been recently reported using the HRTEM in nanocrystals [27, 67], confirming the nucleation at free surfaces and grain boundaries both, under very high stresses.

The critical size of a twin nucleus, specifically the number of atomic layers involved, has been studied but without a definitive answer. The pole model by Bilby and Cottrell suggests the growth is layer-by-layer, but this idea has generally been rejected by the community because simulations have demonstrated that a single layer $\{112\}$ fault is unstable [38]. The most widely recognized twin nucleus thickness, which is three layers, comes from the model of Sleeswyk [37], who hypothesized that the twin nuclei thickness would be three so that the net Burgers vector of twin nucleus would match that of a perfect dislocation: $b = \frac{a}{2}\langle 111 \rangle$. This notion has been quite pervasive and revisited by others [3, 54, 58], including atomic level simulations [60, 62] that have claimed to match that result. However, a careful revisiting of those simulations suggests that the number of layers involved indeed is not three. Furthermore, it is important to note that the three layer model is based on an idea of zonal dislocations [36] with burgers vectors of $\frac{a}{6}\langle 111 \rangle$, which do not match the correct method of formation of the isosceles boundaries that should form in the group VB metals [41, 65]. The most definitive experimental results are those on tungsten nanowires

[27, 67] where the twin thickness could be measured. The authors found that after nucleation of the twins, the minimum thickness they could find was a 6-layer thick twin and concluded this was the minimum size. However, the experiments are very limited in time resolution, specifically a 0.5 second resolution, which is certainly not fast enough to actually see a twin nucleate, and the reported size could be after thickening. Furthermore, if thickening is involved, the sizes observed could be dependent on the magnitude of the stress and the size of the crystal, and thus not a reflection of some limit of the actual material behavior.

DFT stability modeling results have provided some mixed conclusions as well. Ogata et al. examined twins in Molybdenum and found the minimum twin thickness for stability was five layers [63, 64]. However, more recent and thorough work by us suggests that the thickness are two for a reflection twin and three for an isosceles twin [65]. However, these results focus on twin stability at zero stress, while the energetic pathway for twin nucleation occurs under very high stresses, even for heterogenous nucleation [11,40,47-49] [32, 43, 66, 67]. Since the energetics and the structure of a nucleating twin in a BCC metal has never been carefully studied, it is unclear how large the nuclei are and what controls this size. In this work, we have addressed this outstanding question directly using atomic level modeling and settle the size debate once and for all.

However, in answering the question of fundamental twin thickness, it is critical to be consistent in how one measures twin thickness in BCC metals and, in fact, all materials. It is natural to try to assign atoms to twinned and untwinned regions and count the thickness of the twin as the number of atoms inside these regions. However, the potential for twin boundaries to exist on top of atomic layers (e.g., reflection) or between atomic layers (isosceles) creates ambiguity of how atomic layers should be partitioned to twinned and untwinned regions. Examples of this are discussed in detail in Chapter 3. The alternative method is to count twin thickness by counting the number of shearing events that occur between atomic layers, which is the same as counting the number of twinning dislocations. This approach removes the ambiguity, see Chapter 3, and is the method we will employ in the following.

5.1 Critical twin nuclei thicknesses in BCC transition metals

5.1.1 Empirical potential predictions of twin nucleation

5.1.1.1 Tantalum

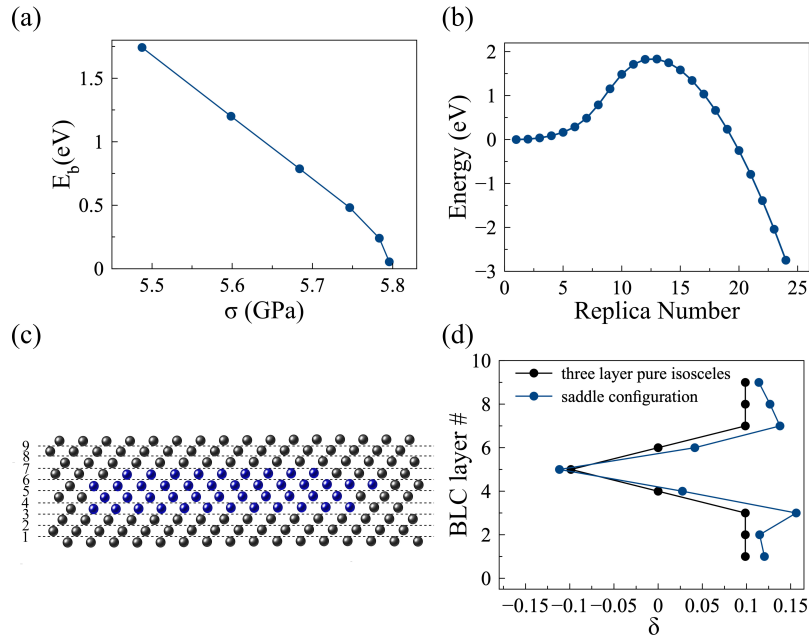


Figure 5.1: (a) The energy barrier for twin nucleation plotted as a function of the applied stress from the free-end string simulations [100] for the model Ta system described by Ravelo2 potential [77]. (b) An example of a minimum energy path of twin nucleation for the smallest stress in (a), which is 5.49 GPa, (c) the twin nucleus at the activated state for an applied stress of 5.49 GPa. The atoms are colored by using common neighbor analysis (CNA) [151] which allows for convenient for locating a twin nucleus in a bulk crystal with nearly 13000 atoms but can be misleading in determining twin thickness, and (d) BLC analysis of the atomic positions of the twin nucleus (blue dots) indicating the presence of a three layer isosceles twin if the BLC parameter δ values are compared to those of an ideal three layer pure isosceles (black dots).

To understand the nucleation process in full atomic level detail, we utilized classical atomistic simulations to compute the energetics of the nucleation process as a function of the applied stress in BCC Ta modeled by Ravelo 2 potential [77]. The activation energy barrier for homogeneous twin nucleation in Ta plotted as a function of stress is shown in Figure 5.1(a) which is extracted from individual string simulations as described in Chapter 3. An example minimum energy path (MEP) from these simulations is shown in Figure 5.1(b) where the activation energy is the peak

dislocation nucleation even though the defect extends over multiple atomic planes. These results indicate that the twin nucleus are roughly the same as those predicted from stability analysis [65] on twinning GSF curves at zero stress. However, it is well known that interatomic potentials, especially EAM-based potentials, can be prone to errors associated with their fitting and thus the results above may not be reliable even if they are insightful. This is particularly true in the case of twin nucleation because interatomic models are frequently fit near equilibrium, while the application here is far from equilibrium i.e., under high stresses. Even if we consider more modern machine learning potentials, it would still be unclear if they represent predictions of much more accurate methods like density functional theory unless we carefully fit this region to features that we knew what controlled the twin stability, which at this point we do not know. On the other hand, DFT potentially can provide very accurate results but is very expensive cannot be used to simulate the roughly 13,000 atoms required for our nucleation simulations. Thus, to extend our results to DFT accuracy, we must better understand the atomistic results by replicating the twin structures with less expensive approaches and then apply them using DFT.

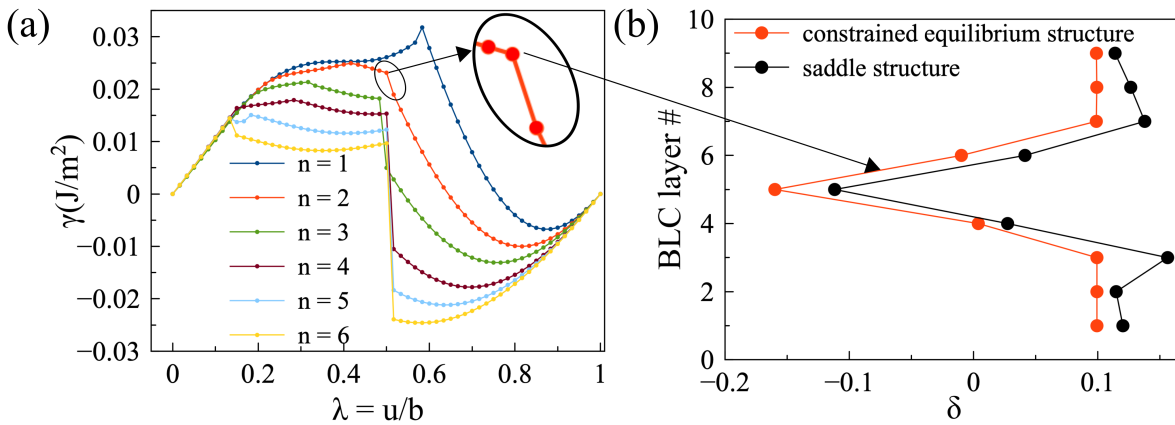


Figure 5.3: (a) The constrained twin stability curves for BCC Ta, described by the Ravelo2 EAM potential [77], under 5.49 GPa pure shear stress. (b) The BLC parameter, δ , plotted for both the saddle structure (black dots) and one of the constrained equilibrium structures exhibiting a similar 3 layer distorted isosceles twin (red dots).

Table 5.1: BLC analysis results for constrained equilibrium structures found in the twin stability curves under 5.49 GPa pure shear stress for BCC Ta, described by Ravelo2 EAM potential [77] shown in Figure 5.3(a). Faulted layers are counted if the bond length difference, δ deviates from the bond length differences in strained BCC crystals by more than 10% of the magnitude of the repeat lattice vector.

Number of relaxed atom layers, n	Linear elastic loading interval	Single layer ($N_{\text{twin}} = 1$) fault interval	Two layer ($N_{\text{twin}} = 2$) twin interval	Three layer ($N_{\text{twin}} = 3$) twin interval	Dislocation nucleation interval
1	$0 \leq \lambda \leq 0.133$	$\lambda = 0.15$	$0.167 \leq \lambda \leq 0.567$	—	$0.583 \leq \lambda \leq 1.0$
2	$0 \leq \lambda \leq 0.150$	$0.167 \leq \lambda \leq 0.2$	$0.217 \leq \lambda \leq 0.433$	$0.45 \leq \lambda \leq 0.5$	$0.517 \leq \lambda \leq 1.0$
3	$0 \leq \lambda \leq 0.150$	$\lambda = 0.167$	$0.183 \leq \lambda \leq 0.383$	$0.4 \leq \lambda \leq 0.4833$	$0.5 \leq \lambda \leq 1.0$
4	$0 \leq \lambda \leq 0.150$	—	$0.167 \leq \lambda \leq 0.283$	$0.3 \leq \lambda \leq 0.5$	$0.517 \leq \lambda \leq 1.0$
5	$0 \leq \lambda \leq 0.133$	—	$0.15 \leq \lambda \leq 0.267$	$0.283 \leq \lambda \leq 0.5$	$0.517 \leq \lambda \leq 1.0$
6	$0 \leq \lambda \leq 0.133$	—	$0.15 \leq \lambda \leq 0.183$	$0.2 \leq \lambda \leq 0.5$	$0.517 \leq \lambda \leq 1.0$

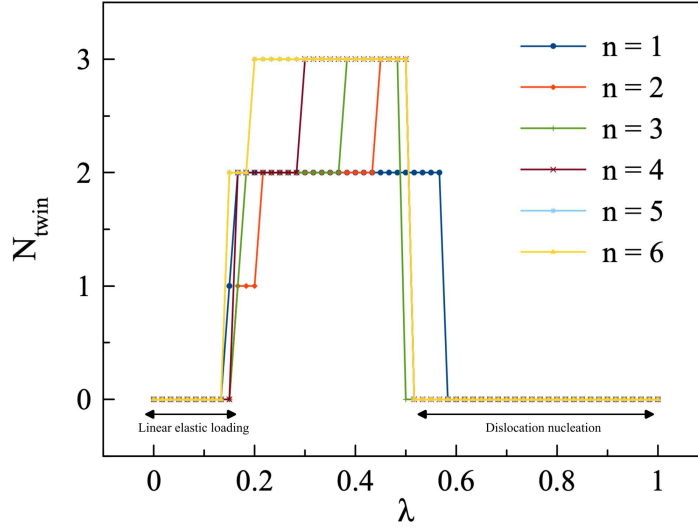


Figure 5.4: Twin thickness vs. normalized displacement for the constrained twin stability curves in Figure 5.3(a).

To examine the stability of the twin structures using EAM interatomic potentials, we constructed the constrained GSF curves described in Chapter 3 for Ravelo2 Ta under 5.49 GPa, Figure 5.3(a). With initial shearing ($0 \leq \lambda \leq 0.15$), these curves show a linear elastic loading as expected. With sufficient shear ($0.15 \leq \lambda \leq 0.5$), however, the atoms are able to rearrange and form constrained equilibrium structures with twins, which, when analyzed by the BLC analysis, show structures very similar to those seen in our nucleation simulations shown in Figure 5.1. One such constrained equilibrium structure is analyzed with the BLC analysis in Figure 5.3(b) which is compared to the saddle structure we found in our energy barrier path simulations. These twin structures typically exist after the linear (elastic) portion of the curve, but before dislocation nucleation is observed. Dislocation nucleation beyond $\lambda \geq 0.5$ is observed because large shear in the twinning direction is equivalent to shearing in the anti-twinning sense. While the structures are not identical due to differences in local atomic constraints, we are able to see that the structures are indeed the same. The advantage of this approach is that it can be used to produce potential twin structures utilizing DFT simulations since the constrained twin stability analysis only requires 24 atoms, which is tenable using direct DFT simulations as opposed to prohibitively expensive direct nucleation

simulations. As mentioned earlier, with initial shearing, these curves show a linear elastic loading and with sufficient shear, however, the atoms are able to rearrange and form constrained equilibrium twin structures, which, when analyzed by the BLC analysis, show structures very similar to those seen in our nucleation simulations. These twin structures typically exist after the linear (elastic) portion of the curve, but before the large drop-off where dislocation nucleation is observed. In table ??, BLC analysis results are summarized for all 6 curves in Figure 5.3(a). Under large applied stresses, e.g. the red circles shown in Figures 5.17, we see the curves do change slightly but the favored structures essentially don't change i.e., under large applied stresses Ta prefers an isosceles structure similar to zero stress TBGSF curve (blue curve).

A graphical representation of the twin thickness observed at different displacement values as a function of number of relaxed atom layers is shown in Figure 5.4.

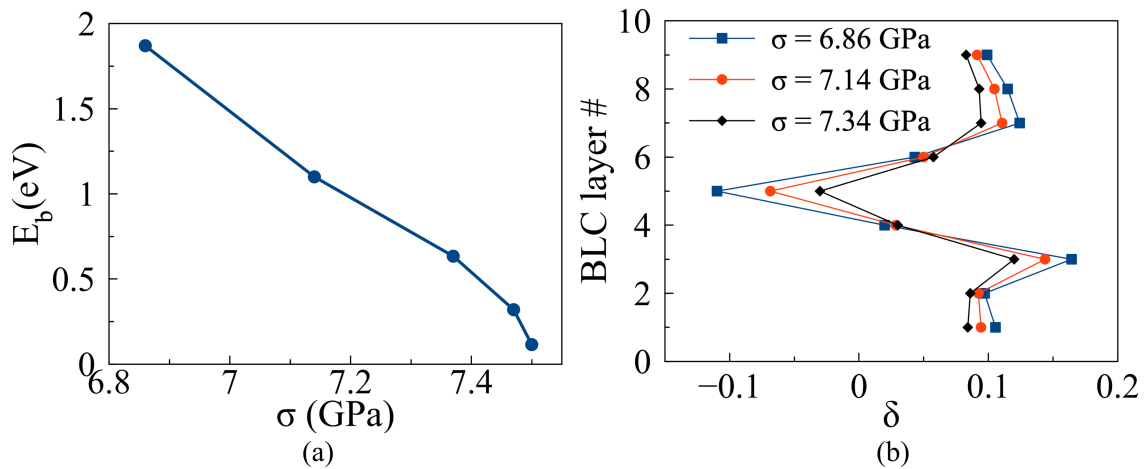


Figure 5.5: (a) Energy barrier for twin nucleation vs. applied pure shear stress using Ta-ATFS potential (b) Determination of twin thickness in the saddle structures found in the free-end string simulations using the BLC analysis for 3 stresses.

Free-end string simulations were also performed to observe direct nucleation of twins with the ATFS [78] potential. The saddle point structures of the MEPs for this EAM potential has the same trend as those found for the Ravelo2 [77] potential. Specifically, the twin structure found for the ATFS potential, a three layer thick twin with two isosceles TBs and a reflection layer in between them, similar to those found in Ravelo 2 potential study. Also the magnitude of the

BLC parameter decreases and flattens out as the stress approaches the ideal strength of the Ta-ATFS potential considered here. This indicates that the magnitude of the slip in the twin structure decreases towards the ideal strength, similar to the nucleation of dislocations. Figure 5.5 shows that the 3 layer thick twins are nucleated.

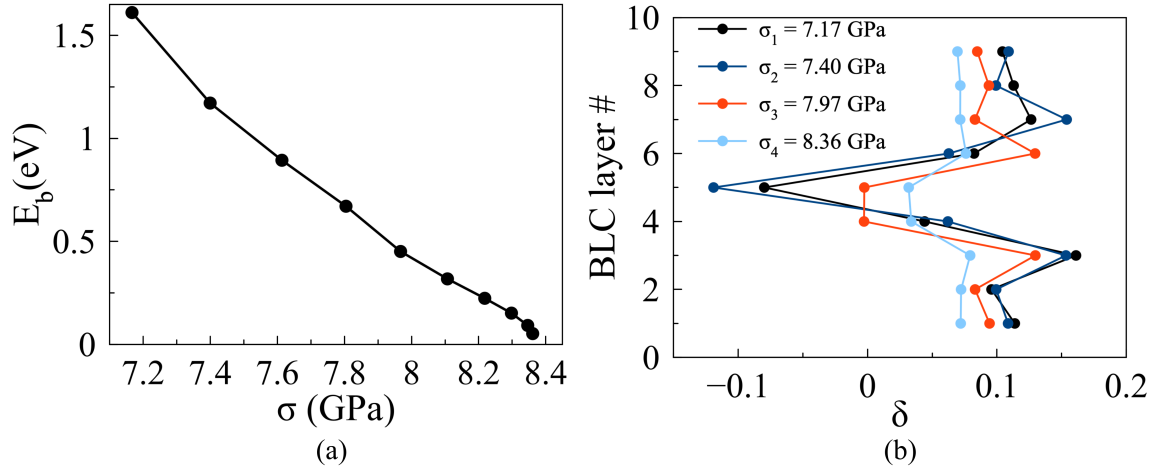


Figure 5.6: (a) Energy barrier for twin nucleation vs. applied pure shear stress in Ta-Zhou EAM potential (b) Determination of twin thickness in the saddle structures found in the free-end string simulations using the BLC analysis for 3 stresses.

Similar analysis of free-end string twin nucleation simulations were performed using Zhou [80] EAM potential and at low stresses, the twin nuclei has similar atomic structures as Ravelo 2 and ATFS potentials. However, unlike those two potentials, near ideal strength, the twin nuclei are two layer thick twins with near isosceles structures in both layers. This is shown in Figure 5.6. In conclusion, comprehensive survey of twin nucleation via direct atomistic simulations reveal three layer thick twins with isosceles TB layers and a reflection layer in between. This is, to our knowledge, the first ever unambiguous analysis of critical twin nucleus thickness. Additionally, with the constrained twin stability analysis producing similar twin structures, we have been able to develop a computationally efficient method to explore possible metastable twin structures with DFT calculations which will be discussed in the next section of this chapter.

5.1.1.2 Molybdenum

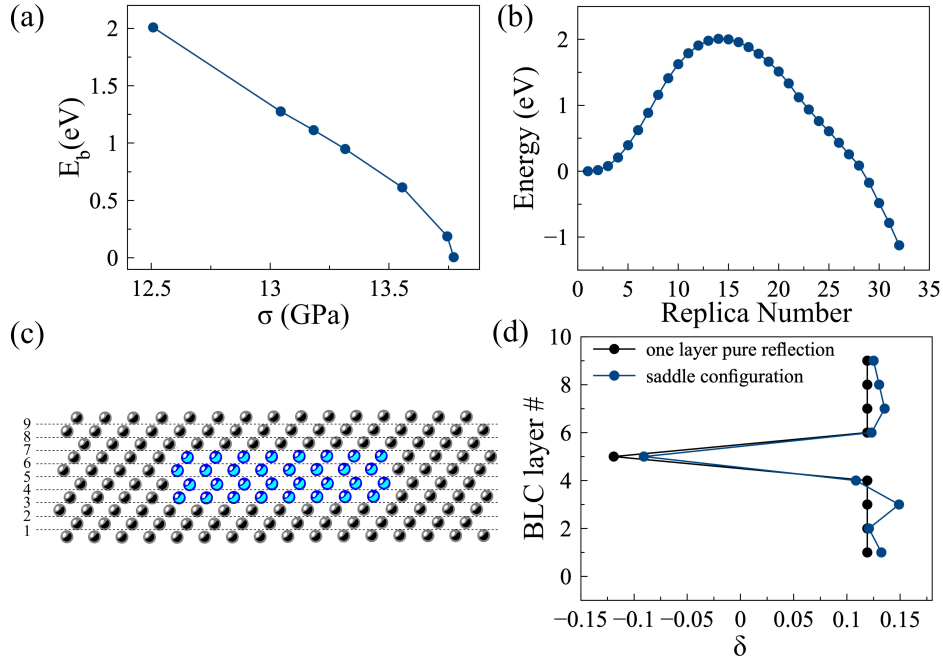


Figure 5.7: (a) The energy barrier for twin nucleation plotted as a function of the applied stress from the free-end string simulations [100] for the model Mo system described by ATFS potential [78]. (b) An example of a minimum energy path of twin nucleation for the smallest stress in (a), which is 12.51 GPa, (c) the twin nucleus at the activated state for an applied stress of 12.51 GPa. The atoms are colored by using common neighbor analysis (CNA) [151] which allows for convenient for locating a twin nucleus in a bulk crystal with nearly 13000 atoms but can be misleading in determining twin thickness, and (d) BLC analysis of the atomic positions of the twin nucleus (blue dots) indicating the presence of a single layer reflection twin if the BLC parameter δ values are compared to those of an ideal one layer pure reflection (black dots).

The activation energy barrier for homogeneous twin nucleation in Mo-ATFS potential plotted as a function of stress is shown in Figure 5.7(a) which is extracted from individual string simulations as described in Chapter 3. An example minimum energy path (MEP) from these simulations is shown in Figure 5.7(b) where the activation energy is the peak of this curve. The atomic positions of the twin nucleus, taken at the activated state for the lowest applied stress, is shown in Figure 5.7(c). The BLC analysis of this twin structure, which is shown in Figure 5.1(d) point to a single layer reflection twin structure (shown with the blue dots in Figure 5.7(d)) and this can be confirmed by by comparing to the BLC analysis on a single layer pure reflection structure (shown

with black dots in Figure 5.7(d)) under 12.51 GPa. Our work in Chapter 4 has identified the zero stress equilibrium structure to be distorted reflection structure [65], but here we can see that the nucleus is actually a single layer reflection structure.

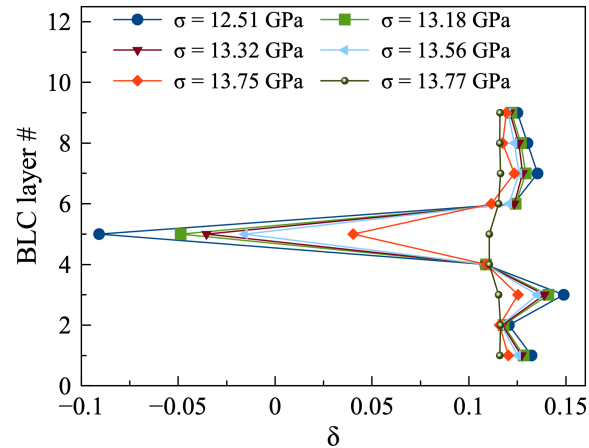


Figure 5.8: BLC analysis of the saddle point atomic configurations of Mo modeled using the ATFS potential for 6 different stress levels, taken from the curve in Figure 5.7(a). As the stress increases, the magnitude of the BLC values decrease, nearly vanishing at the highest stress. However, the structure of the twin seems to remain despite the decrease in magnitude.

Under further applied stress, the single layer structure remains but collapses near the ideal strength, similar to Ta EAM potentials discussed earlier, and the full results are shown in Figure 5.8. These results, contrary to the Ta case, indicate that the nucleus structure is not the same structure as that predicted using zero stress GSF curves.

Similar to the analysis with Ta-Ravelo2, constrained twin stability analysis has also been performed here with the goal of establishing a computationally efficient method to probe probable metastable twin structures in Mo modeled by the ATFS potential. To examine the stability of the twin structures using interatomic potentials, we constructed the constrained GSF curves for ATFS Mo under 12.51 GPa, Figure 5.9(a). With initial shearing, these curves show a linear elastic loading and with sufficient shear, however, the atoms are able to rearrange and form constrained equilibrium twin structures, which, when analyzed by the BLC analysis, show structures very similar to those seen in our nucleation simulations. These twin structures typically exist after the linear (elas-

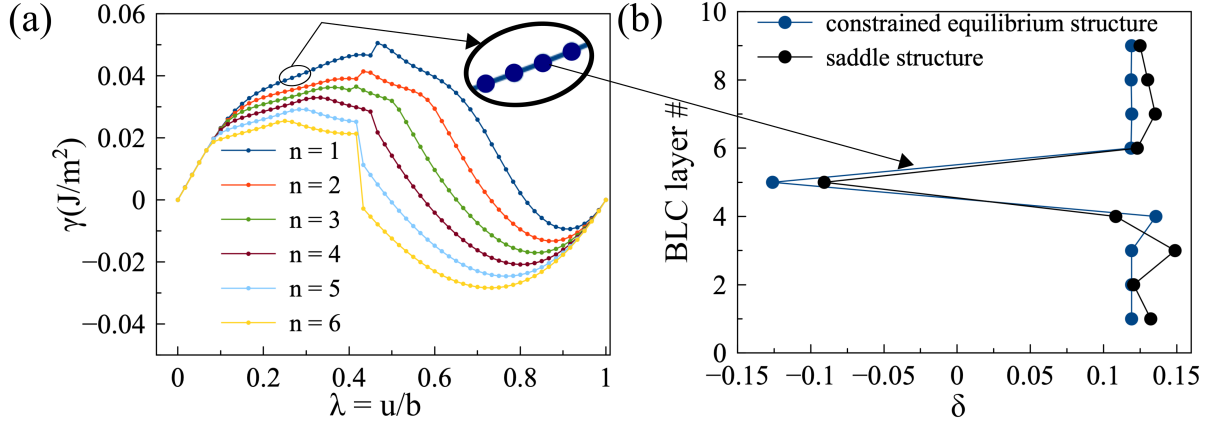


Figure 5.9: (a) The constrained twin stability curves for BCC Mo, described by the ATFS EAM potential [78], under 12.51 GPa pure shear stress. (b) The BLC parameter, δ , plotted for both the saddle structure (black dots) and one of the constrained equilibrium structure exhibiting a 1 layer distorted reflection twin (blue dots).

tic) portion of the curve, but before the large drop-off where dislocation nucleation is observed. In Table 5.2, BLC analysis results are summarized for all 6 curves in Figure 5.9(a). A graphical representation of the twin thickness observed at different displacement values as a function of number of relaxed atom layers is shown in Figure 5.10.

Table 5.2: BLC analysis results for constrained equilibrium structures found in the twin stability curves under 12.51 GPa pure shear stress for BCC Mo, described by ATFS EAM potential [78] shown in Figure 5.9(a). Faulted layers are counted if the bond length difference, δ deviates from the bond length differences in strained BCC crystals by more than 10% of the magnitude of the repeat lattice vector.

Number of relaxed atom layers, n	Linear elastic interval	Single layer ($N_{\text{twin}} = 1$) interval	Two layer ($N_{\text{twin}} = 1$) interval	Dislocation nucleation interval
1	$0 \leq \lambda \leq 0.1$	$0.117 \leq \lambda \leq 0.4$	$0.417 \leq \lambda \leq 0.45$	$0.467 \leq \lambda \leq 1.0$
2	$0 \leq \lambda \leq 0.083$	$0.1 \leq \lambda \leq 0.35$	$0.367 \leq \lambda \leq 0.417$	$0.433 \leq \lambda \leq 1.0$
3	$0 \leq \lambda \leq 0.083$	$0.1 \leq \lambda \leq 0.35$	$0.333 \leq \lambda \leq 0.4$	$0.417 \leq \lambda \leq 1.0$
4	$0 \leq \lambda \leq 0.067$	$0.083 \leq \lambda \leq 0.3$	$0.317 \leq \lambda \leq 0.417$	$0.433 \leq \lambda \leq 1.0$
5	$0 \leq \lambda \leq 0.067$	$0.083 \leq \lambda \leq 0.267$	$0.283 \leq \lambda \leq 0.417$	$0.433 \leq \lambda \leq 1.0$
6	$0 \leq \lambda \leq 0.067$	$0.083 \leq \lambda \leq 0.233$	$0.25 \leq \lambda \leq 0.417$	$0.433 \leq \lambda \leq 1.0$

Free-end string simulations were also performed to observe direct nucleation of twins with the Zhou [80] potential for BCC Mo. The saddle point structures of the MEPs for this EAM potential has the same trend as those found for the ATFS [78] potential. Specifically, the twin structure

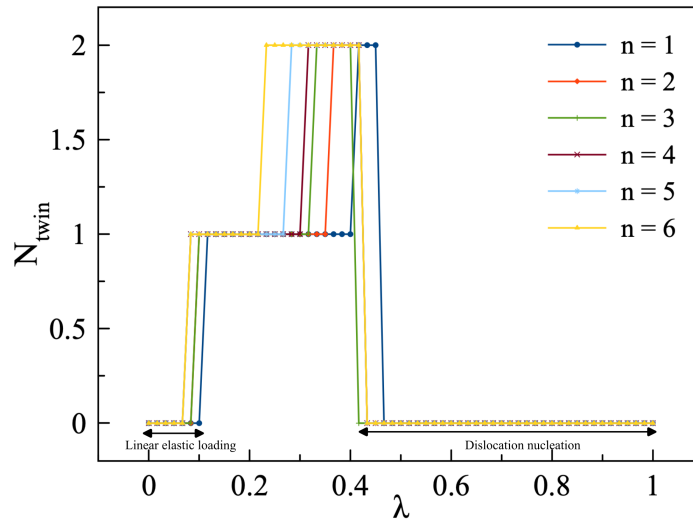


Figure 5.10: Twin thickness vs. normalized displacement for the constrained twin stability curves in Figure 5.9(a).

found for the Zhou potential, a single layer near reflection twin, is similar to those found in Mo-ATFS potential. Also the magnitude of the BLC parameter decreases and flattens out as the stress approaches the ideal strength of the Mo-Zhou potential considered here. This indicates that the magnitude of the slip in the twin structure decreases towards the ideal strength. Figure 5.11 shows that the single layer near reflection twins are nucleated.

So, in Molybdenum, the free-end string simulations with both ATFS and Zhou potentials point to single layer near reflection twins. Constrained twin stability curves from the ATFS potential also enables us to extend our analysis to more reliable DFT simulations which will be discussed in the next section.

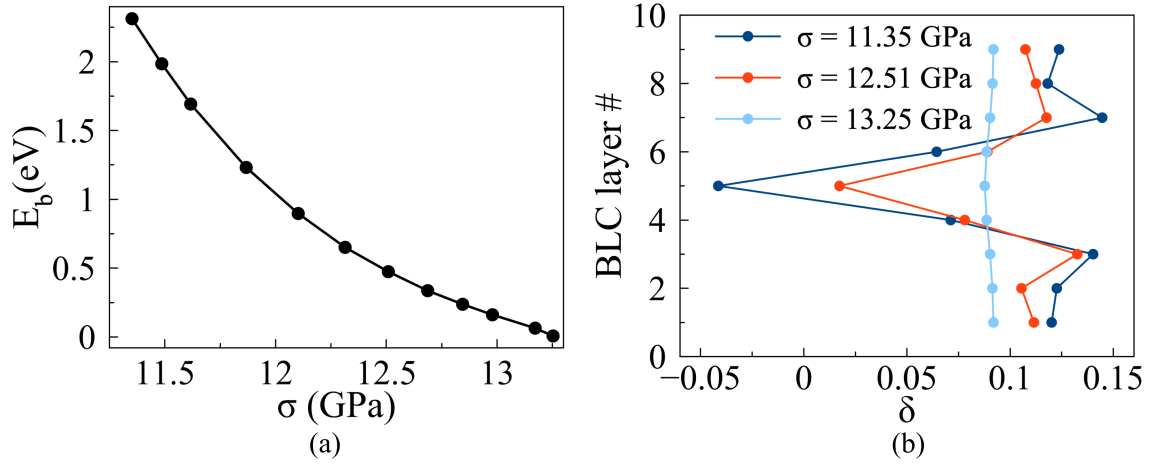


Figure 5.11: (a) Energy barrier for twin nucleation vs. applied pure shear stress for Mo-Zhou EAM potential (b) Determination of twin thickness in the saddle structures found in the free-end string simulations using the BLC analysis for 3 stresses.

5.1.1.3 Tungsten

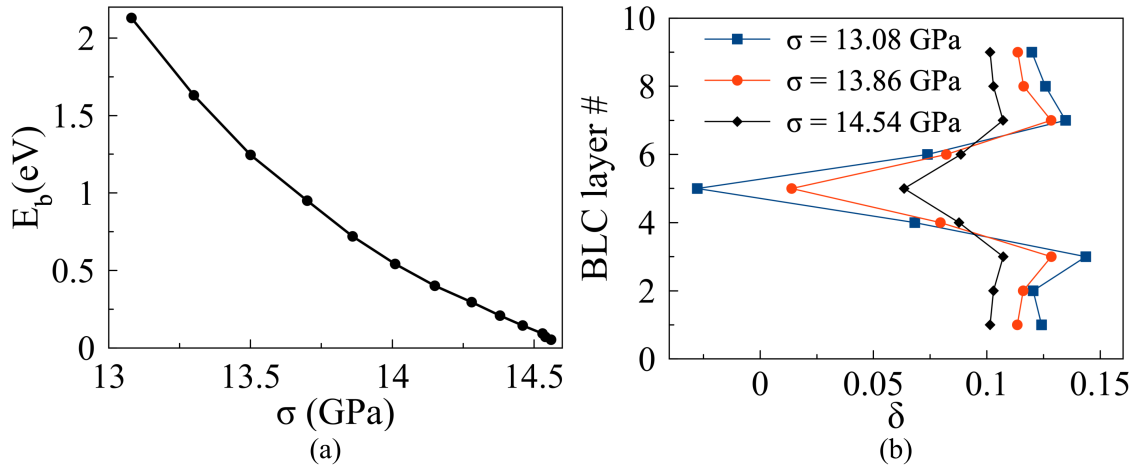


Figure 5.12: (a) Energy barrier for twin nucleation vs. applied pure shear stress in W-Zhou EAM potential (b) Determination of twin thickness in the saddle structures found in the free-end string simulations using the BLC analysis for 3 stresses.

Free-end string simulations were also performed for BCC Tungsten using the Zhou [80] EAM potential. Saddle structure analysis using the bond length comparison (BLC) method in these simulations also indicate a single layer near reflection twin structure, similar to the Mo-ATFS and Mo-Zhou. See Figure 5.12 for energy barriers as a function of applied pure shear stress and analysis of saddle structures using the BLC analysis showing 1 layer twinning faults at three different stresses. The trend of twin structure collapse is also evident as the magnitude of the pure shear stress approaches the ideal strength of the material modeled by the potential.

5.1.1.4 Iron

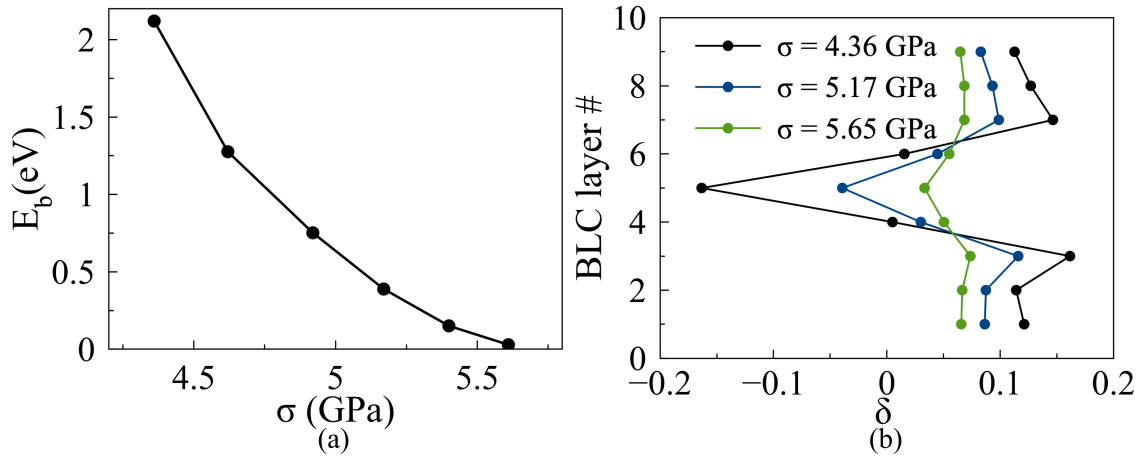


Figure 5.13: (a) Energy barrier for twin nucleation vs. applied pure shear stress for string simulations with ATFS Fe potential. (b) Determination of twin thickness in the saddle structures found in the free-end string simulations using the BLC analysis for 3 stresses.

Another set of direct twin nucleation simulation using the free-end string has been performed for Fe-ATFS potential. In this case, the twin nuclei are similar to those found in Ta-ATFS and Ta-Ravelo2 potentials as in the three layer twins with near isosceles TBs and near reflection layer sandwiched between them. This is illustrated in Figure 5.13.

In addition to the ATFS potential, we also performed similar direct nucleation study with the Chamati [123] potential for BCC Fe. The saddle point structures for this potential has the similar trend as the Fe-ATFS, Ta-ATFS and Ta-Ravelo2 potentials. Three layer thick twins with two isosceles layers and one reflection layer is shown with the BLC analysis for 3 stress levels are shown in Figure 5.14.

5.1.1.5 Summary of findings from EAM potentials

Our EAM potential survey using free-end string simulations has indicated two main types of twin nuclei in BCC transition metals studied. For Ta-ATFS, Ta-Ravelo2, Fe-ATFS, and Fe-Chamati EAM potentials, the saddle structures of the MEPs closely approximate the predicted zero stress metastable structure that consists of two isosceles TBs and a reflection layer in between

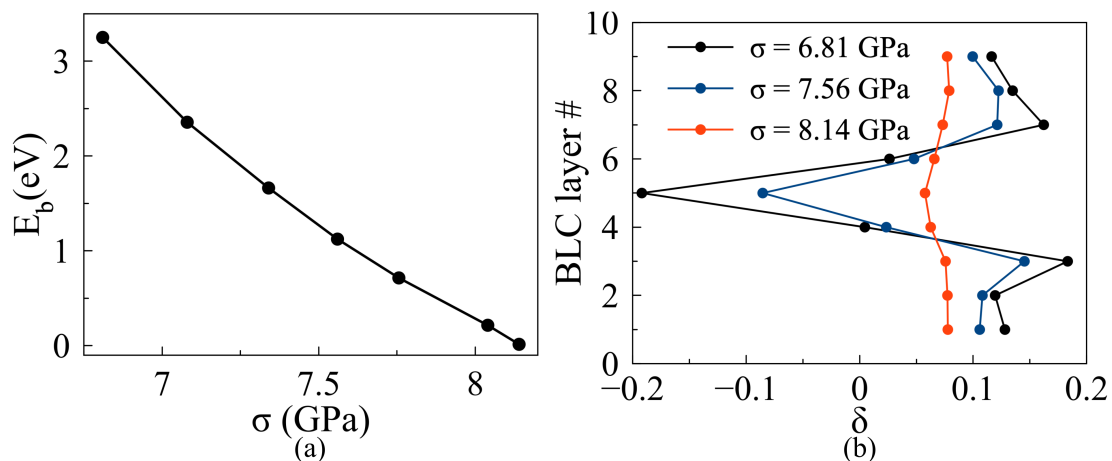


Figure 5.14: (a) Energy barrier for twin nucleation vs. applied pure shear stress for string simulations with Fe-Chamati potential. (b) Determination of twin thickness in the saddle structures found in the free-end string simulations using the BLC analysis for 3 stresses.

them. However the saddle point structures in Mo-ATFS, Mo-Zhou and W-Zhou EAM potentials are single layer near reflection faults which are different from the metastable two layer reflection twins under zero stress in group VIB BCC transition metals. Hence we will explore the critical twin nuclei thickness problem with DFT simulations starting with constrained twin stability analysis and twinning GSF curves.

5.1.2 DFT predictions of critical twin thickness in BCC transition metals

5.1.2.1 Tantalum

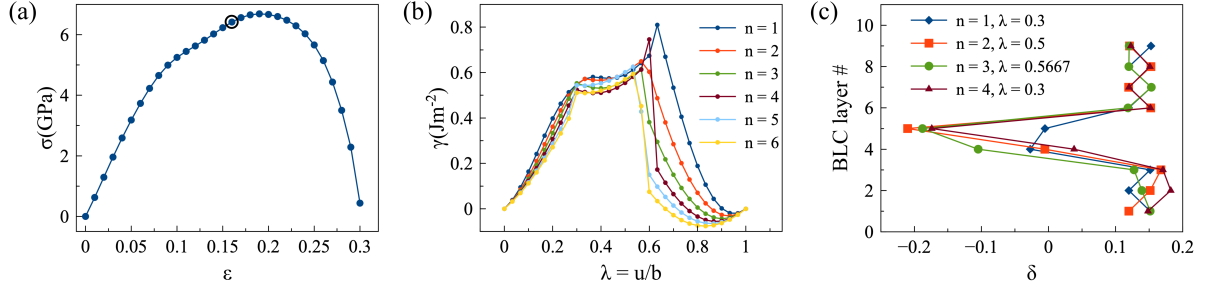


Figure 5.15: (a) The pure shear stress-strain curves in BCC Ta as computed by our DFT simulations. (b) The constrained twin stability curves for BCC Ta with DFT simulations under 6.42 GPa pure shear stress. (c) The smallest and most prevalent observed twin structure identified by our constrained GSF curves as identified by BLC analysis.

In the case of twin nucleation predictions from density functional theory, we start by investigating Ta. To understand the twinning under stresses close to nucleation, we first computed the pure shear stress-strain curves for BCC Ta using DFT simulations in the twinning sense. We expect that the twins will homogeneously nucleate near the peak of these stress-strain curves and thus we perform our constrained twin stability analysis near the peak of the stress strain curves, highlighted by the open circles in Figure 5.15(a) to detect probable metastable twin structures and then analyzed the structures using the BLC analysis outlined in Chapter 3.

The constrained GSF curves are shown in Figure 5.15(b) for Ta, at the stress indicated in Figures 5.15(a). Similar to the EAM constrained twin stability curves shown in Figures 5.3(a), with initial shearing, these curves show a linear elastic loading and with sufficient shear, the atoms are able to rearrange and form constrained equilibrium twin structures. These twin structures typically exist after the linear (elastic) portion of the curve, but before the large drop-off where dislocation nucleation is observed. In Table 5.3, BLC analysis results are summarized for all 6 curves in Figure 5.15(b). A graphical representation of the twin thickness observed at different displacement values as a function of number of relaxed atom layers is shown in Figure 5.16.

Table 5.3: BLC analysis results for constrained equilibrium structures found in the twin stability curves with DFT simulations under 6.42 GPa pure shear stress for BCC Ta shown in Figure 5.15(b) in the main text. Faulted layers are counted if the bond length difference, δ deviates from the bond length differences in strained BCC crystals by more than 10%.

Number of relaxed atom layers, n	Linear elastic interval	Single layer ($N_{\text{twin}} = 2$) interval	Two layer ($N_{\text{twin}} = 3$) interval	Dislocation nucleation interval
1	$0 \leq \lambda \leq 0.133$	$0.167 \leq \lambda \leq 0.6$	—	$0.633 \leq \lambda \leq 1.0$
2	$0 \leq \lambda \leq 0.167$	$0.2 \leq \lambda \leq 0.567$	—	$0.6 \leq \lambda \leq 1.0$
3	$0 \leq \lambda \leq 0.267$	$0.3 \leq \lambda \leq 0.567$	—	$0.6 \leq \lambda \leq 1.0$
4	$0 \leq \lambda \leq 0.267$	$0.3 \leq \lambda \leq 0.567$	—	$0.6 \leq \lambda \leq 1.0$
5	$0 \leq \lambda \leq 0.267$	$0.3 \leq \lambda \leq 0.533$	$\lambda = 0.567$	$0.6 \leq \lambda \leq 1.0$
6	$0 \leq \lambda \leq 0.027$	$0.3 \leq \lambda \leq 0.533$	$\lambda = 0.567$	$0.6 \leq \lambda \leq 1.0$

This is a surprising result in regard to the structure predicted in our constrained twin stability curves especially compared to the EAM potentials. The most prevalent twin structures in DFT constrained twin stability curves contain one BLC parameter that is reflection and one that is isosceles. Only one structure with the least constraints just before dislocation nucleation a three layer twin similar to the Ta EAM potentials is observed. This is the first ever observation that both structures might exist in the same deformation twin. However, this raises the question of which is the more favorable twin structure in Ta and if this two layer thick twin structure with both an isosceles layer and a reflection is truly metastable. We will now investigate the metastability of twin structures with GSF curves. To better answer the question of which structure is more stable, we first computed twin boundary GSF (TBGSF) curves under stress. The description of how these curves are generated in Chapter 3. We computed the TBGSF curves in Ta shown in Figure 5.17. The starting point ($\lambda = 0$) is the perfect reflection structure at zero stress and $\lambda = \frac{1}{6}$ corresponds to an isosceles structure and $\lambda = \frac{1}{3}$ corresponds again to a reflection twin. Thus, Ta prefers to form an isosceles structure at zero stress. However, it is still curious to note that in Ta the isosceles structure is favored, but the nucleus, as determined above using the constrained twin stability analysis, would appear to be two layer reflection-isosceles combination. We can presume that the two layer isosceles structure is unstable, as it is near zero stress, and that a two-layer isosceles-reflection is

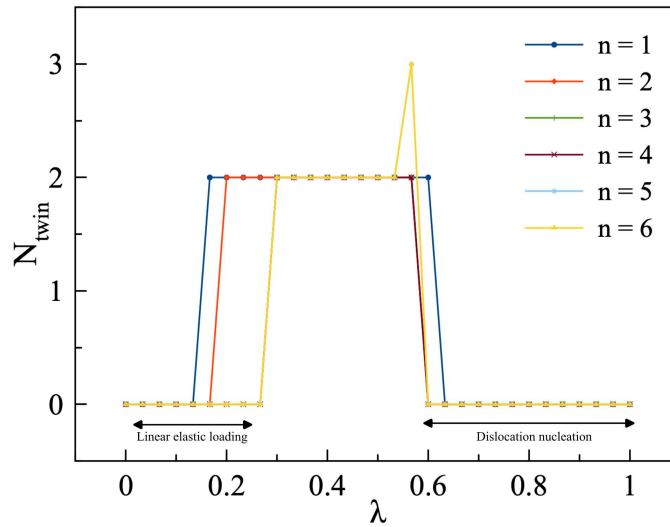


Figure 5.16: Twin thickness vs normalized displacement for the constrained twin stability curves in Figure 5.15(b)

thinner and thus requires less elastic energy than a three layer pure isosceles structure found in EAM potentials.

To confirm this idea, we then computed the sequentially twinning GSF curves (introduced in Chapter 3) for Ta under large applied stresses. The curves demonstrate that in Ta the double-isosceles structure is always unstable while the isosceles-reflection structure is unstable at zero stress but becomes stable under an applied stress of 6.42GPa, Figure 5.18. Figure 5.18 shows the sequential GSF curve in Ta for the formation of a isosceles-reflection two layer structure under both zero stress and an applied stress. These curves are able to completely explain our observed results in Ta. Under zero stress, Figure 5.18, a single layer isosceles (at the cusp), a two layer isosceles, and a two layer reflection-isosceles are all unstable. Stability is only achieved when a three layer isosceles structure forms as shown in [65]. However, under significant applied stress, we see a change in that the two layer isosceles structure becomes a local maximum and the isosceles-reflection exhibits a local minimum at $\lambda = 0.433$, indicating metastability. In fact, this stabilization occurs with modest amounts of stress, as low as 4.23 GPa (see Figure 5.19), while our analysis shown here is for much larger stresses, 6.42 GPa.

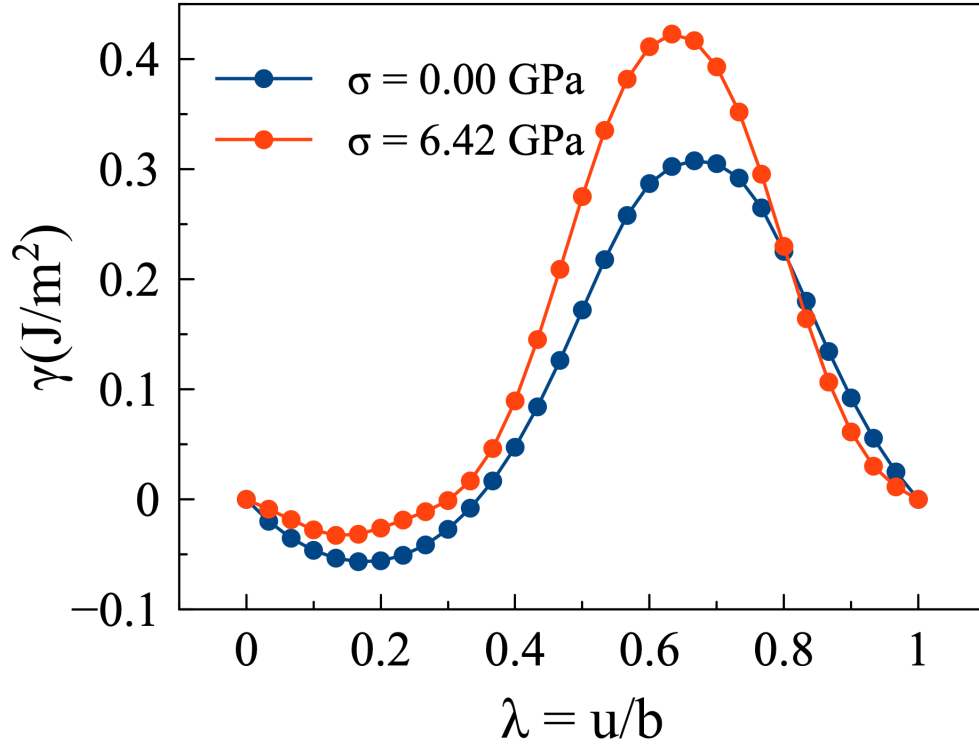


Figure 5.17: The TBGSF curves for BCC Ta. Minimums near $\lambda = \frac{1}{6}$ indicates a preference for an isosceles twin boundary

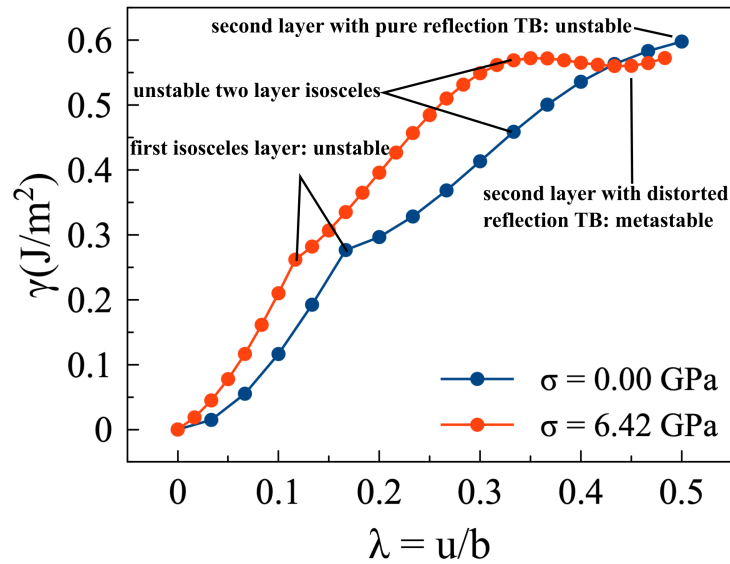


Figure 5.18: The sequential twinning GSF curves for BCC Ta using DFT simulations demonstrating that in Ta the double-isosceles structure is always unstable while the isosceles-reflection structure is unstable at zero stress but becomes stable under an applied stress of 6.42 GPa.

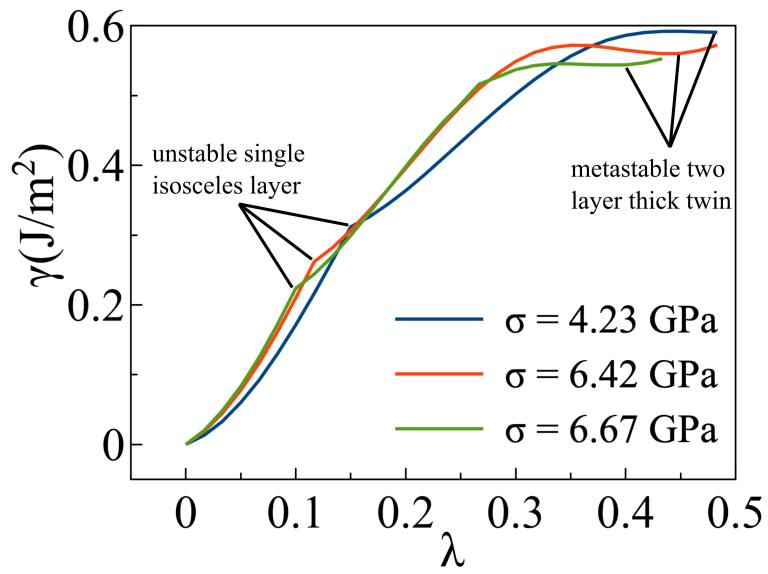


Figure 5.19: The sequential twinning GSF curves for BCC Ta using DFT simulations under three large pure shear stresses.

5.1.2.2 Molybdenum

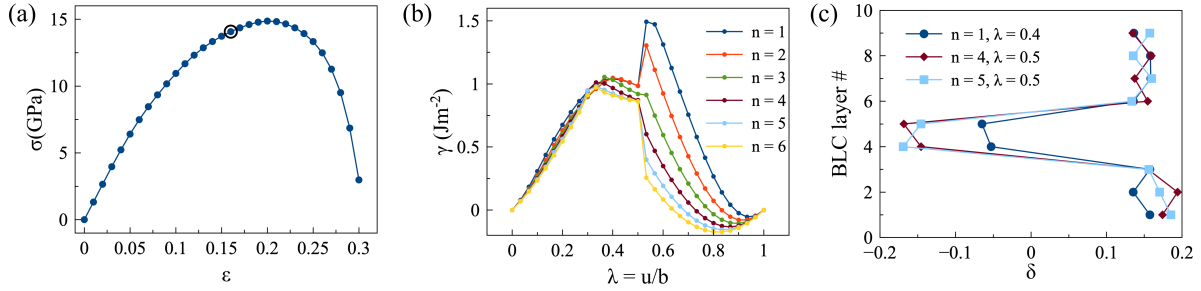


Figure 5.20: (a) The pure shear stress-strain curves in BCC Ta as computed by our DFT simulations. (b) The constrained twin stability curves for BCC Ta with DFT simulations under 6.42 GPa pure shear stress. (c) The smallest and most prevalent observed twin structure identified by our constrained GSF curves as identified by BLC analysis.

The next case of twin nucleation predictions from density functional theory is BCC Mo. We start by computing the pure shear stress-strain curves for BCC Ta using DFT simulations in the twinning sense. As before, we expect that the twins will homogeneously nucleate near the peak of these stress-strain curves and thus we perform our constrained twin stability analysis near the peak of the stress-strain curves, highlighted by the open circles in Figure 5.20(a) to detect probable metastable twin structures and then analyzed the structures using the BLC analysis outlined in Chapter 3.

Table 5.4: BLC analysis results for constrained equilibrium structures found in the twin stability curves with DFT simulations under 14.07 GPa pure shear stress for BCC Mo shown in Figure 5.20(b). Faulted layers are counted if the bond length difference, δ deviates from the bond length differences in strained BCC crystals by more than 10%.

Number of relaxed atom layers, n	Linear elastic interval	Single layer ($N_{\text{twin}} = 1$) interval	Two layer ($N_{\text{twin}} = 2$) interval	Dislocation nucleation interval
1	$0 \leq \lambda \leq 0.167$	$0.2 \leq \lambda \leq 0.267$	$0.3 \leq \lambda \leq 0.5$	$0.533 \leq \lambda \leq 1.0$
2	$0 \leq \lambda \leq 0.2$	$0.233 \leq \lambda \leq 0.367$	$0.4 \leq \lambda \leq 0.5$	$0.533 \leq \lambda \leq 1.0$
3	$0 \leq \lambda \leq 0.233$	$0.267 \leq \lambda \leq 0.333$	$0.367 \leq \lambda \leq 0.5$	$0.533 \leq \lambda \leq 1.0$
4	$0 \leq \lambda \leq 0.233$	$0.267 \leq \lambda \leq 0.3$	$0.333 \leq \lambda \leq 0.5$	$0.533 \leq \lambda \leq 1.0$
5	$0 \leq \lambda \leq 0.267$	—	$0.3 \leq \lambda \leq 0.5$	$0.533 \leq \lambda \leq 1.0$
6	$0 \leq \lambda \leq 0.267$	$0.3 \leq \lambda \leq 0.333$	$0.367 \leq \lambda \leq 0.567$	$0.6 \leq \lambda \leq 1.0$

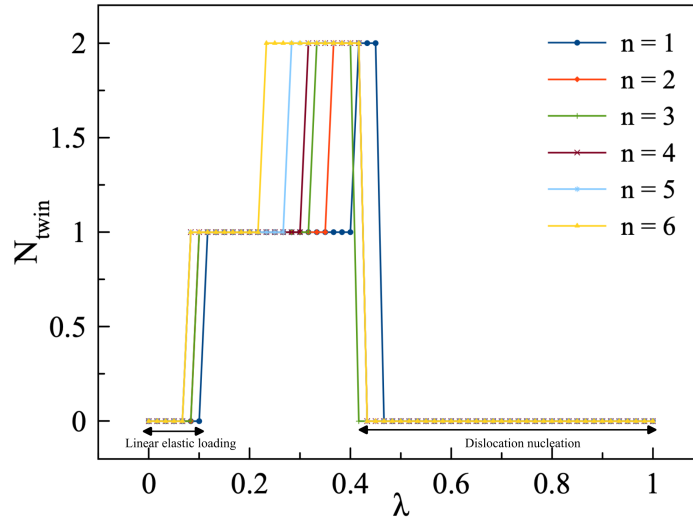


Figure 5.21: Twin thickness vs normalized displacement for the constrained twin stability curves in Figure 5.20(b)

The constrained GSF curves are shown in Figure 5.20(b) for Mo, at the stress indicated in Figures 5.20(a). Similar to the EAM constrained twin stability curves shown in Figures 5.9(a), with initial shearing, these curves show a linear elastic loading and with sufficient shear, the atoms are able to rearrange and form constrained equilibrium twin structures. These twin structures typically exist after the linear (elastic) portion of the curve, but before the large drop-off where dislocation nucleation is observed. In Table 5.4, BLC analysis results are summarized for all 6

curves in Figure 5.20(b). A graphical representation of the twin thickness observed at different displacement values as a function of number of relaxed atom layers is shown in Figure 5.21.

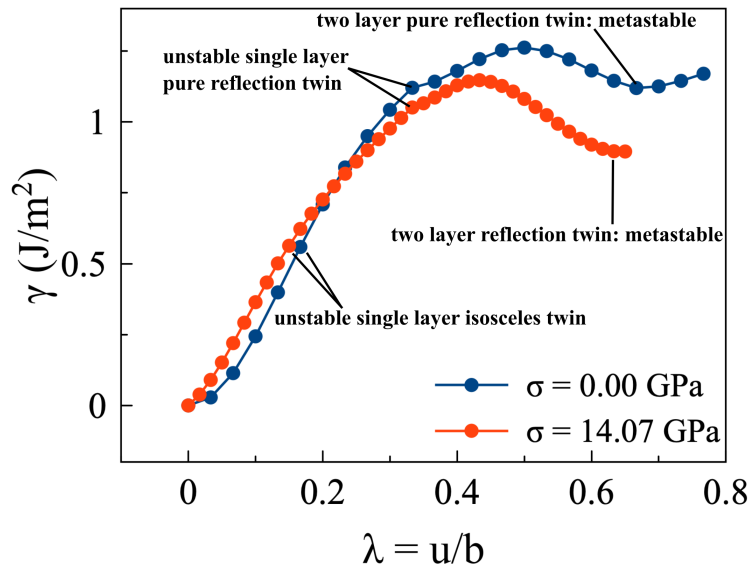


Figure 5.22: The sequential twinning GSF curves for BCC Mo using DFT simulations under 14.07GPa.

The case of Molybdenum is much more straightforward, as shown in Figure 5.22. The isosceles structures are always unstable, even though we have seen a few instances of this twin boundary structure in our constrained stability analysis, as the formation of the reflection structures always pass through an isosceles structure. This indicates the one-layer isosceles structure observed are minor artifacts of the applied constraints. Furthermore, a single layer reflection is unstable, as labeled on the curves. The only metastable structure that emerges is the double reflection structure which is the most prevalent structure in the constrained stability analysis (Table 5.4). Since this structure appears metastable and has the lowest thickness, it is clear this is the nucleus in BCC Mo. Additionally, the two layer isosceles-reflection twin, similar to the metastable twin obtained for Ta in Figure 5.18, is unstable.

The discussions above on BCC Ta and Mo have established a set of consistent and robust steps to build a method of determining critical twin nuclei size and structure. Not only this method

is easily adoptable to other BCC transition metals such as Nb, V, Cr, W and Fe, nucleation of extended defects in any crystalline material can be thoroughly examined. To recap, the steps are:

- Generate constrained twin stability curves (CTSC) with varying degrees of freedom to identify possible metastable structures.
- Generate sequential twinning GSF curves for the thinnest and/or most prevalent twin structures obtained from CTS curves.
- Verify that the metastable structure and the thinnest and/or most prevalent twin structures obtained from CTS curves are the same (within reasonable tolerance) using the BLC analysis.

5.1.2.3 Niobium

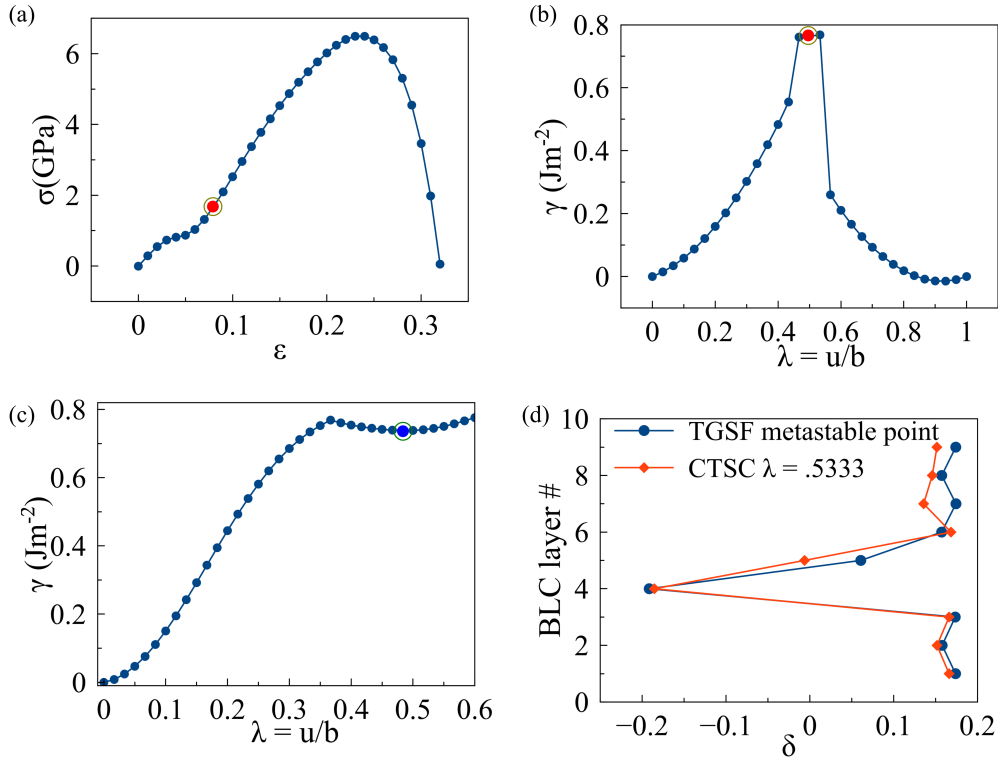


Figure 5.23: (a) Stress-strain curve in BCC Nb with DFT. 1.69 GPa stress is selected (highlighted by red circle) to probe twin nucleation. (b) Constrained twin stability curves (CTSC) with $n = 6$ atom layers allowed to relax at each incremental displacement $u = \lambda b$. (c) Sequential twinning GSF curve under 1.69 GPa; the metastable point is highlighted. (d) BLC analysis to show that the metastable point in the TGSF curve is a two layer isosceles-reflection twin whereas the structure at the red circle of (b) also closely approximate the metastable structure.

Unsurprisingly, Niobium which is a group VB BCC transition metal has the same critical twin nuclei as BCC Ta which also belongs to group VB. To demonstrate this, we have performed our analysis for three different stress levels. For 1.69 GPa, we first generated the CTS curve by allowing 6 atom layers to relax freely. In this curve (Figure 5.23(b)), the only twin structures found are two layer isosceles-reflection twin. This structure was reproduced at the metastable point denoted by the highlighted blue circle in Figure 5.23(c). The BLC analysis (Figure 5.23(d)) confirms that the highlighted points in curves in Figures 5.23(b) and (c).

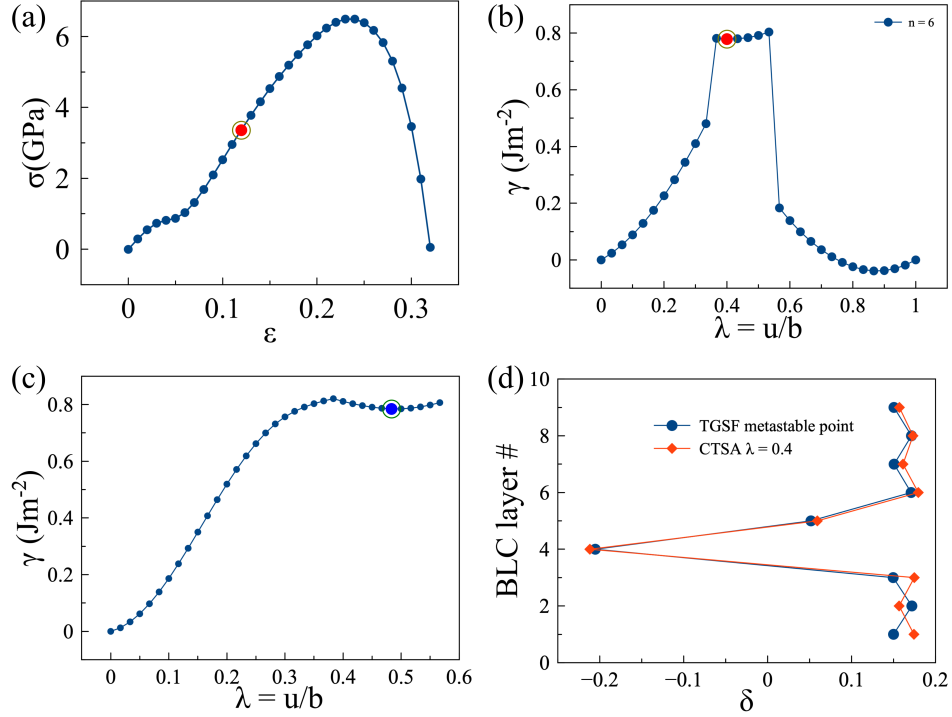


Figure 5.24: (a) Stress-strain curve in BCC Nb with DFT. 3.37 GPa stress is selected (highlighted by red circle) to probe twin nucleation. (b) Constrained twin stability curves (CTSC) with $n = 6$ atom layers allowed to relax at each incremental displacement $u = \lambda b$. (c) Sequential twinning GSF curve under 3.37 GPa; the metastable point is highlighted. (d) BLC analysis to show that the metastable point in the TGSF curve is a two layer isosceles-reflection twin whereas the structure at the red circle of (b) also closely approximate the metastable structure.

Two layer isosceles-reflection twins are also found to be the thinnest metastable twin structures for 3.37 GPa pure shear stress. In the CTS curves Figure 5.24(b), more twinned structures are obtained compared to 1.69 GPa CTS curve (Figure ??)(b). Here we analyze the structure at $\lambda = 0.4$ in Figure 5.24 with BLC analysis and compare the results with the structure corresponding to the metastable point in the TGSF curve Figure 5.24(c). BLC analysis results shown in Figure 5.24(d) conclusively points to similar two layer isosceles-reflection twin nuclei structures in BCC Ta.

Two layer isosceles-reflection twins similarly have been found to be the thinnest metastable twin structures for 6.02 GPa (near ideal strength) pure shear stress. To come to this conclusion, we analyze the structure at $\lambda = 0.3$ in Figure 5.25 with BLC analysis and compare the results with the structure corresponding to the metastable point in the TGSF curve Figure 5.25(c). BLC analysis

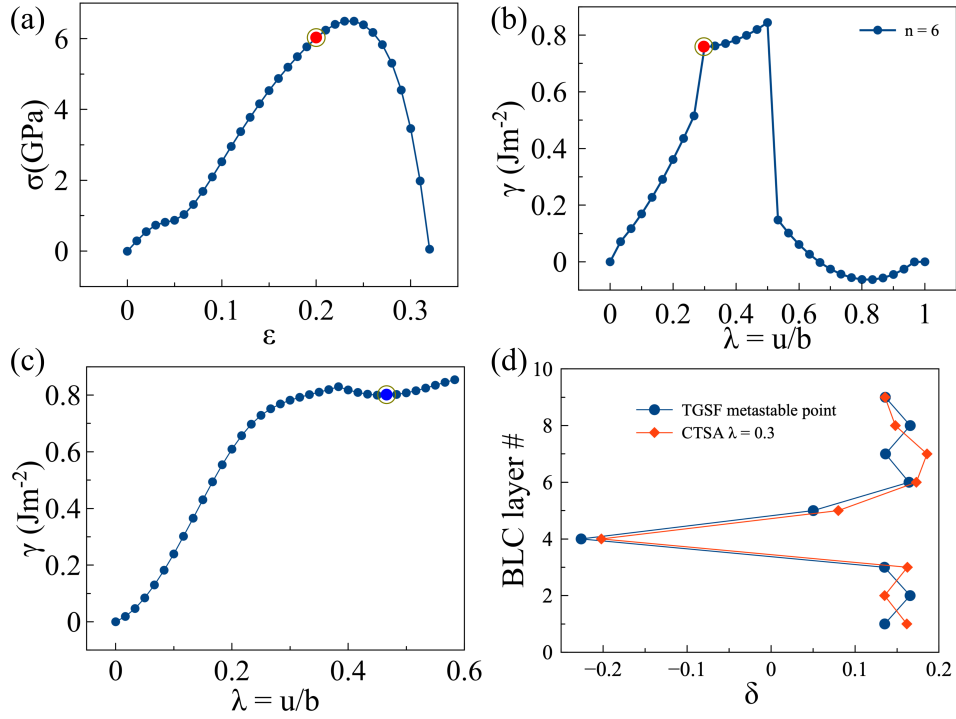


Figure 5.25: (a) Stress-strain curve in BCC Nb with DFT. 6.02 GPa stress is selected (highlighted by red circle) to probe twin nucleation. (b) Constrained twin stability curves (CTSC) with $n = 6$ atom layers allowed to relax at each incremental displacement $u = \lambda b$. (c) Sequential twinning GSF curve under 6.02 GPa; the metastable point is highlighted. (d) BLC analysis to show that the metastable point in the TGSF curve is a two layer isosceles-reflection twin whereas the structure at the red circle of (b) also closely approximate the metastable structure.

results shown in Figure 5.25(d) conclusively points to similar two layer isosceles-reflection twin nuclei structures in BCC Ta.

5.1.2.4 Vanadium

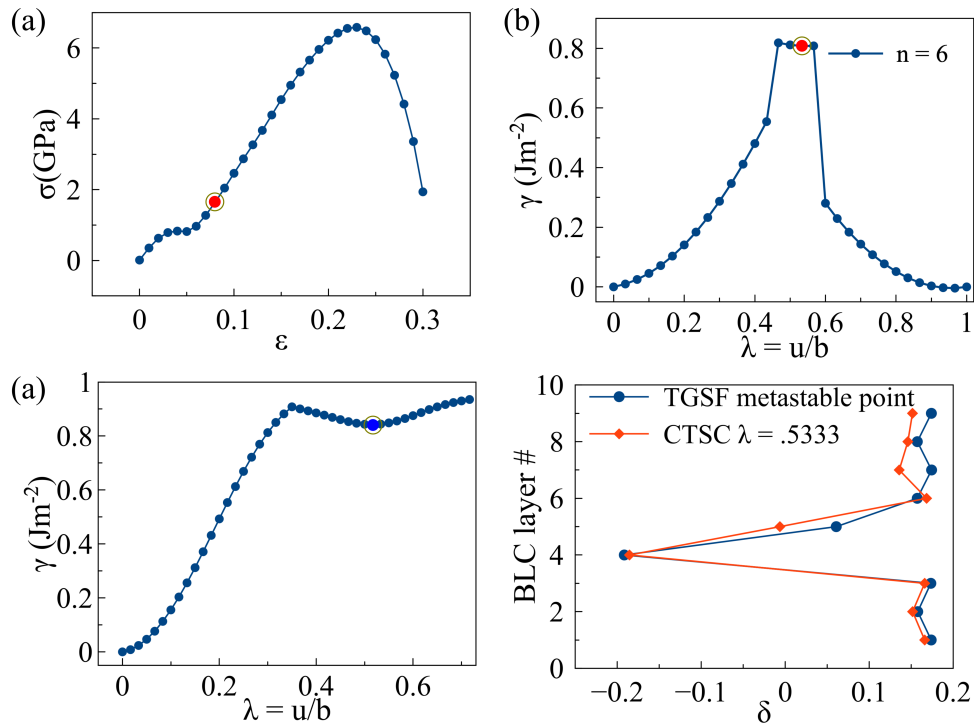


Figure 5.26: (a) Stress-strain curve in BCC V with DFT. 1.64 GPa stress is selected (highlighted by red circle) to probe twin nucleation. (b) Constrained twin stability curves (CTSC) with $n = 6$ atom layers allowed to relax at each incremental displacement $u = \lambda b$. (c) Sequential twinning GSF curve under 1.64 GPa; the metastable point is highlighted. (d) BLC analysis to show that the metastable point in the TGSF curve is a two layer isosceles-reflection twin whereas the structure at the red circle of (b) also closely approximate the metastable structure.

Vanadium, also a group VB BCC transition metal, also exhibits the same critical twin nuclei as BCC Ta and Nb. This is demonstrated by our analysis for three different stress levels. For 1.64 GPa, we first generated the CTS curve by allowing 6 atom layers to relax freely. In this curve (Figure 5.26(b)), the only twin structures found are two layer isosceles-reflection twin. This structure was reproduced at the metastable point denoted by the highlighted blue circle in Figure 5.26(c). The BLC analysis (Figure 5.26(d)) confirms that the highlighted points in curves in Figures 5.26(b) and (c).

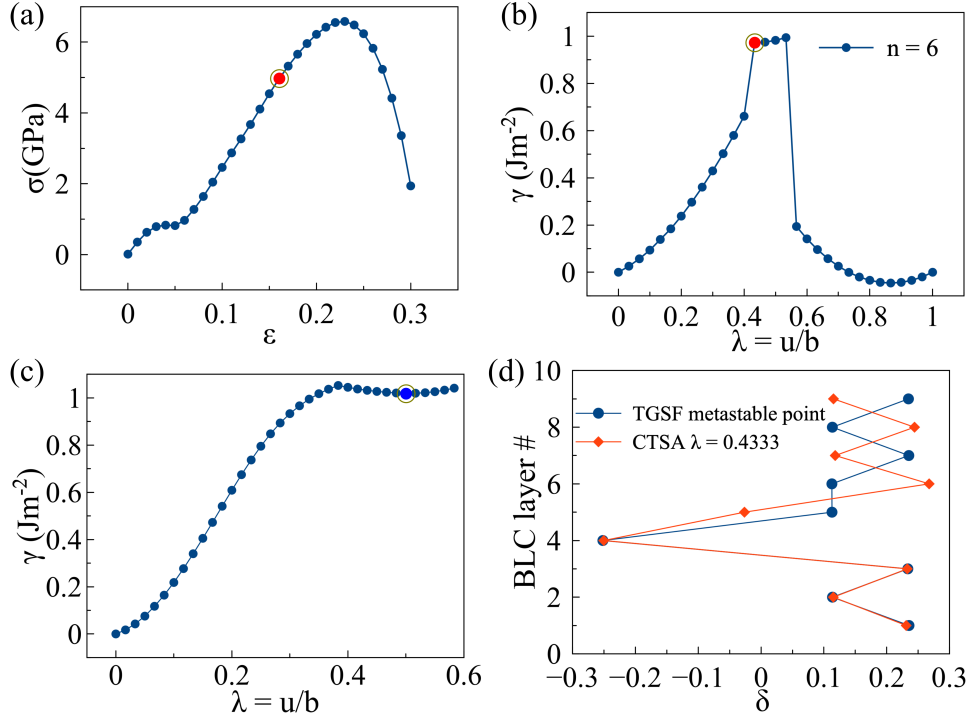


Figure 5.27: (a) Stress-strain curve in BCC V with DFT. 4.95 GPa stress is selected (highlighted by red circle) to probe twin nucleation. (b) Constrained twin stability curves (CTSC) with $n = 6$ atom layers allowed to relax at each incremental displacement $u = \lambda b$. (c) Sequential twinning GSF curve under 4.95 GPa; the metastable point is highlighted. (d) BLC analysis to show that the metastable point in the TGSF curve is a two layer isosceles-reflection twin whereas the structure at the red circle of (b) also closely approximate the metastable structure.

Two layer isosceles-reflection twins are also found to be the thinnest metastable twin structures for 4.95 GPa pure shear stress. To come to this conclusion, we analyze the structure at $\lambda = 0.433$ in Figure 5.27 with BLC analysis and compare the results with the structure corresponding to the metastable point in the TGSF curve Figure 5.27(c). BLC analysis results shown in Figure 5.27(d) conclusively points to similar two layer isosceles-reflection twin nuclei structures in BCC Ta and Nb.

Two layer isosceles-reflection twins similarly have been found to be the thinnest metastable twin structures for 5.96 GPa (near ideal strength) pure shear stress. To come to this conclusion, we analyze the structure at $\lambda = 0.433$ in Figure 5.28 with BLC analysis and compare the results with the structure corresponding to the metastable point in the TGSF curve Figure 5.28(c). BLC analysis

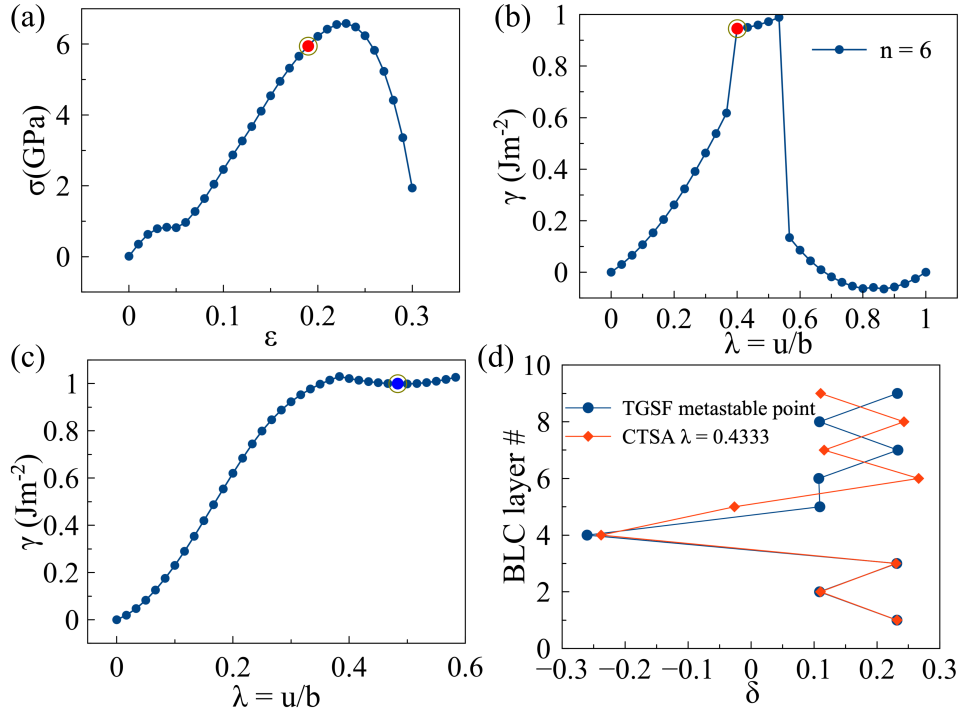


Figure 5.28: (a) Stress-strain curve in BCC V with DFT. 5.96 GPa stress is selected (highlighted by red circle) to probe twin nucleation. (b) Constrained twin stability curves (CTSC) with $n = 6$ atom layers allowed to relax at each incremental displacement $u = \lambda b$. (c) Sequential twinning GSF curve under 6.02 GPa; the metastable point is highlighted. (d) BLC analysis to show that the metastable point in the TGSF curve is a two layer isosceles-reflection twin whereas the structure at the red circle of (b) also closely approximate the metastable structure.

results shown in Figure 5.28(d) conclusively points to similar two layer isosceles-reflection twin nuclei structures in BCC Ta and Nb.

5.1.2.5 Tungsten

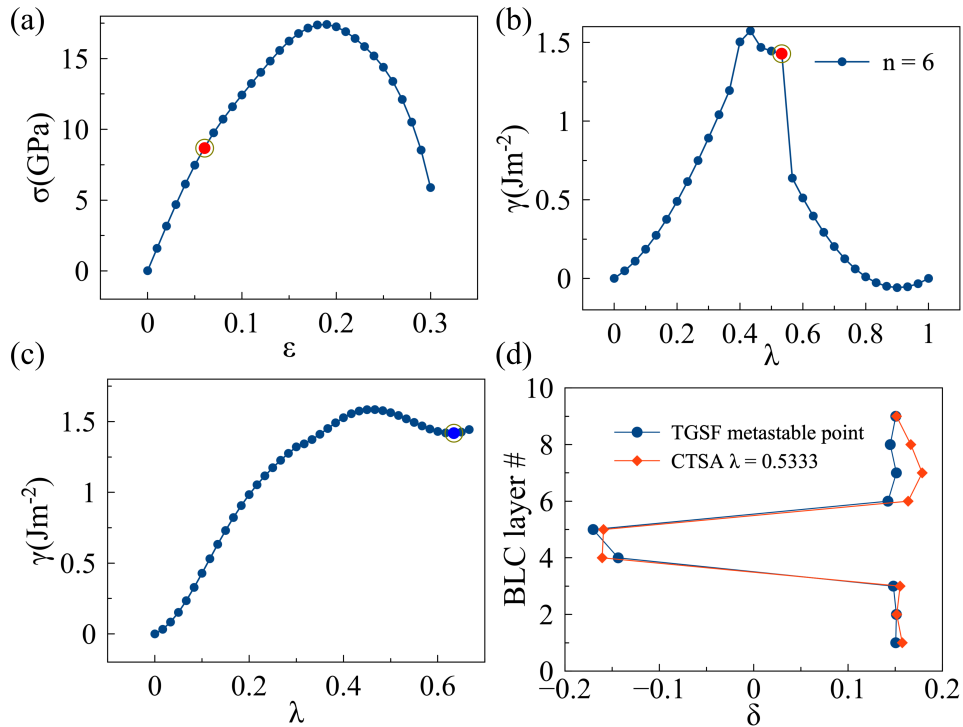


Figure 5.29: (a) Stress-strain curve in BCC W with DFT. 9.76 GPa stress is selected (highlighted by red circle) to probe twin nucleation. (b) Constrained twin stability curves (CTSC) with $n = 6$ atom layers allowed to relax at each incremental displacement $u = \lambda b$. (c) Sequential twinning GSF curve under 9.76 GPa; the metastable point is highlighted. (d) BLC analysis to show that the metastable point in the TGSF curve is a two layer reflection twin whereas the structure at the red circle of (b) also closely approximate the metastable structure.

Tungsten, a group VIB BCC transition metal like Molybdenum, also exhibits the same critical twin nuclei as BCC Mo. This is demonstrated by our analysis for three different stress levels. For 9.76 GPa, we first generated the CTS curve by allowing 6 atom layers to relax freely. In this curve (Figure 5.29(b)), the only twin structures found are two layer reflection twin. This structure was reproduced at the metastable point denoted by the highlighted blue circle in Figure 5.29(c). The BLC analysis (Figure 5.29(d)) confirms that the highlighted points in curves in Figures 5.29(b) and (c).

Two layer reflection twins are also found to be the thinnest metastable twin structures for 12.43 GPa pure shear stress. To come to this conclusion, we analyze the structure at $\lambda = 0.433$ in Figure

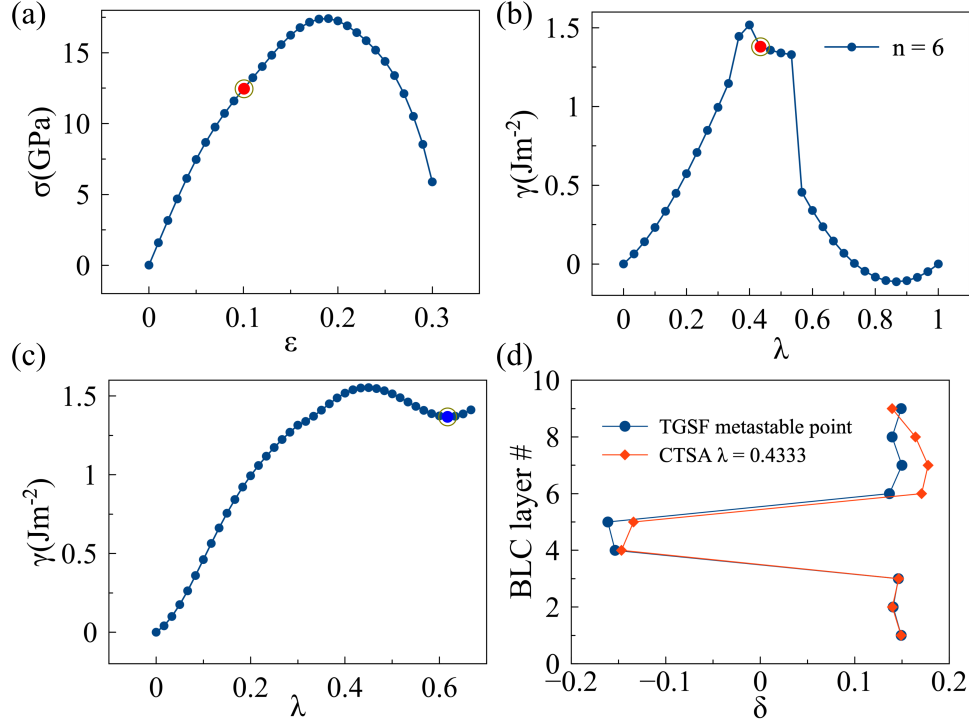


Figure 5.30: (a) Stress-strain curve in BCC W with DFT. 12.43 GPa stress is selected (highlighted by red circle) to probe twin nucleation. (b) Constrained twin stability curves (CTSC) with $n = 6$ atom layers allowed to relax at each incremental displacement $u = \lambda b$. (c) Sequential twinning GSF curve under 12.43 GPa; the metastable point is highlighted. (d) BLC analysis to show that the metastable point in the TGSF curve is a two layer reflection twin whereas the structure at the red circle of (b) also closely approximate the metastable structure.

5.30 with BLC analysis and compare the results with the structure corresponding to the metastable point in the TGSF curve Figure 5.30(c). BLC analysis results shown in Figure 5.30(d) conclusively points to similar two layer reflection twin nuclei structures in BCC Mo.

Two layer reflection twins similarly have been found to be the thinnest metastable twin structures for 17.38 GPa (near ideal strength) pure shear stress. To come to this conclusion, we analyze the structure at $\lambda = 0.433$ in Figure 5.31 with BLC analysis and compare the results with the structure corresponding to the metastable point in the TGSF curve Figure 5.31(c). BLC analysis results shown in Figure 5.31(d) conclusively points to similar two layer reflection twin nuclei structures in BCC Mo.

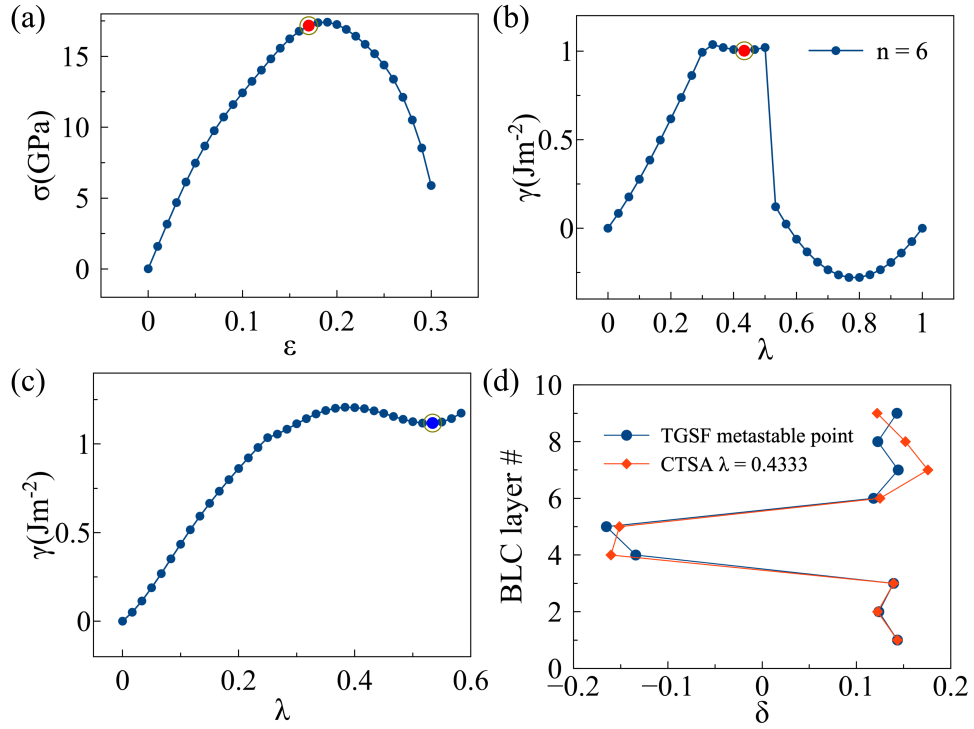


Figure 5.31: (a) Stress-strain curve in BCC W with DFT. 17.38 GPa stress is selected (highlighted by red circle) to probe twin nucleation. (b) Constrained twin stability curves (CTSC) with $n = 6$ atom layers allowed to relax at each incremental displacement $u = \lambda b$. (c) Sequential twinning GSF curve under 17.38 GPa; the metastable point is highlighted. (d) BLC analysis to show that the metastable point in the TGSF curve is a two layer reflection twin whereas the structure at the red circle of (b) also closely approximate the metastable structure.

5.1.2.6 Chromium

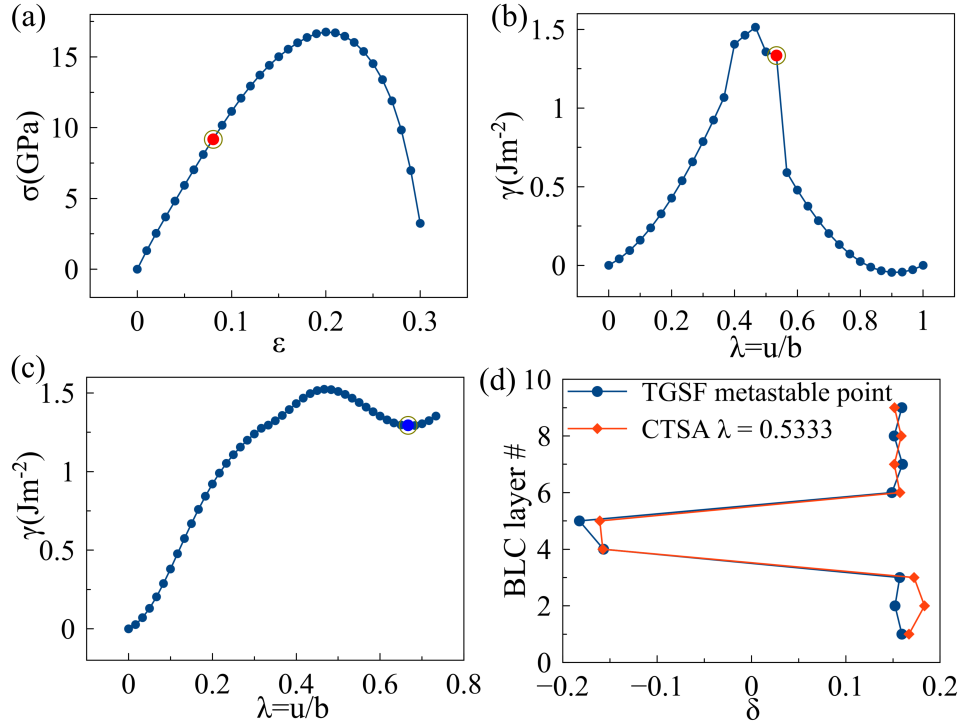


Figure 5.32: (a) Stress-strain curve in BCC Cr with DFT. 9.15 GPa stress is selected (highlighted by red circle) to probe twin nucleation. (b) Constrained twin stability curves (CTSC) with $n = 6$ atom layers allowed to relax at each incremental displacement $u = \lambda b$. (c) Sequential twinning GSF curve under 9.15 GPa; the metastable point is highlighted. (d) BLC analysis to show that the metastable point in the TGSF curve is a two layer reflection twin whereas the structure at the red circle of (b) also closely approximate the metastable structure.

Chromium, also a group VIB BCC transition metal like Mo and W, also exhibits the same critical twin nuclei as BCC Mo and W. This is demonstrated by our analysis for three different stress levels. For 9.15 GPa, we first generated the CTS curve by allowing 6 atom layers to relax freely. In this curve (Figure 5.32(b)), the only twin structures found are two layer reflection twin. This structure was reproduced at the metastable point denoted by the highlighted blue circle in Figure 5.32(c). The BLC analysis (Figure 5.32(d)) confirms that the highlighted points in curves in Figures 5.32(b) and (c).

Two layer reflection twins are also found to be the thinnest metastable twin structures for 12.94 GPa pure shear stress. To come to this conclusion, we analyze the structure at $\lambda = 0.533$ in Figure

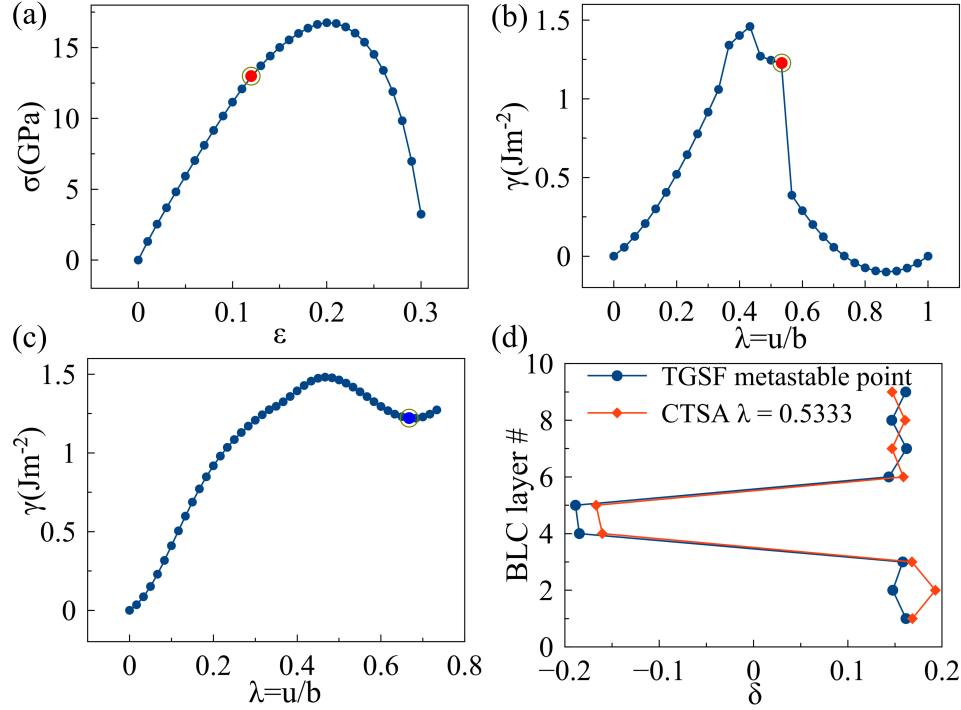


Figure 5.33: (a) Stress-strain curve in BCC Cr with DFT. 12.94 GPa stress is selected (highlighted by red circle) to probe twin nucleation. (b) Constrained twin stability curves (CTSC) with $n = 6$ atom layers allowed to relax at each incremental displacement $u = \lambda b$. (c) Sequential twinning GSF curve under 12.94 GPa; the metastable point is highlighted. (d) BLC analysis to show that the metastable point in the TGSF curve is a two layer reflection twin whereas the structure at the red circle of (b) also closely approximate the metastable structure.

5.33 with BLC analysis and compare the results with the structure corresponding to the metastable point in the TGSF curve Figure 5.33(c). BLC analysis results shown in Figure 5.33(d) conclusively points to similar two layer reflection twin nuclei structures in BCC Mo and W.

Two layer reflection twins similarly have been found to be the thinnest metastable twin structures for 16.37 GPa (near ideal strength) pure shear stress. To come to this conclusion, we analyze the structure at $\lambda = 0.533$ in Figure 5.34 with BLC analysis and compare the results with the structure corresponding to the metastable point in the TGSF curve Figure 5.34(c). BLC analysis results shown in Figure 5.34(d) conclusively points to similar two layer reflection twin nuclei structures in BCC Mo and W.

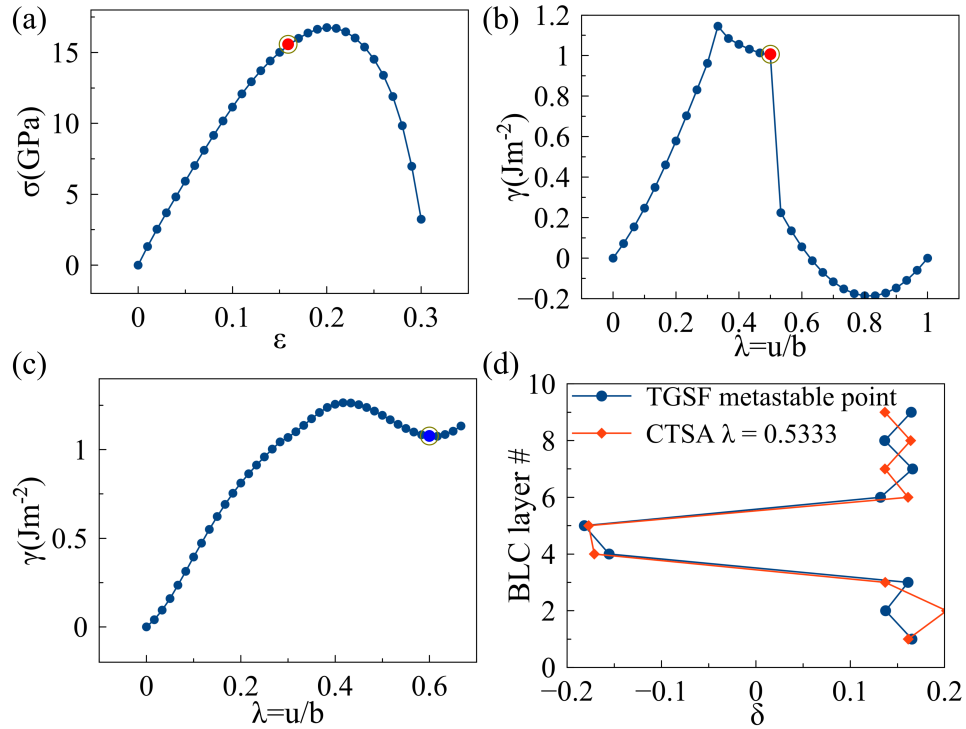


Figure 5.34: (a) Stress-strain curve in BCC Cr with DFT. 16.37 GPa stress is selected (highlighted by red circle) to probe twin nucleation. (b) Constrained twin stability curves (CTSC) with $n = 6$ atom layers allowed to relax at each incremental displacement $u = \lambda b$. (c) Sequential twinning GSF curve under 16.37 GPa; the metastable point is highlighted. (d) BLC analysis to show that the metastable point in the TGSF curve is a two layer reflection twin whereas the structure at the red circle of (b) also closely approximate the metastable structure.

5.1.2.7 Iron

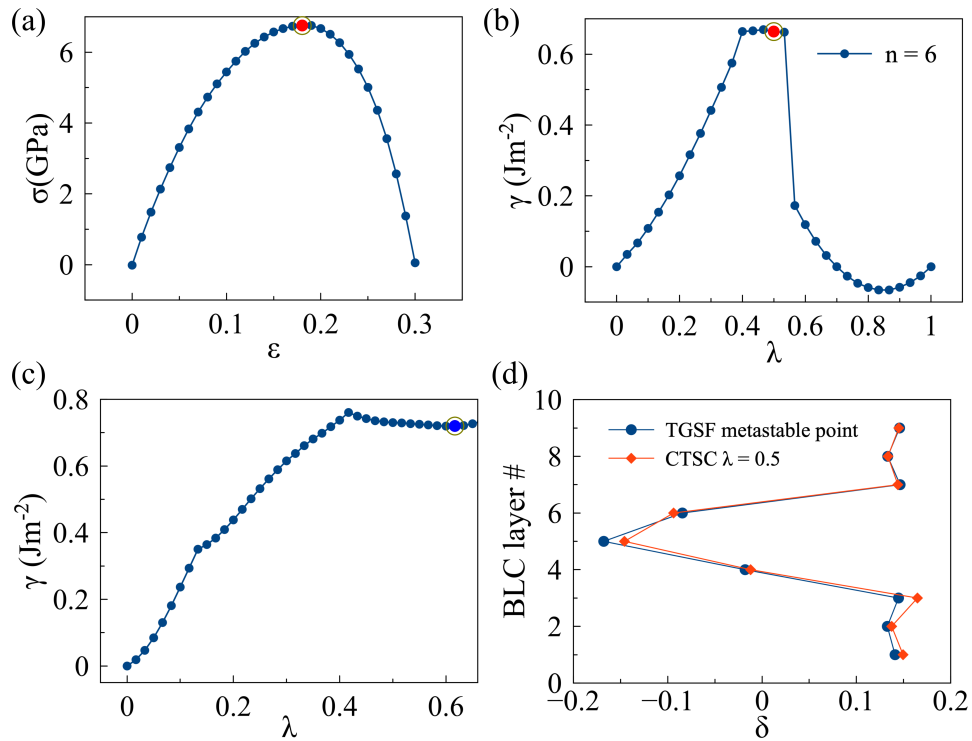


Figure 5.35: (a) Stress-strain curve in BCC Fe with DFT. 6.77 GPa stress is selected (highlighted by red circle) to probe twin nucleation. (b) Constrained twin stability curves (CTSC) with $n = 6$ atom layers allowed to relax at each incremental displacement $u = \lambda b$. (c) Sequential twinning GSF curve under 6.77 GPa; the metastable point is highlighted. (d) BLC analysis to show that the metastable point in the TGSF curve is a two layer reflection twin whereas the structure at the red circle of (b) also closely approximate the metastable structure.

Iron, the final BCC transition metal we analyzed for critical twin nucleus using DFT simulations, exhibits a three layer thick twin to be the thinnest metastable twin unlike Ta, Nb, V, Mo, W, and Cr. This twin is somewhat similar to the three layer twins found with EAM potentials however one of the TB layer is more scalene i.e., the BLC parameter $-0.155 \leq \delta \leq 0.0$, than isosceles. This is shown in Figure 5.35 where a stress value of 6.77 GPa is selected near ideal strength. The constrained twin stability curve (Figure 5.35(b)), generated by allowing 6 atom layer relaxation, shows three layer twin with one isosceles layer and two near reflection layers to be metastable around $\lambda = 0.5$. Other twin structures found from the CTS curve also exhibit similar three layer

twin structures. Based on this twin structure, the sequential TGSF curve in Figure 5.35(c) is created and the structure in this curve also matches the three layer twins in the CTS curve. This is shown with the BLC analysis results in Figure 5.35. Of all 7 BCC transition metal analyzed here, Iron exhibits the thickest metastable twin structure.

5.1.3 Conclusion

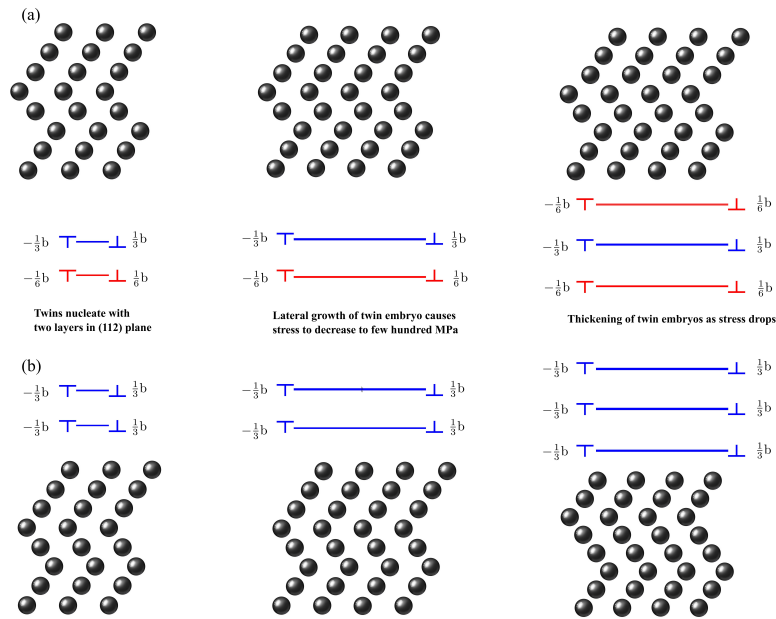


Figure 5.36: Graphical description of twin formation in (a) group VB and (b) group VIB BCC transition metals. First, two layer thick twin embryos nucleate under the appropriate applied stresses as twinning dislocations. Isosceles type twinning dislocations for group VB are shown as red dislocation pairs and are denoted as $\pm\frac{1}{6}b$ while reflection type twinning dislocations for both groups are shown as blue dislocation pairs and are denoted as $\pm\frac{1}{3}b$. Then these nascent twins grow laterally on $\{112\}$ planes while causing stress levels to drop. Finally, at smaller stresses twin embryos grow vertically to become three layers twins. The magnitude of the Burgers vector can deviate by small amounts depending on the stress applied.

Our analysis on group VB and VIB metals means that under applied stresses required to nucleate twins, the twins would nucleate as a two-layer structure with an isosceles-reflection structure in Ta, Nb, and V whereas they would nucleate as two layer reflection structures in Mo, W and Cr. As the twins grow, the stress would drop and the reflection structure in group VB BCC transition metals would become less stable and the twin should very quickly evolve to a three layer isosceles structure and maintain that structure under growth stresses, which are a few hundred MPa. This idea is shown in Figure 5.36. In the case of group VIB BCC transition metals, the twin would nucleate as a two layer near reflection structure and would grow simply by thickening this structure even as the stress drops.

In this section, we have demonstrated that deformation twins in BCC crystals nucleate in a manner that is consistent with dislocations. They have an energy barrier that is very sensitive to stress and decays towards the ideal strength. Thus, it stands to reason that these defects nucleate by thermal activation in the same manner and compete with dislocations from a nucleation perspective, which is consistent with the observations of twinning and slip in tungsten nanocrystals [27, 67]. Furthermore, we have demonstrated that these nuclei can be more than one atomic layer thick, clearly demonstrating that it is possible to nucleate extended defects in a manner consistent with dislocation nucleation.

We have also shown that the thickness of the twins that nucleate depends on the method of describing the atomic interactions. Predictions using specific EAM potentials show a three layer twin thickness with isosceles boundaries in Ta using Ravelo2, ATFS and Zhou potentials, in Fe using ATFS and Chamati potentials and a single reflection layer using the ATFS and Zhou potential for Mo as well as Zhou potential for W. However, our DFT simulations show a two layer isosceles-reflection structure in Ta, Nb and V whereas a two layer reflection structure in Mo, W and Cr are the minimum stable thicknesses. For α -Fe, the twin nuclei is three layer thick with one isosceles TBs and two near reflection layers. Since DFT is more accurate description of the interatomic forces, we can conclude the DFT results are most likely to represent actual twin nuclei.

It is also critical to consider the effects of the applied stress on the atomic interactions. In both DFT and EAM models, the twin structure and thickness predicted by stability analysis using GSF curves under zero stress could be different from those predicted from at high stresses, though not always. Thus, we cannot ignore the effects of stress on the energetic landscape in describing the nucleation of twins in BCC metals, and likely other types of extended defects in other materials. This observation is critical in our understanding of how defects nucleate and grow under stress.

Our results indicate that twins in BCC metals likely nucleate as two layer thick extended defects except for α -Fe. As they grow and stress is relieved, they will adopt configurations that are much closer to the zero stress stability predictions. Thus, twins in Ta, and presumably Nb and V, nucleate as an isosceles-reflection structures but will quickly thicken to a three layer double

isosceles structure and likely continue to thicken with this structure. Twins in Mo, W and Cr, will nucleate as two layer reflection structures and will thicken quickly while preserving the reflection structure of the boundaries.

The approaches here are easily adaptable to other materials where twins and other extended defects nucleate and compete with dislocations as carriers of plastic deformation. This includes, most notably, HCP metals [44], intermetallics like NiTi [154, 155] and Ag₃Sn [156] and geologic materials like quartz, feldspars, and wollastonite [145]. Our results indicate that the effects of the applied stress cannot be ignored and may affect, fundamentally, the thickness of nucleating extended defects.

5.2 Growth of twins in BCC transition metals

Mahajan's classic experimental studies on Mo-35 at% Re alloy specimens [54, 56, 57] mentioned earlier also explored the growth of deformation twins. He suggested that if the twins were nucleated by dissociation of perfect dislocations, they can thicken by chance encounters with one another as the twinning faults extend in the $\{112\}$ planes. He further visualized the coalescence of multiple twin embryos and thus creating $3n$ -thick twins. Although this seems to require a high density of dislocations to produce a macroscopic twin, Mahajan suggested that this slip band conversion might obviate the need for pole type mechanism of twin thickening, especially if the screw dislocations are able to multiply by cross slip over short distances under combined effects of applied and internal stress fields [3]. Lagerlof's work [36] based on Sleeswyk's hypothesis proposed that lateral propagation and thickening can occur by double cross slip of the screw dislocations. Based on the double cross slip mechanism, Chen et al. [58] argued that after a three-layer twin embryo is nucleated a subsequent screw dislocation cannot dissociate and glide on the same $\{112\}$ plane in the same way as the prior one did, since a second $\frac{a}{6}\langle 111 \rangle$ dislocation on the same $\{112\}$ layer would result in $\frac{a}{6}\langle 111 \rangle$ displacement which is the same as the situation caused by a partial dislocation in the anti-twinning direction and would require prohibitively high stress and energy. Thus the authors of this experimental study speculate that a subsequent dislocation will tend to

grow the existing twin nucleus by three layers. The aforementioned study by Ogata et al. [63] on BCC Mo by density functional theory simulations suggests that once a deformation twin reaches critical thickness, subsequent growth is easy and proceeds in a layer-by-layer fashion. As mentioned earlier most deformation twins in BCC metals typically possess stepwise twin boundaries (TBs) with the step heights much larger than the size of a single twinning dislocation [58, 59]. Recent in-situ observations in Tantalum and Niobium films [59] show that twin lamella grow from coherent twin boundaries by repeatedly extruding and subsequently expanding of bulges on the twin boundaries and the twin growth was described by a self-thickening mechanism through dislocation reactions at steps on coherent twin boundaries without a continuous supply of dislocations. These observations suggest that the twinning front in BCC metals may proceed in a completely different mode of growth, e.g. via stable zonal dislocations, rather than the well-accepted mode of single-layer twinning dislocation [3, 40, 45].

The alternative to a layer-by-layer growth is the possibility that multiple twinning dislocations could be nucleated simultaneously. This would correspond to the nucleation of a zonal dislocation with a Burgers vector that is integer multiple of b_p . Growth of deformation twins will depend on the magnitude of the migration energy barrier. To this end, twin boundary migration GSF (TBMGSF) curves will be computed starting with a single twin boundary as shown in Figure 2.9(a) in order to compute energy barriers for the simultaneous propagation of a single, double, triple, and quadruple twinning dislocations.

5.2.1 Twin growth in BCC Tungsten

In order to generate twin boundary migration GSF curves, we start with a twinned BCC crystal as shown in Figure 2.9(a). Then we begin to incrementally translate the upper half crystal in the $[\bar{1}\bar{1}\bar{1}]$ direction as opposed to the translation in the $[111]$ direction for the twin boundary GSF curves mentioned earlier. However, the translation in the $[\bar{1}\bar{1}\bar{1}]$ direction has to be performed in such a manner that the migration of the twin boundary can be simulated accurately. For this reason, if we want to simulate twin boundary migration by 2 layers at a time rather than a layer-by-layer

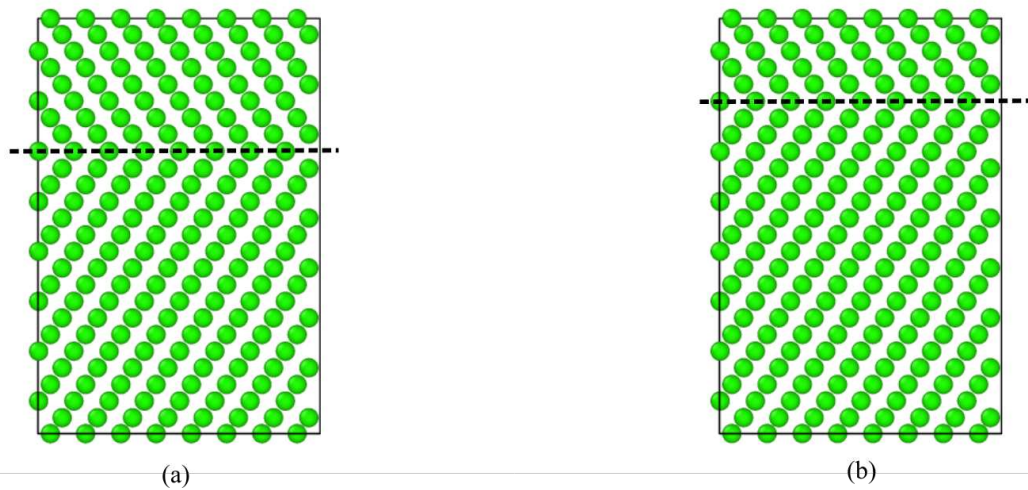


Figure 5.37: (a) a twinned crystal with the twin boundary shown by the dashed line and (b) the twin boundary has migrated by 3 layers and moved upwards.

manner, we have to translate the atomic layer most adjacent to the twin boundary by $1b_p$ and all the atomic layers above this one by $2b_p$. Similarly, if we want to simulate twin boundary migration by 3 layers, we have to translate the atomic layer most adjacent to the twin boundary by $1b_p$, the atomic layers above this one by $2b_p$ and all the other layers above by $3b_p$. These TBMGSF curves were generated by DFT simulations in VASP with the same parameters used for TBGSF and TGSF curves. Figure 5.37(a) shows a twinned crystal and (b) shows that the twin boundary has migrated by 3 layers via the translation in the $[111]$ direction described above.

The TBMGSF curves for BCC Tungsten is shown in Figure 5.38 which demonstrate that twin growth by the simultaneous nucleation of more than one twinning partials is very energetically unfavorable, indicating that the dynamics of twinning growth should occur via the nucleation of individual twinning partials in batches of roughly three that coalesce, or bunch up, on the TB.

However, a very recent in-situ experimental observation by our collaborators show that deformation twins in BCC Tungsten grow vertically in a manner that does not appear to be layer-by-layer but instead through the propagation of several layers at once. Figure 5.39 shows the growth of a deformation twin in a Tungsten nanowire. Upon further loading, the twin thickened with a growth increment of 0.41 nanometer, corresponding to three layers of $\{112\}$ planes as shown in (Fig. 5.39

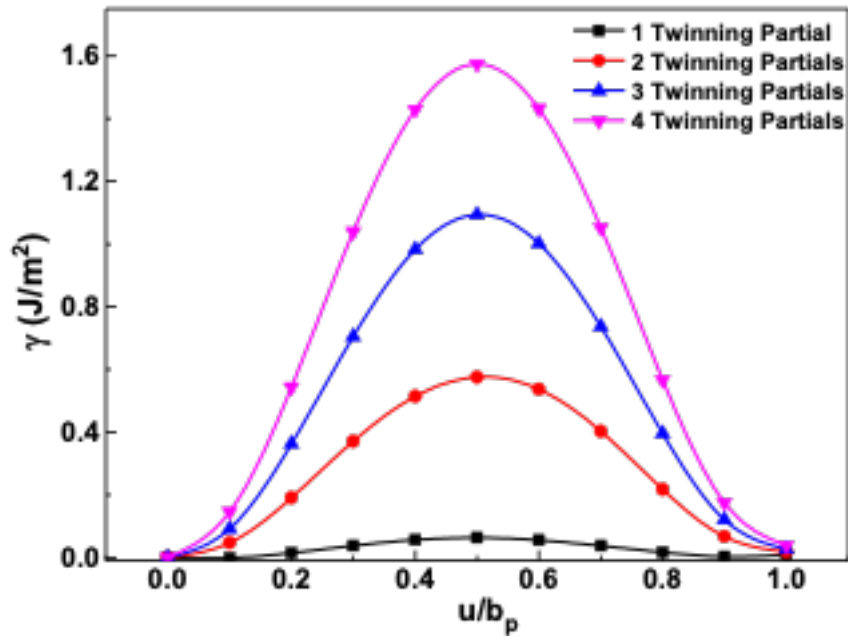


Figure 5.38: TBMGSF curves for simultaneous nucleation in BCC Tungsten of more than one twinning partials.

(a-e)). This observation suggests that in BCC metals, the twinning front may consist of three twinning dislocations on adjacent $\{112\}$ planes, with a net Burgers vector of $\frac{a}{2}[111]$ at the twinning front. The three-layers twin front propagated along the TB (indicated by the red arrows in Fig. 5.39(b-d)), resulting in vertical thickening of the twin (Fig. 5.39(e)). The measurements of the twin thickness during the growth support this observation that the twin thickening events appear to occur in groups of three twinning dislocations.

To explain this observation of growth in BCC Tungsten we point to an important feature in the TGSF curve shown in Figure 5.40 for BCC Tungsten where the resistance to twin thickening is not constant and it varies layer to layer during the twin growth. To further understand this behavior, frequency analysis of the growth resistance of twinning is performed using the discrete Fourier transform. This Fourier analysis of the data from the TGSF curve will reveal frequency for twin propagation.

To perform the frequency analysis, we computed the TGSF curve for BCC Tungsten which is shown in Figure 5.40. As our study of twin boundary structure has revealed that the isosceles

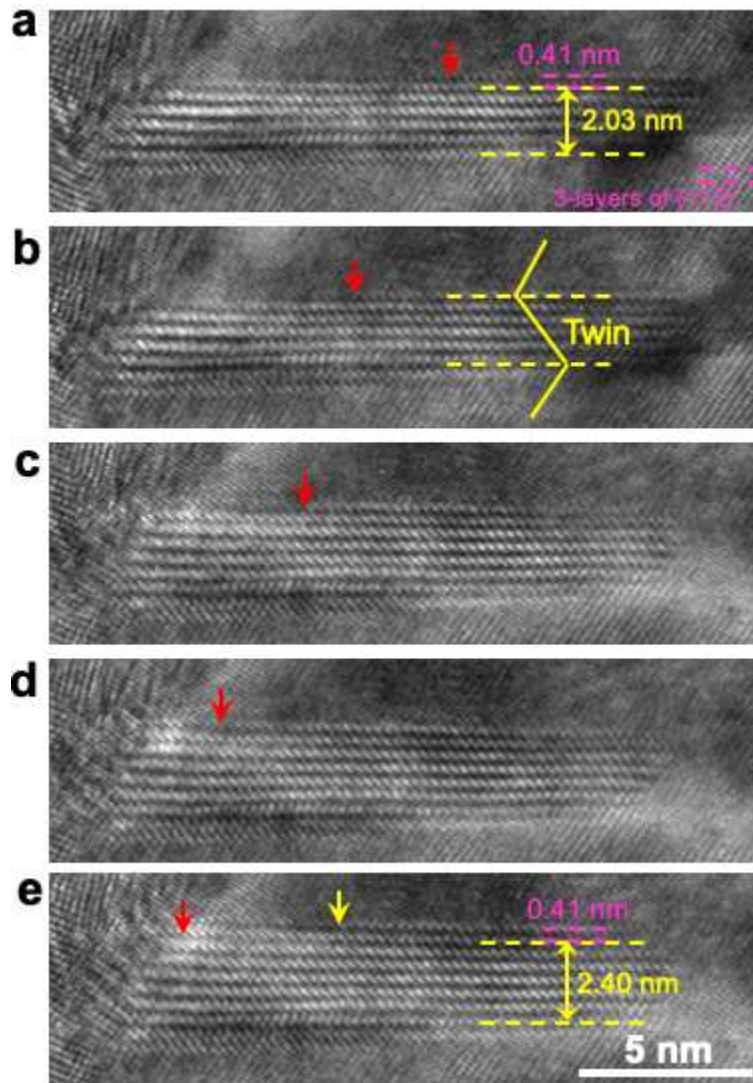


Figure 5.39: TEM images of deformation twins in BCC Tungsten

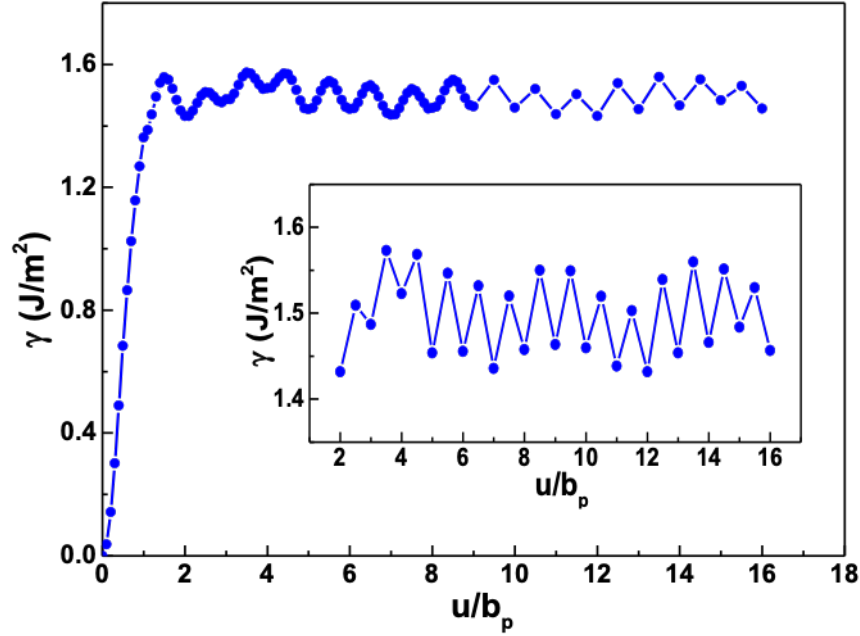


Figure 5.40: The TGSF curve generated for BCC W with DFT simulations, peak-trough data from $2b_p$ to $16b_p$ are shown in the inset.

structure is unstable in Group 6 BCC metals, the TGSF curve is only computed for pure reflection twinning pathway. Since the data must be uniformly spaced for the discrete Fourier transform, only peak-trough data (from $3b_p$ to $16b_p$) of the twinning GSF curve is used for the analysis. The mean value of the peak-trough data was subtracted from the entire data set for discrete Fourier transform analysis in order to standardize the data. The frequency analysis was performed using a Fast Fourier Transform algorithm [102].

The Fourier analysis shows two primary frequencies in the TGSF curve for BCC Tungsten as shown in Figure 5.41. The main frequency occurs at 1 cycles/ b_p , which is associated with the nature of twin propagation since the GSF curve naturally repeats with the slip of every twinning dislocation as the twin is built layer-by-layer. More importantly, the Fourier analysis also presents a secondary peak during the twin growth, which occurs at 0.276 cycles/ b_p . This subharmonic corresponds to a frequency of $\sim 3.6b_p$, which means that the resistance to twin thickening varies with a frequency of around $3.6b_p$. If the GSF curve only has a primary amplitude, it can be expected that the resistance to twin thickening would be uniform in a layer-by-layer manner, which is typically assumed. However, the existence of secondary frequency indicates that if the applied

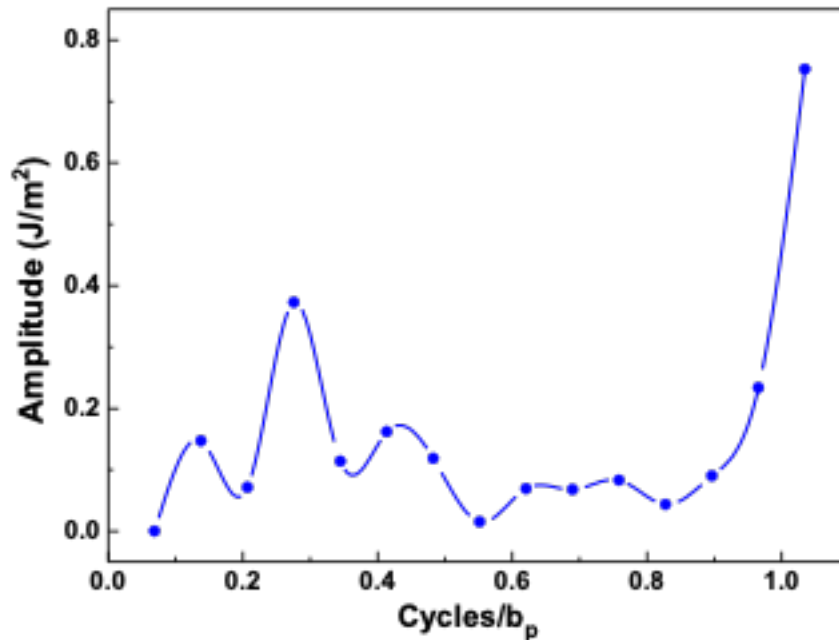


Figure 5.41: Fourier analysis of the peak-trough data from TGSF curve of BCC W.

stress/strain exceed one of the large peaks for twin growth, it could have an enough driving force for the twin migrate in a manner of multiple b_p (around 3-4 based on the secondary frequency). This provides a rationale as to how twins in BCC metals grow in a three-layer manner. It should be noted that the DFT simulations and corresponding frequency analysis assumed the uniform nucleation and propagation of each twinning dislocation, and no interaction between them was considered in the simulation. In the three-layers thickening of W nanowire, interactions should exist between the three $\frac{a}{6}\langle 111 \rangle$ dislocations composing a super-dislocation at the twin front. However, this interaction energy increases monotonically as the number of partial dislocations increases.

Chapter 6

Modeling energetics of twin nucleation

As reported in Chapter 5, we have performed free-end string simulations to model twin nucleation in BCC transition metals using EAM potentials. The saddle structures of the minimum energy paths (MEP) of these simulations can point to metastable twin nuclei structures which we have analyzed in Chapter 5. Additionally, these simulations also output energy barrier for twin nucleation as a function of applied stress. However, homogeneous twin nucleation is expected to occur near ideal strength and some available potentials available in NIST repository [73] breaks down under such large stresses. Moreover, DFT simulations are known to be more accurate in describing atomic bonding but direct nucleation simulations in bulk crystals is prohibitively expensive. So for the purpose of modeling twin nucleation energetics, we have developed continuum model of homogeneous twin nucleation assuming nucleation of circular twinning partial dislocation loops. The model is adapted from dislocation nucleation models proposed by Aubry et al. [152] and Jennings et al. [126] to represent the physics behind nucleation of twinning partials dislocations. The dislocation nucleation models in [126,152] only describe single dislocation loop nucleation in FCC metals where single layer faults are metastable whereas for our case, as discussed in Chapter 5, multi-layer twins nucleate and so an elastic interaction term has to be incorporated. Before discussing our efforts for the twin nucleation model, we have first analyzed the existing continuum model of dislocation behavior under large stresses prior to partially implementing these models to explore twin nucleation energetics.

6.1 Modeling partial dislocation nucleation

Dislocations, line defect in crystals, are central to our understanding of plastic deformation and mechanical strength of crystalline materials. While bulk plasticity is well described by continuum plasticity, it is well established that the rules of plasticity change as crystal dimensions are reduced in the micro range and the strength of materials becomes size dependent [157, 158]. This idea was

first examined by the works of Brenner [159, 160] on metallic whiskers and has been examined more thoroughly by the microcompression and tension tests on Focus Ion Beam (FIB) milled micropillars [29, 161, 162].

This interest in size affected flow created significant interest in how pristine (defect free materials) would respond to mechanical loading and when a transition between size affected flow and dislocation nucleation would occur [163, 164]. This has led to the investigation of the strength of metallic nanowires [27, 165–170], nanoparticles [171–173] and other nanostructured materials [163, 174, 175]. The strengths of many of these materials, especially the nanowires, have shown to approach the theoretical strength of the materials [170, 176, 177]. Finally, dislocation nucleation also occurs during nanoindentation and can be attributed, sometimes, to the pop-in events noted in load-displacement curves [178–180].

Molecular dynamics simulations have been instrumental in understanding the mechanisms of dislocation emission and evolution in nanostructures [45, 181] which have, in conjunction with the aforementioned experiments, provided significant insight into plastic flow at small scales. However, the difference in strain rates between molecular dynamics and experiments is often many orders of magnitude, which raises concern as to the exact nature of the predictions of this method. This, in turn, has created interest in exploring dislocation emission as a classical nucleation process. From this viewpoint, dislocation nucleation occurs when there is sufficient energy and time, aided by applied stress, for the dislocation to overcome the free energy barrier preventing its spontaneous nucleation. The nucleation rate, following transition state theory, is:

$$\nu = N\nu_0 \exp\left(-\frac{\Delta G^*(\sigma, T)}{k_B T}\right) \quad (6.1)$$

where N is the number of nucleation sites, ν_0 is a frequency prefactor, ΔG^* is the activation Gibbs free energy and k_B is the Boltzmann constant [141, 174]. The nucleation rate, according to Equation (6.1), is strongly dependent on the activation free energy for dislocation nucleation and thus an understanding of dislocation nucleation is tied to the stress and temperature dependence of this activation energy. Zhu et al. [182] used the free end nudged-elastic band method (a chain-

of-states method) to examine the internal energy barrier for dislocation nucleation in a copper nanowire as a function of stress. The authors found, as expected, that the activation energy was a strong function of stress and they fit their atomistic results to an empirical equation:

$$\Delta E^*(\sigma) = E_0 \left[1 - \frac{\sigma}{\sigma_0} \right]^\alpha \quad (6.2)$$

where E_0 and α are fitting parameters, σ the applied stress and σ_0 the athermal strength. This form comes from general empirical models for activation energies used in the literature [183]. However, this expression was only fit to activation internal energies (or enthalpies) at zero Kelvin. To account for finite temperature, Zhu et al. used the thermodynamic compensation law (Meyer-Neldel rule) so that the activation free energy can be written as:

$$\Delta A^*(\sigma, T) = E_0 \left[1 - \frac{\sigma}{\sigma_0} \right]^\alpha \left(1 - \frac{T}{T_m} \right) \quad (6.3)$$

Where T_m is a characteristic temperature at which the energy barrier vanishes for all stresses. Zhu et al. then extended nucleation equation (Equation (6.1)) to predict the most probable nucleation stress as:

$$\frac{\Delta G^*(\sigma, T)}{k_B T} = \ln \frac{k_B T N \nu_0}{Y \dot{\epsilon} \Omega(\sigma, T)} \quad (6.4)$$

where Y is the Young's modulus of the material, $\dot{\epsilon}$ is the applied strain rate and Ω is the activation volume defined as $\Omega = -\frac{d\Delta G^*}{d\sigma}$.

Ryu et al. [184] re-examined the same copper nanowire nucleation problem to specifically address the temperature dependence and the thermodynamic compensation law using umbrella sampling to directly calculate the activation free energies. The authors demonstrated that the activation Gibbs free energy and Helmholtz free energy are equal, $\Delta G^* \approx \Delta A^*$ and similarly $\Delta H^* \approx \Delta E^*$. Their work also points out that the thermodynamic compensation law does not always work and that the characteristic temperatures T_m depends on whether the stress or strain is the controlled

thermodynamic variable and is not related to the melting temperature (or surface disordering temperature) as is often assumed.

The computation of energies barriers in atomistics, nevertheless, is still a powerful method to gain insight into the nucleation process even if the temperature dependence is still not fully understood. Several investigators have used similar approaches to study dislocation nucleation in gold nanowires [125], from surface steps in FCC metals [185–187], and from pores in aluminum [188]. In addition, these energy barrier calculations have been used in conjunction with continuum models of dislocation nucleation to gain a better understanding of the nucleation phenomenon or to develop better continuum models of dislocation nucleation [126, 152].

Despite the interest in calculating energy barriers directly from chain-of-state atomistic calculations or similar methods, these approaches are often expensive and difficult to use. Thus, it is desirable to determine if such information can be obtained from direct atomistic simulations. In an attempt to solve this problem, recently Chachamovitz et al. [189] introduced a method to extract the activation free energies from direct MD simulations by examining statistical distribution of nucleation strengths as a function of temperature during constant stress rate simulations. The key point the authors make is that if we assume the nucleation rate follows Equation (6.1), then the cumulative distribution function of failure is:

$$F(\sigma, T) = 1 - \exp \left[- \frac{N\nu_0}{\dot{\sigma}} \int_0^\sigma \exp(-\beta\Delta G^*(\eta)) d\eta \right] \quad (6.5)$$

Where $\dot{\sigma}$ is the applied stress rate and $\beta = \frac{1}{k_B T}$. This theoretical cumulative distribution function can then be fit to cumulative distribution functions determined from direct MD simulations as long as a functional form of ΔG^* is assumed. The authors further argue that the activation volume can be directly related to the standard deviation of the nucleation strengths, which simplifies the parameterization of ΔG^* . For convenience, they assume a functional form of

$$\Delta G^*(\sigma, T) = G_0 \left[1 - \frac{\sigma}{\sigma_0} \right]^\alpha \left(1 - \frac{T}{T_m} \right) \quad (6.6)$$

With G_0 , α and T_m (as well as ν_0) determined from numerical fitting of the cumulative distribution functions.

Chachamovitz et al. [189] used this method to examine nucleation in their molybdenum nanoparticles and found that the exponent, α , was approximately 1.68. They noted that this exponent was close to the value of 1.5 that has been argued to characterize plastic flow associated with dislocation glide in bulk crystals near the yield point [190–192]. This led to a hypothesis that perhaps a exponent of around 1.5 is a universal exponent for dislocation nucleation near the point of spontaneous nucleation, i.e. the athermal limit. One key point to make by assuming such an exponent is that this implies the activation volume goes to zero in the athermal limit, as would be true for any exponent greater than 1.

The postulate of a universal exponent is intriguing and a worthy point of investigation. It is further worth pointing out that the only other exponent determined was 4.1 by Zhu et al. which Chachamovitz et al. suggested was a result of the predictions accounting for data too far from the athermal limit. Hence, the objective of this paper is to explore the nature of the activation energy as a function of stress. Notably, we will attempt to determine if the exponent α is indeed universal, i.e. does it have specific value for nucleation, and generally should the activation volume approach zero as the stress approaches the athermal limit. To this end, we analyze atomistic data published in the open literature to determine if there is a universal trend. In addition, we will also investigate the energy barriers as a function stress using continuum models to understand how dislocation nucleation behaves in the athermal limit of spontaneous nucleation.

6.1.1 Analysis of MD simulation results and the exponent α

Here, our goal is to determine if atomistic simulations support a universal stress exponent. To this end, we examined existing atomistic simulation data for the activation free energy as a function of stress. We fit the activation free energy data from Zhu et al. [163], Aubry et al. [152], Jennings et al. [126] and Weinberger et al. [125] to Equation (6.2) in order to extract the exponent. To determine α , we used a non-linear fitting procedure to minimize the mean square error between

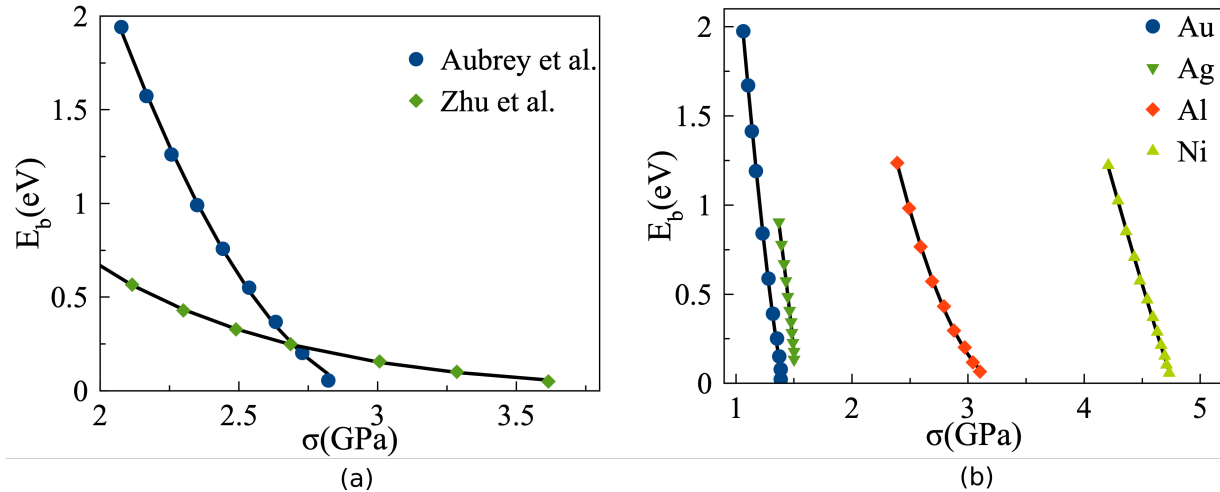


Figure 6.1: (a) The energy barrier vs. stress for Cu under pure shear (Aubrey et al.) and compression (Zhu et al.) (b) The energy barrier vs. stress for Au, Ag, Al and Ni (Jennings et al.).

the atomistic energy barrier data and the power law model. An example of this fit is shown in Figure 6.1(a) for a Cu nanowire under pure shear (Aubrey et al.) and in Figure 6.1(b) for a Cu nanowire under uniaxial compression (Zhu et al.). For the pure shear data of Jennings et al., σ_0 was included as a free variable in the fitting as no such value was reported by the authors. For the rest of the data, σ_0 was fixed based on previous reported values. In some cases, such as the data of Zhu et al., α is sensitive to the inclusion of σ_0 due to the lack of data near the ideal strength limit. This sensitivity suggests that α may not be an ideal parameter for characterizing the energy barrier beyond an empirical fit.

Table 6.1 lists the fitting parameters for the surveyed atomistic data. The exponent, α , for the nanowires exhibits a wide range of values under uniaxial loading from 1.4 to 5.8 while under pure shear the α values range from 0.8 to 1.9. Clearly, this data does not support a hypothesis that α may have a universal value over the stress range that we have considered. Furthermore, we see that in some cases, especially in pure shear, some of the exponents are close to 1 and in one case, Ag, is less than one. The case of silver is intriguing because the exponent actually implies a divergent activation volume as the stress approaches the athermal limit, a point that will become important later. The lack of a universal exponent in our data, however, does not completely rule out the hypothesis of Chachamovitz et al. as their suggestion should be limited to the athermal limit.

Table 6.1: The best fit parameters for Equation (6.2) for the atomistic data surveyed in the literature.

Metal	Reference	Loading Condition	σ_0 (GPa)	α
Cu	Zhu et al.	compression	5.2	4.1
Cu	Aubry et al.	pure shear	3.0	1.8
Au	Jennings et al.	pure shear	1.4	1.3
Ag			1.5	0.8
Al			3.3	1.9
Ni			4.8	1.1
Au	Weinberger et al.	$\langle 100 \rangle$ compression rectangular cross-section	1.7	2.6
		$\langle 100 \rangle$ compression circular cross-section	1.8	1.4
		$\langle 100 \rangle$ tension rectangular cross-section	4.5	4.8
		$\langle 100 \rangle$ tension circular cross-section	4.6	2.1
		$\langle 110 \rangle$ compression rectangular cross-section	18.4	5.8
		$\langle 110 \rangle$ compression circular cross-section	21.8	4.6
		$\langle 110 \rangle$ tension circular cross-section	3.4	1.5

However, in many of the atomistic results, it would appear that the activation energies approach the athermal limit with a constant slope, or an exponent of 1, rather than a slope of zero which is necessary for alpha to be greater than 1.

6.1.2 Continuum Models

Since the power law fitting of the atomistic data does not indicate any universal behavior of the exponent value but is perhaps limited in scope, we proceed to the analysis of continuum models for dislocation nucleation. The continuum models have the advantage of greatly reducing the complexity of the problem to just a few variables, which makes the solutions expedient and potentially quite general. Furthermore, these models will be much easier to examine numerically in the limit as the stress approaches its athermal limit. However, it is important to note that continuum models can also introduce artifacts associated with continuum approximations and this must be kept in mind when analyzing and generalizing the results of such models.

To start, we first examine a continuum model for the nucleation of a circular dislocation under pure shear. While we know that dislocations will not nucleate as a perfect circular loop, this assumption makes the model slightly simpler without compromising too much of the physics. Our approach follows the method of Aubry et al. [152], which is an adaptation of the model in Anderson

et al. [141], which includes the energy of the nucleating dislocation line with a constant Burgers vector. The model we will analyze here only differs from that of Aubry et al. in the assumed form of the line energy which is taken from [126]

$$\Delta G(\tau, R) = \frac{\mu b^2}{4} \frac{2 - \nu}{1 - \nu} R \ln \frac{R}{r_c} - \tau b \pi R^2 \quad (6.7)$$

where ΔG represents the change in Gibbs free energy due to the formation of the dislocation loop, μ is the shear modulus, ν is the Poisson's ratio, R is the dislocation loop radius, r_c is the dislocation core radius, τ is the applied shear stress, and b is the Burgers vector of the nucleating dislocation. The activation Gibbs free energy, $\Delta G^*(\tau)$, is typically taken as the saddle of the $\Delta G(R, \tau)$ function and can be found by solving R as a function of τ by finding the maximum of ΔG^* with respect to R . This saddle can be found by solving $\frac{\partial \Delta G}{\partial R}(R, \tau) = 0$, which establishes the critical radius R^* for the applied stress τ . Solving for R^* gives an implicit equation:

$$\frac{R^*}{r_c} = A \left[\ln \frac{R^*}{r_c} + 1 \right] \quad (6.8)$$

where $A = \frac{\mu b(2-\nu)}{8\pi r_c \tau(1-\nu)}$. An analytical solution for Equation (6.19) is possible in the form of:

$$\frac{R^*}{r_c} = -A \mathbf{W} \left(-\frac{1}{Ae} \right) \quad (6.9)$$

where $\mathbf{W}(x)$ is the Lambert's \mathbf{W} -function or the product log function. Lambert's \mathbf{W} -function is a complex set of functions with an infinite number of branches with only two of them being real valued. If x is real, then for $-\frac{1}{e} \leq x < 0$ there are two possible real values of $\mathbf{W}(x)$, as illustrated in Figure 6.2. The branch satisfying $-1 \leq \mathbf{W}(x)$ is denoted as $\mathbf{W}_0(x)$ and is referred to as the principal branch while the branch satisfying $\mathbf{W}(x) \leq -1$ is denoted as $\mathbf{W}_{-1}(x)$ in the literature [194].

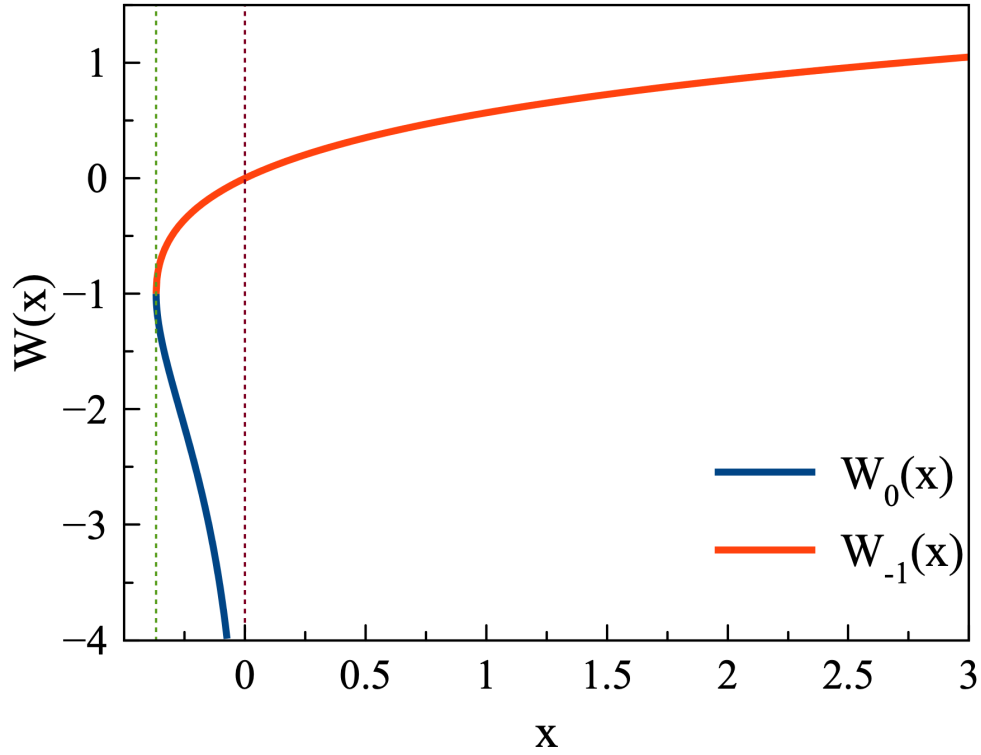


Figure 6.2: The real valued Lambert W-function with branches W_0 and W_{-1} [193].

From $\frac{\partial \Delta G}{\partial R}(R, \tau) = 0$, we can define τ^* as:

$$\tau^* = \frac{\mu b(2 - \nu)}{8\pi R^*(1 - \nu)} \left[\ln \frac{R^*}{r_c} + 1 \right] \quad (6.10)$$

substituting this τ^* into Equation (6.17) allows us to express the saddle ΔG^* as a function of R^* as:

$$\Delta G^* = \frac{\mu b^2(2 - \nu)}{8(1 - \nu)} R^* \left[\ln \frac{R^*}{r_c} - 1 \right] \quad (6.11)$$

When $\Delta G^* = 0$, then we have spontaneous nucleation which corresponds to the ideal strength τ_0 . From Equation (6.22), this will occur when $\left[\ln \frac{R^*}{r_c} - 1 \right] = 0$, which results in $R^* = er_c$. Substituting $R^* = er_c$ in Equation (6.21), the athermal strength, or ideal strength, τ_0 can be determined as:

$$\tau_0 = \frac{\mu b(2 - \nu)}{8\pi(1 - \nu)} \frac{2}{er_c} \quad (6.12)$$

Using Equation (6.20) and the definition of τ_0 we can determine the relationship between R^* and τ as:

$$R^* = -\frac{er_c}{2} \frac{1}{y} \mathbf{W} \left(\frac{-2y}{e^2} \right) \quad (6.13)$$

where $y = \frac{\tau}{\tau_0}$. Now, substituting the expression for R^* from Equation (6.24) in Equation (6.22) we have:

$$\Delta G^*(\tau) = \frac{\mu b^2 (2 - \nu) e}{8(1 - \nu)} \left[-\frac{r_c}{2y} \mathbf{W} \left(\frac{-2y}{e^2} \right) \right] \left[\ln \left(-\frac{e}{2y} \mathbf{W} \left(\frac{-2y}{e^2} \right) \right) - 1 \right] \quad (6.14)$$

As discussed above and illustrated in Figure 6.2, the real valued branches of the Lambert-W function are: \mathbf{W}_0 and \mathbf{W}_{-1} . We consider the \mathbf{W}_{-1} branch as it has been found to be the solution to other dislocation problems [193] and provides positive values of the change in Gibbs free energy here. We note that $\mathbf{W}_{-1} \left(\frac{-2y}{e^2} \right)$ is infinitely differentiable at $y = 1$ and thus Equation (6.25) has a power series expansion. This means that α must be a non-negative integer. To determine the value of α as $\tau \rightarrow \tau_0$, we expand ΔG^* about $\tau = \tau_0$ as:

$$\Delta G^*(\tau) = G_0 \left[\left(1 - \frac{\tau}{\tau_0} \right) + 2 \left(1 - \frac{\tau}{\tau_0} \right)^2 + \frac{8}{3} \left(1 - \frac{\tau}{\tau_0} \right)^3 + \frac{10}{3} \left(1 - \frac{\tau}{\tau_0} \right)^4 + \mathcal{O} \left(1 - \frac{\tau}{\tau_0} \right)^5 \right] \quad (6.15)$$

where $G_0 = \frac{\mu b^2 (2 - \nu) er_c}{8(1 - \nu)}$. The power series expansion clearly demonstrates that $\alpha \rightarrow 1$ as $\tau \rightarrow \tau_0$. Detailed derivation of this power series expansion is shown below.

Consider a circular dislocation loop under pure shear as shown in Figure 6.3. The energy of this dislocation loop can be modeled based on the ideas of Aubry et al. [152], which is an adaptation of the model in Anderson et al. [141]. This model includes the energy of the nucleating dislocation line with a constant Burgers vector and the work done by the shear stress on the dislocation loop and can be written as:

$$\Delta G(\tau, R) = 2\pi RT - \pi R^2 \tau b \quad (6.16)$$

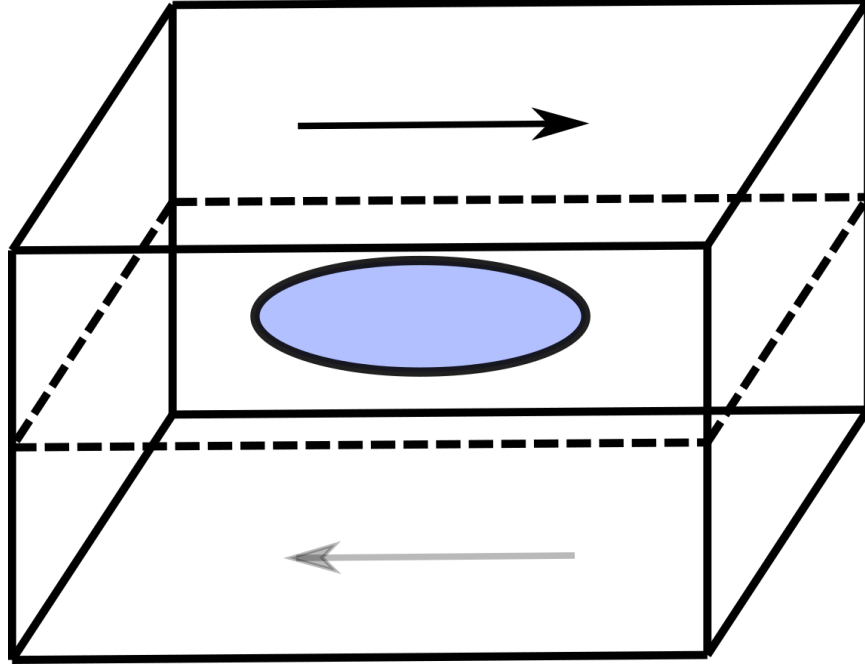


Figure 6.3: A dislocation loop under pure shear loading

where T is the line energy, R is the radius of the dislocation loop, τ is the applied shear stress, and b is the Burgers vector. If we take the line energy form of [126], then the change in Gibbs free energy associated with the formation of a dislocation loop ΔG is:

$$\Delta G(\tau, R) = \frac{\mu b^2}{4} \frac{2 - \nu}{1 - \nu} R \ln \frac{R}{r_c} - \tau b \pi R^2 \quad (6.17)$$

where μ is the shear modulus, ν is the Poisson's ratio and r_c is the dislocation core radius. The activation Gibbs free energy, $\Delta G^*(\tau)$, should be the saddle of $\Delta G(R, \tau)$ and can be found by solving R as a function of τ by determining the maximum of $\Delta G(R, \tau)$ with respect to R . To find the activation Gibbs free energy, ΔG^* , we differentiate both sides of Equation (6.17) as:

$$\frac{\partial \Delta G}{\partial R}(R, \tau) = \frac{\mu b^2 (2 - \nu)}{4(1 - \nu)} \left[\ln \frac{R}{r_c} + 1 \right] - 2\tau b \pi R \quad (6.18)$$

Setting $\frac{\partial \Delta G}{\partial R}(R, \tau)|_{R=R^*} = 0$ and solving for R^* yields an implicit equation of the form:

$$\frac{R^*}{r_c} = A \left[\ln \frac{R^*}{r_c} + 1 \right] \quad (6.19)$$

where $A = \frac{\mu b(2-\nu)}{8\pi r_c \tau(1-\nu)}$. An analytical solution to the implicit Equation (6.19) is:

$$\frac{R^*}{r_c} = -A \mathbf{W} \left(-\frac{1}{Ae} \right) \quad (6.20)$$

where $\mathbf{W}(x)$ is the Lambert's \mathbf{W} -function or the product log function. Lambert's \mathbf{W} -function is a complex set of functions with an infinite number of branches but only two of them are real valued. If x is real, then for $-1/e \leq x < 0$ there are two possible real values of $\mathbf{W}(x)$, as illustrated in Figure 6.2. The branch satisfying $-1 \leq \mathbf{W}(x)$ is denoted as $\mathbf{W}_0(x)$ and is referred to as the principal branch while the branch satisfying $\mathbf{W}(x) \leq -1$ is denoted as $\mathbf{W}_{-1}(x)$ in the literature [194].

By rearranging Equation (6.18), we can also define the applied shear stress as a function of R^* as:

$$\tau = \frac{\mu b(2-\nu)}{8\pi R^*(1-\nu)} \left[\ln \frac{R^*}{r_c} + 1 \right] \quad (6.21)$$

and substituting this τ into Equation (6.17) allows us to express the saddle point ΔG^* as a function of R^* as:

$$\Delta G^* = \frac{\mu b^2(2-\nu)}{8(1-\nu)} R^* \left[\ln \frac{R^*}{r_c} - 1 \right] \quad (6.22)$$

When $\Delta G^* = 0$, then we have spontaneous nucleation which corresponds to the ideal strength τ_0 . From Equation (6.22), this will occur when $\left[\ln \frac{R^*}{r_c} - 1 \right] = 0$, which results in $R^* = er_c$. Substituting $R^* = er_c$ in Equation (6.21), the athermal strength, or ideal strength, τ_0 can be determined as:

$$\tau_0 = \frac{\mu b(2-\nu)}{8\pi(1-\nu)} \frac{2}{er_c} \quad (6.23)$$

Using Equation (6.20) and the definition of τ_0 we can determine the relationship between R^* and τ as:

$$R^* = -\frac{\text{er}_c}{2} \frac{1}{y} \mathbf{W} \left(\frac{-2y}{e^2} \right) \quad (6.24)$$

where $y = \tau/\tau_0$. Now, substituting the expression for R^* from Equation (6.24) in Equation (6.22) we have:

$$\Delta G^*(\tau) = -\frac{\mu b^2(2-\nu)\text{er}_c}{16(1-\nu)} \left[\frac{1}{y} \mathbf{W} \left(\frac{-2y}{e^2} \right) \right] \left[\ln \left(-\frac{e}{2y} \mathbf{W} \left(\frac{-2y}{e^2} \right) \right) - 1 \right] \quad (6.25)$$

As discussed above and illustrated in Figure 6.2, the real valued branches of the Lambert-W function are: \mathbf{W}_0 and \mathbf{W}_{-1} . We consider the \mathbf{W}_{-1} branch as it has been found to be the solution to other dislocation problems [193] and provides positive values of the change in Gibbs free energy here. We note that $\mathbf{W}_{-1} \left(\frac{-2y}{e^2} \right)$ is infinitely differentiable at $y = 1$ and thus Equation (6.25) has a power series expansion with non-negative integer exponents. The first term in Equation (6.25), $\frac{\mu b^2(2-\nu)\text{er}_c}{16(1-\nu)}$, is only dependent on material constants. The second and third terms inside brackets in Equation (6.25) both have the term $\left[\frac{1}{y} \mathbf{W}_{-1} \left(\frac{-2y}{e^2} \right) \right]$ which can be expanded as:

$$\begin{aligned} \frac{1}{y} \mathbf{W}_{-1} \left(\frac{-2y}{e^2} \right) &= \mathbf{W}_{-1} \left(-\frac{2}{e^2} \right) - \frac{(y-1) \left(\mathbf{W}_{-1} \left(-\frac{2}{e^2} \right) \right)^2}{\mathbf{W}_{-1} \left(-\frac{2}{e^2} \right) + 1} + \\ &\quad \frac{(y-1)^2 \left(\mathbf{W}_{-1} \left(-\frac{2}{e^2} \right) \right)^3 (2\mathbf{W}_{-1} \left(-\frac{2}{e^2} \right) + 3)}{2 \left(\mathbf{W}_{-1} \left(-\frac{2}{e^2} \right) + 1 \right)^3} - \\ &\quad \frac{(y-1)^3 \left(\mathbf{W}_{-1} \left(-\frac{2}{e^2} \right) \right)^4 \left(19\mathbf{W}_{-1} \left(-\frac{2}{e^2} \right) + 6 \left(\mathbf{W}_{-1} \left(-\frac{2}{e^2} \right) \right)^2 + 16 \right)}{6 \left(\mathbf{W}_{-1} \left(-\frac{2}{e^2} \right) + 1 \right)^5} + \dots \end{aligned}$$

Substituting $\mathbf{W}_{-1} \left(-\frac{2}{e^2} \right) = -2$ in the above equation results in:

$$\frac{1}{y} \mathbf{W}_{-1} \left(\frac{-2y}{e^2} \right) = -2 + 4(y-1) - 4(y-1)^2 + \frac{16}{3}(y-1)^3 - 4(y-1)^4 + \dots$$

Substituting this result in Equation (6.25) gives:

$$\Delta G^*(\tau) = \frac{\mu b^2(2-\nu)er_c}{16(1-\nu)} \left(2 - 4(y-1) + 4(y-1)^2 - \frac{16}{3}(y-1)^3 + 4(y-1)^4 - \dots \right) \\ \left(\ln \left[-\frac{e}{2} \left(-2 + 4(y-1) - 4(y-1)^2 + \frac{16}{3}(y-1)^3 - 4(y-1)^4 + \dots \right) \right] - 1 \right)$$

Multiplying the second and third term of the above equation results in a power series expansion of $\Delta G^*(\tau)$ as:

$$\Delta G^*(\tau) = G_0 \left[\left(1 - \frac{\tau}{\tau_0} \right) + 2 \left(1 - \frac{\tau}{\tau_0} \right)^2 + \frac{8}{3} \left(1 - \frac{\tau}{\tau_0} \right)^3 + \frac{10}{3} \left(1 - \frac{\tau}{\tau_0} \right)^4 + \mathcal{O} \left(1 - \frac{\tau}{\tau_0} \right)^5 \right]$$

which is identical to Equation 6.15 exhibiting $\Delta G^* \propto \left(1 - \frac{\tau}{\tau_0} \right)^1$ as $\tau \rightarrow \tau_0$.

For stress values less than τ_0 , an empirical fit of $\Delta G = G_0 \left(1 - \frac{\tau}{\tau_0} \right)^\alpha$ would give rise to an $\alpha > 0$. The activation volume can be analytically derived, since $b = \text{constant}$, as:

$$\Omega = \pi R^2 b = \frac{e^2 r_c^2 \tau_0^2}{4 \tau^2} \mathbf{W}_{-1}^2 \left(-\frac{2\tau}{e^2 \tau_0} \right) \pi b = \frac{1}{4} e^2 r_c^2 \pi b \mathbf{W}_{-1}^2 \left(-\frac{2\tau}{e^2 \tau_0} \right)$$

In the limit $\tau \rightarrow \tau_0$, Ω approaches a constant:

$$\Omega(\tau = \tau_0) = e^2 r_c^2 \pi b \quad (6.26)$$

This result contradicts the postulate of a exponent of 1.5, but also assumes that the activation free energy is referenced to a loop of zero radius. This reference is problematic because a dislocation of zero radius is a local maximum as the energy initially decreases with loop growth and reaches a real local minimum of finite radius before it increases again to the saddle. This is important because the universal exponent of 1.5, a result of catastrophe theory [195], is derived by assuming the saddle collides with a local minimum which is not analyzed in the above derivation.

However, this simple model does predict a local minimum and the system can be analyzed as the saddle (or maximum) approaches this local minimum. The negative one branch of the Lambert

function corresponds the saddle (maximum) and thus the other branch, the zero branch solution we discarded earlier, corresponds to the minimum. Thus, we can define the actual activation Gibbs free energy barrier as:

$$\Delta G^\dagger = \Delta G_{-1}^* - \Delta G_0^* \quad (6.27)$$

where ΔG_{-1}^* and ΔG_0^* can be found by using the \mathbf{W}_{-1} and \mathbf{W}_0 branches of the Lambert- \mathbf{W} function in Equation (6.20) to solve for R^* and substituting R^* into Equation (6.22). In order for ΔG_{-1}^* and ΔG_0^* to collapse and give rise to $\Delta G^\dagger = 0$, Equation (6.20) needs to be expanded about $\mathbf{W}\left(-\frac{1}{e}\right)$, the point where \mathbf{W}_{-1} and \mathbf{W}_0 converge as shown in Figure 6.2. This requires the term $A = \frac{\mu b(2-\nu)}{8\pi r_c \tau(1-\nu)}$ we defined for Equation (6.20) to be unity. Since our objective is to analyze the energy barrier near $\tau \rightarrow \tau_0$ we have to redefine $\tau_0 = \frac{\mu b(2-\nu)}{8\pi r_c(1-\nu)}$ such that $A = \frac{\tau_0}{\tau}$. With this definition of τ_0 we can rewrite Equation (6.20) as:

$$R^* = -\frac{r_c}{y} \mathbf{W}\left(-\frac{y}{e}\right)$$

where $y = \frac{\tau}{\tau_0}$. Now ΔG_{-1}^* and ΔG_0^* are:

$$\Delta G_{-1}^* = K \left(\frac{-1}{y}\right) \mathbf{W}_{-1}\left(\frac{-y}{e}\right) \left[\ln \left(\left(\frac{-1}{y}\right) \mathbf{W}_{-1}\left(\frac{-y}{e}\right) \right) - 1 \right]$$

$$\Delta G_0^* = K \left(\frac{-1}{y}\right) \mathbf{W}_0\left(\frac{-y}{e}\right) \left[\ln \left(\left(\frac{-1}{y}\right) \mathbf{W}_0\left(\frac{-y}{e}\right) \right) - 1 \right]$$

where $K = \frac{\mu b^2 r_c(2-\nu)}{8(1-\nu)}$.

A series expansion of \mathbf{W}_0 can be done at the branch point by defining $p = \sqrt{2(1-y)}$ where $y = \frac{\tau}{\tau_0}$ resulting in:

$$\mathbf{W}_0(z) = -1 + p - \frac{p^2}{3} + \frac{11p^3}{72} + \dots$$

For the \mathbf{W}_{-1} branch, a similar series expansion is defined for $p = -\sqrt{2(1-y)}$ [196]. Substituting the series expansion in the equations for ΔG_{-1}^* and ΔG_0^* and taking their differences in Equation (6.27) we obtain for $y \rightarrow 1$:

$$\Delta G^\dagger = K \left[\frac{8\sqrt{2}}{3}(1-y)^{3/2} \left(1-(1-y)+(1-y)^2-\dots \right) + \frac{11\sqrt{2}}{54}(1-y)^{5/2} \left(1-(1-y)+(1-y)^2-\dots \right) \right] \quad (6.28)$$

The leading term on the right hand side of the above equation has an exponent of $\frac{3}{2}$ in accordance with the results from [190–192]. Derivation of this power series expansion is shown below.

The actual activation Gibbs free energy barrier of the above problem is more accurately modeled as the difference between a local minimum and a saddle, which in this case is described by Equation 6.27 with ΔG_{-1}^* and ΔG_0^* can be found by using the \mathbf{W}_{-1} and \mathbf{W}_0 branches of the Lambert- \mathbf{W} function respectively in Equation (6.25). For ΔG_{-1}^* and ΔG_0^* to collapse, we have to redefine Equation (6.20) and substitute this redefined R^* into Equation (6.22). Also in order for $\Delta G^\dagger = 0$, Equation (6.20) needs to be expanded about the branch point $-\frac{1}{e}$ where \mathbf{W}_{-1} and \mathbf{W}_0 converge as shown in Figure 6.2. In other words the expansion has to be done for $\mathbf{W}\left(-\frac{1}{e}\right)$ which requires the term $A = \frac{\mu b(2-\nu)}{8\pi r_c \tau(1-\nu)}$ we defined for Equation (6.20) to be unity. Since our objective is to analyze the energy barrier near $\tau \rightarrow \tau_0$ i.e., $\frac{\tau}{\tau_0} \rightarrow 1$, we also have to redefine $\tau_0 = \frac{\mu b(2-\nu)}{8\pi r_c(1-\nu)}$ such that $A = \tau_0/\tau$. With this definition of τ_0 we can rewrite Equation (6.20) as:

$$R^* = -\frac{r_c}{y} \mathbf{W}\left(-\frac{y}{e}\right)$$

where $y = \frac{\tau}{\tau_0}$. Substituting this result in Equation (6.22) we have:

$$\Delta G^*(\tau) = \frac{\mu b^2(2-\nu)r_c}{8(1-\nu)} \left[-\frac{1}{y} \mathbf{W}\left(\frac{-y}{e}\right) \right] \left[\ln\left(-\frac{1}{y} \mathbf{W}\left(\frac{-y}{e}\right)\right) - 1 \right] \quad (6.29)$$

Now using the appropriate branches of \mathbf{W} , we have:

$$\Delta G_{-1}^* = K \left(\frac{-1}{y} \right) \mathbf{W}_{-1} \left(\frac{-y}{e} \right) \left[\ln \left(\left(\frac{-1}{y} \right) \mathbf{W}_{-1} \left(\frac{-y}{e} \right) \right) - 1 \right] \quad (6.30)$$

and

$$\Delta G_0^* = K \left(\frac{-1}{y} \right) \mathbf{W}_0 \left(\frac{-y}{e} \right) \left[\ln \left(\left(\frac{-1}{y} \right) \mathbf{W}_0 \left(\frac{-y}{e} \right) \right) - 1 \right] \quad (6.31)$$

where $K = \frac{\mu b^2 r_c (2-\nu)}{8(1-\nu)}$. To perform series expansion of the term inside the brackets in above equations we recall that the Lambert- \mathbf{W} function is defined as

$$W e^W = z$$

Taking logarithm on both sides and changing sides we have

$$\ln W = \ln z - W$$

This is a useful result which enables us to reduce the term $\left[\ln \left[-\frac{1}{y} \mathbf{W} \left(-\frac{y}{e} \right) \right] - 1 \right]$ into two simple terms:

$$\begin{aligned} \ln \left[-\frac{1}{y} \mathbf{W} \left(-\frac{y}{e} \right) \right] - 1 &= \ln \left(-\frac{1}{y} \right) + \ln \left(\mathbf{W} \left(-\frac{y}{e} \right) \right) - 1 \\ &= \ln \left(-\frac{1}{y} \right) + \ln \left(-\frac{y}{e} \right) - \mathbf{W} \left(-\frac{y}{e} \right) - 1 \\ &= \ln \left(\frac{1}{e} \right) - \mathbf{W} \left(-\frac{y}{e} \right) - 1 \\ &= -2 - \mathbf{W} \left(-\frac{y}{e} \right) \end{aligned}$$

Substituting $\left[\ln \left[-\frac{1}{y} \mathbf{W} \left(-\frac{y}{e} \right) \right] - 1 \right] = -2 - \mathbf{W} \left(-\frac{y}{e} \right)$ in Equation (6.30) we have

$$\Delta G_{-1}^* = K \left(\frac{-1}{y} \right) \mathbf{W}_{-1} \left(\frac{-y}{e} \right) \left(-2 - \mathbf{W}_{-1} \left(-\frac{y}{e} \right) \right) \quad (6.32)$$

Also substituting $\left[\ln \left[-\frac{1}{y} \mathbf{W} \left(-\frac{y}{e} \right) \right] - 1 \right] = -2 - \mathbf{W} \left(-\frac{y}{e} \right)$ in Equation (6.31) we have

$$\Delta G_0^* = K \left(\frac{-1}{y} \right) \mathbf{W}_0 \left(\frac{-y}{e} \right) \left(-2 - \mathbf{W}_0 \left(-\frac{y}{e} \right) \right) \quad (6.33)$$

A series expansion of \mathbf{W}_0 can be done at the branch point $\frac{-1}{e}$, by defining $p = \sqrt{2(1-y)}$ [196] where $y = \tau/\tau_0$ resulting in:

$$\mathbf{W}_0(z) = -1 + p - \frac{p^2}{3} + \frac{11p^3}{72} + \dots \quad (6.34)$$

Now multiplying both sides of Equation (6.33) by $\frac{y}{K}$ and performing the above series expansion we have

$$\begin{aligned} \frac{y\Delta G_0^*}{K} &= -1 - \sqrt{2(1-y)} + \frac{2}{3}(1-y) - \frac{11 \times 2^{3/2}}{72}(1-y)^{3/2} + \dots \\ &+ \sqrt{2(1-y)} + 2(1-y) - \frac{2\sqrt{2}}{3}(1-y)^{3/2} + \frac{11 \times 2^2}{72}(1-y)^2 + \dots \\ &- \frac{2}{3}(1-y) - \frac{2\sqrt{2}}{3}(1-y)^{3/2} + \frac{4}{9}(1-y)^2 - \frac{11 \times 2^{5/2}}{72}(1-y)^{5/2} + \dots \\ &+ \frac{11 \times 2^{3/2}}{72}(1-y)^{3/2} + \frac{11 \times 2^2}{72}(1-y)^2 - \frac{11 \times 2^{5/2}}{72}(1-y)^{5/2} + \\ &\qquad \qquad \qquad \left(\frac{11 \times 2^{3/2}}{72} \right)^2 (1-y)^3 + \dots \end{aligned} \quad (6.35)$$

Also multiplying both sides of Equation (6.32) by $\frac{y}{K}$ and performing the same series expansion we have

$$\begin{aligned}
\frac{y\Delta G_0^*}{K} &= -1 - \sqrt{2(1-y)} + \frac{2}{3}(1-y) + \frac{11 \times 2^{3/2}}{72}(1-y)^{3/2} + \dots \\
&\quad - \sqrt{2(1-y)} + 2(1-y) + \frac{2\sqrt{2}}{3}(1-y)^{3/2} + \frac{11 \times 2^2}{72}(1-y)^2 + \dots \\
&\quad - \frac{2}{3}(1-y) + \frac{2\sqrt{2}}{3}(1-y)^{3/2} + \frac{4}{9}(1-y)^2 + \frac{11 \times 2^{5/2}}{72}(1-y)^{5/2} + \dots \\
&\quad - \frac{11 \times 2^{3/2}}{72}(1-y)^{3/2} + \frac{11 \times 2^2}{72}(1-y)^2 + \frac{11 \times 2^{5/2}}{72}(1-y)^{5/2} + \\
&\quad \quad \quad \left(\frac{11 \times 2^{3/2}}{72}\right)^2 (1-y)^3 + \dots \quad (6.36)
\end{aligned}$$

Now subtracting Equation (6.35) from Equation (6.36)

$$\begin{aligned}
\frac{y}{K} (\Delta G_{-1}^* - \Delta G_0^*) &= \frac{2^{5/2} \times 11}{72}(1-y)^{3/2} + \frac{4\sqrt{2}}{3}(1-y)^{3/2} + \frac{4\sqrt{2}}{3}(1-y)^{3/2} + \\
&\quad \frac{4 \times 11 \times 2^{3/2}}{72 \times 3}(1-y)^{5/2} - \frac{2^{5/2} \times 11}{72}(1-y)^{3/2} + \frac{4 \times 11 \times 2^{3/2}}{72 \times 3}(1-y)^{5/2} + \dots
\end{aligned}$$

Rearranging the above equation and substituting from Equation (6.27) we obtain

$$\Delta G^\dagger = K \left[\frac{8\sqrt{2}}{3} \frac{(1-y)^{3/2}}{y} + \frac{8 \times 11 \times 2^{3/2}}{72 \times 3} \frac{(1-y)^{5/2}}{y} + \dots \right] \quad (6.37)$$

Now we see that there is a $\frac{1}{y}$ term in the above equation. We can perform Taylor expansion of this term near $y = 1$ as

$$\frac{1}{y} = 1 + (1-y) + (1-y)^2 + (1-y)^3 + \dots$$

Substituting this expansion for $\frac{1}{y}$ in Equation (6.37) we arrive at our final expression for ΔG^\dagger :

$$\begin{aligned}
\Delta G^\dagger &= K \left[\frac{8\sqrt{2}}{3} (1-y)^{3/2} \left(1 - (1-y) + (1-y)^2 - \dots \right) + \right. \\
&\quad \left. \frac{11\sqrt{2}}{54} (1-y)^{5/2} \left(1 - (1-y) + (1-y)^2 - \dots \right) \right]
\end{aligned}$$

which is the same as Equation 6.28 exhibiting $\Delta G^\ddagger \propto \left(1 - \frac{\tau}{\tau_0}\right)^{3/2}$ as $\tau \rightarrow \tau_0$.

This result, even though it auspiciously matches the energy barrier scaling prediction from the catastrophe theory, is fortuitous. This is because the conditions under which the universal exponent was derived are not met in this problem. First, the derivation of the universal exponent of $\frac{3}{2}$ assumes smoothness of the free energy barrier near the collapse. However, in this example the free energy is not smooth, it has a branch point at the athermal limit which negates any universal exponent behavior. Thus, we should not expect agreement of the exponents.

Another reason, which is perhaps more important, is that standard catastrophe theory assumes the driving force is assumed to be linear in the reaction coordinate [195]. However, this is not appropriate for dislocation nucleation. The generalized driving force is the stress τ , which in nucleation, scales with the area and thus for a circular loop, R^2 .

To extend the ideas of developed previously in catastrophe theory specifically to dislocation nucleation we consider a general form for the activation Gibbs free energy for nucleation, ΔG^* as:

$$\Delta G(\tau, R) = f(R) - \frac{1}{2}\tau R^2 \quad (6.38)$$

with the assumption, for a simple model, that the Burgers vector b is a constant. The function $f(R)$ represents the line energy of the dislocation nucleus which presumably is quadratic in R near $R = 0$ and linear in R for large R . We will further assume that the function $f(R)$ is smooth. We have dropped some of the constants (such as a factor of 2π) for simplicity.

The minimum of the function is assumed to occur at $R = 0$ and the saddle can be found by taking $\frac{\partial \Delta G}{\partial R}(R, \tau) = 0$ which results in:

$$\tau = \frac{1}{R^*} f'(R^*)$$

and provides a relationship between the stress and radius at the saddle point. This can be substituted back into the Gibbs free energy equation to obtain:

$$\Delta G^* = f(R^*) - \frac{1}{2}R^* f'(R^*) \quad (6.39)$$

However, again we need to write this equation in terms of τ and the athermal strength τ_0 , notably in terms of $\left(1 - \frac{\tau}{\tau_0}\right)$.

The athermal strength can be defined as stress at which $R^* \rightarrow 0$. This can be obtained by examining the functional form of $f(R)$ for small R which, based on our previous assumptions, is:

$$f(R^*) = a_2 R^{*2} + a_3 R^{*3} + a_4 R^{*4} \dots \quad (6.40)$$

Thus, the athermal strength is:

$$\begin{aligned} \tau_0 &= \lim_{R^* \rightarrow 0} \frac{1}{R^*} f'(R^*) \\ &= 2a_2 = f''(0) \end{aligned}$$

This allows us to write an expression for $\left(1 - \frac{\tau}{\tau_0}\right)$ as:

$$\begin{aligned} 1 - \frac{\tau}{\tau_0} &= 1 - \frac{f'(R^*)}{R f''(R^*)} \\ &= -\frac{3}{2} \frac{a_3}{a_2} R^* - 2 \frac{a_4}{a_2} R^{*2} - \dots \end{aligned}$$

Which, for sufficiently small R^* , is:

$$R^* = -\frac{2}{3} \frac{a_2}{a_3} \left(1 - \frac{\tau}{\tau_0}\right) \quad (6.41)$$

Now, substituting Equation (6.41) into Equation (6.39) we have:

$$\Delta G^*(R^*) = \frac{1}{2}a_3 \left[\frac{2}{3} \frac{a_2}{a_3} \left(1 - \frac{\tau}{\tau_0} \right) \right]^3 - a_4 \left[\frac{2}{3} \frac{a_2}{a_3} \left(1 - \frac{\tau}{\tau_0} \right) \right]^4 + \dots$$

So, for small R^*

$$\Delta G^* \propto \left(1 - \frac{\tau}{\tau_0} \right)^3$$

If an $f(R)$ is chosen such that $a_3 = 0$, e.g. $f(R)$ is an even function about $R = 0$, then the R^* scales with $\left(1 - \frac{\tau}{\tau_0} \right)^{1/2}$ which results in

$$\Delta G^* \propto \left(1 - \frac{\tau}{\tau_0} \right)^2$$

We verify these two scaling relations, first, by choosing an $f(R)$ such that it is consistent with our assumed power series expansion given in Equation (6.40) at $R^* = 0$:

$$\begin{aligned} f(R) &= R \tanh \left(\frac{R}{r_c} \right) + R^2 \exp \left(\frac{-R}{r_c} \right) \\ &= \left(1 + \frac{1}{r_c} \right) R^2 - \frac{R^3}{r_c} + \frac{(3r_c - 2)R^4}{6r_c^3} + \dots \end{aligned}$$

To verify this, the saddle point ($\frac{d\Delta G}{dR} = 0$), is computed relative to the minimum and examined as $\tau \rightarrow \tau_0$ which results in a numerical result of:

$$\Delta G^* \propto \left(1 - \frac{\tau}{\tau_0} \right)^3$$

The exponential term is included above because it ensures that the equation has a cubic term, resulting in an exponent of three. If we eliminate this term, $f(R^*) = R^* \tanh(R^*/r_c)$ is even and

hence lacks all odd exponents. Numerical analysis demonstrate that the free energy scales as:

$$\Delta G^* \propto \left(1 - \frac{\tau}{\tau_0}\right)^2 \quad (6.42)$$

in agreement with the results of the power series expansion.

Thus, it is clear that scaling of the activation free energy with the applied stress varies with the choice of line tension term and the continuity of that term at the bifurcation point as we have seen exponents of 2, 3 and, in one special case, 1.5. While this behavior does not contradict the atomistic data presented above (the lack of a universal exponent), this result may still be an artifact of the simple nature of model. The athermal strength, τ_0 , is set artificially by a cutoff radius or regularization parameter, r_c , instead of the more common notion that $\tau \rightarrow \tau_0$ as the Burgers vector, $b \rightarrow 0$. This is precluded in the simple model since the Burgers vector is held constant. Thus, our analyzed behavior near $\tau = \tau_0$ may be an artifact of fixing the Burgers vector and an improved model where b is a variable is needed to better understand how ΔG^* should behave near the athermal limit.

To examine the shortcomings of the first continuum model, we also analyze an augmented model where the variable Burgers vector, b_f , is allowed to vary between 0 and b_0 , again following the ideas of Aubry et al. but with a line tension term of $R \tanh(R/r_c)$ which is the same $f(R)$ we have used in our generalized simple model that produces $\alpha = 2$. The change in free energy in this model due to the nucleation of a circular dislocation loop is:

$$\Delta G(\tau, R, b_f) = \frac{\mu b_f^2}{4} \frac{2 - \nu}{1 - \nu} R \tanh \frac{R}{r_c} - \tau b_f \pi R^2 + \pi R^2 [\gamma(u_0 + b_f) - \gamma(u_0)] \quad (6.43)$$

where γ is the GSF energy and the displacement, u_0 , along the Burgers vector direction can be determined by equating the derivative of the GSF energy and the applied stress: $\left. \frac{d\gamma}{du} \right|_{u_0} - \tau = 0$ [126]. For the purpose of examining general nucleation, we choose to first analyze the nucleation of a perfect dislocation. In this case, the GSF curve can be readily modeled with a sinusoidal function as: $\gamma(u) = \frac{\gamma_0}{2} \left[1 - \cos \left(\frac{2\pi u}{b_0} \right) \right]$. We were unable to find an analytical solution for the activation

free energy, so a numerical approach is used. In order to numerically solve for the saddle point ΔG^* , the material constants were non-dimensionalized in the above equation (Equation (6.43)) as follows: $\mu = 4\pi^2$, $\nu = 0.0$, $b_0 = 1.0$, $r_c = 1.0$, $\gamma_0 = \frac{1}{2\pi}$. τ_0 can be determined by finding the maximum stress the crystal can withstand, defined by the GSF curve, prior to rigid sliding of the crystal. This is the maximum of $\frac{d\gamma}{du}$, which can be solved analytically as: $\tau_0 = \pi \frac{\gamma_0}{b_0}$. The value of τ can be related to the GSF curve as noted above, as: $\tau = \left. \frac{d\gamma}{du} \right|_{u_0}$.

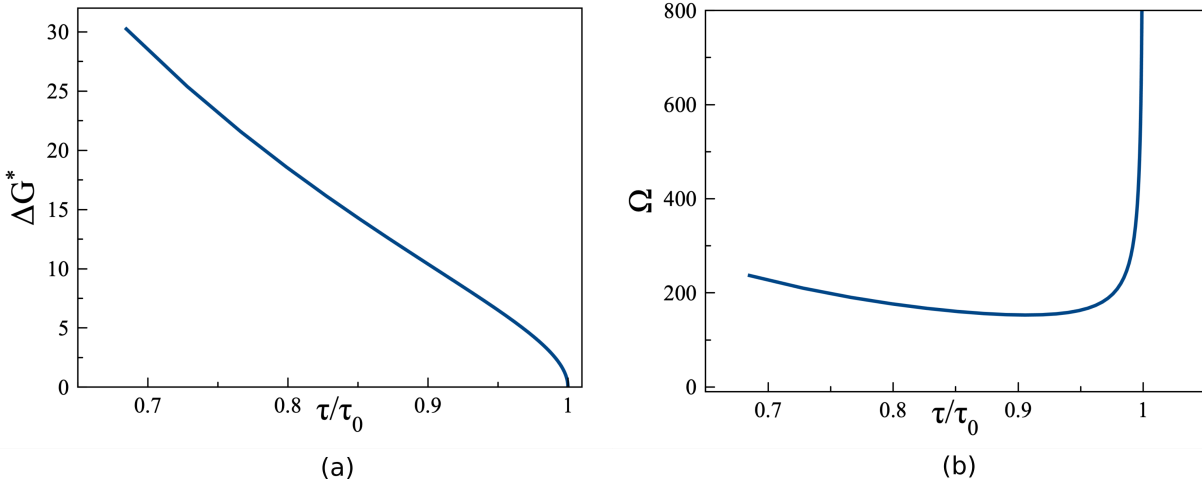


Figure 6.4: (a) The activation free energy barrier vs. stress behavior for homogeneous dislocation nucleation for the model with variable Burgers vector, i.e. model 2. Activation energies are calculated from Equation (6.43). (b) The activation volume vs. stress behavior for dislocation nucleation for the augmented model proposed in Equation (6.43).

Now, to find the activation Gibbs free energy ΔG^* which is the saddle point of $\Delta G(b_f, R, \tau)$ we differentiate Equation (6.43) with respect to both R and b_f . Then, we set $\frac{\partial \Delta G}{\partial b_f} = 0$ and $\frac{\partial \Delta G}{\partial R} = 0$. The two equations $\frac{\partial \Delta G}{\partial R} = 0$ and $\frac{\partial \Delta G}{\partial b} = 0$ were numerically solved using the Newton-Raphson method.

To explore how the line tension argument affects this new exponent, α , we carried out a similar numerical analysis of the augmented model with an alternative line energy term which is the same

$f(R)$ we have used in our generalized simple model that produces $\alpha = 3$ as:

$$\Delta G(\tau, R, b_f) = \frac{\mu b_f^2}{4} \frac{2 - \nu}{1 - \nu} \left(R \tanh(R/r_c) + R^2 \exp(-R/r_c) \right) - \tau b_f \pi R^2 + \pi R^2 [\gamma(u_0 + b_f) - \gamma(u_0)]$$

A similar analysis of this model also gives rise to $\alpha = 0.5$ for this version of the augmented model. Finally, we have also analyzed the case in which the dislocation energy term is linear in R , i.e. $\frac{\mu b_f^2}{4} \frac{2 - \nu}{1 - \nu} R$, which also results in an $\alpha = 0.5$. Thus we infer that $\alpha = \frac{1}{2}$ is relatively invariant to the choice of the line tension term as long as ΔG is continuous when the saddle meets the minimum. We further point out that the results are not dependent on the choices of r_c or γ_0 in this model, the exponents remain the same.

At this point, we return to the augmented model proposed by Jennings et al. in [126]:

$$\Delta G(\tau, R, b_f) = \frac{\mu b_f^2}{4} \frac{2 - \nu}{1 - \nu} R \ln \frac{R}{r_c} - \tau b_f \pi R^2 + \pi R^2 [\gamma(u_0 + b_f) - \gamma(u_0)] \quad (6.44)$$

The simple version of this model, which does not include the generalized stacking fault energy penalty term, introduces an artificial minimum. This required the introduction of ΔG^\dagger , which was the difference between the saddle (maximum) and the artificial minimum, which was discontinuous at the athermal limit and resulted in an exponent of 1.5. As we will demonstrate later, the function ΔG as represented by Equation (6.44) does not have a local minimum. Instead there is only a saddle point and a local maximum at $(R, b_f) = (0, 0)$ for all $\tau \leq \tau_0$. The local minimum artificially introduced by the logarithm term is no longer a minimum but creates a path in which there is no free energy barrier for dislocation nucleation as the Burgers vector can grow unbounded.

To illustrate this behavior, consider a numerical implementation of Equation (6.44). For this example, we consider the numerical case where $\tau = 0.684\tau_0$, $\mu = 4\pi^2$, $\nu = 0.0$, $b_0 = 1.0$, $r_c = 1.0$. The GSF term is described by $\gamma(u) = \frac{\gamma_0}{2} \left[1 - \cos \left(\frac{2\pi u}{b_0} \right) \right]$ as before with $\gamma_0 = \frac{1}{2\pi}$. A contour plot of ΔG as a function of R and b is shown Figure 6.5 which shows that for small R , as the Burgers vector is increased ΔG continuously decreases (Figure 6.5(b)). While this is certainly mathemat-

ically possible, it is often ignored as a artifact in the dislocation model. Never-the-less, it makes the $(R, b_f) = (0, 0)$ a maximum and not a minimum due to the ability to decrease the free energy by increasing R .

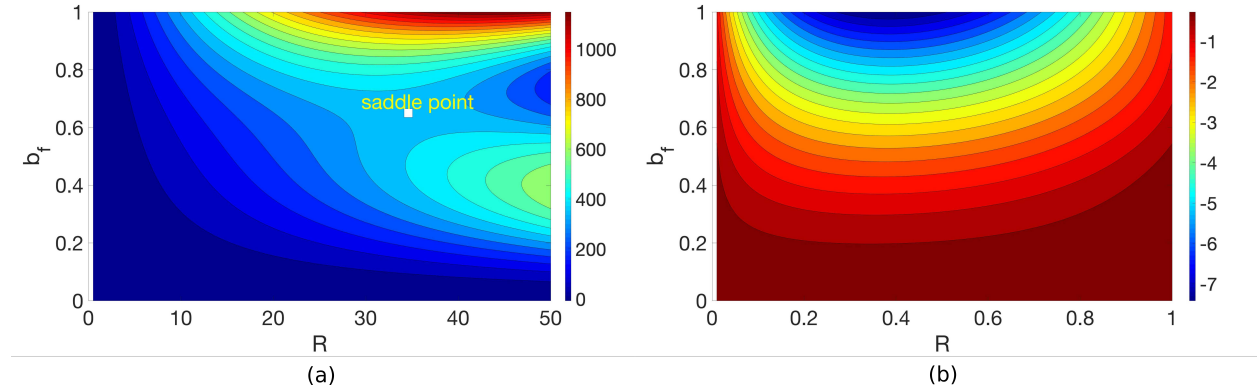


Figure 6.5: (a) A contour plot of the free energy surface, $\Delta G(R, b_f)$ modeled as Equation (6.44) for $\frac{\tau}{\tau_0} = 0.683$ over the range $R \in [0, 50]$ and $b \in [0, 1]$. (b) the free energy surface over the range $R \in [0, 1]$ and $b \in [0, 1]$

Despite the obvious mathematical issues with this model, it is still insightful to examine how the saddle approaches the $(R, b_f) = (0, 0)$ maximum as this has been regularly used in modeling dislocation nucleation. The solution strategy is the exact same as that used for the other models with varying Burgers vectors. The two key peices of information obtained from the analysis are shown in Figure 6.6 , the behavior of the activation volume and a plot of the effective exponent. Just as occurred in the other cases, the activation volume diverges when the stress reaches the athermal limit. Figure 6.6(b) shows that as the stress reaches the athermal limit, the exponent approaches a value of approximately 0.4, distinctly different from that of the other models with variable Burgers vectors in which the exponent was 0.5. The difference in exponents between the models appears to be a result of the $(R, b_f) = (0, 0)$ point being a maximum in this case, as opposed to a minimum in the case of the other models. To illustrate more clearly the differences in the free energy models, consider a contour plot of the free energy using the model of Equation (6.43) as shwon in Figure 6.7 . This figure shows in this case there is a clear saddle and that the point $(R, b_f) = (0, 0)$ is

indeed the local minimum. A zoomed in region near the origin, Figure 6.7(b), confirms that the function is a minimum at the origin.

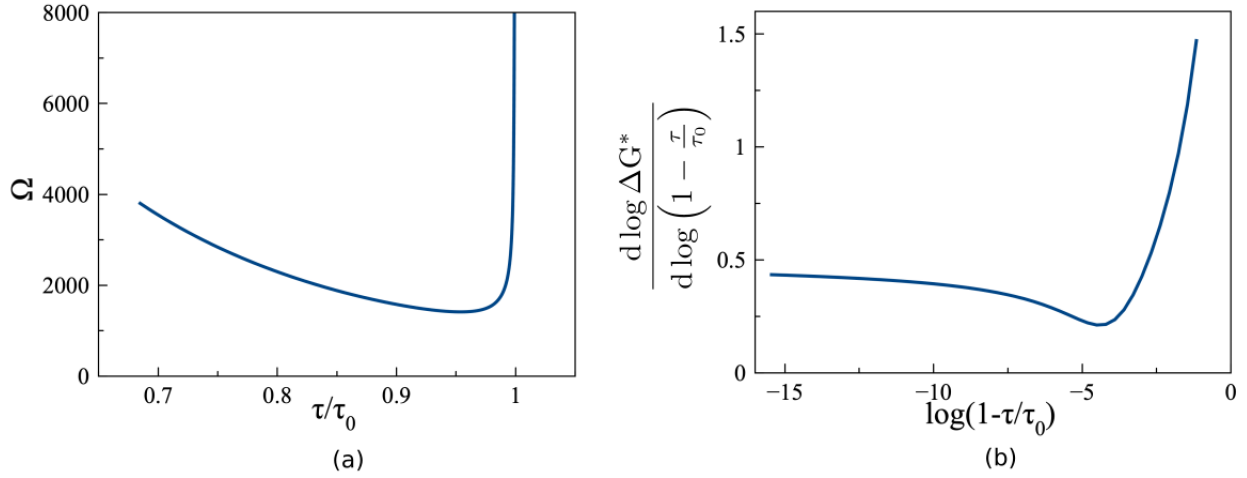


Figure 6.6: (a) The activation volume vs. stress behavior for dislocation nucleation modeled by Equation (6.44). (b) A log-log plot of $\frac{d \log \Delta G^*}{d \log(1 - \frac{\tau}{\tau_0})}$ as a function of $(1 - \frac{\tau}{\tau_0})$ for the augmented model of Equation (6.44). The exponent α approaches a value of 0.4 as $\tau \rightarrow \tau_0$.

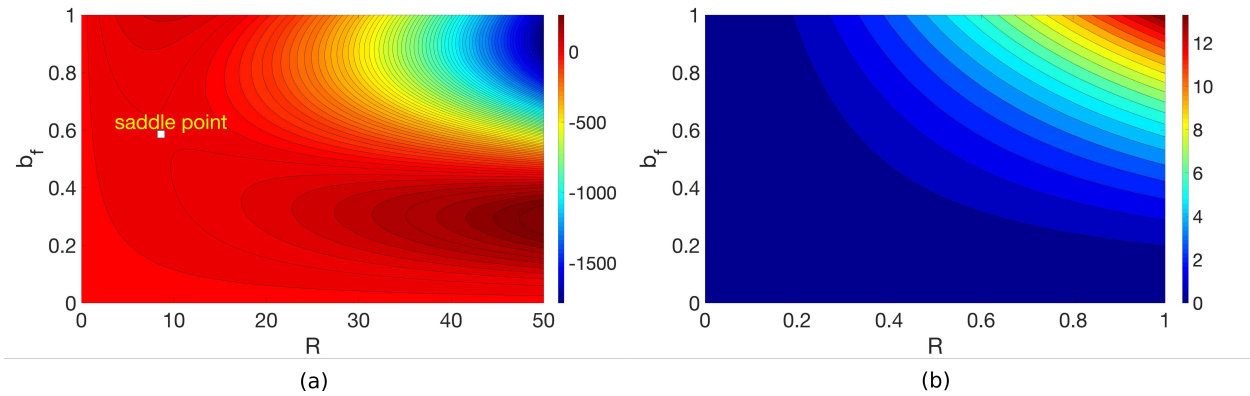


Figure 6.7: (a) A contour plot of the free energy surface, $\Delta G(R, b_f)$ modeled as Equation (6.43) for $\frac{\tau}{\tau_0} = 0.683$ over the range $R \in [0, 50]$ and $b \in [0, 1]$. (b) the free energy surface over the range $R \in [0, 1]$ and $b \in [0, 1]$

To ensure the generality of our results, we have also computed the exponents for different GSF terms. For example, models of the dislocation nucleation process originally used a GSF term of the form $\gamma(u) = \frac{\gamma_0}{2} \left[1 - \cos\left(\frac{2\pi u}{b_0}\right) \right]$ where b_f represents the Burgers vector of a perfect dislocation.

Alternatively, we can also analyze the model with a GSF term that represents the nucleation of a partial dislocation, as Aubry et al. did [152]. To achieve this in our numerical implementation in which a continuous GSF is needed, we fit the GSF curve for copper given in [152] using a 5th order polynomial with the first two coefficients set to zero. This GSF model was implemented into our free energy calculations and while the numerical values of the free energies changed the extracted exponents did not.

For bulk plastic deformation [190, 191], dislocation nucleation [189] and transitions from elastic to inelastic deformation [192, 195, 197–199], it has been proposed that $\Delta G \propto (1 - \tau/\tau_0)^\alpha$ with a universal $\alpha = \frac{3}{2}$. In this work, we examined all previous atomistic data in which the energy barriers were explicitly computed from atomistic chain-of-states methods, and found the exponents varied between 0.8 and 5.8, indicating that there is little support for a universal exponent from such atomistic simulations. However, the analysis was performed on all available data and not necessarily just limited to the athermal limit and as such, we cannot refute a universal exponent for dislocation nucleation from available atomistic data.

To provide additional insight into the behavior of the activation free energy as a function of stress, we analyzed several continuum models of dislocation nucleation. For stress sufficiently far from the athermal limit, it is clear that an empirical model of the form $\Delta G = G_0(1 - \tau/\tau_0)^\alpha$ can be used and will predict a value of $\alpha > 1$, but this value is not a constant and will depend on the range of stresses used in the empirical fit. As for applied stress $\tau \rightarrow \tau_0$ the numerical value of the exponent will depend on the assumed form of the line energy as well as how the driving force scales with dislocation loop radius. For a defect-free crystal, where a dislocation has to be nucleated first to induce failure, the applied stress scales with R^{*2} since the stress is applied over the dislocation loop being nucleated. These considerations suggest that the equation (Equation (6.2)) introduced by Zhu et al. [163] is best described as an empirical relationship.

In the first class of continuum models we analyzed, the Burgers vector was held constant which allowed us to derive an analytic expressions for the activation free energy and activation volume as a function of stress by setting an artificial athermal strength. In all of the cases analyzed, the

exponent was greater than one and the activation free energy and activation volume decreased to zero at the athermal limit. The value of the exponent depended on the form of the line energy. For the line energy that scaled as $R \log(R/r_c)$, the exponent was $\frac{3}{2}$, a result of the lack of continuity when the saddle collides with the minimum. When the line energy is continuous, the exponent was found to be three if the line energy term has third order power in its expansion and a value of two if the first term in the expansion is fourth order. Presumably, other exponents would be found if the expansion of the free energy was missing the fourth order term in the expansion of the free energy.

In the second class of models, we allow the Burgers vector to change and include a energy penalty associated with the generalized stacking fault energy as a function of the Burgers vector. In this case, if the line energy creates a minimum at $R = 0$ and the function is smooth, the activation volume is found to diverge. The divergence of the activation volume is a result of the critical radius diverging while the Burgers vector goes to zero. The extracted activation energy exponent α is $\frac{1}{2}$. However, if the line energy includes the standard logarithm term, we find that the behavior is similar but that the exponent becomes roughly 0.4.

These exponents appear to violate catastrophe theory as well as our previous results regarding the general nature of exponents in dislocation nucleation. However, we should also note that the exponents derived in this way assume, as noted before, that the free energy is smooth when the saddle approaches the minimum. In the cases when the exponent is less than one, the radius diverges invalidating the assumptions made regarding smoothness. It is further clear that it is the introduction of the GSF term that causes the radius to diverge while allowing the Burgers vector to go to zero. The GSF term acts to cause the activation free energy to rapidly decrease to zero, which in turn causes the activation volume to diverge.

This raises a question regarding the divergence of the activation volume; can this be physical or is it a numerical artifact? We know that exponents that are larger than one as derived in our first class of models in which the Burgers vector is held constant, are indeed artifacts of the model. This is because the athermal strength in each case is directly related to r_c , a regularization constant used to create a smooth quadratic local minimum. However, in the cases where the Burgers vector

was allowed to change and $R \rightarrow \infty$, the result appears to be a physically meaningful result. As τ approaches the ideal strength, $b_f \rightarrow 0$ and thus the crystal is able to rigidly shear, which can readily occur over the whole crystal at once and thus physically represents $R \rightarrow \infty$. Thus, it is possible to accept the results obtained here on physical grounds, not just mathematical ones.

This then raises the question of what is the correct exponent in the athermal limit, the value of $\frac{1}{2}$ or the value of roughly 0.4. While we cannot say for sure, we can speculate that the value of $\frac{1}{2}$ appears more appropriate. As noted previously, all the models that have a minimum at ($R = 0, b_f = 0$) also have an exponent of $\frac{1}{2}$. The only exception is the model with the $R \log(R/r_c)$ line energy term which, as stated before, has some numerical artifacts as a result of the logarithm term. Given that the logarithm may not be representative of the energy for R values less than r_c physically, the free energy near the athermal limit may not be particularly accurate for dislocation nucleation. Thus, we speculate that the exponent of $\frac{1}{2}$ is the most likely correct exponent for dislocation nucleation.

While the detailed continuum models provide some insight into how the activation energy and activation volume behave very close to the athermal limit, these results may not, at first, appear particularly relevant to actually modeling dislocation nucleation. However, these results, in conjunction with the atomistic modeling results, do offer some important insights into empirical modeling of the activation energy equations. To better understand this, consider the empirical activation energy equation proposed by Zhu et al [182]. The assumed form of the activation energy predicts an activation volume of: $\Omega = \frac{E_0 \alpha}{\tau_0} (1 - \tau/\tau_0)^{\alpha-1} (1 - T/T_m)$. This particular form almost entirely precludes the possibility of having a constant activation volume at $\tau \rightarrow \tau_0$. If we examine the results of our continuum model the activation volume goes to a constant before sharply diverging. Similar conclusions can be drawn by visual examination of the activation energy plots from direct atomistics, as shown earlier: the activation volume appears to approach a constant. This suggest that empirically fitting the activation volume to an equation that enforces the activation volume to go to zero in the athermal limit can cause numerical issues in the modeling dislocation nucleation, especially when the activation volume is determined and integrated to the activation

energy. If this is the case, it would appear choosing an empirical form for the activation energy that can accommodate a non-zero activation volume at the athermal limit is beneficial. Such a form has been proposed by Weinberger et al. [125], although this is not the only form that one could suggest.

6.2 Continuum model of twin nucleation in BCC transition metals

As discussed earlier, any defect nucleation phenomenon is controlled by the energy barrier associated with nucleation of the defect [200]. Free-end string simulations are employed in this study not only to observe twin nucleation in bulk BCC crystals described by EAM potentials but also these simulations provide us with energy barrier for twin nucleation as a function of applied pure shear stress. However, string simulations with available EAM potentials for BCC Nb, V, and Cr were not performed because numerical issues perhaps caused by fitting of parameters with equilibrium properties. To calculate the energy barrier for twin nucleation in all BCC transition metals it is imperative that analytical models are developed for twin nucleation based on continuum theory so that energy barriers can be computed for BCC metals that are modeled by imperfect EAM potentials. More importantly, since our DFT computations indicate that two layer twins are the critical twin nuclei in BCC transition metals as opposed to one and three layer twins predicted by EAM potentials, we can compute the energy barrier for twin nucleation using DFT inputs by developing a robust analytic model. The idea is that the model will describe the activation Gibbs free energy in terms of dislocation loop size and Burgers vector at specified applied stresses as discussed in Chapter 5. To determine the activation energy of the dislocation nucleation process, the saddle point between the nanocrystal without a dislocation (the pristine crystal) and dislocated crystal needs to be found. The number of mechanically stable layers with the lowest energy barrier then determines the critical size of twin nucleus. The analytical model is developed for homogeneous nucleation because we can compare the predicted energy barriers with the energy barriers from our string simulations.

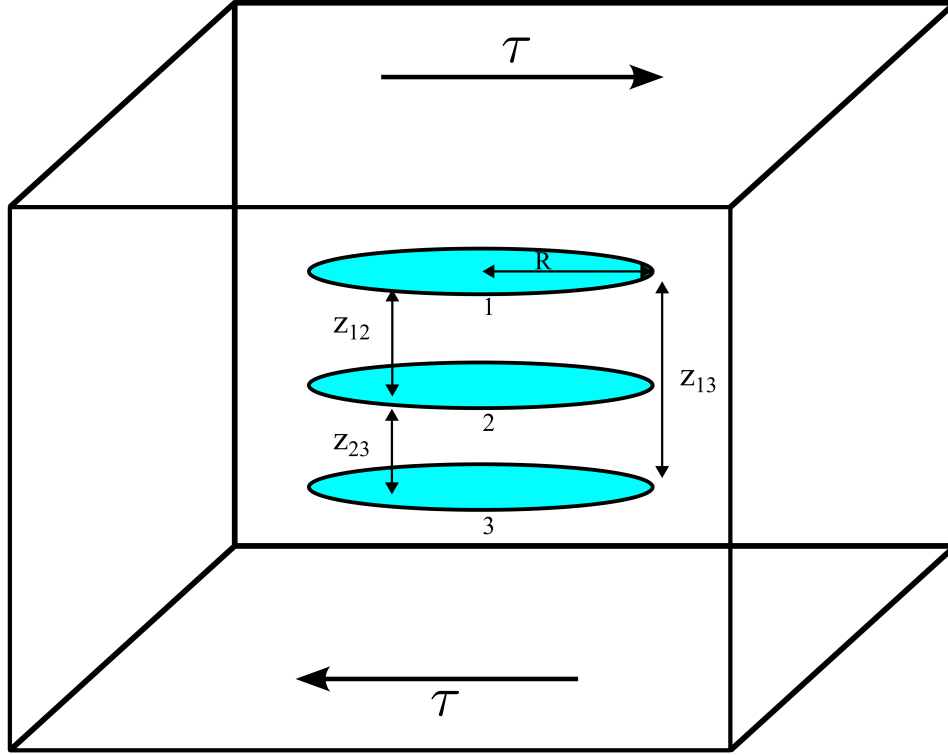


Figure 6.8: Three twinning dislocation loops (denoted by numbers 1, 2 and 3) nucleated in bulk BCC crystal. The loops have equal Radii, R and they are separated by distance z_{ij} . The displacement (Burgers vector) associated with each loop is determined from twin structures found or produced in string or DFT simulations.

Hirth and Lothe [141] introduced a simple model of the activation Gibbs free energy of dislocation nucleation in terms of the increase in energy associated with the line length of the dislocation, the stacking fault energy, and the work done in the nucleation of the dislocation. Following this, simple model for homogeneous nucleation of a circular dislocation loop, the increase in Gibbs free energy under pure shear can be written as:

$$\Delta G(\tau, R) = \frac{\mu b^2}{4} \frac{2 - \nu}{1 - \nu} R \ln \frac{R}{r_c} + \pi R^2 \gamma_{sf} - \tau b \pi R^2 \quad (6.45)$$

Here it is assumed that the dislocation loop is circular with a radius R (see Figure 6.8), r_c is the inner cutoff radius, γ_{sf} is the stacking fault energy and the material is linear elastic with shear modulus μ and ν is the Poisson's ratio. Since our goal is to use this model for twin nucleation, the Burgers vector b in Equation 6.45 is equal to the magnitude of the twinning partial dislocation.

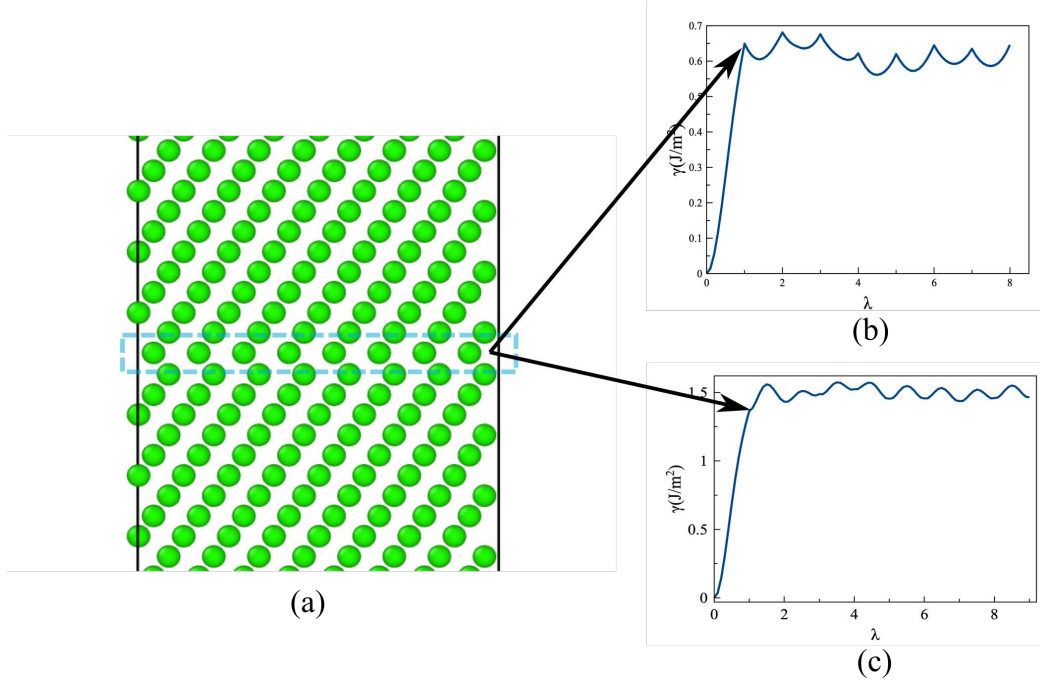


Figure 6.9: (a) a single layer fault produced from rigidly translating a pure BCC crystal by an amount $\frac{a}{6}\langle 111 \rangle$, (b) TGSF curve for Ta and (c) TGSF curve for W with relative displacement, $\lambda = \frac{u}{b_p}$ where u is any arbitrary amount of displacement and $b_p = \frac{a}{6}\langle 111 \rangle$ is the twinning partial, in the horizontal axis and the stacking fault energy γ in the vertical axis.

The activation Gibbs free energy ΔG^* is typically taken as the saddle of the $\Delta G(\tau, R)$ and can be found by solving $\frac{d\Delta G}{dR} = 0$. However, if more than one dislocation loops are nucleated which is the case for deformation twinning, these dislocations will interact with each other. To incorporate the interactions between nucleated dislocations, we must include the elastic interaction terms between the twinning partials in Equation 6.45:

$$\Delta G(\tau, R) = \sum_i \frac{\mu b_i^2}{4} \frac{2-\nu}{1-\nu} R \ln \frac{R}{r_c} + \sum_i \pi R^2 \gamma_{sf,i} - \sum_i \tau b_i \pi R^2 + \sum_i \frac{\mu b_i b_j R k}{1-\nu} (K(k) - E(k)) \quad (6.46)$$

where $k^2 = \frac{4R^2}{z^2 + 4R^2}$ with z being the distance between dislocation loops. Furthermore, K and E are the complete elliptic integrals of the first and second kind [141], respectively. This model is more complex than Equation 6.45 hence no analytical solution is possible. The energy barrier can be found by using the Nelder-Mead simplex algorithm as described in Lagarias et al. [201].

Energy barrier calculations from the model described by Equation 6.46 predicts that the lowest energy barrier is associated with a single dislocation loop in BCC metals. However, the twinning GSF curves shown in Figures 6.9 (b) and (c) clearly show that a one layer fault (aka single dislocation loop) is unstable in both Ta and W. Moreover, the twinning GSF curve (Figure 6.9 (b)) for BCC Ta shows that a two layer thick twin with isosceles boundary structure is also unstable. Hence energy barriers were computed by finding the saddle point for the model represented by Equation 6.46 as a function of applied shear stress for three, four, five and six twinning dislocation loops in BCC Ta assuming two isosceles TBs. From Figure 6.10, we see that the energy barrier as well as the nucleation strength predicted by the model increases with the number of twinning dislocation loops. Hence the smallest size of stable twin nucleus is three layers thick with isosceles twin boundary structure which implies a total displacement of $2b_p = 2b_t = \frac{2b}{3}$. This is also supported by the TGSF curve (Figure 6.9 (b)) where the first metastable point also represents a three layers thick twin nucleus with isosceles twin boundary.

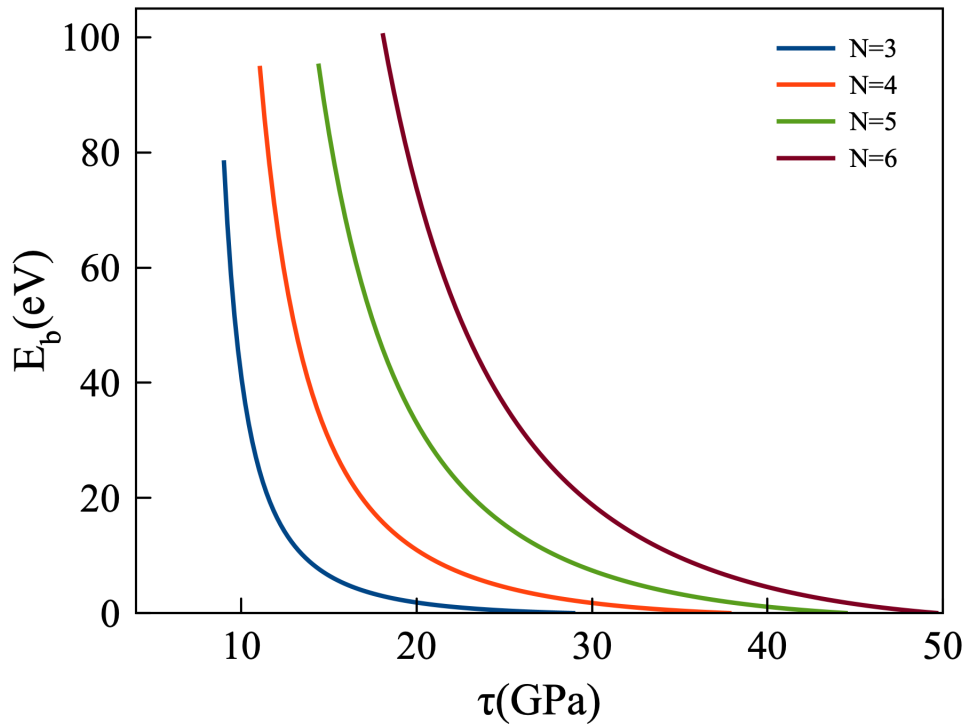


Figure 6.10: Energy barrier vs stress in BCC Ta for varying number of twinning dislocation loops calculated by finding saddle points for Equation 6.46.

The analytical model developed for homogeneous nucleation of twinning dislocation loops in Equation 6.46 can be improved by incorporating a variable magnitude of the Burgers vector that goes from 0 to b . The concept of variable Burgers vector originates from the Peierls-Nabarro model of dislocation [202, 203] and recently Aubry et al. [152] showed that by incorporating a variable Burgers vector in Equation 6.45, the energy barrier computation closely approximates the energy barrier of homogeneous dislocation nucleation predicted by explicit atomistic calculations. Aubry et al. also showed that a stress dependent stacking fault energy term improves the model in Equation 6.45 for homogeneous nucleation of single dislocation loops. Hence the augmented model in Equation 6.46 can be further enhanced by including a stress dependent stacking fault energy term. The energy barrier calculations shown in Figure 6.10 is carried out for BCC Ta only and so the model in Equation 6.46 along with the improvements discussed can also be applied for the other BCC metals in consideration.

Another important observation by inspecting the snapshots of the string simulations is that twinning is initiated by concurrent nucleation of twinning dislocation loops. If this indeed is the case, sequential TGSF curves, even though useful in determining twin stability in BCC transition metals, do not model the lattice resistance accurately. For this reason, the analytic model developed here will employ concurrent TGSF curves described in Chapter 3. The robust model we propose can be written as:

$$\Delta G(\tau, R, b) = \sum_i \frac{\mu b_i^2}{4} \frac{2-\nu}{1-\nu} R \ln \frac{R}{r_c} + \pi R^2 \left[\gamma \left(u_0 + \sum_i b_i \right) - \gamma(u_0) \right] - \sum_i \tau b_i \pi R^2 + \sum_i \frac{\mu b_i b_j R^2}{4(1-\nu)} [(2-\nu)I_1 - z^2 I_2] \quad (6.47)$$

where $I_1 = 2 \frac{k}{\sqrt{R^2}} \left(\frac{2-k^2}{k^2} K(k) - \frac{2}{k^2} E(k) \right)$, $I_2 = \frac{k^3}{\sqrt{R^{3/2}}} \left(\frac{-1}{k^2} K(k) + \frac{2-k^2}{2k^2(1-k^2)} E(k) \right)$ and γ is the concurrent TGSF term. This model is capable of closely fitting the Energy barrier vs stress data obtained from the sting simulations in Ta-Ravelo2 as shown in Figure 6.11.

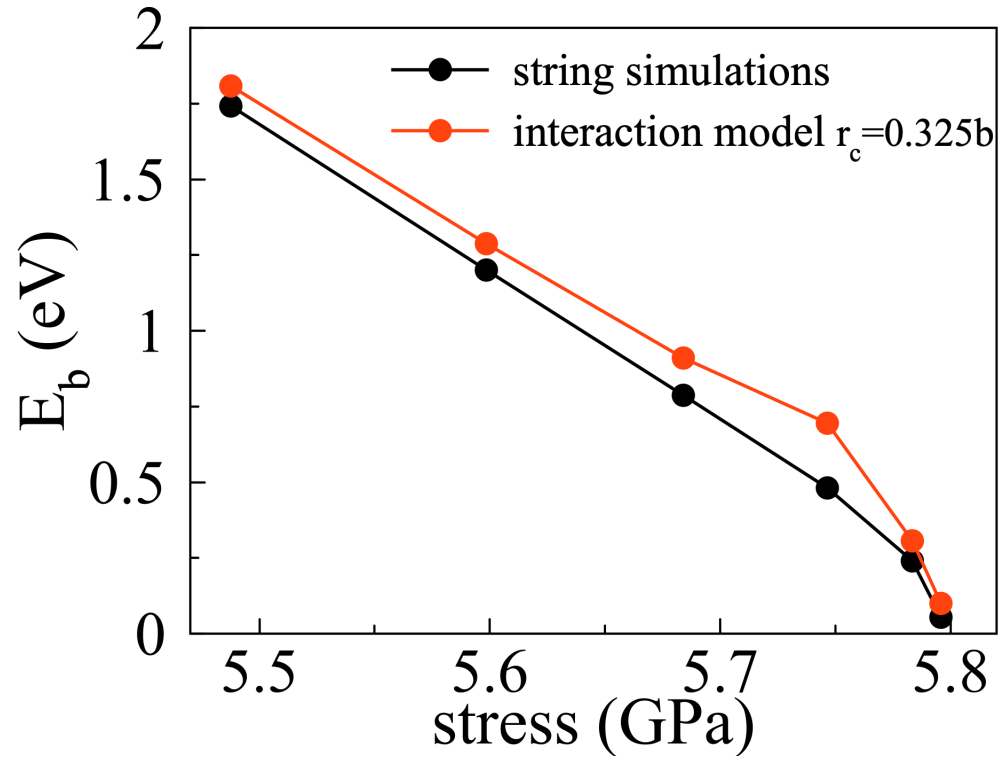


Figure 6.11: Energy barrier vs stress in BCC Ta modeled by Ravelo2 potential. The energy barrier predictions from the continuum model is very close to the string simulations.

The model in Equation 6.47 also models the energy barriers for twin nucleation as a function of applied stress for BCC Fe described by the Fe-ATFS potential. This is shown in Figure 6.12.

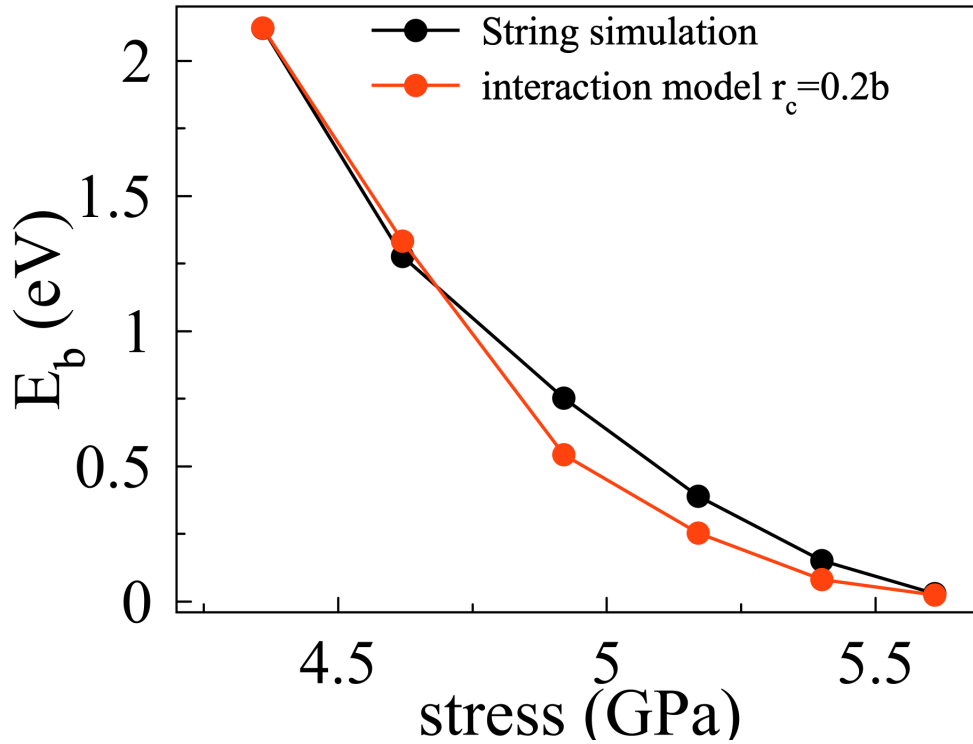


Figure 6.12: Energy barrier vs stress in BCC Ta modeled by Ravelo2 potential. The energy barrier predictions from the continuum model is very close to the string simulations.

In conclusion, our continuum model (Equation 6.47) is capable of matching energy barrier vs stress data from string simulations. This model incorporates variable burgers vector, concurrent TGSF curve data from DFT simulations and elastic interaction between dislocation loops which makes it first of its kind to describe homogeneous twin nucleation in bulk BCC crystals.

Chapter 7

Modeling twinning stress in BCC transition metals

As discussed in Chapter 2 (Literature review), the existence and importance of a critical resolved shear stress for deformation twinning has been a topic of interest starting with Christian and Mahajan [3] arguing that the significance of a critical resolved shear stress (CRSS) may be negligible because of considerable variation in twinning stress depending on the nucleation mechanism. Homogeneous nucleation of twins requires the resolved shear stress on the composition plane resolved along the twinning direction to approach the theoretical strength of the material whereas for heterogeneous nucleation the stress required to nucleate twins are expected to be not as high and will depend on the nature of the defect/stress concentration that acts as the nucleation site. Also mentioned in Chapter 2, other factors such as the three dimensional non-planar geometry of dislocations in BCC metals [68], composition, pressure or temperature can play a role in twin nucleation and thus affecting the twinning stress.

Also outlined in Chapter 2, several mechanisms have been proposed for nucleation of twins in BCC metals such as the pole mechanism by Cottrell and Bilby [48], the slip dislocation interaction mechanism proposed by Priestner and Leslie [51], the screw dislocation core dissociation mechanism suggested by Sleeswyk [37] and Lagerlof [36] and the edge dislocation dissociation mechanism by Ogawa [50]. The twinning stress prediction from the pole mechanism is estimated to be around 1050 MPa for α -Fe which is at least five times higher than the experimental value of 206 MPa [22]. Sleeswyk's hypothesis yields a twinning stress close to 2.5 GPa for α -Fe. Ogawa's edge dislocation dissociation model a twinning stress of 430 MPa for α -Fe which is in the same order of magnitude for the experimental report however calculation of this stress involves empirical fitting of parameters which only applies to the particular experimental set up rather than generalizable parameters. A few papers [39, 42] on modeling twin nucleation stresses incorrectly points to the expression $\tau = \frac{\pi\gamma_{TBM}}{b_p}$ derived by Ogata et al. [63, 64] as the theoretical twinning stress model, however, it is clear from the expression itself that this stress prediction pertains to twin boundary

migration aka twin growth rather than twin nucleation. Meyers et al. proposed a model that takes grain size and Hall-Petch effects into consideration [69] and the twinning stress predictions they made were only fit to experimental data from a single paper [22] on Iron single crystals which is not a robust method for modeling. The modified Peierls-Nabarro formalism introduced by Ojha et al. to predict twinning stresses in BCC transition metals [42] attempts to incorporate energy barriers from twinning GSF curves. However, in deriving their twinning stress expression Ojha et al. assumes equilibrium conditions for the twinning dislocations which cannot be the case during nucleation. Another issue with this work is the stacking fault energy term used in the analytical model as discussed in Chapter 2. Discrepancies in reported CRSS values in experimental literature and the predictions from nucleation models raises the question whether the bulk stress values obtained from experiments are the local stresses required for twin nucleation.

To address this, the upper and lower limits of twinning stress for twin nucleation are computed first and compared with the experimental values in Table 2.1. The upper and lower bounds for twinning stress can be useful in providing valuable insights into the validity of the modeling work done by Ojha et al. [39, 42] where they compute twinning stresses and compared these stresses to experimental values. Then, a semi-empirical expression is derived for predicting most probable dislocation nucleation strength in defect-free crystals [204]. The implicit solution to this semi-empirical expression can give us homogeneous nucleation stresses as a function of temperature and strain rate given energy barrier for homogeneous nucleation is computed and fed into the semi-empirical relation.

7.1 Upper and lower limits of twin nucleation stress

7.1.1 Upper bound

The concept of theoretical strength of materials was first introduced by J. Frenkel in 1926 [205]. Frenkel modeled the theoretical strength of a material by considering rigid slip of upper half of a crystal relative to the lower half. In this model, the maximum stress required for plastic deformation by slip was roughly $\frac{\mu}{10}$ where μ is the shear modulus. This prediction is many orders

of magnitude greater than the critical shear stress needed cause plastic flow in a typical metallic materials. This significant discrepancy led to the idea of dislocations almost simultaneously in 1934 by Taylor [206], Orowan [207] and Polanyi [202]. Continuum elasticity theory has been employed to describe dislocation properties and dislocation interactions at distances much larger compared to atomistic scales. However, continuum elasticity breaks down at the dislocation core and an atomistic description is required for the material specific, discrete atomic core structure of the dislocation. Peierls proposed a hybrid model [203] in which some of the details of the discrete dislocation core are incorporated in an essentially continuum framework. The analytic solution of this model, by Peierls and Nabarro [208], gave the first meaningful estimate of the lattice resistance to dislocation motion. The Peierls-Nabarro analytical solution is based on a sinusoidal approximation of the nonlinear stress term in terms of the displacement field similar to Frenkel's. Christian and Vitek [209] suggested that the nonlinear stress relation could be obtained from an effective interplanar potential, called the generalized stacking fault (GSF) energy, which can be calculated directly from interatomic force laws. The GSF energy provides a direct link between the PN continuum model of a dislocation and details of interatomic forces in the dislocation core. The PN model initially assumes a continuous dislocation energy functional which includes an elastic energy term as well as the energy cost for the misfit across the slip interface. However, in this formulation the dislocation energy functional is invariant with respect to arbitrary translation of the misfit density and the dislocation is a continuous object. As a consequence, the only effect of the lattice is that the misfit energy and the stress are periodic functions of the misfit with the lattice repeat period of Burgers vector. To regain the lattice discreteness, Peierls and Nabarro constructed a different form of the nonlinear potential where the misfit is not sampled continuously across the slip plane, but only at the positions of the atomic rows immediately adjacent to the slip plane. This discrete form of the misfit energy varies periodically as a function of translation and the amplitude of these periodic variations is identified as the Peierls energy and its maximum derivative with respect to translation as the Peierls stress [210]. The PN model was developed in order to analyze dislocation core structures as well as lattice resistance to dislocation motion for slip. However, the

concept of maximum derivative of misfit energy can also be applied to compute maximum stress required to nucleate twins homogeneously by taking the maximum derivative of the twinning GSF curves:

$$\tau_{\max} = \max \left(\frac{d\gamma_{\text{TGSF}}}{du} \right) \quad (7.1)$$

where γ_{TGSF} represents the array of stacking fault energies that generate the twinning GSF curves in BCC transition metals and u is the displacement in the $[11\bar{1}]$ direction.

Table 7.1: Maximum stresses computed from sequential TGSF curves and $\sigma - \epsilon$ curves.

BCC Transition Metal	σ_{\max} computed from DFT TGSF curves	σ_{\max} from $\sigma - \epsilon$ curve
Ta	7.81 GPa	6.48 GPa
Nb	8.08 GPa	6.49 GPa
Mo	15.25 GPa	14.87 GPa
W	18.40 GPa	17.41 GPa

Here we have computed the σ_{\max} from DFT sequential twinning GSF curves (under zero stress) for BCC Ta, Nb, Mo, and W. These values are listed in Table 7.1. Additionally, $\sigma - \epsilon$ curves have been generated (shown in Chapter 6) and the maximum stresses of those curves have also been tabulated in Table 7.1. The maximum stress values for both cases differ by less than 1 GPa in Mo and W whereas in Ta and Nb the difference is larger. The discrepancy arises from the stress-dependence of the twinning GSF curves [211] and this is evident in the twinning GSF curves under zero and nonzero stresses in this work (shown in Chapter 5). Despite the discrepancies in maximum strengths, Table 7.1 establishes an upper bound for homogeneous twin nucleation in BCC transition metals.

7.1.2 Lower bound

To estimate the lower limit of twinning stress, let us consider a pure BCC crystal schematically shown in Figure 6.8 where a twin embryo is nucleated by the application of shear stress τ . As mentioned earlier, Hirth and Lothe [141] introduced a simple model of the activation Gibbs free

energy of dislocation nucleation in terms of the increase in energy associated with the line length of the dislocation, the stacking fault energy, and the work done in the nucleation of the dislocation. For the lowest stress calculation, we can make the model described in Equation 6.45 even simpler by ignoring the line tension term and so this model will have the form:

$$\Delta G(\tau, R) = \sum_i \pi R^2 \gamma_{sf,i} - \sum_i \tau b_i \pi R^2 \quad (7.2)$$

In equilibrium, $\Delta G = 0$ and hence we obtain $\tau_{\min} = \frac{\gamma_{\text{twin}}}{\sum_i b_i}$. To compute minimum stress for homogeneous twin nucleation stress values, we take the γ values in sequential TGSF curves corresponding to metastable points with thinnest twin structure. In BCC Ta and Nb, the metastable points in the isosceles sequential TGSF curves for thinnest metastable twin correspond to three layer twins with two isosceles TBs and a reflection layer sandwiched between them. For Mo and W, we take the metastable points associated with two layer pure reflection twins. Table 7.2 lists the minimum stresses obtained from computed from the TGSF curves.

Table 7.2: Minimum stress for twin nucleation in BCC transition metals

BCC Transition Metal	σ_{\min} computed from DFT TGSF curves
Ta	2.53 GPa
Nb	2.62 GPa
Mo	5.33 GPa
W	6.77 GPa

Specifically, stacking fault energy, γ corresponding to the metastable points in TGSF curve is divided by $\sum_i b_i = b_1 + b_2 + b_3 = \frac{a}{12}\langle 111 \rangle + \frac{a}{6}\langle 111 \rangle + \frac{a}{12}\langle 111 \rangle$ for group VB metals. For group VIB metals $\sum_i b_i = b_1 + b_2 + b_3 = \frac{a}{6}\langle 111 \rangle + \frac{a}{6}\langle 111 \rangle$. The minimum twin nucleation stresses are compiled in Table 7.3 for comparison with predicted values by Ojha et al. [42] as well as the experimental values. From these values, we can see that the stress values predicted by the model proposed by Ojha et al. do not represent homogeneous nucleation stresses. Also, from Equation 7.2, we can see that the minimum stress calculation does not depend on the shape or size of the

dislocation loop and so the minimum stress values computed here also applies for heterogeneous twin nucleation. As mentioned earlier, Ojha et al. ignored the total stacking fault energy associated with twinning faults and instead, they chose to take the difference in energy between a one-layer unstable fault and a three layers stable fault for their stress calculation. This assumption, as pointed out earlier in this chapter, models twin growth instead of describing nucleation. And so this is the reason why Ojha et al. [42] obtained stress values that are a few orders of magnitude smaller than the minimum nucleation stresses obtained from our simple model in Equation 7.2. So this analysis refutes the modeling predictions by Ojha et al. that the bulk stress values reported in experiments are indeed the twin nucleation stresses.

Table 7.3: Minimum stress for twin nucleation compared against Ojha et al. prediction

BCC Metal	τ_{\min} for nucleation	τ_{pred} by Ojha et al.	$\tau_{\text{experimental}}$ (MPa)
Ta	2.526 GPa	252 MPa	198
			345
			181
			520
			224
Nb	2.620 GPa	254 MPa	137
			228
			198
			212
Mo	5.331 GPa	448 MPa	333
			440
W	6.772 GPa	720 MPa	750

7.2 Twin stress prediction as a function of temperature and strain rate

In addition to the calculation of upper and lower limits which provides insights into the range of stress level required for homogeneous twin nucleation in BCC metals, a model to predict nucleation strengths as a function of temperature and strain rate is developed in this section. This model has been used to predict dislocation nucleation strengths FCC nanowires [6, 126] and nanocrystals [80].

Here we have modified the derivation for twin nucleation in bulk crystals. The motivation is: in Table 2.1, we see that some variation in reported CRSS values exist with varying temperature and strain rate. The model is capable to predicting variations in nucleation stresses despite homogeneous twin nucleation in the experimental studies being highly unlikely. For this purpose, the first assumption in deriving the aforementioned semi-empirical expression is that crystal is defect free, so nucleation strength we will predict from this model will be applicable for homogeneous nucleation. We also have to assume that the rate of nucleation of under constant strain rate or stress rate loading conditions is equivalent to that under equilibrium conditions i.e., $\nu = N\nu_0 \exp\left(-\frac{\Delta G^*}{k_B T}\right)$ where N is the number of nucleation site, ν_0 is the frequency prefactor, ΔG^* is the energy barrier for nucleation of twinning partial dislocation, k_B is the Boltzmann constant and T is the temperature [212].

Now consider an ensemble of defect-free bulk single crystals all being subjected to the same strain rate conditions and define f as the fraction of bulk single crystals that have not nucleated a dislocation. Over any given time, if the dislocation nucleation rate is ν , then νf bulk single crystals nucleated a dislocation and the rate of change of surviving bulk single crystals can be described as:

$$\frac{df}{dt} = -\nu f \quad (7.3)$$

This can be rewritten as:

$$\frac{df}{d\sigma} \dot{\epsilon} E = -\nu f \quad (7.4)$$

where $\dot{\epsilon} E = \frac{d\sigma}{dt}$, $\dot{\epsilon}$ is the strain rate and $E = \frac{d\sigma}{d\epsilon}$ the elastic modulus. Taking the derivative with respect to stress:

$$\frac{d^2 f}{d\sigma^2} \dot{\sigma} = -\nu \frac{df}{d\sigma} - f \frac{d\nu}{d\sigma} \quad (7.5)$$

The most probable nucleation rate can be defined as:

$$\left. \frac{d^2 f}{d\sigma^2} \right|_{\sigma_{\text{crit}}} = 0 \quad (7.6)$$

Combining Equations 7.5 and 7.6 yields the following expression:

$$\left. \frac{df}{d\sigma} \right|_{\sigma_{\text{crit}}} = -\frac{f}{\nu} \left. \frac{d\nu}{d\sigma} \right|_{\sigma_{\text{crit}}} \quad (7.7)$$

This can be combined with Equation 7.4 to remove all the f terms.

$$\left. \frac{d\nu}{d\sigma} \right|_{\sigma_{\text{crit}}} = -\frac{\nu^2}{\dot{\sigma}} \left. \frac{d\nu}{d\sigma} \right|_{\sigma_{\text{crit}}} \quad (7.8)$$

Taking the derivative of nucleation rate with respect to stress yields:

$$\frac{d\nu}{d\sigma} = -\frac{N\nu_0}{k_B T} \Omega \exp\left(-\frac{\Delta G^*}{k_B T}\right) \quad (7.9)$$

where $\Omega = -\frac{\partial \Delta G^*(\sigma)}{\partial \sigma}$ is the activation volume for nucleation. Combining Equations 7.9 and 7.8 and assuming a constant strain rate result in the following implicit equation for the critical nucleation strength:

$$\frac{\Delta G^*}{k_B T} = \ln\left(\frac{N k_B T \nu_0}{E \dot{\epsilon} \Omega}\right) \quad (7.10)$$

We can now compute the nucleation strength as a function of temperature and strain rate by implicitly solving Equation 7.10. To solve for nucleation stress, we need to know the energy barrier $\Delta G^*(\tau)$ and the activation volume, $\Omega = -\frac{\partial \Delta G^*}{\partial \tau}$. For this purpose, energy barriers computed as a function of applied pure shear stress discussed in Chapter 6 (free-end string simulations) are used as input to this model for the activation energy, $\Delta G^*(\tau)$, on the zero-T potential energy surface using the Ravelo potential [77] for BCC Ta (see Figure 5.1(a)). As a first order approximation of temperature dependence on the activation free energy, we take $\Delta G^*(\sigma) = G_0 \left(1 - \frac{T}{T_m}\right)$ where T_m is a surface disordering temperature and we have chosen a value of 3293.15K (the melting temperature of Tantalum) for this temperature. We have taken $N = 12976$ which is the number of atoms in our free-end string simulations, $\nu_0 = \frac{k_B T}{h}$ (where h is the Planck constant) and $\mu = 59.6404$ GPa. The stress values obtained are listed in Table ?? along with the experimentally obtained bulk CRSS values for BCC Ta.

Table 7.4: Experimental CRSS values for BCC Ta, Mo, W, and Fe in literature compared with our prediction of homogeneous nucleation strength using nucleation energy barriers computed using Ravelo 2 [77] for Ta, ATFS [78] potentials for Mo and Fe as well as Zhou potential [80] for W.

BCC Metal	Reference	Temperature (K)	Strain rate (s^{-1})	CRSS (MPa)	Nucleation stress (GPa) from Eqn. }
Ta	Mitchell et al.	4.2	9.3×10^{-4}	198	5.80
	Shields et al.	4.2	5.0×10^{-4}	345	5.80
	Sherwood et al.	4.2	9.0×10^{-4}	181	5.80
	Chen et al.	77	1.0×10^4	520	5.79
	Florando et al.	77	1	224	5.79
Mo	Shaw et al.	104	4.2×10^{-4}	333	13.72
	Sherwood et al.	77	7.0×10^{-5}	440	13.73
W	Chiem et al.	298	1.8×10^3	750	13.52
Iron	Harding	195	1.0×10^{-3}	206	4.96

As evident from Tables 7.4, the stress obtained by implicitly solving Equation 7.10 are much larger than the bulk stress values from existing literature. This is because Equation 7.10 predicts nucleation stresses based on the assumption that the twinning partial dislocations are being nucleated homogeneously i.e., in defect free crystals. So the CRSS values in the experimental literature do not represent twin nucleation stresses. Since the stress prediction model by Ojha et al. [42] is based on twin migration energies and their predicted stresses match a few of the experimental CRSS values. So it seems that the CRSS values in the literature represents twin migration instead of nucleation. Hence we can conclude that twin nucleation in experimental studies can involve either one or both of the following mechanisms:

1. The BCC transition metal test specimens in the experimental studies [7, 11, 12, 14, 17, 20, 22, 58] contain impurities which can act as local stress concentrations, raising the local stress near ideal strength and facilitating homogeneous twin nucleation as suggested by Orowan [47].
2. Heterogeneous twin nucleation may occur from existing dislocations, free surfaces, or stacking faults in single crystal test specimens for references [7, 11, 12, 20, 22, 58]. Also for experimental studies that use polycrystalline samples [14, 17], grain boundaries can also be heterogeneous nucleation sites as demonstrated in the in-situ experiments by Wang et al. [67]. Additionally, Shaw et al. [17] observed twins emanating in BCC Mo specimens from an advancing crack. Heterogeneous nucleation, from the above mentioned sites, can significantly reduce the energy barrier for twin nucleation thus reducing the stress required to initiate twinning.

Chapter 8

Concluding Remarks

Deformation mechanisms in metallic elements under extreme conditions has been a topic of active research interest for several decades. Extreme loading conditions such as low temperature and/or high strain rate conditions, both of which imply high stress, can lead to plastic deformation via deformation twinning in BCC transition metals. The first evidence of plastic deformation via deformation twinning was reported by Barrett et al. [213] by impact loading Ta at liquid Nitrogen temperature in 1958. Shortly after that, Anderson et al. were able to twin high purity Ta at room temperature by hammering (high strain rate). Since then, several experimental studies on bulk BCC transition metals demonstrated deformation twinning all the way through 1975 [8, 12, 17–19, 21, 22, 26]. Then since the 2000s, the development of nanomechanical testing and impact loading techniques has also lead to experimental studies demonstrating plastic deformation by deformation twinning [23, 24, 27, 28, 58, 67]. Despite numerous experimental evidence of twinning which is a nucleation and growth phenomenon, atomic level insights such as critical nuclei size, their local atomic structures and energetics which are important parameters in modeling twin nucleation has been lacking. In this study, using atomistic and continuum modeling techniques, scientific questions on atomic level mechanisms of twin nucleation and propagation have been answered by rigorous implementation of the scientific method.

The first topic of interest is the local twin boundary structures and their energetics. Crystallographic description of twinning in BCC crystals imply pure reflection twin boundary structure however, isosceles triangle type twin boundaries have also been proposed in computational literature [38, 39, 41, 42]. In this study, conclusive evidences of metastability of isosceles twin boundaries in group VB BCC transition metals and α -Fe have been established using twin boundary GSF curves and full structural relaxation. These modeling techniques have also shown that a distorted reflection twin boundary structure is the lowest energy TB structure in group VIB BCC transition metals.

Next, nucleation of deformation twins in BCC transition metals has been investigated. As mentioned earlier, in the 1960-1970s experimental evidences of deformation twinning mediated plasticity in BCC transition metals were reported. Around that time, the pole mechanism [48] (which was proven to be aphysical later) and dislocation core dissociation mechanisms [37, 53] were formulated to explain the nucleation of twins. The dislocation dissociation mechanism, which points to a three layer thick critical twin nucleus size, has been widely recognized as the nucleation mechanism without experimental or computational proof since then. In this study, three layer thick pure reflection critical twin nucleus proposed by the dissociation mechanism has been refuted. Two layer thick isosceles-reflection twin in group VB metals, two layer thick double reflection in group VIB metals, and three layer thick isosceles-reflection-reflection structure in α -Fe have been shown to be the critical twin nuclei size using a combination of atomistic modeling techniques.

The third topic of interest is the growth phenomenon of deformation twins in BCC transition metals. Until the early 2000s, it was hypothesized that twins would first nucleate by the dislocation dissociate mechanism by three layer and then they would coalesce with one another by chance encounters resulting in $3n$ -layer microtwins [54]. This hypothesis has never been confirmed by experimental evidence. Decades later, with the development of computational techniques, small twin boundary migration energy barriers seen in twinning GSF curves led to the idea of layer-by-layer growth once a metastable critical twin is formed. However, recent in-situ experiments in Tungsten bicrystals by our collaborators has indicated that growth by multiple twinned layers can also be possible. However the twin boundary migration GSF curves generated in this study for BCC W have shown that the lowest migration barrier is indeed associated with layer-by-layer growth. Furthermore, frequency analysis of lattice resistance represented by twinning GSF curves has also helped explain the multi-layer growth observed by the in-situ experiment.

The final topic of interest is related to nucleation stresses for deformation twinning. Many experimental studies that demonstrated twinning also reported critical resolved shear stress (CRSS) values when plastic deformation took place. A modeling study by Ojha et al. [42] claimed that these CRSS values are associated with twin nucleation. However, the modeling techniques used

by these authors use twin migration energies from twinning GSF curves to predict stress values that are in the same order of magnitude of a few experimental studies they picked while excluding others. To refute this claim, upper and lower bounds of nucleation stresses for twinning have been computed in this study. Additionally, a semi-empirical model is developed for computing nucleation stresses as a function of temperature and strain rate. Combination of these modeling techniques show that the BCC transition metal test specimens in the experimental studies [7, 11, 12, 14, 17, 20, 22, 58] contain impurities which can act as local stress concentrations, raising the local stress near ideal strength and facilitating homogeneous twin nucleation as suggested by Orowan [47]. Also heterogeneous twin nucleation may occur from existing dislocations, free surfaces, or stacking faults in single crystal test specimens for references [7, 11, 12, 20, 22, 58]. Also for experimental studies that use polycrystalline samples [14, 17], grain boundaries can also be heterogeneous nucleation sites as demonstrated in the in-situ experiments by Wang et al. [67]. Additionally, Shaw et al. [17] observed twins emanating in BCC Mo specimens from an advancing crack. Heterogeneous nucleation, from the above mentioned sites, can significantly reduce the energy barrier for twin nucleation thus reducing the stress required to initiate twinning.

Chapter 9

Future Work

While this work has sought to provide a thorough study of twin nucleation and growth in BCC transition metals, there is still a significant amount of work that could still be conducted in this field. Several potential avenues of research will be summarized in this chapter.

Extend continuum modeling with DFT data

The critical twin nuclei thickness discussed in Chapter 5 points to disparate twin thickness predictions from atomistic and DFT simulations. Specifically, free-end string simulations using EAM potentials give three layer twin nuclei as saddle structures for Ta modeled by Ravelo 2 [77], ATFS [78], and Zhou [80] potentials as well as Fe modeled by ATFS and Chamati [123]. Also from the string simulations, one layer reflection twins are found to be the saddle structures for Mo modeled by ATFS potential and W modeled by Zhou potential. DFT predictions, on the other hand, are more consistent predicting two layer thick twin nuclei for BCC Ta, Nb, V, Mo, W and Cr with the exception of α -Fe for which the critical twin nucleus is three layer thick.

In Chapter 6, it has been shown that the continuum model in Equation 6.47 is capable of reproducing the energy barrier data from string simulations using Ta-Ravelo2 and Fe-ATFS potentials. The GSF and elastic energy terms of the model for these two EAM potentials are based on the three layer thick twin nuclei observed in the string simulations. Since the thickness predictions are different for the two modeling techniques, it can be worth modeling energy barrier as a function of applied shear stress using DFT inputs. To do this, twinning GSF curves generated by DFT simulations can be fed into this model to compute energy barriers as a function of applied shear stress. Since DFT simulations are more reliable in modeling atomic bonding, the energy barrier predictions with DFT TGSF curves can then be considered more accurate estimates of homogeneous twin nucleation in BCC transition metals.

Modeling heterogeneous twin nucleation

The nucleation stresses computed from our semi-empirical model in Eqn. 7.10 are close to the ideal strengths of the BCC transition metals indicating that if twins nucleate under such large stresses in the experimental studies, then local stress concentrations from impurities present in the test specimens can increase the local stress closer to the ideal strength. However one might speculate that heterogeneous nucleation in the few experiments with polycrystalline test specimens may also occur from grain boundaries [14, 17, 67] or, in the case of Mo specimens in the work by Shaw et al. [17], existing cracks. Heterogeneous nucleation potentially can significantly reduce the energy barrier for twin nucleation thus reducing the stress required to initiate twinning to get close to the CRSS values in the experimental literature.

To this end, our continuum model in Equation 6.47 can be modified to study heterogeneous nucleation of twins from a surface or otherwise named half space nucleation by Jennings et al. [126]. The authors point out that in order to model heterogeneous nucleation of dislocations from a nanowire surface, two additional pieces of physics need to be included in the nucleation model:

1. the image effects from the proximity of a dislocation to the free surface
2. the creation of a surface ledge following dislocation nucleation

The simplest case chosen was the simple case of nucleation of a semicircular dislocation from a half-space such that its Burgers vector is parallel to the surface plane. The image effects can be included in the model in the form of a reduction in dislocation line energy. The dislocation line energy, as currently written, describes the energy required to nucleate a dislocation in bulk. However, near a free surface, a dislocation's line energy is expected to decrease relative to the bulk as a result of the zero-traction condition on the free surface [214]. As generating the full solution for the image field of an arbitrarily nucleating dislocation is cumbersome, Beltz and Freund have analytically solved the dislocation line energy for a particular case, namely a dislocation nucleating at the surface of an isotropic elastic half-space, and have found a correction factor m inside the natural log term in the expression for dislocation line energy, as shown in Eqn. 9.1. Jennings et al.

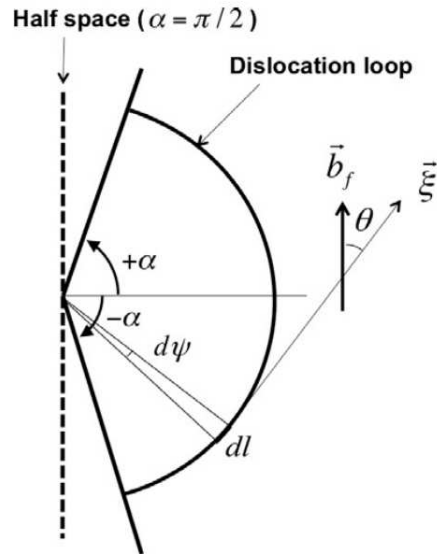


Figure 9.1: Schematic diagram of heterogeneous dislocation nucleation. Reproduced from [126] with permission.

found that the nucleation strengths obtained by using Eqn. 7.10 with the energy barrier predictions from this heterogeneous nucleation model with the line tension energy term in Eqn. 9.1 were a factor of 15-35% less than those for homogeneous nucleation.

$$E_{\text{line}} = \int_{-\alpha}^{\alpha} \frac{\mu b^2}{4\pi(1-\nu)} (1 - \nu(\cos(\theta))^2) R \ln \left(m \frac{R}{r_c} \right) d\psi \quad (9.1)$$

Bibliography

- [1] A Kelly and G Groves. *Crystallography and defects in crystals*. 1974.
- [2] Wei Cai and William D Nix. *Imperfections in crystalline solids*. Cambridge University Press, 2016.
- [3] John Wyrill Christian and Subhash Mahajan. Deformation twinning. *Progress in materials science*, 39(1-2):1–157, 1995.
- [4] Cedric Nicholas Reid. *Deformation geometry for materials scientists: international series on materials science and technology*, volume 11. Elsevier, 2016.
- [5] JW Christian. Some surprising features of the plastic deformation of body-centered cubic metals and alloys. *Metallurgical transactions A*, 14(7):1237–1256, 1983.
- [6] Christopher Robert Weinberger, Brad Lee Boyce, and Corbett Chandler Battaile. Slip planes in bcc transition metals. *International Materials Reviews*, 58(5):296–314, 2013.
- [7] TE Mitchell, RA Foxall, and PB Hirsch. Work-hardening in niobium single crystals. *Philosophical Magazine*, 8(95):1895–1920, 1963.
- [8] TE Mitchell and WA Spitzig. Three-stage hardening in tantalum single crystals. *Acta metallurgica*, 13(11):1169–1179, 1965.
- [9] RL Smialek and TE Mitchell. Interstitial solution hardening in tantalum single crystals. *Philosophical Magazine*, 22(180):1105–1127, 1970.
- [10] J Richter. The influence of temperature on slip behaviour of molybdenum single crystals deformed in tension in the range from 293 to 573 K. *physica status solidi (b)*, 40(2):565–572, 1970.
- [11] JA Shields, SH Goods, R Gibala, and TE Mitchell. Deformation of high purity tantalum single crystals at 4.2 k. *Materials Science and Engineering*, 20:71–81, 1975.

- [12] PJ Sherwood, F Guiu, Ho Chul Kim, and Po L Pratt. Plastic anisotropy of tantalum, niobium, and molybdenum. *Canadian Journal of Physics*, 45(2):1075–1089, 1967.
- [13] CQ Chen, G Hu, JN Florando, M Kumar, KJ Hemker, and KT Ramesh. Interplay of dislocation slip and deformation twinning in tantalum at high strain rates. *Scripta Materialia*, 69(10):709–712, 2013.
- [14] Jeffrey N Florando, Bassem S El-Dasher, Changqiang Chen, Damian C Swift, Nathan R Barton, James M McNaney, Kalit T Ramesh, Kevin J Hemker, and Mukul Kumar. Effect of strain rate and dislocation density on the twinning behavior in tantalum. *AIP Advances*, 6(4):045120, 2016.
- [15] CN Reid, A Gilbert, and GT Hahn. Twinning, slip and catastrophic flow in niobium. *Acta metallurgica*, 14(8):975–983, 1966.
- [16] Roman Gröger, Zdeněk Chlup, Tereza Kuběnová, and Ivo Kuběna. Interplay of slip and twinning in niobium single crystals compressed at 77 k. *Journal of Materials Research*, 34(2):261–270, 2019.
- [17] B Jo Shaw. Twinning and the low temperature mechanical properties of polycrystalline niobium and molybdenum. *Journal of the Less Common Metals*, 13(3):294–306, 1967.
- [18] JW Edington and RE Smallman. On mechanical twinning in single crystals of vanadium. *Acta Metallurgica*, 13(7):765–770, 1965.
- [19] TG Lindley and RE Smallman. The plastic deformation of polycrystalline vanadium at low temperatures. *Acta metallurgica*, 11(5):361–371, 1963.
- [20] CY Chiem and Woei-Shyan Lee. The influence of dynamic shear loading on plastic deformation and microstructure of tungsten single crystals. *Materials Science and Engineering: A*, 187(1):43–50, 1994.

- [21] MJ Marcinkowski and HA Lipsitt. The plastic deformation of chromium at low temperatures. *Acta Metallurgica*, 10(2):95–111, 1962.
- [22] J Harding. The yield and fracture behaviour of high-purity iron single crystals at high rates of strain. *Proceedings of the Royal Society of London. Series A. Mathematical and Physical Sciences*, 299(1459):464–490, 1967.
- [23] V Livescu, JF Bingert, and TA Mason. Deformation twinning in explosively-driven tantalum. *Materials Science and Engineering: A*, 556:155–163, 2012.
- [24] LE Murr, MA Meyers, C-S Niou, YJ Chen, S Pappu, and C Kennedy. Shock-induced deformation twinning in tantalum. *Acta materialia*, 45(1):157–175, 1997.
- [25] RW Anderson and SE Bronisz. Twinning in tantalum. *Acta Met.*, 7, 1959.
- [26] HB Probst. Observations on twinning in zone-refined tungsten. 1961.
- [27] Jiangwei Wang, Zhi Zeng, Christopher R Weinberger, Ze Zhang, Ting Zhu, and Scott X Mao. In situ atomic-scale observation of twinning-dominated deformation in nanoscale body-centred cubic tungsten. *Nature materials*, 14(6):594–600, 2015.
- [28] YM Wang, AM Hodge, J Biener, AV Hamza, DE Barnes, Kai Liu, and TG Nieh. Deformation twinning during nanoindentation of nanocrystalline ta. *Applied Physics Letters*, 86(10):101915, 2005.
- [29] Michael D Uchic, Dennis M Dimiduk, Jeffrey N Florando, and William D Nix. Sample dimensions influence strength and crystal plasticity. *Science*, 305(5686):986–989, 2004.
- [30] Ting Zhu and Ju Li. Ultra-strength materials. *Progress in Materials Science*, 55(7):710–757, 2010.
- [31] Yongfeng Zhang, Paul C Millett, Michael Tonks, and Bulent Biner. Deformation-twin-induced grain boundary failure. *Scripta Materialia*, 66(2):117–120, 2012.

- [32] Søren L Frederiksen, Karsten W Jacobsen, and Jakob Schiøtz. Simulations of intergranular fracture in nanocrystalline molybdenum. *Acta materialia*, 52(17):5019–5029, 2004.
- [33] Zhiliang Pan, Yulong Li, and Q Wei. Tensile properties of nanocrystalline tantalum from molecular dynamics simulations. *Acta Materialia*, 56(14):3470–3480, 2008.
- [34] G Sainath and BK Choudhary. Orientation dependent deformation behaviour of bcc iron nanowires. *Computational Materials Science*, 111:406–415, 2016.
- [35] Peng Wang, Wu Chou, Anmin Nie, Yang Huang, Haimin Yao, and Hongtao Wang. Molecular dynamics simulation on deformation mechanisms in body-centered-cubic molybdenum nanowires. *Journal of Applied Physics*, 110(9):093521, 2011.
- [36] KPD Lagerlöf. On deformation twinning in bcc metals. *Acta metallurgica et materialia*, 41(7):2143–2151, 1993.
- [37] AW Sleswyk. $1/2\langle 111 \rangle$ screw dislocations and the nucleation of $\{112\}\langle 111 \rangle$ twins in the bcc lattice. *Philosophical Magazine*, 8(93):1467–1486, 1963.
- [38] V Vitek. Multilayer stacking faults and twins on $\{211\}$ planes in bcc metals. *Scripta Metallurgica*, 4(9):725–732, 1970.
- [39] A Ojha, H Sehitoglu, L Patriarca, and HJ Maier. Twin nucleation in fe-based bcc alloys—modeling and experiments. *Modelling and Simulation in Materials Science and Engineering*, 22(7):075010, 2014.
- [40] Suzhi Li, Xiangdong Ding, Junkai Deng, Turab Lookman, Ju Li, Xiaobing Ren, Jun Sun, and Avadh Saxena. Superelasticity in bcc nanowires by a reversible twinning mechanism. *Physical Review B*, 82(20):205435, 2010.
- [41] Zhe Shi and Chandra Veer Singh. Competing twinning mechanisms in body-centered cubic metallic nanowires. *Scripta Materialia*, 113:214–217, 2016.

- [42] Avinesh Ojha and Huseyin Sehitoglu. Twinning stress prediction in bcc metals and alloys. *Philosophical magazine letters*, 94(10):647–657, 2014.
- [43] YT Zhu, XZ Liao, and XL Wu. Deformation twinning in nanocrystalline materials. *Progress in Materials Science*, 57(1):1–62, 2012.
- [44] Irene J Beyerlein, Xinghang Zhang, and Amit Misra. Growth twins and deformation twins in metals. *Annual Review of Materials Research*, 44:329–363, 2014.
- [45] Christopher R Weinberger and Wei Cai. Plasticity of metal nanowires. *Journal of Materials Chemistry*, 22(8):3277–3292, 2012.
- [46] Vaclav Vitek. Intrinsic stacking faults in body-centred cubic crystals. *Philosophical Magazine*, 18(154):773–786, 1968.
- [47] E Orowan et al. Dislocations in metals. *AIME, New York*, 131, 1954.
- [48] AH Cottrell and BA Bilby. Lx. a mechanism for the growth of deformation twins in crystals. *The London, Edinburgh, and Dublin Philosophical Magazine and Journal of Science*, 42(329):573–581, 1951.
- [49] André Wegener Sleeswyk. Emissary dislocations: Theory and experiments on the propagation of deformation twins in α -iron. *Acta Metallurgica*, 10(8):705–725, 1962.
- [50] K Ogawa. Edge dislocations dissociated in $\{112\}$ planes and twinning mechanism of bcc metals. *Philosophical Magazine*, 11(110):217–233, 1965.
- [51] R Priestner and WC Leslie. Nucleation of deformation twins at slip plane intersections in bcc metals. *Philosophical Magazine*, 11(113):895–916, 1965.
- [52] Piyas Chowdhury and Huseyin Sehitoglu. Atomistic energetics and critical twinning stress prediction in face and body centered cubic metals: recent progress. *Journal of Engineering Materials and Technology*, 140(2), 2018.

- [53] K Ogawa and R Maddin. Transmission electron-microscopic studies of twinning in mo-re alloys. *Acta metallurgica*, 12(6):713–721, 1964.
- [54] S Mahajan. Nucleation and growth of deformation twins in mo-35 at.% re alloy. *Philosophical Magazine*, 26(1):161–171, 1972.
- [55] P Pirouz. Deformation mode in silicon, slip or twinning? *Scripta metallurgica*, 21(11):1463–1468, 1987.
- [56] S Mahajan. Interrelationship between slip and twinning in bcc crystals. *Acta Metallurgica*, 23(6):671–684, 1975.
- [57] S Mahajan. Evaluation of slip patterns observed in association with deformation twins in mo-35 at% re alloy. *Journal of Physics F: Metal Physics*, 2(1):19, 1972.
- [58] CQ Chen, JN Florando, M Kumar, KT Ramesh, and KJ Hemker. Incipient deformation twinning in dynamically sheared bcc tantalum. *Acta materialia*, 69:114–125, 2014.
- [59] Binbin Jiang, Aidong Tu, Hao Wang, Huichao Duan, Suyun He, Hengqiang Ye, and Kui Du. Direct observation of deformation twinning under stress gradient in body-centered cubic metals. *Acta Materialia*, 155:56–68, 2018.
- [60] Jaime Marian, Wei Cai, and Vasily V Bulatov. Dynamic transitions from smooth to rough to twinning in dislocation motion. *Nature materials*, 3(3):158–163, 2004.
- [61] GJ Ackland, DJ Bacon, AF Calder, and T Harry. Computer simulation of point defect properties in dilute Fe-Cu alloy using a many-body interatomic potential. *Philosophical Magazine A*, 75(3):713–732, 1997.
- [62] HJ Chu, J Wang, and IJ Beyerlein. Anomalous reactions of a supersonic coplanar dislocation dipole: Bypass or twinning? *Scripta Materialia*, 67(1):69–72, 2012.
- [63] S Ogata, J Li, and S Yip. Twinning pathway in bcc molybdenum. *EPL (Europhysics Letters)*, 68(3):405, 2004.

- [64] Shigenobu Ogata, Ju Li, and Sidney Yip. Energy landscape of deformation twinning in bcc and fcc metals. *Physical Review B*, 71(22):224102, 2005.
- [65] Anik HM Faisal and Christopher R Weinberger. Modeling twin boundary structures in body centered cubic transition metals. *Computational Materials Science*, 197:110649, 2021.
- [66] QH Tang and TC Wang. Deformation twinning and its effect on crack extension. *Acta materialia*, 46(15):5313–5321, 1998.
- [67] Jiangwei Wang, Anik HM Faisal, Xiyao Li, Youran Hong, Qi Zhu, Hongbin Bei, Ze Zhang, Scott X Mao, and Christopher R Weinberger. Discrete twinning dynamics and size-dependent dislocation-to twin transition in body-centred cubic tungsten. *Journal of Materials Science & Technology*, 106:33–40, 2022.
- [68] V Vitek and V Paidar. Non-planar dislocation cores: a ubiquitous phenomenon affecting mechanical properties of crystalline materials. *Dislocations in solids*, 14:439–514, 2008.
- [69] MA Meyers, O Vöhringer, and VA Lubarda. The onset of twinning in metals: a constitutive description. *Acta materialia*, 49(19):4025–4039, 2001.
- [70] Julien Chaussidon, Marc Fivel, and David Rodney. The glide of screw dislocations in bcc fe: atomistic static and dynamic simulations. *Acta materialia*, 54(13):3407–3416, 2006.
- [71] MR Gilbert, S Queyreau, and J Marian. Stress and temperature dependence of screw dislocation mobility in α -fe by molecular dynamics. *Physical Review B*, 84(17):174103, 2011.
- [72] Hyounki Park, Michael R Fellingner, Thomas J Lenosky, William W Tipton, Dallas R Trinkle, Sven P Rudin, Christopher Woodward, John W Wilkins, and Richard G Hennig. Ab initio based empirical potential used to study the mechanical properties of molybdenum. *Physical Review B*, 85(21):214121, 2012.
- [73] NIST Interatomic Potential Repository. <https://www.ctcms.nist.gov/potentials/>, 2020.

- [74] Murray S Daw and Michael I Baskes. Embedded-atom method: Derivation and application to impurities, surfaces, and other defects in metals. *Physical Review B*, 29(12):6443, 1984.
- [75] Pär AT Olsson. Semi-empirical atomistic study of point defect properties in bcc transition metals. *Computational materials science*, 47(1):135–145, 2009.
- [76] Michael R Fellingner, Hyoungki Park, and John W Wilkins. Force-matched embedded-atom method potential for niobium. *Physical Review B*, 81(14):144119, 2010.
- [77] R Ravelo, TC Germann, O Guerrero, Q An, and BL Holian. Shock-induced plasticity in tantalum single crystals: Interatomic potentials and large-scale molecular-dynamics simulations. *Physical Review B*, 88(13):134101, 2013.
- [78] GJ Ackland and R Thetford. An improved n-body semi-empirical model for body-centred cubic transition metals. *Philosophical Magazine A*, 56(1):15–30, 1987.
- [79] Li Zhong, Jiangwei Wang, Hongwei Sheng, Ze Zhang, and Scott X Mao. Formation of monatomic metallic glasses through ultrafast liquid quenching. *Nature*, 512(7513):177–180, 2014.
- [80] XW Zhou, RA Johnson, and HNG Wadley. Misfit-energy-increasing dislocations in vapor-deposited coFe/nife multilayers. *Physical Review B*, 69(14):144113, 2004.
- [81] AM Guellil and JB Adams. The application of the analytic embedded atom method to bcc metals and alloys. *Journal of materials research*, 7(3):639–652, 1992.
- [82] CA Howells and Y Mishin. Angular-dependent interatomic potential for the binary ni–cr system. *Modelling and Simulation in Materials Science and Engineering*, 26(8):085008, 2018.
- [83] Alexander Stukowski, Babak Sadigh, Paul Erhart, and Alfredo Caro. Efficient implementation of the concentration-dependent embedded atom method for molecular-dynamics and

- monte-carlo simulations. *Modelling and Simulation in Materials Science and Engineering*, 17(7):075005, 2009.
- [84] MW Finnis and JE Sinclair. A simple empirical n-body potential for transition metals. *Philosophical Magazine A*, 50(1):45–55, 1984.
- [85] DE Smirnova, A Yu Kuksin, SV Starikov, VV Stegailov, Z Insepov, J Rest, and AM Yacout. A ternary eam interatomic potential for u–mo alloys with xenon. *Modelling and Simulation in Materials Science and Engineering*, 21(3):035011, 2013.
- [86] Ellad B. Tadmor and Ronald E. Miller. *Modeling Materials: Continuum, Atomistic and Multiscale Techniques*. Cambridge University Press, 2011.
- [87] Frank H Stillinger and Thomas A Weber. Hidden structure in liquids. *Physical Review A*, 25(2):978, 1982.
- [88] Frank H Stillinger and Thomas A Weber. Packing structures and transitions in liquids and solids. *Science*, 225(4666):983–989, 1984.
- [89] Frank H Stillinger and Thomas A Weber. Dynamics of structural transitions in liquids. *Physical Review A*, 28(4):2408, 1983.
- [90] Elijah Polak. *Computational methods in optimization: a unified approach*, volume 77. Academic press, 1971.
- [91] Andrzej Ruszczynski. *Nonlinear optimization*. Princeton university press, 2011.
- [92] David J Wales. Rearrangements of 55-atom lennard-jones and (c60) 55 clusters. *The Journal of chemical physics*, 101(5):3750–3762, 1994.
- [93] David J Wales and Tiffany R Walsh. Theoretical study of the water pentamer. *The Journal of chemical physics*, 105(16):6957–6971, 1996.

- [94] Tiffany R Walsh and David J Wales. Rearrangements of the water trimer. *Journal of the Chemical Society, Faraday Transactions*, 92(14):2505–2517, 1996.
- [95] Lindsey J Munro and David J Wales. Defect migration in crystalline silicon. *Physical Review B*, 59(6):3969, 1999.
- [96] GT Barkema and Normand Mousseau. Event-based relaxation of continuous disordered systems. *Physical review letters*, 77(21):4358, 1996.
- [97] Rachid Malek and Normand Mousseau. Dynamics of lennard-jones clusters: A characterization of the activation-relaxation technique. *Physical Review E*, 62(6):7723, 2000.
- [98] Graeme Henkelman and Hannes Jónsson. A dimer method for finding saddle points on high dimensional potential surfaces using only first derivatives. *The Journal of chemical physics*, 111(15):7010–7022, 1999.
- [99] Hannes Jónsson, Greg Mills, and Karsten W Jacobsen. Nudged elastic band method for finding minimum energy paths of transitions. In *Classical and quantum dynamics in condensed phase simulations*, pages 385–404. World Scientific, 1998.
- [100] E Weinan, Weiqing Ren, and Eric Vanden-Eijnden. String method for the study of rare events. *Physical Review B*, 66(5):052301, 2002.
- [101] Ting Zhu, Ju Li, Amit Samanta, Hyoungh Gyu Kim, and Subra Suresh. Interfacial plasticity governs strain rate sensitivity and ductility in nanostructured metals. *Proceedings of the National Academy of Sciences*, 104(9):3031–3036, 2007.
- [102] David S Sholl and Janice A Steckel. *Density functional theory: a practical introduction*. John Wiley & Sons, 2022.
- [103] Feliciano Giustino. *Materials modelling using density functional theory: properties and predictions*. Oxford University Press, 2014.

- [104] Christopher R Weinberger and Garritt J Tucker. Multiscale materials modeling for nanomechanics. 2016.
- [105] Georg Kresse and Jürgen Furthmüller. Efficiency of ab-initio total energy calculations for metals and semiconductors using a plane-wave basis set. *Computational materials science*, 6(1):15–50, 1996.
- [106] Georg Kresse and Jürgen Furthmüller. Efficient iterative schemes for ab initio total-energy calculations using a plane-wave basis set. *Physical review B*, 54(16):11169, 1996.
- [107] Peter W Atkins and Ronald S Friedman. *Molecular quantum mechanics*. Oxford university press, 2011.
- [108] Ian N Bakst. *Modeling pseudo-elasticity in small-scale ThCr₂Si₂-type crystals*. PhD thesis, Colorado State University Libraries.
- [109] Ramamurti Shankar. *Principles of quantum mechanics*. Springer Science & Business Media, 2012.
- [110] Walter Kohn and Lu Jeu Sham. Self-consistent equations including exchange and correlation effects. *Physical review*, 140(4A):A1133, 1965.
- [111] Walter Wolf and Peter Herzig. First-principles investigations of transition metal dihydrides, th₂: T= sc, ti, v, y, zr, nb; energetics and chemical bonding. *Journal of Physics: Condensed Matter*, 12(21):4535, 2000.
- [112] John P Perdew, Kieron Burke, and Matthias Ernzerhof. Generalized gradient approximation made simple. *Physical review letters*, 77(18):3865, 1996.
- [113] V Milman, B Winkler, and MIJ Probert. Stiffness and thermal expansion of zrb₂: an ab initio study. *Journal of physics: Condensed matter*, 17(13):2233, 2005.
- [114] C Fonseca Guerra, JG Snijders, G t Te Velde, and E Jan Baerends. Towards an order-n dft method. *Theoretical Chemistry Accounts*, 99:391–403, 1998.

- [115] PJ De Pablo, F Moreno-Herrero, J Colchero, J Gómez Herrero, P Herrero, AM Baró, Pablo Ordejón, José M Soler, and Emilio Artacho. Absence of dc-conductivity in λ -dna. *Physical review letters*, 85(23):4992, 2000.
- [116] Peter E Blöchl. Projector augmented-wave method. *Physical review B*, 50(24):17953, 1994.
- [117] Hendrik J Monkhorst and James D Pack. Special points for brillouin-zone integrations. *Physical review B*, 13(12):5188, 1976.
- [118] Richard Phillips Feynman. Forces in molecules. *Physical review*, 56(4):340, 1939.
- [119] William H Press, Saul A Teukolsky, William T Vetterling, and Brian P Flannery. *Numerical recipes 3rd edition: The art of scientific computing*. Cambridge university press, 2007.
- [120] Reeves Fletcher and Colin M Reeves. Function minimization by conjugate gradients. *The computer journal*, 7(2):149–154, 1964.
- [121] Steve Plimpton. Fast parallel algorithms for short-range molecular dynamics. *Journal of computational physics*, 117(1):1–19, 1995.
- [122] Matous Mrovec, Thorsten Ochs, Christian Elsässer, Vaclav Vitek, Duc Nguyen-Manh, and David G Pettifor. Never ending saga of a simple boundary. *energy*, 22:24, 2003.
- [123] H Chamati, NI Papanicolaou, Y Mishin, and DA Papaconstantopoulos. Embedded-atom potential for fe and its application to self-diffusion on fe (1 0 0). *Surface Science*, 600(9):1793–1803, 2006.
- [124] Keonwook Kang. *Atomistic Modelling of Fracture Mechanisms in Semiconductor Nanowires Under Tension*. Stanford University, 2010.
- [125] Christopher R Weinberger, Andrew T Jennings, Keonwook Kang, and Julia R Greer. Atomistic simulations and continuum modeling of dislocation nucleation and strength in gold nanowires. *Journal of the Mechanics and Physics of Solids*, 60(1):84–103, 2012.

- [126] Andrew T Jennings, Christopher R Weinberger, Seok-Woo Lee, Zachary H Aitken, Lucas Meza, and Julia R Greer. Modeling dislocation nucleation strengths in pristine metallic nanowires under experimental conditions. *Acta materialia*, 61(6):2244–2259, 2013.
- [127] Jonathan A Zimmerman, CL Kelchner, PA Klein, JC Hamilton, and SM Foiles. Surface step effects on nanoindentation. *Physical Review Letters*, 87(16):165507, 2001.
- [128] Alexander Stukowski, Vasily V Bulatov, and Athanasios Arsenlis. Automated identification and indexing of dislocations in crystal interfaces. *Modelling and Simulation in Materials Science and Engineering*, 20(8):085007, 2012.
- [129] Jian Wang, JP Hirth, and CN Tomé. $(1\bar{1}0)_{12}$ twinning nucleation mechanisms in hexagonal-close-packed crystals. *Acta Materialia*, 57(18):5521–5530, 2009.
- [130] John P Perdew, John A Chevary, Sy H Vosko, Koblar A Jackson, Mark R Pederson, Dig J Singh, and Carlos Fiolhais. Atoms, molecules, solids, and surfaces: Applications of the generalized gradient approximation for exchange and correlation. *Physical review B*, 46(11):6671, 1992.
- [131] David Vanderbilt. Soft self-consistent pseudopotentials in a generalized eigenvalue formalism. *Physical review B*, 41(11):7892, 1990.
- [132] Frank H Stillinger and Thomas A Weber. Computer simulation of local order in condensed phases of silicon. *Physical review B*, 31(8):5262, 1985.
- [133] PW Tasker and TJ Bullough. An atomistic calculation of extended planar defects in ionic crystals application to stacking faults in the alkali halides. *Philosophical Magazine A*, 43(2):313–324, 1981.
- [134] I Jęń Beyerlein, M Jęń Demkowicz, Ań Misra, and BP Uberuaga. Defect-interface interactions. *Progress in Materials Science*, 74:125–210, 2015.

- [135] Zhao Cheng, Haofei Zhou, Qihong Lu, Huajian Gao, and Lei Lu. Extra strengthening and work hardening in gradient nanotwinned metals. *Science*, 362(6414):eaau1925, 2018.
- [136] Ke Lu, Lei Lu, and S Suresh. Strengthening materials by engineering coherent internal boundaries at the nanoscale. *science*, 324(5925):349–352, 2009.
- [137] CRM Grovenor. Grain boundaries in semiconductors. *Journal of Physics C: Solid State Physics*, 18(21):4079, 1985.
- [138] OL Krivanek. High resolution imaging of grain boundaries and interfaces. In *Direct Imaging of Atoms in Crystals and Molecules \ Proc. Conf. \, Lidingo, Sweden, Aug. 1977,*, pages 213–218, 1979.
- [139] JQ Liu, M Skowronski, C Hallin, R Söderholm, and H Lendenmann. Structure of recombination-induced stacking faults in high-voltage sic p–n junctions. *Applied physics letters*, 80(5):749–751, 2002.
- [140] Hisaomi Iwata, Ulf Lindelfelt, Sven Öberg, and Patrick R Briddon. Localized electronic states around stacking faults in silicon carbide. *Physical Review B*, 65(3):033203, 2001.
- [141] Peter M Anderson, John P Hirth, and Jens Lothe. *Theory of dislocations*. Cambridge University Press, 2017.
- [142] J Wang, RG Hoagland, JP Hirth, L Capolungo, IJ Beyerlein, and CN Tomé. Nucleation of a (1 012) twin in hexagonal close-packed crystals. *Scripta materialia*, 61(9):903–906, 2009.
- [143] Hao Zhang, Bingqiang Wei, Xiaoqin Ou, Song Ni, Hongge Yan, and Min Song. Atomic-level study of {101 1} deformation twinning in pure ti and ti-5at.% al alloy. *International Journal of Plasticity*, 153:103273, 2022.
- [144] Xin-Yao Li, Ya-Fang Guo, Yong Mao, and Xiao-Zhi Tang. Nucleation and growth of {101⁻ 1} compression twin in mg single crystals. *International Journal of Plasticity*, 158:103437, 2022.

- [145] Alex C McLaren. *Transmission electron microscopy of minerals and rocks*. 1991.
- [146] S Mendelson. Zonal dislocations and twin lamellae in hcp metals. *Materials Science and Engineering*, 4(4):231–242, 1969.
- [147] S Mendelson. Dislocation dissociations in hcp metals. *Journal of applied physics*, 41(5):1893–1910, 1970.
- [148] N Thompson and DJ Millard. Xxxviii. twin formation, in cadmium. *The London, Edinburgh, and Dublin Philosophical Magazine and Journal of Science*, 43(339):422–440, 1952.
- [149] AJ Cao, YG Wei, and Scott X Mao. Deformation mechanisms of face-centered-cubic metal nanowires with twin boundaries. *Applied physics letters*, 90(15):151909, 2007.
- [150] Aleksandr V Korchuganov, Aleksandr N Tyumentsev, Konstantin P Zolnikov, Igor Yu Litovchenko, Dmitrij S Kryzhevich, Elazar Gutmanas, Shouxin Li, Zhongguang Wang, and Sergey G Psakhie. Nucleation of dislocations and twins in fcc nanocrystals: Dynamics of structural transformations. *Journal of Materials Science & Technology*, 35(1):201–206, 2019.
- [151] J Dana Honeycutt and Hans C Andersen. Molecular dynamics study of melting and freezing of small lennard-jones clusters. *Journal of Physical Chemistry*, 91(19):4950–4963, 1987.
- [152] Sylvie Aubry, Keonwook Kang, Seunghwa Ryu, and Wei Cai. Energy barrier for homogeneous dislocation nucleation: Comparing atomistic and continuum models. *Scripta Materialia*, 64(11):1043–1046, 2011.
- [153] Anik HM Faisal and Christopher R Weinberger. Exponent for the power-law relation between activation energy for dislocation nucleation and applied stress. *Physical Review Materials*, 3(10):103601, 2019.

- [154] Li Hu, Shuyong Jiang, Siwei Liu, Yanqiu Zhang, Yanan Zhao, and Chengzhi Zhao. Transformation twinning and deformation twinning of niti shape memory alloy. *Materials Science and Engineering: A*, 660:1–10, 2016.
- [155] Yang He, Bin Li, Chongmin Wang, and Scott X Mao. Direct observation of dual-step twinning nucleation in hexagonal close-packed crystals. *Nature communications*, 11(1):2483, 2020.
- [156] Ian N Bakst, Hang Yu, Mohammadreza Bahadori, Haibo Yu, Seok-Woo Lee, Mark Aindow, and Christopher R Weinberger. Insights into the plasticity of ag3sn from density functional theory. *International Journal of Plasticity*, 110:57–73, 2018.
- [157] Julia R Greer and Jeff Th M De Hosson. Plasticity in small-sized metallic systems: Intrinsic versus extrinsic size effect. *Progress in Materials Science*, 56(6):654–724, 2011.
- [158] Jaafar A El-Awady. Unravelling the physics of size-dependent dislocation-mediated plasticity. *Nature communications*, 6:5926, 2015.
- [159] Sidney S Brenner. Tensile strength of whiskers. *Journal of Applied Physics*, 27(12):1484–1491, 1956.
- [160] SS Brenner. Plastic deformation of copper and silver whiskers. *Journal of Applied Physics*, 28(9):1023–1026, 1957.
- [161] Claire Chisholm, Hongbin Bei, MB Lowry, Jason Oh, SA Syed Asif, OL Warren, ZW Shan, Easo P George, and Andrew M Minor. Dislocation starvation and exhaustion hardening in mo alloy nanofibers. *Acta Materialia*, 60(5):2258–2264, 2012.
- [162] Michael D Uchic, Paul A Shade, and Dennis M Dimiduk. Plasticity of micrometer-scale single crystals in compression. *Annual Review of Materials Research*, 39:361–386, 2009.
- [163] Ting Zhu, Ju Li, Shigenobu Ogata, and Sidney Yip. Mechanics of ultra-strength materials. *Mrs Bulletin*, 34(3):167–172, 2009.

- [164] Andrew T Jennings, Ju Li, and Julia R Greer. Emergence of strain-rate sensitivity in copper nanopillars: Transition from dislocation multiplication to dislocation nucleation. *Acta Materialia*, 59(14):5627–5637, 2011.
- [165] Lisa Y Chen, Mo-rigen He, Jungho Shin, Gunther Richter, and Daniel S Gianola. Measuring surface dislocation nucleation in defect-scarce nanostructures. *Nature materials*, 14(7):707, 2015.
- [166] Yong Zhu, Qingquan Qin, Feng Xu, Fengru Fan, Yong Ding, Tim Zhang, Benjamin J Wiley, and Zhong Lin Wang. Size effects on elasticity, yielding, and fracture of silver nanowires: In situ experiments. *Physical review B*, 85(4):045443, 2012.
- [167] He Zheng, Ajing Cao, Christopher R Weinberger, Jian Yu Huang, Kui Du, Jianbo Wang, Yanyun Ma, Younan Xia, and Scott X Mao. Discrete plasticity in sub-10-nm-sized gold crystals. *Nature communications*, 1:144, 2010.
- [168] Bin Wu, Andreas Heidelberg, and John J Boland. Mechanical properties of ultrahigh-strength gold nanowires. *Nature materials*, 4(7):525, 2005.
- [169] Jong-Hyun Seo, Youngdong Yoo, Na-Young Park, Sang-Won Yoon, Hyoban Lee, Sol Han, Seok-Woo Lee, Tae-Yeon Seong, Seung-Cheol Lee, Kon-Bae Lee, et al. Superplastic deformation of defect-free Au nanowires via coherent twin propagation. *Nano Letters*, 11(8):3499–3502, 2011.
- [170] Andreas Sedlmayr, Erik Bitzek, Daniel S Gianola, Gunther Richter, Reiner Mönig, and Oliver Kraft. Existence of two twinning-mediated plastic deformation modes in Au nanowhiskers. *Acta Materialia*, 60(9):3985–3993, 2012.
- [171] Dan Mordehai, Seok-Woo Lee, Björn Backes, David J Srolovitz, William D Nix, and Eugen Rabkin. Size effect in compression of single-crystal gold microparticles. *Acta Materialia*, 59(13):5202–5215, 2011.

- [172] Wei-Zhong Han, Ling Huang, Shigenobu Ogata, Hajime Kimizuka, Zhao-Chun Yang, Christopher Weinberger, Qing-Jie Li, Bo-Yu Liu, Xi-Xiang Zhang, Ju Li, et al. From “smaller is stronger” to “size-independent strength plateau”: Towards measuring the ideal strength of iron. *Advanced Materials*, 27(22):3385–3390, 2015.
- [173] Dariusz Chrobak, Natalia Tymiak, Aaron Beaber, Ozan Ugurlu, William W Gerberich, and Roman Nowak. Deconfinement leads to changes in the nanoscale plasticity of silicon. *Nature nanotechnology*, 6(8):480, 2011.
- [174] Ju Li. The mechanics and physics of defect nucleation. *MRS bulletin*, 32(2):151–159, 2007.
- [175] Xiaoyan Li, Yujie Wei, Lei Lu, Ke Lu, and Huajian Gao. Dislocation nucleation governed softening and maximum strength in nano-twinned metals. *Nature*, 464(7290):877, 2010.
- [176] Gunther Richter, Karla Hillerich, Daniel S Gianola, Reiner Monig, Oliver Kraft, and Cynthia A Volkert. Ultrahigh strength single crystalline nanowhiskers grown by physical vapor deposition. *Nano Letters*, 9(8):3048–3052, 2009.
- [177] Hongbin Bei, Sanghoon Shim, Easo P George, Michael K Miller, EG Herbert, and George Mathews Pharr. Compressive strengths of molybdenum alloy micro-pillars prepared using a new technique. *Scripta Materialia*, 57(5):397–400, 2007.
- [178] Ju Li, Krystyn J Van Vliet, Ting Zhu, Sidney Yip, and Subra Suresh. Atomistic mechanisms governing elastic limit and incipient plasticity in crystals. *Nature*, 418(6895):307, 2002.
- [179] CA Schuh, JK Mason, and AC Lund. Quantitative insight into dislocation nucleation from high-temperature nanoindentation experiments. *Nature Materials*, 4(8):617, 2005.
- [180] Peter Schall, Itai Cohen, David A Weitz, and Frans Spaepen. Visualizing dislocation nucleation by indenting colloidal crystals. *Nature*, 440(7082):319, 2006.
- [181] Harold S Park and Jonathan A Zimmerman. Modeling inelasticity and failure in gold nanowires. *Physical Review B*, 72(5):054106, 2005.

- [182] Ting Zhu, Ju Li, Amit Samanta, Austin Leach, and Ken Gall. Temperature and strain-rate dependence of surface dislocation nucleation. *Phys. Rev. Lett.*, 100:025502, Jan 2008.
- [183] UF Kocks, AS Argon, and MF Ashby. Thermodynamics and kinetics of slip, volume 19 in progress in materials science, b. chalmers, jw christian and tb massalsk, eds, 1975.
- [184] Seunghwa Ryu, Keonwook Kang, and Wei Cai. Predicting the dislocation nucleation rate as a function of temperature and stress. *Journal of Materials Research*, 26(18):2335–2354, 2011.
- [185] Shotaro Hara, Satoshi Izumi, and Shinsuke Sakai. Reaction pathway analysis for dislocation nucleation from a ni surface step. *Journal of Applied Physics*, 106(9):093507, 2009.
- [186] S Brochard, P Hirel, L Pizzagalli, and J Godet. Elastic limit for surface step dislocation nucleation in face-centered cubic metals: Temperature and step height dependence. *Acta Materialia*, 58(12):4182–4190, 2010.
- [187] P Hirel, J Godet, S Brochard, L Pizzagalli, and P Beauchamp. Determination of activation parameters for dislocation formation from a surface in fcc metals by atomistic simulations. *Physical Review B*, 78(6):064109, 2008.
- [188] LD Nguyen and DH Warner. Improbability of void growth in aluminum via dislocation nucleation under typical laboratory conditions. *Physical review letters*, 108(3):035501, 2012.
- [189] Doron Chachamovitz and Dan Mordehai. The stress-dependent activation parameters for dislocation nucleation in molybdenum nanoparticles. *Scientific reports*, 8(1):1–10, 2018.
- [190] R Becker. Über die plastizität amorpher und kristalliner fester körper. *Physikalische Zeitschrift*, 26:919–925, 1925.
- [191] John W Cahn and FRN Nabarro. Thermal activation under shear. *Philosophical Magazine A*, 81(5):1409–1426, 2001.

- [192] AH Cottrell. Thermally activated plastic glide. *Philosophical Magazine Letters*, 82(2):65–70, 2002.
- [193] A. Braun, K.M. Briggs, and P. BřÁŃi. Analytical solution to matthews’s and blakeslee’s critical dislocation formation thickness of epitaxially grown thin films. *Journal of Crystal Growth*, 241(1):231 – 234, 2002.
- [194] S R Valluri, D J Jeffrey, and R M Corless. Some applications of the lambert w function to physics. *Canadian Journal of Physics*, 78(9):823–831, 2000.
- [195] Craig E Maloney and Daniel J Lacks. Energy barrier scalings in driven systems. *Physical Review E*, 73(6):061106, 2006.
- [196] Robert M Corless, Gaston H Gonnet, David EG Hare, David J Jeffrey, and Donald E Knuth. On the lambertw function. *Advances in Computational mathematics*, 5(1):329–359, 1996.
- [197] Smarajit Karmakar, Edan Lerner, and Itamar Procaccia. Statistical physics of the yielding transition in amorphous solids. *Physical Review E*, 82(5):055103, 2010.
- [198] Craig Maloney and Anael Lemaitre. Universal breakdown of elasticity at the onset of material failure. *Physical review letters*, 93(19):195501, 2004.
- [199] David Rodney, Anne Tanguy, and Damien Vandembroucq. Modeling the mechanics of amorphous solids at different length scale and time scale. *Modelling and Simulation in Materials Science and Engineering*, 19(8):083001, 2011.
- [200] Peter Hänggi, Peter Talkner, and Michal Borkovec. Reaction-rate theory: fifty years after kramers. *Reviews of modern physics*, 62(2):251, 1990.
- [201] Jeffrey C Lagarias, James A Reeds, Margaret H Wright, and Paul E Wright. Convergence properties of the nelder–mead simplex method in low dimensions. *SIAM Journal on optimization*, 9(1):112–147, 1998.

- [202] Michael Polanyi. Über eine art gitterstörung, die einen kristall plastisch machen könnte. *Zeitschrift für Physik*, 89(9):660–664, 1934.
- [203] Rudolf Peierls. The size of a dislocation. *Proceedings of the Physical Society (1926-1948)*, 52(1):34, 1940.
- [204] Ting Zhu, Ju Li, Krystyn J Van Vliet, Shigenobu Ogata, Sidney Yip, and Subra Suresh. Predictive modeling of nanoindentation-induced homogeneous dislocation nucleation in copper. *Journal of the Mechanics and Physics of Solids*, 52(3):691–724, 2004.
- [205] JA Frenkel. Zur theorie der elastizitätsgrenze und der festigkeit kristallinischer körper. *Zeitschrift für Physik*, 37(7-8):572–609, 1926.
- [206] Geoffrey Ingram Taylor. The mechanism of plastic deformation of crystals. part i. theoretical. *Proceedings of the Royal Society of London. Series A, Containing Papers of a Mathematical and Physical Character*, 145(855):362–387, 1934.
- [207] Egon Orowan. Zur kristallplastizität. i. *Zeitschrift für Physik*, 89(9-10):605–613, 1934.
- [208] FRN Nabarro. Dislocations in a simple cubic lattice. *Proceedings of the Physical Society (1926-1948)*, 59(2):256, 1947.
- [209] JW Christian and V Vitek. Dislocations and stacking faults. *Reports on Progress in Physics*, 33(1):307, 1970.
- [210] Vasily V Bulatov and Efthimios Kaxiras. Semidiscrete variational peierls framework for dislocation core properties. *Physical Review Letters*, 78(22):4221, 1997.
- [211] Predrag Andric, Binglun Yin, and WA Curtin. Stress-dependence of generalized stacking fault energies. *Journal of the Mechanics and Physics of Solids*, 122:262–279, 2019.
- [212] Matthew Guziewski, Hang Yu, and Christopher R. Weinberger. *Modeling Dislocation Nucleation in Nanocrystals*, pages 373–411. Springer International Publishing, Cham, 2016.

- [213] CS Barrett and R Bakish. Twinning and cleavage in tantalum. *Transactions of the American Institute of Mining, Metallurgical and Petroleum Engineers*, 212:122–123, 1958.
- [214] E Rabkin, H-S Nam, and DJ Srolovitz. Atomistic simulation of the deformation of gold nanopillars. *Acta materialia*, 55(6):2085–2099, 2007.